

**School of Earth and Planetary Sciences**

**Small baseline subset InSAR data processing: design of  
interferogram networks and noise analysis in InSAR-derived  
deformation time series**

**Luyen Khac Bui**

**0000-0003-1091-5573**

**This thesis is presented for the Degree of  
Doctor of Philosophy  
of  
Curtin University**

**April 2021**

**Declaration**

To the best of my knowledge and belief this thesis contains no material previously published by any other person except where due acknowledgment has been made.

This thesis contains no material which has been accepted for the award of any other degree or diploma in any university.

Signature: .....

Date: .....

## LIST OF PUBLICATIONS

### Journal paper

1. Bui, L. K., Featherstone, W. E., and Filmer, M. S. (2020). Disruptive Influences of Residual Noise, Network Configuration and Data Gaps on InSAR-derived Land Motion Rates Using the SBAS Technique. *Remote Sensing of Environment*, 247, 111941. doi:[10.1016/j.rse.2020.111941](https://doi.org/10.1016/j.rse.2020.111941)

### Conference presentation

2. Bui, L. K., Featherstone, W. E., and Filmer, M. S. (2020). Noise analysis of InSAR SBAS-derived Deformation Time Series: Tests on Simulated Data. *AGU Fall Meeting 9-13 December 2019, San Francisco, U.S.*, 500636.

### Credit author statement

Author: Luyen K. Bui

Publication number	1	2
Devising of the simulations	✓	✓
Processing and analysing the data simulations	✓	✓
Writing, editing and revising the manuscripts	✓	✓

I acknowledge that these represent my contributions to the above research.

Sign:

Author: W.E. Featherstone

Publication number	1	2
Devising of the simulations	✓	✓
Processing and analysing the data simulations		
Writing, editing and revising the manuscripts	✓	✓

I acknowledge that these represent my contributions to the above research.

Sign:

Author: M.S. Filmer

Publication number	1	2
Devising of the simulations	✓	✓
Processing and analysing the data simulations		
Writing, editing and revising the manuscripts	✓	✓

I acknowledge that these represent my contributions to the above research.

Sign:

## ABSTRACT

Interferometric synthetic aperture radar (InSAR) has been applied in land surface deformation studies, in which the small baseline subset (SBAS) is one of the most commonly used multi-temporal InSAR (MT-InSAR) techniques. However, SBAS works by defining a network of interferograms (i.e., phase differences between pairs of SAR images) limited by temporal and perpendicular baseline thresholds that are often applied arbitrarily, or in an apparently subjective way. Some more objective ways by which to select these thresholds are therefore useful for InSAR SBAS data processing. This dissertation first assesses the influence of residual interferometric noise and data gaps on SBAS-derived rates and root mean square (RMS) of the difference between simulated and SBAS-derived deformation time series, and utilises redundancy numbers from the geodetic network “optimisation” problem to design an “optimal” SBAS network.

InSAR datasets of 1000 independent pixels experiencing simulated land subsidence of a linear trend superimposed by an annual sinusoidal oscillation of  $-2$  mm/yr plus 2 mm,  $-20$  mm/yr plus 5 mm and  $-100$  mm/yr plus 10 mm contaminated by Gaussian residual noise bounded within  $[-2, +2]$  mm,  $[-5, +5]$  mm, and  $[-10, +10]$  mm are simulated. The investigations on linear deformation signal indicate that the unweighted linear-fit deformation trend may become contradictory for small-magnitude deformation, which results from a network of fewer interferograms selected based on a small temporal baseline threshold of 33 days or less.

In the case of linear plus annual periodic signals, the linear-fit rates were biased compared to the simulated rate. Alternatively, when the rates were estimated using a more appropriate periodic functional model (i.e., not only linear), the estimated rates were not biased. This indicates that errors may potentially be introduced by simply using a linear regression model when nonlinear deformation may also be occurring.

Due to scheduling or other technical issues, SAR images are not always captured regularly, or in other cases, blocks of images acquired during, e.g., winter snowfall, may have to be omitted because of very low coherence, which is defined by a cross-correlation product from two complex-valued SAR images. The influence of this data gap phenomenon is also assessed with missing images assumed 1) random in time and 2) in blocks termed as “winter” gaps. The winter gaps have shown a larger influence

than random gaps in terms of rate errors and RMSs of the difference between simulated and SBAS-derived deformation time series. When networks of the same number of interferograms are used, which are chosen based on temporal baseline thresholds and according to random gaps, the influences of limiting temporal baseline is of larger rate errors. This suggests that the configuration of the SBAS network is more important because the trade-off may be a geometrically weak SBAS network.

Redundancy numbers from geodetic network design theory are investigated to determine if they are appropriate to design an “optimal” SBAS network. 144 interferometric networks determined by combinations of temporal and perpendicular baseline thresholds were tested with the minimum and maximum number of interferograms being 251 and 8778, respectively. A 1/10 ratio RMS criterion is then applied as a trade-off value to identify the “optimal” network with the results suggesting that redundancy numbers between  $\sim 0.8$  and  $\sim 0.9$  are a suitable range to design an “optimal” SBAS network.

This dissertation then conducts noise analysis on the InSAR SBAS deformation time series. A SAR image of  $500 \times 500$  pixels at a one-arc-second spatial resolution is simulated setting that, at each pixel, the Earth’s surface undergoes a deformation with a linear rate assumed between  $-40$  mm/yr and  $+40$  mm/year plus an annual trend with the amplitude limited within the range of  $[10, 20]$  mm. Interferometric noise and error sources are then simulated, consisting of digital surface model errors, atmospheric artefacts, orbital error, and temporal decorrelation. The noise analysis in the SBAS-derived deformation time series indicates that both white and coloured noise is present with the amplitudes of noise dominated by white noise. The spectral indices of coloured noise vary between  $-3.0$  and  $0$  with the mean value being  $-0.8$  which is close to the flicker noise spectral index of  $-1$ .

It is concluded that contradictory trends may be derived from InSAR SBAS if a network of fewer interferograms is applied in the case of low signal-to-noise ratios (SNR). Conversely, if too many interferograms are used with an SBAS network, high computation time and large data storage will be required. In this case, the redundancy number is of assistance. Because of the existence of coloured noise in residuals time series tested on simulated data in this dissertation, a model incorporating both white and coloured noise should be considered in the InSAR deformation time series modelling and interpretation.

## ACKNOWLEDGEMENTS

Firstly, I would like to thank my academic supervisors, Prof. Will Featherstone and Dr Mick Filmer for their guidance, assistance, and encouragement throughout this Ph.D. project. I am grateful to the Department of Foreign Affairs and Trade, Australian Government, for providing the Australia Award Scholarship (AAS) for postgraduate study. During the four-year studying as an AAS Ph.D. student at Curtin University, I have been supported by the manager and staff at the International Sponsored Students Unit, Curtin University. I therefore would like to thank Julie Craig, Kristen Soon, Hoa Pham, Ian Tsen, Raquel Tsuji Iliano for their patient and kind support.

I appreciate the Department of Geodesy, the Faculty of Geomatics and Land Administration, Hanoi University of Mining and Geology, Vietnam, for their support before and during my Ph.D. I would also like to thank Bert Veenendaal (former Head), Jon Kirby (former Head), and all staff at the [former] Department of Spatial Sciences for providing a warm, friendly, and enjoyable working environment.

Thanks also to Dr Amy Parker for her advice and discussions, particularly on the InSAR topic and during my Ph.D. candidacy progress when InSAR was totally new to me. Her help on ISCE software usage is especially thankful. I would also like to thank Todd Lyon for his guidance on LINUX server use. I acknowledge Dr Simon Williams (National Oceanography Centre Liverpool, UK) for providing guidance on CATS software usage. Many thanks are expressed to Ropesh Goyal for coming and being my labmate as well as his discussions on research and our life. I am grateful to Dr Paul Johnston for his invaluable discussions. California Institute of Technology (Caltech) is thanked for providing the source code of the Generic InSAR Analysis Toolbox (GIANt).

Finally, I would like to express my deepest thanks to my wife, Loan Nguyen, for her love and support, particularly in taking care of me and our children. Without her support, I would not be able to undertake this Ph.D. My love and thanks also to my children, Linh Bui (Nhim) and Khanh Bui (Bob) for quietly and patiently looking after themselves when I had to spend my time on research, though I would like to share my time with them. I have indebted my parents, Chu Bui and Gai Ngo, for giving birth to me and encouraging me to do this Ph.D. I am also thankful to my parent-in-law, my sister, and my brother for their encouragement.

## TABLE OF CONTENTS

ABSTRACT .....	i
ACKNOWLEDGEMENTS .....	iii
TABLE OF CONTENTS .....	iv
LIST OF FIGURES .....	vii
LIST OF TABLES .....	xi
LIST OF ACRONYMS AND ABBREVIATIONS.....	xii
LIST OF MATHEMATICAL SYMBOLS .....	xv
<b>1. INTRODUCTION</b> .....	<b>1</b>
1.1 Background .....	1
1.2 Contributions.....	8
1.3 Dissertation Structure.....	10
<b>2. GENERAL CONCEPTS OF INTERFEROMETRIC SYNTHETIC APERTURE RADAR (INSAR)</b> .....	<b>11</b>
2.1 Radar .....	11
2.2 Synthetic Aperture Radar .....	13
2.3 SAR Interferometry.....	17
2.3.1 Sensor Configuration .....	17
2.3.2 SAR Geometry .....	20
2.3.3 SAR phase filtering, unwrapping and geocoding .....	22
2.4 Chapter Summary.....	23
<b>3. PRINCIPLES OF NOISE AND ERROR REDUCTION IN INSAR INTERFEROGRAMS</b> .....	<b>25</b>
3.1 Sources of Errors and Noise in InSAR Interferograms.....	25
3.2 Orbital Error Reduction.....	27
3.2.1 Reduction Using a Polynomial Function .....	27
3.2.2 Reduction Using Other Geodetic Data.....	27
3.3 Atmospheric Error Reduction .....	28
3.3.1 Ionospheric Reduction .....	29
3.3.2 Tropospheric Reduction .....	32
3.4 Digital Surface Model Error Reduction .....	42
3.4.1 Reduction to Wrapped Interferograms.....	42
3.4.2 Reduction to Unwrapped Interferograms.....	44

3.5	Chapter Summary.....	45
4.	AN OVERVIEW OF THE SMALL BASELINE SUBSET (SBAS)	
	TECHNIQUE .....	48
4.1	SBAS Algorithms .....	48
4.2	Interferogram Selection.....	49
4.2.1	Selection Based on Baseline Thresholds .....	49
4.2.2	Selection Based on Other Strategies .....	53
4.3	Coherent Pixels Selection .....	56
4.3.1	Selection Based on Interferometric Coherence.....	56
4.3.2	Selection Based on Amplitude and Phase Stability .....	58
4.3.3	Selection Based on Interferometric Phase Misclosure.....	59
4.4	Error and Noise Reduction in SBAS.....	61
4.4.1	Orbital Error Reduction in SBAS .....	61
4.4.2	Atmospheric Error Reduction in SBAS .....	62
4.4.3	Digital Surface Model Error Reduction in SBAS .....	62
4.5	Small Baseline Subset Inversion.....	65
4.6	Chapter Summary.....	67
5.	SIMULATED INFLUENCE OF RESIDUAL INTERFEROMETRIC NOISE	
	AND DATA GAPS ON SBAS INSAR.....	69
5.1	InSAR Data Simulation .....	69
5.2	Interferogram Networks Chosen by Temporal and Perpendicular Baseline Thresholds.....	73
5.3	Influence of Residual Noise and Network Configuration.....	76
5.3.1	Influences on Simulated Linear Signals.....	76
5.3.2	Influences on Simulated Non-linear Signals.....	81
5.4	Influence of Data Gaps on SBAS-derived Rates .....	85
5.4.1	Random Data Gaps .....	85
5.4.2	“Winter” Data Gaps .....	94
5.5	Comparison With Other Network Types .....	98
5.5.1	Interferogram Network Formation.....	98
5.5.2	Results of Comparison .....	103
5.6	Chapter Summary.....	108
6.	GEODESY-BASED DESIGN OF SBAS INTERFEROGRAM NETWORKS ....	
	.....	110

6.1	Background on Design of Geodetic Networks.....	110
6.2	A Review of Design of Geodetic Networks.....	113
6.3	Design of InSAR SBAS Networks Using Redundancy Numbers .....	118
6.4	Tests With Other Network Types .....	129
6.5	Chapter Summary.....	133
7.	SIMULATED NOISE ANALYSIS OF INSAR SBAS DEFORMATION TIME SERIES .....	135
7.1	Correlated Noise.....	135
7.2	InSAR Data Simulation .....	138
7.2.1	Simulation of Surface Deformation and Noiseless Interferograms .....	138
7.2.2	Simulation of Interferogram Error due to DSM Uncertainty.....	140
7.2.3	Simulation of Atmospheric Artefacts .....	143
7.2.4	Simulated Orbital Error.....	145
7.2.5	Simulation of Temporal Decorrelation .....	146
7.3	InSAR Data Processing.....	148
7.4	Noise Analysis of Simulated Deformation Time Series .....	149
7.4.1	Deformation Rates, Amplitudes and Their Uncertainties Computed by CATS .....	149
7.4.2	Noise Amplitude and Spectral Indices.....	156
7.5	Chapter Summary.....	163
8.	SUMMARY, CONCLUSIONS AND RECOMMENDATIONS.....	164
8.1	Conclusions.....	164
8.1.1	Influence of Simulated Residual Interferometric Errors and Noise on SBAS InSAR.....	164
8.1.2	Design of InSAR SBAS Interferogram Networks .....	166
8.1.3	Noise Analysis of Simulated InSAR Deformation Time Series .....	168
8.2	Recommendations .....	169
8.2.1	Further Investigations Relying on Actual InSAR Data .....	169
8.2.2	Futher Investigations with Other Noise Models and Methods.....	170
	Appendix A RSE PAPER .....	171
	REFERENCES.....	186
	BIBLIOGRAPHY STATEMENT .....	217

## LIST OF FIGURES

Figure 2.1. An illustration of a SAR system. ....	14
Figure 2.2. Simplified scenario of different SAR modes.....	16
Figure 2.3. Components of a TSX SLC image. ....	17
Figure 2.4. InSAR interferogram imaging geometry. ....	20
Figure 2.5. An interferogram processed by the ISCE software (Rosen et al., 2018) from TSX data over Perth, Western Australia. ....	23
Figure 3.1. The correlation between InSAR LoS range change and topography from Cavalié et al. (2007). ....	33
Figure 4.1. A Delaunay triangulation interferogram network from ERS-1/2 SAR data from Pepe and Lanari (2006). ....	54
Figure 4.2. A hierarchical thresholds interferogram network from TSX SAR data from Zhao (2017). ....	55
Figure 4.3. A minimum spanning tree interferogram network from ERS-1/2 SAR data from Refice et al. (2006). ....	55
Figure 4.4. A coherence map generated by the ISCE software (Rosen et al., 2018) from TSX data over Perth, Western Australia. ....	58
Figure 4.5. A sketch of an interferogram phase loop between three image acquisitions. ....	60
Figure 5.1. Scatter plot of simulated perpendicular baseline history. ....	70
Figure 5.2. Different SBAS interferogram networks chosen relying on temporal baseline thresholds shown in Table 5.3 and a fixed perpendicular baseline threshold of 200 m.....	75
Figure 5.3. Comparison of rates computed by unweighted linear fit from combinations of different deformation signals. ....	77
Figure 5.4. Comparison of rate errors computed from different networks for four example pixels.....	79
Figure 5.5. Comparison of unweighted linear-fit rates from linear plus annual signals. ....	82
Figure 5.6. Comparison of unweighted least squares rates (left panel) and annual amplitudes (right panel) computed from linear plus annual signals. ....	84
Figure 5.7. Comparison of the interferogram network gaps in percentage of image removed.....	87

<a href="#">Figure 5.8.</a> Comparison of unweighted least squares rates computed from linear plus annual signals between the interferogram network of no gaps and those with randomly chosen gaps of various percentages. ....	89
<a href="#">Figure 5.9.</a> Comparison of RMSs of the difference between simulated and SBAS-derived deformation time series of all pixels between the SBAS interferogram network of no gaps and those with random gaps. ....	90
<a href="#">Figure 5.10.</a> (left) A network of 50% random data gaps formed by the temporal baseline threshold of 99 days, (right) unweighted least squares rates computed from linear plus annual signals between the interferogram network of no gaps and those with randomly chosen gaps of various percentages, of which the results of the 50% gaps case are from the network in the left panel. ....	91
<a href="#">Figure 5.11.</a> The influence of the change in number of interferograms chosen by various temporal baseline thresholds (blue) and due to random data gaps (green) on SBAS-derived unweighted least squares rates from simulated signal cases 1 ( <a href="#">Table 5.1</a> ). ....	92
<a href="#">Figure 5.12.</a> The influence of the change in number of interferograms chosen by various temporal baseline thresholds (blue) and due to random data gaps (green) on SBAS-derived unweighted least squares rates from simulated signal cases 2 ( <a href="#">Table 5.1</a> ). ....	93
<a href="#">Figure 5.13.</a> The influence of the change in number of interferograms chosen by various temporal baseline thresholds (blue) and due to random data gaps (green) on SBAS-derived unweighted least squares rates from simulated signal cases 3 ( <a href="#">Table 5.1</a> ). ....	94
<a href="#">Figure 5.14.</a> Interferogram networks without (top-left) and with (top-right, bottom) missing images. ....	95
<a href="#">Figure 5.15.</a> Comparison of unweighted least squares rates computed from linear plus annual signals according to interferogram networks with no gaps, random gaps and “winter” gaps. ....	97
<a href="#">Figure 5.16.</a> Comparison of RMSs of the difference between simulated and SBAS-derived deformation time series for all pixels between the interferogram networks of no gaps and those with randomly chosen gaps and “winter” gaps corresponding to ~25% missing images. ....	98
<a href="#">Figure 5.17.</a> Examples of disconnected, connected, and full Delaunay interferogram networks chosen based on different temporal baseline thresholds in <a href="#">Table 5.6</a> . ....	100

Figure 5.18. Hierarchical thresholds interferogram networks formed by multiple pairs of temporal and perpendicular baseline thresholds listed in Table 5.7.....	102
Figure 5.19. A minimum spanning tree interferogram network selected by the weights of normalised baseline lengths. ....	103
Figure 5.20. Comparison of unweighted linear-fit rates between SBAS networks, Delaunay triangulations, hierarchical thresholds networks, and a minimum spanning tree in the cases of simulated linear signals of $-2$ mm/yr (top-left), $-20$ mm/year (top-right), and $-100$ mm/yr (bottom). ....	104
Figure 5.21. Comparison between SBAS networks and Delaunay triangulations in estimated linear-fit rates and the number of selected interferograms applying the same temporal baseline thresholds. ....	105
Figure 5.22. Comparison of unweighted linear-fit rates and unweighted least squares rates from linear plus annual signals between four types of interferogram networks of SBAS, Delaunay triangulations, hierarchical thresholds, and a minimum spanning tree. ....	107
Figure 6.1. Examples of interferogram networks chosen based on different temporal and perpendicular baseline thresholds. $r$ -numbers computed corresponding to these networks are $\sim 0.2$ (top-left), $\sim 0.8$ (top-right) and $\sim 0.9$ (bottom).....	120
Figure 6.2. Dependence of the $r$ -numbers and SBAS-derived unweighted LS rates for 1000 pixels on the number of chosen interferograms with various linear plus annual signals.....	125
Figure 6.3. (top): Comparison of the change in the $r$ -numbers and the RMSs of the difference between simulated and SBAS-derived deformation time series, (bottom): Comparison of the change in the $r$ -numbers according to SBAS network interferogram numbers and computation time. ....	126
Figure 6.4. An example of simulated and SBAS-derived deformation time series of simulated signal case 1 in Table 5.1 contaminated by residual interferogram noise cases A (top-left), B (top-right) and C (bottom) as listed in Table 5.2.....	128
Figure 6.5. $r$ -numbers computed for the Delaunay triangulation networks with independent interferograms.....	130
Figure 6.6. $r$ -numbers computed for several Delaunay triangulation networks with dependent interferograms.....	131
Figure 6.7. $r$ -numbers computed for hierarchical thresholds networks.....	132

Figure 6.8. $r$ -numbers computed for the minimum spanning tree network.....	133
Figure 7.1. Histogram (left) and scatter plot (right) of 332 images of which locations are represented by temporal and perpendicular baselines.....	139
Figure 7.2. Network of interferograms chosen based on temporal and perpendicular baseline thresholds of 90 days and 200 m, respectively. ....	140
Figure 7.3. Map of fractal surface simulated DSM error. ....	142
Figure 7.4. Interferogram errors caused by simulated DSM uncertainties in Figure 7.3 of the first interferogram. ....	143
Figure 7.5. Histograms of standard deviation ( $\sigma$ ) (left) and wavelength ( $\lambda$ ) (right) of simulated atmospheric delays of 2510 interferograms.....	144
Figure 7.6. Simulated atmospheric artefacts of the first interferogram at the down-sampled resolution of 100×100 pixel (left) and at the full resolution of 500×500 pixels (right).....	145
Figure 7.7. Simulated orbital errors of the first interferogram.....	146
Figure 7.8. Simulated temporal decorrelation of the first interferogram. ....	148
Figure 7.9. Noisy deformation map of the first interferogram.....	148
Figure 7.10. Comparison between CATS-derived and simulated deformation rates and annual sinusoidal amplitudes. ....	150
Figure 7.11. Synthetic (yellow lines), SBAS-retrieved (blue lines) and CATS-derived (black lines) deformation time series for 25 pixels regularly distributed over the image in Figure 7.9. ....	152
Figure 7.12. Histograms of white noise amplitudes (left) and coloured noise amplitudes (right).....	157
Figure 7.13. Comparison between white and coloured noise magnitudes over 500×500 pixels. ....	158
Figure 7.14. Spatial patterns (left) and histograms (right) of power law spectral indices tested over the entire image of 500×500 pixels.....	158
Figure 7.15. Power spectral density in the deformation residuals of the 25 studied locations shown in Figure 7.9. ....	160

## LIST OF TABLES

Table 1.1. An interrogation of SCOPUS on 27 July 2020 shows the number of articles that use SBAS in relation to other DInSAR techniques.....	3
Table 1.2. Summary of the main SBAS approaches.....	5
Table 2.1. Radar bands with corresponding frequency and wavelength ranges. ....	12
Table 2.2. List of several SAR platforms classified by radar bands. ....	19
Table 3.1. Atmospheric models utilised in InSAR tropospheric correction. ....	40
Table 4.1. Examples of baseline thresholds used in several SBAS applications.....	51
Table 5.1. The three cases of simulated signals showing linear rates and annual amplitudes. ....	71
Table 5.2. Simulated noise with various ranges and standard deviations.....	72
Table 5.3. List of networks tested based on various temporal baseline thresholds. ..	74
Table 5.4. Number of images and interferograms removed after randomly choosing gaps. ....	86
Table 5.5. Number of removed and remaining images and interferograms corresponding to random and winter gaps cases.....	95
Table 5.6. List of Delaunay networks based on various temporal baseline thresholds. ....	99
Table 5.7. List of hierarchical thresholds networks based on various combinations of temporal and perpendicular baseline thresholds. ....	101
Table 6.1. A number of studies on the optimal design of networks from the geodetic literature .....	114
Table 6.2. Results of $r$ -numbers computation according to networks defined by various temporal and perpendicular baseline thresholds. ....	122
Table 7.1. Examples of error in InSAR interferograms caused by DSM uncertainties. ....	142
Table 7.2. Statistics of the errors in rate and amplitude determinations.....	151
Table 7.3. Statistics of white and coloured noise amplitudes and power law spectral indices estimated by CATS.....	157

## LIST OF ACRONYMS AND ABBREVIATIONS

AAS	Australia Award Scholarship
AGU	American Geophysical Union
BIQUE	Best Invariant Quadratic Unbiased Estimator
BLUE	Best Linear Unbiased Estimator
BOOM	Bi-Objective Optimisation Model
Caltech	California Institute of Technology
CATS	Create and Analyse Time Series
CPT	Coherent Pixels Technique
CSK	COSMO/SkyMed
DInSAR	Differential Interferometric Synthetic Aperture Radar
DOP	Dilution-of-Precision
DS	Distributed Scatterers
DSM	Digital Surface Model
ECMWF	the European Centre for Medium-Range Weather Forecasts
EDM	Electronic Distance Measurement
ENV	ENVISAT
ERS	European Remote Sensing
ESA	European Space Agency
FFT	Fast Fourier Transform
FOD	First-Order Design
GDOP	Geometrical Dilution-of-Precision
GIAnt	Generic InSAR Analysis Toolbox
GNSS	Global Navigation Satellite System
GPS	Global Positioning System
InSAR	Interferometric Synthetic Aperture Radar
IPTS	Interferometric Point Target Analysis
ISCE	InSAR Scientific Computing Environment
ITD	Iterative Tropospheric Decomposition
L-BFGS	Limited-memory bounded Broyden-Fletcher-Goldfarb-Shanno
LoS	Line-of-sight
LS	Least squares

LS-VCE	Least squares VCE
MCF	Minimum Cost Flow
MDB	Minimal Detectable Bias
MIB	Minimal Identifiable Bias
MINQUE	Minimum Norm Quadratic Unbiased Estimator
MInTS	Multiscale InSAR Time Series
MLE	Maximum Likelihood Estimation
MODIS	Moderate Resolution Imaging Spectroradiometer
MOOM	Multi-Objective Optimisation Model
MT-InSAR	Multi-temporal InSAR
NASA	The National Aeronautics and Space Administration
NSBAS	New Small Baseline Subset
PDF	Probability Density Function
PS	Persistent Scatterer
PSD	Power Spectral Density
PSInSAR	Persistent Scatterer InSAR
PSP	Persistent Scatterer Pairs
QPS	Quasi Persistent Scatterers
Radar	RAdio Detection And Ranging
RAM	Random-access Memory
RMS	Root Mean Square
RSE	Remote Sensing of Environment
SAR	Synthetic Aperture Radar
SB	Small Baseline
SBAS	Small Baseline Subset
SDFP	Slowly-decorrelating Filtered Phase
SENT-1	Sentinel-1
SLC	Single Look Complex
SNAPHU	Statistical-cost Network-flow Algorithm for Phase Unwrapping
SNR	Signal-to-noise Ratio
SOD	Second-Order Design
SOOM	Single-Objective Optimisation Model
SPN	Stable Points Network

SRTM	Shuttle Radar Topography Mission
SVD	Singular Value Decomposition
TanDEM-X	TerraSAR-X add-on for Digital Elevation Measurement
TDX	TanDEM-X
TEC	Total Electron Content
TOD	Third-Order Design
TOPS	Terrain Observation by Progressive Scan
TSX	TerraSAR-X
VCE	Variance Component Estimation
VCV	Variance-covariance
WGS84	World Geodetic System 1984
ZHD	Zenith Hydrostatic Delay
ZOD	Zero-Order Design
ZTD	Zenith Total Delay
ZWD	Zenith Wet Delay

## LIST OF MATHEMATICAL SYMBOLS

$A$	Annual amplitude
$\bar{a}$	Mean acceleration
$\alpha$	Slope angle
$\alpha_h$	Heading angle
$\vec{B}$	Spatial baseline
$B_{\perp}$	Perpendicular baseline
$B_T$	Temporal baseline
$d_{ij}$	Interferometric deformation between the $i^{th}$ and the $j^{th}$ images
$d^{neu}$	Interferometric deformation corresponding to the path delay due to the neutral atmosphere
$d^{def}$	Interferometric deformation component due to the Earth movement
$d^{GNSS}$	GNSS-derived deformation projected to the LoS direction
$d^{ion}$	Interferometric deformation component corresponding to ionospheric path delay
$d^{nd}$	Interferometric deformation due to non-dispersive components
$d^{orb}$	Interferometric deformation component caused by orbital errors
$d^{top}$	Interferometric deformation component caused by DSM uncertainty
$d_{LOS}$	Earth deformation in the LOS direction
$d_E$	Earth deformation in the east direction
$d_N$	Earth deformation in the north direction
$d_U$	Earth deformation in the up direction
$D_{\Delta A}$	Amplitude difference dispersion
$\Delta\bar{a}$	Mean acceleration variation
$\Delta L^{tropo}$	Excess path due to the delay caused by tropospheric refraction
$\Delta L_h^{tropo}$	The hydrostatic component of $\Delta L^{tropo}$
$\Delta L_w^{tropo}$	The wet component of $\Delta L^{tropo}$
$\Delta R$	Offsets in the range direction
$\Delta R_{filt}$	Filtered offsets in the range direction
$\Delta TEC$	The variation in total electron content
$\Delta x$	Offsets in the azimuth direction

$\Delta x_{filt}$	Filtered offsets in the azimuth direction
$\Delta x^{ion}$	Ionospheric contribution to the azimuth offset
$\Delta Z^{top}$	The uncertainty of the digital surface model
$\Delta \hat{\phi}_{\theta,x,i}^u$	Spatially uncorrelated phase part at the pixel $x$ of the $i^{th}$ interferogram
$\delta$	Decorrelation
$\delta \Delta Z_x^{top}$	Local gradient of DSM error in the range direction in DSM error correction
$\delta \Delta Z_y^{top}$	Local gradient of DSM error in the azimuth direction in DSM error correction
$\delta V_x$	Local gradient of deformation velocity in the range direction in DSM error correction
$\delta V_y$	Local gradient of deformation velocity in the azimuth direction in DSM error correction
$\varepsilon_i$	Sum of phase shifts induced by the interaction between the microwaves and scatterers on the Earth's surface at the image $i$
$\gamma$	The coherence of an interferogram
$\gamma_G$	Geometric correlation
$\gamma_N$	Thermal noise correlation
$\gamma_T$	Temporal correlation
$\gamma_Z$	Volume correlation
$h$	Ellipsoidal height
$H$	Altitude of the InSAR platform orbit
$id_{x_p}$	Index of pixel $p$ in the range direction in DSM error correction
$id_{y_p}$	Index of pixel $p$ in the azimuth direction in DSM error correction
$kV_1$	Velocity conversion factor of the $l^{th}$ interferogram in DSM error correction
$kZ_1$	Height conversion factor of the $l^{th}$ interferogram in DSM error correction
$\lambda$	Radar wavelength
$L$	Spatial distance between two points
$M$	The number of selected interferograms

$m_k$	Successive interferometric phase increment between the $k^{th}$ and $(k + 1)^{th}$ acquisitions
$\mu_A$	Mean amplitude
$N + 1$	The number SAR images
$P_s$	Surface pressure
$\phi$	InSAR phase of an interferogram generated from the primary and secondary images
$\phi_{ij}$	Interferometric phase between the $i^{th}$ and the $j^{th}$ images
$\phi_{p,l}^{model}$	Phase model of deformation rates of the $l^{th}$ interferogram at the pixel $p$ in DSM error correction
$\phi_P$	InSAR phase of the primary image
$\phi_S$	InSAR phase of the secondary image
$\phi^{atm}$	Phase contribution of the atmospheric artefacts
$\phi^{def}$	Phase contribution of the Earth's surface deformation
$\phi^{ion}$	Phase component due to ionospheric path delay
$\phi^n$	Phase contribution of noise sources
$\phi^{orb}$	Phase contribution of the uncertainties in satellite orbit information
$\phi^{tropo}$	Phase delay caused by tropospheric refraction
$\phi^{tmp}$	Phase component caused by temporal decorrelation
$\phi^{top}$	Phase contribution of the topographic uncertainty
$\phi_{RMS}$	Root mean square of all interferometric deformation misclosure
$\tilde{\phi}_{x,i}$	Spatially correlated phase part at the pixel $x$ of the $i^{th}$ interferogram
$\varphi$	Ellipsoidal latitude
$\sigma_{\Delta A}$	Standard deviation of the difference in amplitude between the primary and secondary images
$r$	Slant range between the target and the SAR antenna
$T$	Temperature
$V$	Deformation velocity
$\bar{v}$	Mean deformation velocity
$\theta$	Radar look angle
$\theta_{inc}$	Radar incidence angle

$y_1^{(n)}$	Complex-valued backscattering coefficients of the $n^{th}$ scatterer from the primary image
$y_2^{(n)}$	Complex-valued backscattering coefficients of the $n^{th}$ scatterer from the secondary image
$y_2^{*(n)}$	Complex conjugate of $y_2^{(n)}$
$Z$	Earth's surface elevation

## 1. INTRODUCTION

To begin this dissertation, the background of InSAR is reviewed and outlined, which is followed by the contributions and structure of the dissertation. In Section 1.1, InSAR technology is described with its working principle, applications, sources of error and noise. An introduction to the Small Baseline Subset (SBAS) method, which is studied primarily in this dissertation, is provided as well. In Section 1.2, the contributions of the dissertation are provided, and its structure is outlined in Section 1.3.

### 1.1 Background

Synthetic Aperture Radar (SAR) Interferometry (InSAR) is among the satellite-based geodetic methods that can be applied to a wide range of applications such as Digital Surface Model (DSM) creation (e.g., [Bürgmann et al., 2000](#); [Zebker & Villasenor, 1992](#)), deformation monitoring (e.g., [Massonnet & Feigl, 1998](#); [Zebker et al., 1997](#)), as well as other studies on ocean currents (e.g., [Bamler & Hartl, 1998](#)) and glacial processes (e.g., [Andersen et al., 2015](#)). InSAR is advantageous in that it can be implemented both day and night thanks to the active illumination nature ([Simons & Rosen, 2015](#)). This method works by acquiring SAR images over the same study area from two separate SAR satellite locations with different viewing angles, which is applicable for DSM generation, or from a similar vantage point but at different times, which is used for deformation monitoring.

In research relating to Earth-surface deformation, InSAR can be applied to resolve and analyse deformation in the line-of-sight (LoS) direction at cm-to-mm precision with high resolution in both space and time ([Rosen et al., 2000](#)). They include diverse applications in measuring the surface motions associated with plate tectonics which is directly relevant to faults (e.g., [Bernard et al., 1997](#); [Fialko et al., 2005](#); [Fialko et al., 2001](#)), volcanoes (e.g., [Hooper et al., 2004](#); [Lu et al., 2005](#); [Parker et al., 2014, 2016](#); [Pritchard & Simons, 2002](#)), landslides (e.g., [Colesanti et al., 2003](#); [Colesanti & Wasowski, 2006](#)), or surface subsidence caused by mining exploitation (e.g., [Ng et al., 2010](#); [Raucoules et al., 2003](#); [Samsonov et al., 2013](#)) or groundwater extraction ([Amelung et al., 1999](#); [Chaussard et al., 2013](#); [Galloway et al., 1998](#)).

As with other types of geodetic measurements, e.g., Global Navigation Satellite System (GNSS) or repeat differential levelling, InSAR measurements are

contaminated by various sources of errors and noise. They involve atmospheric refraction artefacts (e.g., [Doin et al., 2009](#); [Fattahi & Amelung, 2015](#); [Goldstein, 1995](#); [Zebker et al., 1997](#)), orbital errors (or ramps) (e.g., [Biggs et al., 2007](#); [Cavalié et al., 2008](#); [Jolivet et al., 2012](#); [Lin et al., 2010](#)), errors induced by the uncertainty in the DSM used (e.g., [Bombrun et al., 2009](#); [Ducret et al., 2014](#); [Fattahi & Amelung, 2013](#); [Samsonov, 2010](#)), and decorrelation phenomena ([Bamler & Just, 1993](#); [Zebker & Villasenor, 1992](#)). These sources generate errors and noise in individual interferograms ([Hanssen, 2001](#)).

In order to mitigate the influences of these errors and noise, multi-temporal InSAR (MT-InSAR) methods have been proposed, which work by analysing a network of multiple acquisitions to derive deformation time series and thus deformation rate ([Shanker et al., 2011](#)). They include two principal categories, comprising the small baseline subset (SBAS) method (e.g., [Berardino et al., 2002](#); [Cavalié et al., 2007](#); [Hetland et al., 2012](#); [López-Quiroz et al., 2009](#); [Lundgren et al., 2001](#); [Schmidt & Bürgmann, 2003](#); [Usai, 2003](#)), and Persistent Scatterer InSAR (PSInSAR) (e.g., [Ferretti et al., 2001](#); [Hooper et al., 2007](#); [Hooper et al., 2004](#)). The former method is based on Distributed Scatterer (DS) pixels contributed by different scattering objects, whilst the latter method relies on Persistent Scatterer (PS) pixels dominated by a single strong scattering object, where both are stable over time ([Crosetto et al., 2016](#); [Hooper et al., 2012](#)). To inherit the advantages of both methods, i.e., SBAS and PSInSAR, combination methods have been developed such as SqueeSAR ([Ferretti et al., 2011](#)) or that proposed by [Hooper \(2008\)](#).

Of all the MT-InSAR methods, SBAS appears to be the most frequently used ([Crosetto et al., 2016](#)). Different SBAS-based approaches have been developed, namely “classical” SBAS ([Berardino et al., 2002](#); [Lanari et al., 2007](#)), the New Small Baseline Subset (NSBAS) ([Doin et al., 2011](#); [López-Quiroz et al., 2009](#)), and the Multiscale InSAR Time Series (MInTS) ([Hetland et al., 2012](#)). Classical SBAS works by relying on a system of linear equations to invert interferometric phase to SAR image phase values, and thus deformation corresponding to SAR acquisitions ([Berardino et al., 2002](#); [Lanari et al., 2007](#)). NSBAS is an extension of classical SBAS, in which a set of a priori constraints of acquisition dates in terms of a user-defined function and DSM error estimation is combined with a system of linear equations as that used in classical SBAS to derive deformation time series ([Doin et al., 2011](#); [López-Quiroz et al., 2009](#)). MInTS was proposed by [Hetland et al. \(2012\)](#) which works by considering

the spatial correlation between pixels in the first step by wavelet decomposition, and a time-dependent function to derive deformation parameters in the second step.

Classical SBAS is studied in this dissertation as it is one of the most commonly used methods (see [Table 1.1](#)), and it is basic to develop other SBAS-based methods. [Table 1.1](#) compares the number of studies applying SBAS and other techniques interrogating SCOPUS on 27 July 2020. The keywords used combined SAR, InSAR or DInSAR with the technique names, which were searched from the article titles or keywords.

**Table 1.1.** An interrogation of SCOPUS on 27 July 2020 shows the number of articles that use SBAS in relation to other DInSAR techniques.

Technique	Number of articles
Coherent Pixels Technique (CPT)	13
Interferometric Point Target Analysis (IPTA)	36
MInTS	2
NSBAS	16
Permanent Scatterer	267
Persistent Scatterer Pairs (PSP)	12
Persistent Scatterer	639
Quasi Persistent Scatterers (QPS)	7
SBAS	457
SqueeSAR™	38
Stable Points Network (SPN)	8

The SBAS method has been adopted in studies of surface deformation due to groundwater extraction (e.g., [Bui et al., 2021](#); [Chaussard et al., 2013](#); [Chaussard et al., 2014](#); [Parker et al., 2017](#)), mining activities (e.g., [Castañeda et al., 2009](#); [Gourmelen et al., 2007](#)), earthquakes [Casu et al. \(2006\)](#), volcanoes ([Baker & Amelung, 2012](#); [Papoutsis et al., 2013](#)) and rapid urbanisation (e.g., [Dong et al., 2014](#)). It has also been applied to different areas with various deformation magnitudes, ranging from millimetres per year (e.g., [Elliott et al., 2010](#); [Furuya et al., 2007](#); [Jiang et al., 2011](#); [Smith & Sandwell, 2003](#)) to centimetres per year (e.g., [Amelung et al., 1999](#); [Cavalié et al., 2013](#); [Chaussard et al., 2014](#); [Lee et al., 2012](#)) or tens of centimetres per year

(e.g., [Chaussard et al., 2014](#); [López-Quiroz et al., 2009](#); [Motagh et al., 2007](#); [Short et al., 2011](#)).

InSAR time series can be degraded by various errors and noise sources. Although some of the sources can be corrected or reduced by several methods (e.g., [Biggs et al., 2007](#); [Cavalié et al., 2008](#); [Delacourt et al., 1998](#); [Doin et al., 2009](#); [Fattahi & Amelung, 2013](#); [Jolivet et al., 2011](#); [Jolivet et al., 2012](#); [Lin et al., 2010](#); [Williams et al., 1998](#)), these reductions cannot be conducted perfectly, which leads to remaining or residual errors and noise. In addition to various deformation magnitudes, this in turn results in different signal-to-noise ratios (SNRs). In this dissertation, the effects of remaining errors and noise on SBAS-derived rates computed from signals of different magnitudes are tested using simulated InSAR time series.

In InSAR data processing, we aim to minimise the sum decorrelation of the interferograms ( $\rho_{total}$ ) as ([Hooper et al., 2007](#)):

$$\rho_{total} = \left[1 - f\left(\frac{T}{T^c}\right)\right] \left[1 - f\left(\frac{B_{\perp}}{B_{\perp}^c}\right)\right] \left[1 - f\left(\frac{F_{DC}}{F_{DC}^c}\right)\right] \rho_{thermal} \quad (1.1)$$

where  $T$ ,  $B_{\perp}$ , and  $F_{DC}$  are the time span, perpendicular baseline, and the difference in Doppler centroid between two SAR images,  $\rho_{thermal}$  is the thermal noise. The superscript  $c$  in Equation (1.1) indicates the corresponding critical values, which are dependent on satellites ([Hooper et al., 2007](#)). In InSAR SBAS data processing, pairs of scenes are chosen to form interferograms from which an interferogram network is built in such a way to reduce decorrelation noise in Equation (1.1). This is employed through reducing their time spans ( $T$ ), the differences in look and squint angles ([Hooper et al., 2012](#)), which lead to minimising the perpendicular baseline ( $B_{\perp}$ ) and the difference in Doppler centroid frequency ( $F_{DC}$ ) ([Hooper et al., 2007](#)).

Coherent pixels to which a specific SBAS approach are applied can subsequently be selected based on different criteria, e.g., amplitude dispersion, spatial coherence, spectral coherence or their combination ([Crosetto et al., 2016](#)), or interferometric phase misclosure ([Cavalié et al., 2007](#)). Different proposed SBAS approaches are therefore based on thresholds that are, to a lesser or greater extent, different depending on various factors, e.g., applications, data availability or the critical baseline, which in turn depends on the wavelength of the radar sensor, spatial resolution and incidence angle ([Gatelli et al., 1994](#); [Zebker & Villasenor, 1992](#)).

The temporal baseline threshold has been chosen varying from months to years (e.g., [Lanari et al., 2007](#); [López-Quiroz et al., 2009](#)), while the perpendicular baseline

threshold has been chosen ranging between hundreds of metres and over one thousand metres (e.g., [Berardino et al., 2002](#); [Chaussard et al., 2014](#)). These SBAS network thresholds are used with the aim of maximising the number of InSAR interferograms while minimising their temporal and spatial decorrelation, as well as reducing the computation time and data storage quantity. Baseline thresholds and pixel selection criteria used in several main SBAS approaches are listed in [Table 1.2](#).

[Table 1.2](#). Summary of the main SBAS approaches.

Reference	Interferogram selection thresholds	Pixel selection Criterion
<a href="#">Berardino et al. (2002)</a>	Perpendicular baseline (130 m)	Coherence
<a href="#">Mora et al. (2003)</a>	Perpendicular baseline (24 m)	Coherence
<a href="#">Schmidt and Bürgmann (2003)</a>	Perpendicular baseline (200 m)	Coherence
<a href="#">Lanari, Mora, et al. (2004)</a>	Perpendicular baseline (130 m)	Coherence
<a href="#">Cavalié et al. (2007)</a>	Perpendicular baseline (300 m)	Interferometric phase misclosure
<a href="#">Hooper (2008)</a>	Perpendicular baseline Temporal baseline Doppler baseline	Amplitude and phase stability
<a href="#">López-Quiroz et al. (2009)</a>	Perpendicular baseline (500 m) Temporal baseline (9 months)	Coherence
<a href="#">Goel and Adam (2014)</a>	Perpendicular baseline (150 m) Temporal baseline (150 days)	Statistical homogeneity test

In this dissertation, the influence of a different number of interferograms chosen based on various thresholds on SBAS-derived rates are quantified and validated using simulated data. Furthermore, because of some technical and scheduling issues, InSAR images are not always regularly captured, or in other cases, blocks of images acquired during extended periods such as northern winter snowfall may be omitted from data processing due to very low coherence. This causes prolonged gaps in InSAR acquisition and their effects are evaluated in this dissertation using simulations.

As mentioned, different thresholds have been utilised in InSAR SBAS data processing. The question then arises as to whether there are some more objective

means by which to select these thresholds. In this dissertation, the so-called network “optimisation” problem (e.g., [Amiri-Simkooei et al., 2012](#); [Grafarend & Sansò, 1985](#)), which has been successfully applied to geodetic (surveying) networks, is employed as an assistant to design InSAR SBAS interferogram networks. Specifically, the redundancy number defined by [Baarda \(1968\)](#) is utilised as a measure of the reliability of geodetic network. The redundancy number is therefore examined as a metric to determine the likely effectiveness of the SBAS network design, again using simulated data. The redundancy number in geodetic network design has been studied by [Mahapatra et al. \(2015\)](#) to identify the minimum number and optimal locations of InSAR corner reflectors or transponders, which are man-made coherent targets installed on the Earth’s surface. This study is different in that the redundancy number is applied in designing an SBAS network by choosing an “optimal” combination of SBAS interferograms.

In geodesy, different methods can be applied to monitor Earth surface deformation, such as episodic or continuous GNSS (e.g., [Mao et al., 1999](#); [Zhang et al., 1997](#)), repeat levelling (e.g., [Jackson & Bilham, 1994](#); [Lyon et al., 2018](#)), InSAR (e.g., [Amelung et al., 1999](#); [Mora et al., 2003](#); [Parker et al., 2017](#)), using electronic distance measurement (EDM) networks (e.g., [Langbein, 2004](#); [Langbein & Johnson, 1997](#)), or through a combination of different techniques (e.g., [Catalão et al., 2009](#); [Cuenca et al., 2011](#); [Fuhrmann & Garthwaite, 2019](#); [Hu et al., 2011](#)). A series of repeat observations generates time series that are used for annual rate computation (e.g., [Johnson & Agnew, 1995](#); [Zhang et al., 1997](#)) or, in a more general case, determining parameters of a time-dependent deformation functional model (e.g., [Didova et al., 2016](#); [Langbein, 2004](#)) or non-linearity (e.g., [Featherstone et al., 2015](#); [Teatini et al., 2012](#)).

Errors in geodetic measurements are, in many cases, assumed to be statistically independent of each other and the deformation rate is considered to be constantly linear over the duration of the experiment. Any temporal correlation between measurements can affect the uncertainty in the velocity estimate when it is determined from the time series of measurements ([Johnson & Agnew, 1995](#)). However, noises in the time series from some kinds of measurements have been demonstrated to be correlated (e.g., [Langbein & Johnson, 1997](#); [Mao et al., 1999](#); [Zhang et al., 1997](#)), leading to the case that the above assumption is incorrect.

Geodetic research on Earth surface deformation requires a precise estimation in both deformation functional parameters and time series error (Mao et al., 1999). Noise analysis is therefore conducted in order to identify how the noise behaves. This kind of research can be found in several geodetic applications, e.g., in GNSS (e.g., Langbein, 2008; Mao et al., 1999; Williams, 2003; Zhang et al., 1997) or EDM (e.g., Johnson & Agnew, 1995; Langbein, 2004; Langbein & Johnson, 1997). In InSAR data processing, noise models have been developed as the *a priori* precision of InSAR observations, i.e., individual interferograms to estimate earthquake source parameters (Dawson & Tregoning, 2007) or to understand the noise behaviour of tropospheric delay in interferograms (Emardson et al., 2003).

This has also been developed with an interferogram network, which can be applied to SBAS inversion to estimate unknown parameters, i.e., deformation phase of acquisitions and DSM error (Agram & Simons, 2015; Cao et al., 2018; González & Fernández, 2011; Guarnieri & Tebaldini, 2007; Hanssen, 2001; Rocca, 2007). However, in the further step of deformation parameter estimation, e.g., annual rate and other periodic coefficients, a stochastic noise model is also needed, which can be derived via noise analysis, but has not been investigated in great detail to date (cf. Filmer et al., 2020). This dissertation provides estimates of the spectral index from 10 years of simulated InSAR data. A minimum of 256 observations is required to properly resolve time series noise (Williams et al., 2004), which is achieved in the experiments conducted in this research.

This study is significant in that it proves whether or not coloured noise exists in the simulated InSAR SBAS-derived deformation time series. If it is the case, it may affect the uncertainty of the rate, which is usually estimated by the way that a simple linear regression without observations correlation is utilised. Therefore, this kind of noise analysis is conducted relying on simulated data incorporating deformation of linear plus annual signals degraded by various user-controlled error and noise sources, consisting of DSM error, atmospheric artefacts, orbital error and temporal decorrelation. This analysis is carried out by applying the Maximum Likelihood Estimation (MLE) method (Press et al., 1986) due to its advantages over the spectral analysis method (Langbein & Johnson, 1997), which are both incorporated in the public-domain Create and Analyse Time Series (CATS) package (Williams, 2008).

## 1.2 Contributions

There are three main aspects to this dissertation. First, the influence of deformation magnitude and residual noise and data gaps on SBAS-derived rates are assessed. Second, the use of redundancy numbers as diagnostic for an “optimal” interferogram network in SBAS data processing is tested. Third, noise analysis is carried out by making use of the simulated data incorporating linear plus annual sinusoidal deformation degraded by simulated errors and noise of different types.

The main contributions of this dissertation are summarised as follows:

- 1) Design and implement experiments used to assess the influences of signal magnitude and residual noise, data gaps and the number of chosen interferograms on InSAR SBAS-retrieved deformation rates:
  - A dataset consisting of 1000 pixels is simulated assuming they cover a four-year time span with an 11-day interval. All pixels are then assumed to experience linear deformation rates plus sinusoidal annual amplitudes of  $-2$  mm/yr plus 2 mm,  $-20$  mm/yr plus 5 mm, and  $-100$  mm/yr plus 10 mm. The interferometric residual Gaussian noise sets with zero mean are subsequently simulated for all 8778 interferograms assuming their ranges bounded within  $[-2; +2]$  mm,  $[-5; +5]$  mm and  $[-10; +10]$  mm.
  - It is found that contradictory deformation trends can occur, i.e., cases where a location may undergo simulated subsidence but its InSAR SBAS-based results demonstrate uplift. This is likely to occur in areas of slow/small deformation rates, particularly when high noise is present (i.e., low SNR). The SBAS results in terms of deformation trends are therefore affected by not only noise magnitude but also by signal size.
  - When the linear plus sinusoidal annual periodic signal with interferometric noise was tested, the linear-fit rates were biased. When a more appropriate functional model was used instead of simple linear regression, the estimated rates were not biased. This indicates that errors are potentially introduced by using simple linear regression when nonlinear deformation is present.
  - Data gaps have effects on InSAR SBAS-retrieved rates in which “winter” gaps result in larger errors in estimated rates and RMSs of the differences between simulated and SBAS-derived deformation time series, whilst random gaps have lesser influence.

- When the same number of interferograms is used, limiting temporal baselines can result in larger errors in deformation trends compared to the case of random gaps, suggesting that the network configuration is more important. The trade-off in baseline thresholds may result in a geometrically weak SBAS network. This is vulnerable to incorrect estimation of deformation rate in the presence of noisy data with non-linear deformation.
  - Generally, the more interferograms chosen (i.e., higher temporal and/or perpendicular baseline thresholds employed) lead to lower errors in rate determination. Therefore, additional statistical tools working in an objective way can be of assistance to tackle this problem, which will be dealt with in Chapter 6.
- 2) An approach is proposed to make use of redundancy numbers as an assistant in designing an “optimal” InSAR SBAS interferogram network:
- A similar simulated dataset to that used in 1) is designed and implemented prior to computing the redundancy numbers for all interferogram networks to identify the relationships between redundancy numbers and errors in rate determination.
  - The redundancy number is of assistance in gauging the reliability of the estimated rates in cases where the redundancy numbers are between  $\sim 0.8$  and  $\sim 0.9$ . Redundancy numbers of less than  $\sim 0.3$  can deliver erroneous (even contradictory) rates in the presence of noise commensurate with the magnitude of deformation.
- 3) The noise analysis relying on an InSAR simulated dataset is undertaken:
- Another simulated InSAR SBAS dataset is designed and implemented, which consists of linear plus annual sinusoidal deformation contaminated by various sources of errors and noise, including DSM errors, atmospheric artefacts, orbital errors and temporal decorrelation.
  - Through this simulation, after removing the deformation signal, there are two noise types present in residuals with both time-correlated, i.e., coloured noise, and uncorrelated, i.e., white noise.
  - Spectral indices of coloured noise vary between  $-3.0$  and  $0$  with a mean value of  $-0.8$ , which is close to flicker noise of  $-1$ . The noise model should therefore be best described by white plus flicker noise.

### 1.3 Dissertation Structure

- Chapters 5 to 7 of this dissertation are written as independent studies based on the paper published in the Remote Sensing of Environment (RSE) journal (Bui et al., 2020), a manuscript under preparation for submission to a journal in the future, and a poster presented to the American Geophysical Union (AGU) Fall Meeting 2019 conference.
- Chapter 2 provides an overview of the InSAR technique in a general sense.
- Chapter 3 presents the methods used for reducing noise and errors in InSAR interferograms.
- Chapter 4 describes the SBAS method, which is studied in this dissertation.
- Chapter 5 shows the results of evaluating the effects of residual noise in InSAR interferograms, the number of chosen interferograms, and data gaps on SBAS-derived rates. This is conducted by relying on a simulated InSAR dataset with deformation signals of linear rates plus annual sinusoidal amplitudes of  $-2 \text{ mm/yr} + 2 \text{ mm}$ ,  $-20 \text{ mm/yr} + 5 \text{ mm}$ , and  $-100 \text{ mm/yr} + 10 \text{ mm}$ , degraded by Gaussian interferometric noise with zero mean ranging within bounds of  $[-2; +2] \text{ mm}$ ,  $[-5; +5] \text{ mm}$  and  $[-10; +10] \text{ mm}$ .
- Chapter 6 shows the results of designing an “optimal” interferogram network used in SBAS data processing based on the redundancy number used in geodetic network design. This relies on the same simulated dataset as that used in Chapter 5, but with more networks generated based on different thresholds. The results from Chapters 5 and 6 were combined to produce a paper showing a complete study, which has been published in Bui et al. (2020).
- Chapter 7 is concerned with noise analysis applied in InSAR SBAS-derived deformation time series. This uses another simulated dataset with linear and annual deformation, contaminated by various error and noise sources. In this Chapter, the MLE method is used in which the magnitudes and types of noise are estimated and identified. A poster was produced from this Chapter to present at the AGU Fall Meeting conference in December, 2019.
- In Chapter 8, a summary of the dissertation with conclusions and recommendations is provided.

## 2. GENERAL CONCEPTS OF INTERFEROMETRIC SYNTHETIC APERTURE RADAR (INSAR)

This Chapter provides generic information relating to InSAR technology. It starts with Section 2.1 providing fundamentals of radar signals, their historical development and applications. Section 2.2 introduces SAR technology with its main modes of Stripmap, ScanSAR and Spotlight. The InSAR method is then introduced in Section 2.3 with its applications in digital surface model (DSM) generation and deformation studies. The final Section 2.4 summarises the Chapter.

### 2.1 Radar

Radar is the short form of RAdio Detection And Ranging, which is a technique or an instrument using a signal in the radio wave frequency (Levanon, 1988; Skolnik, 1970). Radar instruments operate by transmitting electromagnetic pulses in the radio and microwave bands then receiving the reflected signals from stationary or moving objects. The radar technique uses the two-way time it takes to transmit the radio pulses from the transmitter to the tracked object and return to measure the distance between them and the backscatter intensity to study the object's physical characteristics, e.g., its surface roughness (Skolnik, 2002).

Radar has its long history with secret developments used for military purposes during World War II, followed by an application boom far beyond that in both civilisation and sciences. The first discoveries and inventions in radar are the moments when the Scottish scientist James Clerk Maxwell developed the classical theory of electromagnetism in 1865 (Maxwell, 1865; Nahin, 1992) and the German physicist Heinrich Hertz found that radio waves could be reflected from solid objects in 1886 (Buderi, 1996). They were then followed by some experiments done by the Russian physicist Alexander Popov in the Russian Navy (Kostenko et al., 2001) and the German inventor Christian Hülsmeyer (Griffiths et al., 2019). A series of studies on radar were subsequently conducted which are mentioned and described in, e.g., Schroeder (2015) and Sevgi (2006).

With its ability to provide the positions of tracked objects, radar has a wide range of military, civilian and scientific applications. In the military domain, it can be used in, e.g., target detection and recognition, weapon tracking and navigation (e.g., Bruderer et al., 2012; Gerum et al., 2001; Mortazavi et al., 2013). This can be extended

to similar civil applications in tracking and navigation systems for aircraft, ships, trains and vehicle traffic. Another application of radar is in aviation where it can be used for air traffic control and surveillance (e.g., [Farina & Pardini, 1980](#); [Haykin et al., 1991](#); [Kim & Sivits, 2015](#)). In terms of meteorology, radar is applied in monitoring precipitation, wind, as well as in weather forecasts (e.g., [Donelan & Pierson Jr, 1987](#); [Kummerow et al., 1998](#); [Lin et al., 2005](#)). It can also be adopted in remote sensing applications in Earth's surface topography mapping, crustal deformation measurement, sea and ice studies (e.g., [Goldstein et al., 1993](#); [Rignot et al., 2008](#); [Voronovich & Zavorotny, 2001](#); [Zebker et al., 1997](#)). Table 2.1 shows radar bands associated with their frequency and wavelength ranges, of which the L-, S-, C- and X-band are used in InSAR applications.

**Table 2.1.** Radar bands with corresponding frequency and wavelength ranges. The L-, S-, C- and X-band are used in InSAR.

Band	Frequency range (GHz)	Wavelength range (mm)
HF	0.003 – 0.03	10,000 – 100,000
VHF	0.03 – 0.3	1000 – 10,000
P	< 0.3	> 1000
UHF	0.3 – 1	300 – 1000
L	1 – 2	150 – 300
S	2 – 4	75 – 150
C	4 – 8	37.5 – 75
X	8 – 12	25 – 37.5
K <sub>u</sub>	12 – 18	16.7 – 25
K	18 – 24	11.1 – 16.7
K <sub>a</sub>	24 – 40	7.5 – 11.1
Mm	40 – 300	1.0 – 7.5
V	40 – 75	4.0 – 7.5
W	75 – 110	2.7 – 4.0

## 2.2 Synthetic Aperture Radar

In order to have a desired spatial resolution of several metres or higher, a radar antenna of a size roughly equivalent to a football field is required (Uys, 2016), which is impractical. Synthetic aperture radar (SAR) was therefore invented to overcome this limitation, which is a technology in radar remote sensing where a large antenna is synthesised to improve azimuth resolution and provide larger spatial coverage than *in-situ* discrete methods. SAR satellites actively transmit a series of radar pulses and receive backscattered signals from the Earth's surface. Furthermore, by the use of microwaves, it is mostly unaffected by cloud, fog, mist or precipitation, thus can operate in nearly all weather conditions (Lu et al., 2007).

Figure 2.1 illustrates the working principle of a SAR system with terminological definitions used in SAR processing, e.g., azimuth and range directions, along-track and cross-track, radar swath, and look angle. After transmitting a series of radar pulses, the SAR antenna records the corresponding signals echoing from the Earth's surface from which a raw image is generated. This process is scientifically termed as SAR due to the fact that it is carried out repeatedly during a period of time when a SAR platform moves along its flight path (a.k.a. the azimuth direction or along-track, see Figure 2.1), with a collection of reflected pulses recorded then merged as a large virtual [synthetic] aperture (Raney, 1971).

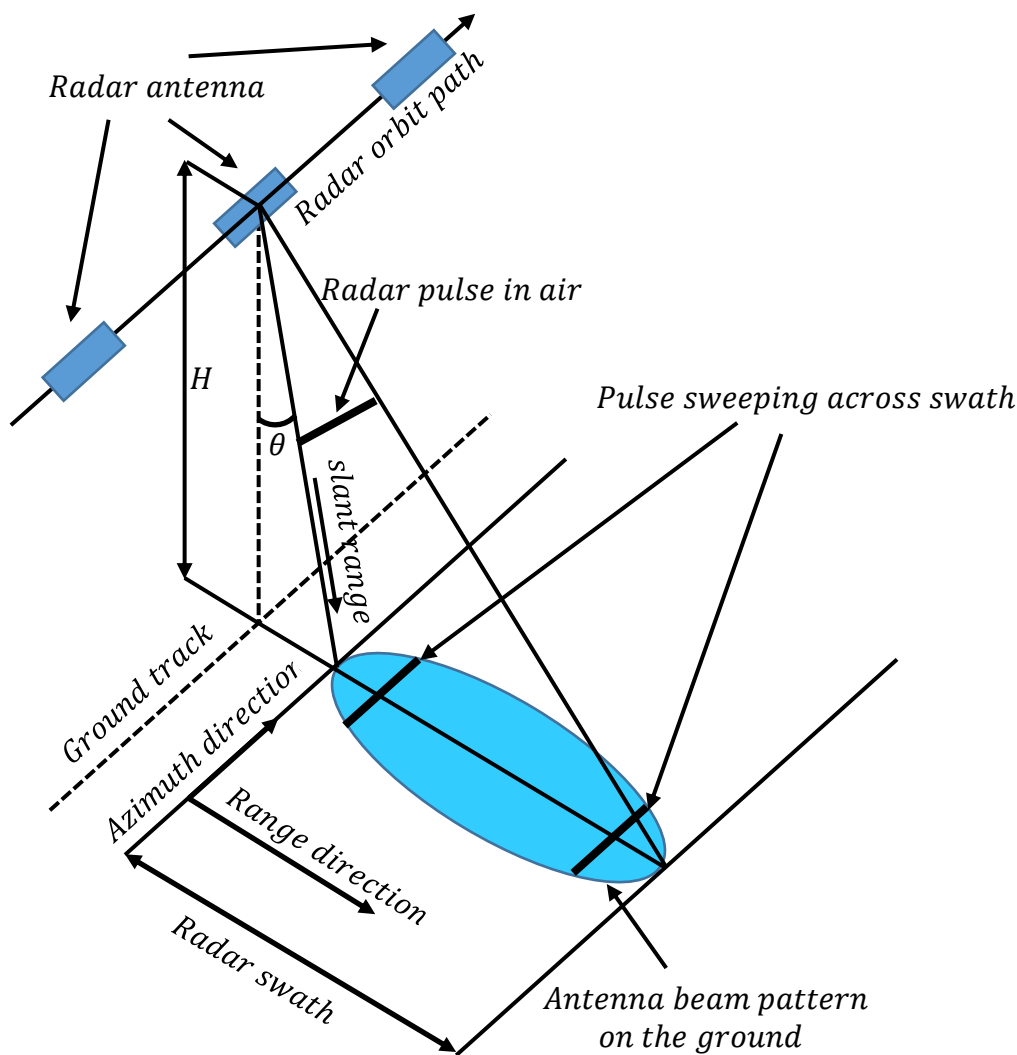


**Figure 2.1.** An illustration of a SAR system. A SAR platform carries a radar antenna, which transmits a pulse toward the Earth through the air and receives the signal reflected. The platform moves along its orbit path which is also known as the azimuth direction or along-track, which is at a right angle to the range direction or cross-track. The surface area bounded within the range of the SAR signal in the range direction is the radar swath.  $\theta$  indicates the look angle and  $H$  refers to the altitude of the platform orbit above the Earth's surface.

Most SAR systems are designed with a configuration that their antenna sizes are of the order of metres and illuminated footprints are on the scale of kilometres, with images acquired in the side-looking directions varying between  $10^\circ$  and  $60^\circ$  (Lu & Dzurisin, 2014; Simons & Rosen, 2015). With this configuration, they can produce SAR scenes with a ground resolution varying within several metres or lower in both the azimuth and the range directions, which is also dependent on the radar band and

operational mode (Lu & Dzurisin, 2014). This SAR system can work on both airborne and spaceborne platforms.

Different SAR modes have been applied to date including Stripmap, ScanSAR, and Spotlight modes (Yague-Martinez et al., 2016). The Stripmap mode works with an antenna carried by a platform pointing its beam to the Earth's surface at a fixed angle to capture a strip or swath, which is parallel to the platform's ground track as shown in Figure 2.1 (Bamler & Hartl, 1998; Hanssen, 2001). This is the most common SAR mode, but its mapping coverage is limited to the order of kilometres. The ScanSAR mode was therefore proposed as a solution to expand the swath coverage. In this mode, an electronic antenna mounted on a platform continuously steers its radar beams in elevation so that the SAR data are captured in various adjacent bursts and sub-swaths, then they are synthesised into a wide-swath image (Ahmed et al., 1990; Bamler & Eineder, 1996; Moore et al., 1981; Moreira et al., 1996; Prati & Guarnieri, 1996; Tomiyasu, 1981).

In the Spotlight mode, a SAR sensor steers its beams while moving along the flight path in such a way that they illuminate the same area on the Earth's surface for a longer time, compared to the Stripmap and ScanSAR modes (Cenzo, 1988; Gough & Hawkins, 1997; Munson et al., 1983). By this approach, it is used with the aim of increasing the spatial resolution, particularly that in the azimuth direction, but also limits the spatial coverage of the scene (Gough & Hawkins, 1997). Figure 2.2 shows a simplified scenario comparing the working principles of those SAR modes of Stripmap, ScanSAR and Spotlight. The Terrain Observation by Progressive Scan (TOPS) mode (De Zan & Guarnieri, 2006) that works similarly to the ScanSAR but overcomes some of its limitations is implemented in the TerraSAR-X (TSX) (e.g., Meta et al., 2010; Werninghaus & Buckreuss, 2010) and Sentinel-1 (e.g., De Zan et al., 2008; Torres et al., 2012) satellite missions.

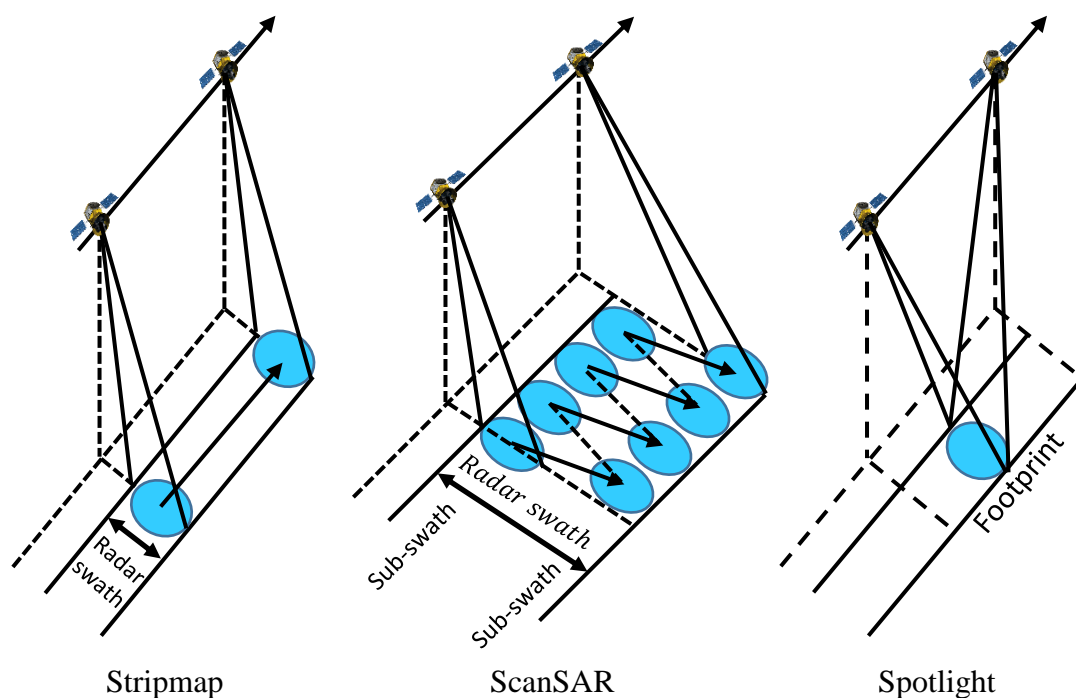
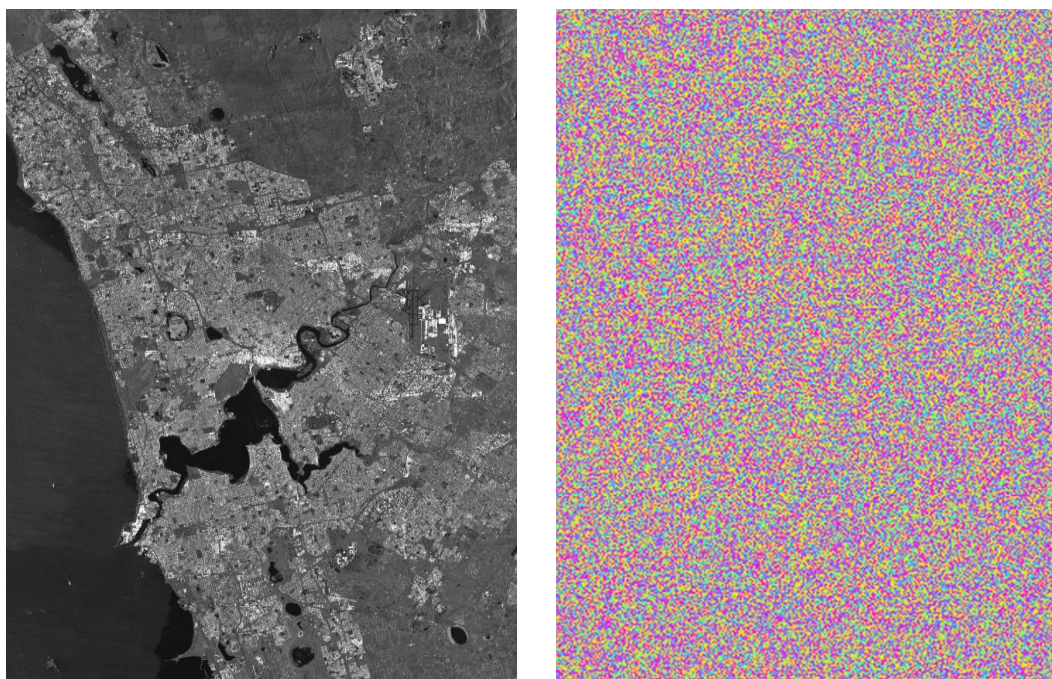


Figure 2.2. Simplified scenario of different SAR modes.

In SAR processing, both the signal's intensity/amplitude and phase backscatter are calculated as complex-numbered values (e.g., Bamler & Hartl, 1998; Rosen et al., 2000). The intensity of a single-look complex (SLC) image reflects the Earth's surface characteristics such as its slope, roughness and dielectric constant, whilst the phase reflects the round-trip distance on which the radar signal transmits from the SAR satellite to the Earth and the interaction between the SAR signal and the Earth's surface (Lu & Dzurisin, 2014). Figure 2.3 shows an example of the amplitude and phase components of a TSX SLC image, which was acquired over Perth, Western Australia, on October 5, 2013. The amplitude signal (Figure 2.3, left) is associated with the ground reflectivity, which shows patterns as it is relevant to the surface slope, roughness and dielectric constant, whilst the phase signal (Figure 2.3, right) is totally random due to the fact that it is produced by random collections of scatterers in resolution cells.



**Figure 2.3.** Components of a TSX SLC image. (Left) amplitude and (right) phase. The image was captured on October 5, 2013 over Perth, Western Australia.

### 2.3 SAR Interferometry

Interferometric SAR (InSAR) is a technique using two SAR images that are captured over the same area but at different times, which is applicable to crustal deformation studies, or from different viewing angles, which is used for DSM generation (Ferretti, 2014). This technique has proven to be a useful and powerful tool to monitor surface deformation related to geodynamic processes (Lu & Dzurisin, 2014). InSAR is able to provide a map of LoS surface deformation with a high spatial resolution, which depends on the radar band and operational mode, with the precision on the order of a fraction of its wavelength, i.e., sub-centimetre (Lu & Dzurisin, 2014).

#### 2.3.1 Sensor Configuration

In the topographic study domain, two SAR sensors are mounted on an airborne or spaceborne platform such as those used in the Shuttle Radar Topography Mission (SRTM) system (Farr et al., 2007), in which the spatial separation between the two sensors is referred to as the spatial baseline (Lu & Dzurisin, 2014). An alternative configuration in which two SAR images are captured by two satellites within a short time interval can also be applied to this topography mapping application, which is implemented in several satellite systems, e.g., the TerraSAR-X add-on for Digital

Elevation Measurement (TanDEM-X, TDX) (e.g., [Krieger et al., 2007](#); [Zink et al., 2014](#)) and the COSMO/SkyMed (CSK) (e.g., [Nitti et al., 2013](#)).

In the other applications of deformation measurement, SAR images capture the same area on the Earth's surface at different times by a single sensor mounted on an airborne or spaceborne platform flying in an almost identical orbit, which is referred to as repeat-pass interferometry ([Massonnet & Feigl, 1998](#)). The temporal and spatial separations between acquisitions of any two SAR images are termed as the temporal and spatial baselines, respectively. SAR sensors have been mounted onboard several spacecraft including those listed in [Table 2.2](#), and enable the generation of crustal displacement maps with millimetre to centimetre precision at metres of spatial resolution covering the ground surface by a swath of tens to hundreds of kilometres wide ([Lu & Dzurisin, 2014](#)).

**Table 2.2.** List of several SAR platforms classified by radar bands. 'L' stands for 'long' wavelength. 'C' means a 'compromise' between L and S bands where 'S' stands for 'short' wavelength. 'X' was chosen relating to the secret frequency of this radar band during the World War II (Lu & Dzurisin, 2014).

Radar band	Frequency Range (GHz)	Wavelength Range (cm)	Platforms	Owner	Operated period
L	1 – 2	15 – 30	Seasat	National Aeronautics and Space Administration	Jun – Oct 1978
			JERS-1	Japan Aerospace Exploration Agency	1992 – 1998
			ALOS/PALSAR	Japan Aerospace Exploration Agency	2006 – 2012
			ALOS-2/PALSAR-2	Japan Aerospace Exploration Agency	2014 – present
C	4 – 8	3.75 – 7.5	ERS-1	European Space Agency	1991 – 2000
			ERS-2	European Space Agency	1995 – 2011
			Radarsat-1	Canadian Space Agency	1995 – 2013
			ENVISAT	European Space Agency	2002 – 2012
			Radarsat-2	Canadian Space Agency	2007 – present
			Sentinel-1A	European Space Agency	2014 – present
X	8 – 12	2.5 – 3.75	COSMO-SkyMed	Italian Space Agency	2007 – present
			TerraSAR-X	German Aerospace Centre	2007 – present
			TanDEM-X	German Aerospace Centre	2010 – present

### 2.3.2 SAR Geometry

Two SAR images referred to as the primary and secondary (formerly master and slave) images are required to generate an interferogram in InSAR. A simplified configuration of InSAR imaging geometry is depicted in [Figure 2.4](#) in which the locations of the satellite where the two images are recorded are indicated as  $P$  and  $S$ , respectively. The phase value of a pixel named as  $M$  situated on the Earth's surface recorded in the primary image can be represented as:

$$\phi_P = -\frac{4\pi}{\lambda}PM + \varepsilon_P \quad (2.1)$$

where  $PM$  is the distance between the SAR sensor ( $P$ ) and the target ( $M$ ),  $\lambda$  is the radar wavelength (cf. [Table 2.1](#)), and  $\varepsilon_P$  is the sum of phase shifts induced by the interaction between the microwaves and scatterers within the pixel  $M$ . The term  $4\pi$  in Equation (2.1) is because the phase value is relevant to the two-way distance between the sensor and the target.

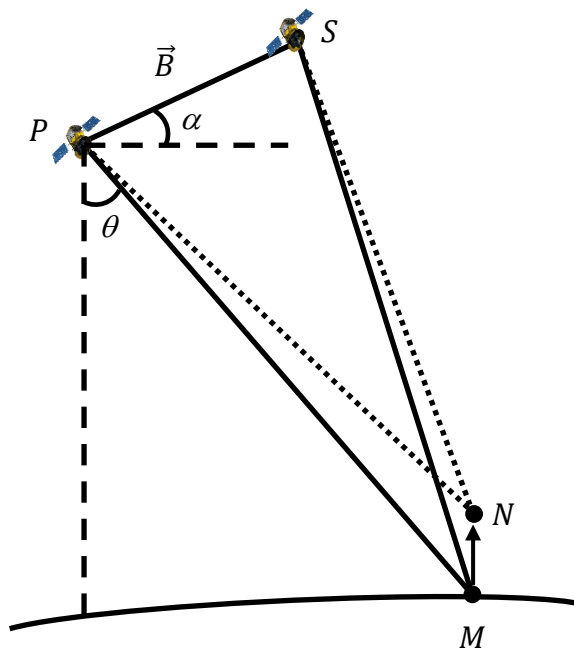


[Figure 2.4](#). InSAR interferogram imaging geometry.  $P$  and  $S$  are the satellite locations where the primary and secondary images are captured at the same area on the Earth's surface at different vantage points.  $M$  is a target recorded at the primary acquisition which moves to  $N$  recorded at the secondary acquisition.  $\theta$  is the look angle and  $\alpha$  is the slope angle. The spatial separation between  $P$  and  $S$  is the spatial baseline ( $\vec{B}$ ).

Due to the assumed randomness of the  $\varepsilon_P$  term in Equation (2.1), a single SAR image is of no use for computing the distance  $PM$  (Lu & Dzurisin, 2014). If we have another image recorded at the sensor location  $S$  (cf. Figure 2.4), which is the secondary image in this case, and assuming that there is no crustal movement at the considered pixel  $M$  between the two acquisitions, another relation between the phase value and the roundtrip sensor-target distance can be formed similar to Equation (2.1) as:

$$\phi_S = -\frac{4\pi}{\lambda}SM + \varepsilon_S \quad (2.2)$$

By combining phases derived from the two radar images, an interferogram can be formed which is the basic principle of InSAR. However, the two SAR images are generally captured at slightly different vantage points because of slight differences in orbit and acquisition start time (as per Figure 2.4), which results in a difference in imaging geometry. The second [secondary] SLC image must therefore be precisely aligned relative to the first [primary] one via the so-called co-registration step (e.g., Bamler & Eineder, 2005; Fattahi et al., 2017; Sansosti et al., 2006; Scheiber & Moreira, 2000). An interferogram can subsequently be formed by multiplying the complex-valued signals between the primary and secondary images of which the result is:

$$\phi = \phi_P - \phi_S = -\frac{4\pi(PM - SM)}{\lambda} + (\varepsilon_P - \varepsilon_S) \quad (2.3)$$

A fundamental assumption in InSAR is that the difference in scattering characteristics of the Earth's surface between the two acquisitions does not change much over time so that the  $(\varepsilon_P - \varepsilon_S)$  term in Equation (2.3) is considered insignificant and can be neglected. With this assumption, the interferometric phase of the generated interferogram is simplified to:

$$\phi = \phi_P - \phi_S = -\frac{4\pi(PM - SM)}{\lambda} \quad (2.4)$$

The interferometric phase in Equation (2.4) is relevant to the range difference  $PM - SM$ , which is the fundamental observable in InSAR DSM generation (Bamler & Hartl, 1998; Rosen et al., 2000). In the case of deformation measurement, assuming that the pixel  $M$  at the primary acquisition has moved to the location  $N$  at the secondary acquisition (see Figure 2.4), the interferometric LoS phase is:

$$\phi = \phi_P - \phi_S = -\frac{4\pi(PM - SN)}{\lambda} \quad (2.5)$$

Equation (2.5) can be re-written as:

$$\phi = \phi_P - \phi_S = -\frac{4\pi(PM - SM)}{\lambda} - \frac{4\pi(SM - SN)}{\lambda} \quad (2.6)$$

By comparing Equation (2.6) with Equation (2.4), it can be seen that the first term in Equation (2.6) is the topographic component, whilst the second term is relevant to the deformation component. If the topographic contribution is provided, e.g., from an existing DSM such as SRTM, and removed, the crustal deformation can be derived from the interferometric phase, which is fundamental in the differential InSAR (DInSAR) method (Hanssen, 2001; Massonnet & Feigl, 1998). This is principally implemented by the use of an existing DSM model in an approach named two-pass interferometry (Massonnet & Feigl, 1998; Rosen et al., 2000). Alternatively, the three-pass or four-pass techniques can be utilised where another interferogram is adopted to estimate the topographic phase component (Zebker et al., 1994; Zebker et al., 1997).

### 2.3.3 SAR phase filtering, unwrapping and geocoding

Interferograms generated as described above are affected by numerous phase noise sources such as thermal noise, temporal, geometric and volume decorrelations (Goldstein & Werner, 1998). In order to reduce the effect of these noises, interferograms are filtered by numerous different methods (e.g., Baran et al., 2003; Fang et al., 2016; Goldstein & Werner, 1998; López-Martínez & Fàbregas, 2002; Martínez et al., 2001). Additionally, the interferometric phase is modulated by  $2\pi$ , i.e., modulo  $-2\pi$ , ranging between  $-\pi$  and  $\pi$ . Its full phase value can be derived by computing the integer ambiguity, which is the number of multiple radar wavelengths, via the unwrapping step (e.g., Chen & Zebker, 2001, 2002; Hooper & Zebker, 2007). Finally, the interferogram is transformed from the radar coordinates to geographical coordinates by the geocoding step (e.g., Curlander, 1982; Nico, 2002; Sansosti, 2004).

A product of these processing steps is shown in Figure 2.5 as an example which was generated by combining two SAR SLC TSX images over Perth, Western Australia. The interferogram was produced from SLC images acquired on September 28, 2016 and October 09, 2016, filtered by the Goldstein method (Goldstein & Werner, 1998), unwrapped by the statistical-cost network-flow algorithm for phase unwrapping (SNAPHU) method (Chen & Zebker, 2000) applying the minimum cost flow (MCF) algorithm (Eineder et al., 1998; Mario Costantini, 1998; Pepe & Lanari, 2006). It was then geocoded to the World Geodetic System 1984 (WGS84) coordinate system.

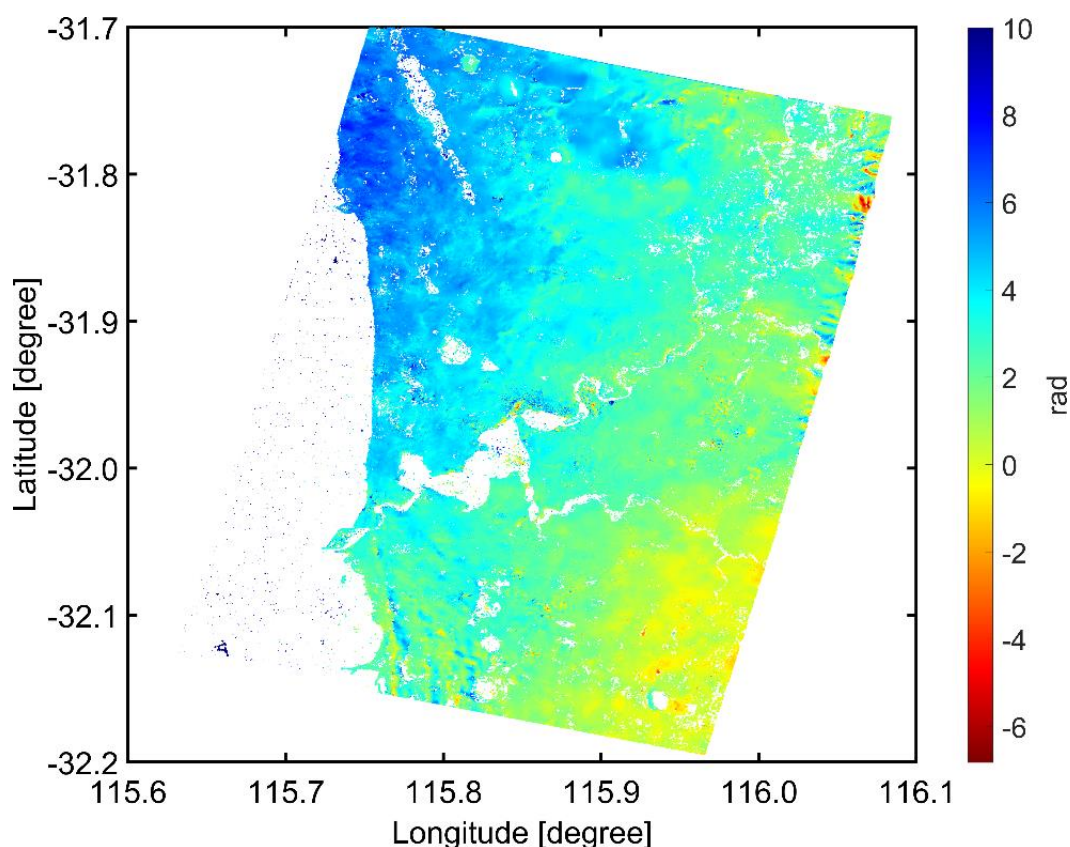


**Figure 2.5.** An interferogram processed by the ISCE software (Rosen et al., 2018) from TSX data over Perth, Western Australia. Pixels with coherence values less than 0.2 were removed from the interferogram. TSX data were provided under the German Space Centre’s Science Project LAN1499 and Australian Research Council Linkage Projects LP110100284 and LP140100155.

## 2.4 Chapter Summary

This Chapter began with the fundamentals of radar technology, which is based on the transmission and reception of electronic pulses in the radio and microwave frequency bands used for tracking and measuring the distance between the instrument and stationary or moving objects. The history of radar applications is then outlined indicating those in civilian, military and scientific applications, together with the classification of radar bands based on their frequencies and wavelength ranges.

SAR was then described, showing that it was invented because of the physical limitations of radar technology that a very large antenna size is required to have the desired spatial resolution and coverage. The working principle of a SAR system, with terminological definitions, were also shown together with its main operational modes of Stripmap, ScanSAR and Spotlight.

InSAR technology was described, showing the use of two SAR images to generate DSM or study Earth's surface deformation. In deformation applications, InSAR has its advantages over *in-situ* methods, e.g., GNSS or levelling, in that it provides a surface deformation map with a high spatial resolution, which is dependent on the radar band and operational modes. The basic principle of InSAR was described finally, showing that if the topographic contribution is provided and removed from an InSAR interferogram, then the Earth's deformation between the two acquisition times can be detected and quantified. An example over Perth was shown.

### 3. PRINCIPLES OF NOISE AND ERROR REDUCTION IN INSAR INTERFEROGRAMS

InSAR interferograms measure Earth surface deformation but are also contaminated by various error and noise sources. In this Chapter, the various sources of error and noise including topographic error, atmospheric artefacts, orbital error and noise are described in Section 3.1. This is followed by methods used to reduce orbital error in Section 3.2, atmospheric artefacts in Section 3.3 and DSM uncertainties in Section 3.4. Finally, Section 3.5 summarises the Chapter.

#### 3.1 Sources of Errors and Noise in InSAR Interferograms

Interferograms generated as described in Section 2.3 are affected by various errors and noise sources (e.g., [Berardino et al., 2002](#); [Lee et al., 2012](#)), which can be represented by:

$$\phi = \phi_P - \phi_S = \phi^{def} + \phi^{top} + \phi^{atm} + \phi^{orb} + \phi^n \quad (3.1)$$

where  $\phi^{def}$  is the phase contribution of the Earth's surface deformation,  $\phi^{top}$  represents the topographic uncertainty contribution,  $\phi^{atm}$  refers the difference in the atmosphere in which the radar signal propagates between the two acquisition dates,  $\phi^{orb}$  is the phase contributed by the uncertainties in satellite orbit information (ephemeris),  $\phi^n$  refers to the contributions of various other noise sources.

The uncertainties in the DSM model used in removing the topographic component in DInSAR can be propagated into the interferometric phase errors, which are proportional to the perpendicular baseline history, defined as the baseline of an image with respect to the first scene, in the set of selected SAR scenes ([Fattahi & Amelung, 2015](#)). This error type can be expressed as ([Fattahi & Amelung, 2013](#); [Lee et al., 2012](#)):

$$\phi^{top} = \frac{4\pi}{\lambda} \frac{B_{\perp}}{r \sin\theta} \Delta Z^{top} \quad (3.2)$$

where  $B_{\perp}$  refers to the perpendicular baseline,  $\lambda$  is the wavelength of the radar signal,  $\theta$  corresponds to the look angle,  $\Delta Z^{top}$  indicates the vertical uncertainty of the DSM used, and  $r$  is the slant range between the target and the SAR antenna. The DSM uncertainty ( $\Delta Z^{top}$ ) reflects the difference between the height extracted from DEM and that of the radar reflection point. This can be the inaccuracy of the DSM and/or a significant change of height in the study area between the time the DSM was generated

and the time the SAR scenes were acquired, e.g., due to open-cut mining or a building constructed after DSM acquisition.

The radar pulses transmitted by a SAR sensor propagate through the atmosphere to the Earth's surface and back. Due to the atmospheric refraction caused during their interaction with the atmosphere, which is different between the two acquisition dates corresponding to the two SAR images used in interferogram generation, atmospheric interferometric phase errors are present. This has been stated as one of the dominant error sources in interferograms (Goldstein, 1995). More specifically, this error source is caused by the variations in time and space of tropospheric water vapour content, temperature and pressure, of which the former is more dominant in magnitude (Zebker et al., 1997). Unlike GNSS or radar altimetry data, this error source is independent of the SAR radar wavelength (i.e., non dispersive), thus the use of multi-wavelength measurements for error reduction is impossible (Zebker et al., 1997). In InSAR data processing for deformation studies, this error source can be accounted for by numerous methods utilising stacking (e.g., Biggs et al., 2007; Tymofyeyeva & Fialko, 2015), local data assimilation, e.g., local atmospheric data (Delacourt et al., 1998), or zenith total delay (ZTD) from GNSS data (e.g., Williams et al., 1998; Yu, Li, & Penna, 2018; C. Yu et al., 2017), global or regional atmospheric models (e.g., Doin et al., 2009; Jolivet et al., 2011; Parker et al., 2015), or integrating a global atmospheric model and GNSS data (Yu, Li, Penna, et al., 2018).

The positions of the radar platform at the acquisition dates must be known with high precision to determine spatial baselines and to reduce the topographic component (Rosen et al., 2000). Although precise orbit data are now available (Calero, 2018; Wermuth et al., 2012; Yoon et al., 2009), remaining imperfection results in errors that propagate directly to InSAR-derived products (Hanssen, 2001). These orbital errors can be estimated using a polynomial model (e.g., Biggs et al., 2007; Cavalié et al., 2008; Jolivet et al., 2012; Lin et al., 2010) or other geodetic measurements such as GNSS (Pollitz et al., 2000; Simons et al., 2002).

The remaining components in the interferometric phase in Equation (3.1) are noise sources such as thermal noise, temporal, geometric and volume decorrelations (Goldstein & Werner, 1998; Zebker & Villasenor, 1992). These noise sources can be reduced in interferogram generation via filtering (Cai et al., 2008; Chen et al., 2005; Dabov et al., 2007; Goldstein & Werner, 1998; López-Martínez & Fàbregas, 2002; Martínez et al., 2001; Yu et al., 2007; Zha et al., 2008) or applying a noise model

whilst implementing the time series analysis (e.g., [Agram & Simons, 2015](#); [Guarnieri & Tebaldini, 2007](#); [Rocca, 2007](#); [Zebker & Villasenor, 1992](#)).

## 3.2 Orbital Error Reduction

### 3.2.1 Reduction Using a Polynomial Function

In this method, orbital errors are first estimated independently for each interferogram relying on selected coherent pixels. For an interferogram joining the  $i^{th}$  and  $j^{th}$  SAR images, the orbital error at a pixel located at the radar coordinates  $x$  (range) and  $y$  (azimuth) can be represented by a polynomial function with three parameters or a planar function as shown in Equation (3.3) ([Biggs et al., 2007](#); [Jolivet et al., 2012](#)), or four parameters or a “twisted plane” as shown in Equation (3.4) ([Cavalié et al., 2007](#); [Cavalié et al., 2008](#); [López-Quiroz et al., 2009](#)).

$$d_{ij}^{orb}(x, y) = a_{ij} \cdot x + b_{ij} \cdot y + c_{ij} \quad (3.3)$$

$$d_{ij}^{orb}(x, y) = a_{ij} \cdot x + b_{ij} \cdot y + c_{ij} + d_{ij}x \cdot y \quad (3.4)$$

In Equations (3.3) and (3.4),  $a_{ij}$ ,  $b_{ij}$ ,  $c_{ij}$  and  $d_{ij}$  are the interferometric orbital parameters that are estimated by least squares minimising the  $L_2$  norm of the difference ( $\Delta d_{ij}(x, y)$ ) between the InSAR interferometric deformation ( $d_{ij}(x, y)$ ) and the interferometric orbital error term ( $d_{ij}^{orb}(x, y)$ ), which is of the form:

$$\Delta d_{ij}(x, y) = d_{ij}(x, y) - d_{ij}^{orb}(x, y) \quad (3.5)$$

The least squares minimisation is applied to a system of equations formed from applying Equation (3.5) to all selected coherent pixels to estimate orbital parameters, which are then used to reduce orbital errors by Equations (3.3) or (3.4).

Alternatively, instead of using the three- or four-parameter model in Equation (3.3) or (3.4), a higher-order polynomial function can be applied ([Tian et al., 2018](#)). Additionally, wavelet multiresolution analysis can also be applied to decompose orbital error from other components in the unwrapped phase before applying a polynomial function to estimate orbital error parameters ([Shirzaei & Walter, 2011](#)).

### 3.2.2 Reduction Using Other Geodetic Data

Alternatively, other geodetic data, such as GNSS, can be used for this error reduction (e.g., [Pollitz et al., 2000](#); [Simons et al., 2002](#)). Only the ground stations situated within the coherent areas in the SAR scene are used. The GNSS displacement in the north

( $d_N$ ), east ( $d_E$ ) and up ( $d_U$ ) directions is first converted to that in the LoS ( $d_{LOS}$ ) direction by (e.g., [Fialko et al., 2001](#); [Hanssen, 2001](#)):

$$d_{LOS} = d_N \sin(\theta_{inc}) \sin(\alpha_h) - d_E \cos(\theta_{inc}) \sin(\alpha_h) + d_U \cos(\theta_{inc}) \quad (3.6)$$

where  $\theta_{inc}$  and  $\alpha_h$  are the radar incidence angle and the heading angle, respectively.

The interferometric orbital error parameters can then be estimated by least squares minimisation of the difference by ([Agram et al., 2012](#)):

$$\Delta d_{ij}(x, y) = d_{ij}(x, y) - d_{ij}^{orb}(x, y) - d_{ij}^{GNSS}(x, y) \quad (3.7)$$

where  $d_{ij}(x, y)$  refers to as the interferometric deformation,  $d_{ij}^{orb}(x, y)$  is the contribution of the orbital errors which is of the planar or “twisted plane” type shown in Equation (3.3) or (3.4),  $d_{ij}^{GNSS}(x, y)$  is the GNSS-derived deformation projected into the LoS direction by Equation (3.6). Again, the estimated orbital parameters are then used to reduce orbital errors by Equations (3.3) or (3.4).

### 3.3 Atmospheric Error Reduction

InSAR measurements exhibit artefacts due to signal propagation delay when transmitted through the atmosphere, which is largely caused by the spatial and temporal changes in water vapour in the troposphere ([Hanssen, 2001](#); [Zebker et al., 1997](#)) and the number of free electrons in the ionosphere ([Gray et al., 2000](#); [Mattar & Gray, 2002](#)). Atmospheric artefacts in InSAR interferograms are principally classified into stratified and turbulent components (e.g., [Doin et al., 2009](#); [Emardson et al., 2003](#); [Hanssen, 2001](#)), in which the former is correlated with topography ([Beauducel et al., 2000](#); [Delacourt et al., 1998](#); [Massonnet & Feigl, 1995](#)), whilst the latter is spatially correlated over a scale of approximately ten kilometres ([Jónsson et al., 2002](#); [Lohman & Simons, 2005](#)).

The ionospheric reduction can be employed by approaches including the multi-frequency split-spectrum technique (e.g., [Meyer et al., 2006b](#); [Rosen et al., 2010](#)), the method based on azimuth pixel shift or “azimuth streaks” (e.g., [De Michele et al., 2010](#); [Mattar & Gray, 2002](#); [Raucoules & De Michele, 2010](#)), or that based on co-registration ([Chen & Zebker, 2014](#)), which will be described in Subsection 3.3.1. The tropospheric part can be reduced by applying the stacking method ([Biggs et al., 2007](#); [Emardson et al., 2003](#)), MT-InSAR methods, e.g., SBAS (e.g., [Berardino et al., 2002](#); [Cavalié et al., 2007](#); [López-Quiroz et al., 2009](#); [Lundgren et al., 2001](#); [Usai, 2003](#)), spatio-temporal filtering of time series (e.g., [Berardino et al., 2002](#); [Ferretti et al., 2001](#);

Gong et al., 2015; Hooper et al., 2007), empirical or predictive approaches (Jolivet et al., 2014), which will be described in Subsection 3.3.2.

### 3.3.1 Ionospheric Reduction

Ionospheric electron density fluctuations or the variation in the total electron content (TEC) have been demonstrated to result in a kilometre-scale modulation in azimuth pixel shift, which is also known as “azimuth streaks” in InSAR results (Gray et al., 2000; Mattar & Gray, 2002). Unlike the neutral atmosphere, the ionospheric path delay is dependent on the inverse of the square of radar frequency (i.e., dispersive) (e.g., Raucoules & De Michele, 2010; Rosen et al., 2010), and thus is significant at C-band and worse for L-band systems (Chen & Zebker, 2012; Mattar & Gray, 2002). Therefore, most of the studies in the literature have addressed the atmospheric path delay on L-band SAR data (e.g., Chen & Zebker, 2012; Raucoules & De Michele, 2010; Rosen et al., 2010).

#### 3.3.1.1 The Multi-frequency Split-spectrum Technique

Because of the dependence of ionospheric path delay on the radar frequency, multi-frequency InSAR data can be utilised for ionospheric reduction. Rosen et al. (2010) introduced a method termed the multi-frequency split-spectrum processing technique. The differential phase of an InSAR interferogram is described as:

$$\phi = \frac{4\pi}{\lambda} \frac{B_{\perp}}{r} Z + \frac{4\pi}{\lambda} d^{def} + \frac{4\pi}{\lambda} d^{atm} + \frac{4\pi}{\lambda} d^{ion} \quad (3.8)$$

where the first term on the right hand side is the Earth’s topography component, the second term indicates the deformation of Earth’s surface, the third term relates to the path delay due to the neutral atmosphere, and the last term is related to the ionospheric path delay.

The ionospheric path delay can be written as (Meyer et al., 2006b; Rosen et al., 2010):

$$\phi^{ion} = \frac{4\pi}{\lambda} d^{ion} = 4\pi \frac{K}{c^2} \lambda \Delta TEC \quad (3.9)$$

where  $K = 40.28 \text{ m}^3\text{s}^{-2}$  and  $\Delta TEC$  is variation of TEC,  $\lambda$  is the radar wavelength, and  $c$  is the speed of light in vacuum. The first three components of Equation (3.8) are non-dispersive, whilst the ionospheric term is dispersive due to its dependence on the radar frequency. Equation (3.8) can therefore be rewritten relying on Equation (3.9) as:

$$\phi = \frac{4\pi}{\lambda} d^{nd} + \frac{4\pi K}{c^2} \lambda \Delta TEC \quad (3.10)$$

where  $d^{nd}$  is the combination of non-dispersive contributions. If the radar bandwidth is divided into two sub-bands centred at the wavelengths  $\lambda_1$  and  $\lambda_2$ , respectively then their interferometric phases will be:

$$\begin{aligned} \phi_1 &= \frac{4\pi}{\lambda_1} d^{nd} + 4\pi \frac{K}{c^2} \lambda_1 \Delta TEC \\ \phi_2 &= \frac{4\pi}{\lambda_2} d^{nd} + 4\pi \frac{K}{c^2} \lambda_2 \Delta TEC \end{aligned} \quad (3.11)$$

The non-dispersive path delay ( $d^{nd}$ ) and the total electron content ( $\Delta TEC$ ) are then computed as:

$$\begin{aligned} d^{nd} &= \frac{\phi_2 - \frac{\lambda_2}{\lambda_1} \phi_1}{\frac{4\pi}{\lambda_1} \left( \frac{\lambda_1}{\lambda_2} - \frac{\lambda_2}{\lambda_1} \right)} \\ \Delta TEC &= \frac{\phi_2 - \frac{\lambda_1}{\lambda_2} \phi_1}{\frac{4\pi K}{\lambda_2 c^2} (\lambda_1^2 - \lambda_2^2)} \end{aligned} \quad (3.12)$$

Equation (3.12) is the basis of the multi-frequency split-spectrum technique by which both the non-dispersive and dispersive components are estimated, then the ionospheric path delay is estimated.

### 3.3.1.2 Ionospheric Reduction Using Azimuth Streaks

The azimuth streaks in InSAR interferograms result from the variation in ionospheric TEC density. The azimuth streaks on subpixel offset maps estimated on co-registered images of interferometric pairs can therefore be used to estimate and reduce the ionospheric contributions as an alternative method (Mattar & Gray, 2002; Raucoules & De Michele, 2010). The relation between the ionospheric contribution to the azimuth offset ( $\Delta x^{ion}$ ) and the ionospheric contribution to the interferometric phase ( $\phi^{ion}$ ) can be described by (Meyer et al., 2006a, 2006b):

$$\Delta x^{ion} = \alpha \frac{\partial}{\partial x} \phi^{ion} \quad (3.13)$$

The azimuth offset ( $\Delta x^{ion}$ ) can be derived for the entire image from the azimuth streaks by various approaches, such as that proposed by De Michele et al. (2010) in which the azimuth offset map is split into three sub-images, then the azimuth offset reduction is approximated by a constant value along the streak direction. Alternatively,

a 1D low-pass filter can be used to derive the azimuth offset, e.g., a third-degree polynomial along the streak direction was applied in [Raucoules and De Michele \(2010\)](#) in which, after rotating the image to align the streaks horizontally, each line is represented by its third-degree fit. The azimuth offset is computed as an integration first, then the ionospheric phase is calculated following the relation shown in Equation (3.13), both are written as ([Raucoules & De Michele, 2010](#)):

$$\begin{aligned} I_{ij}^{ion} &= \sum_i \Delta x_{ij}^{ion} \\ \phi_{ij}^{ion} &= \frac{1}{\alpha} I_{ij}^{ion} \end{aligned} \quad (3.14)$$

where  $I_{i,j}^{ion}$  is the integration of azimuth offset at a pixel located at line  $i$  and column  $j$ ,  $\alpha$  –not to be confused with azimuth–is the coefficient calculated as:

$$\alpha = \frac{std(\Delta x)}{std\left(\frac{\partial}{\partial i} \phi\right)} \quad (3.15)$$

where  $std(.)$  refers to the standard deviation,  $\frac{\partial}{\partial i} \phi$  is the phase partial derivative, which is expressed as:

$$\frac{\partial}{\partial i} \phi_{ij} = \phi_{i+1,j} - \phi_{i,j} \quad (3.16)$$

### 3.3.1.3 Ionospheric Reduction Based on Co-registration

Ionospheric electron density fluctuations cause azimuth pixel shift ( $\Delta x_{i,j}^{ion}$ ) in InSAR interferograms, so a co-registration method proposed by [Chen and Zebker \(2014\)](#) can be applied to reduce this effect. In this case, due to the spatial variation in the azimuth offset, a low-order polynomial model used for co-registration is not appropriate. Instead, these authors proposed to apply a co-registration method, which begins by empirically estimating the azimuth and range offsets on a regular grid of points between two SAR images as:

$$\begin{aligned} \Delta x(iS_x, jS_R), \quad i = 1, \dots, N_x, j = 1, \dots, N_R \\ \Delta R(iS_x, jS_R), \quad i = 1, \dots, N_x, j = 1, \dots, N_R \end{aligned} \quad (3.17)$$

where  $\Delta x(iS_x, jS_R)$  and  $\Delta R(iS_x, jS_R)$  are the offsets in the azimuth and range directions used to convert the second image to the coordinate system of the first image, with  $S_x$  and  $S_R$  being the azimuth and range spacing of pixels,  $N_x$  and  $N_R$  are the numbers of arrays of offset estimates in azimuth and range directions, respectively.

$S_x$  and  $S_R$  can be set equal to 1, which means that the offset calculation is carried out for every pixel. However, this will cause a long computation time, and thus a larger spacing can be applied, then the computed results will be interpolated to all pixels. The offsets in Equation (3.17) are computed based on amplitude cross-correlation between the two SAR images, which are denoted by  $\Delta\hat{x}(i, j)$  and  $\Delta\hat{R}(i, j)$ . They are then low-pass filtered to derive  $\Delta x_{filt}(i, j)$  and  $\Delta R_{filt}(i, j)$ . Finally, the filtered offsets are spatially interpolated to all range and azimuth locations by, e.g., a bilinear interpolator before the second image is converted to the coordinate system of the first image.

### 3.3.2 Tropospheric Reduction

Tropospheric refraction can be reduced by applying the stacking method (e.g., [Biggs et al., 2007](#); [Emardson et al., 2003](#)). However, this method is effective only in the case that atmospheric delays are randomly variable in space and time ([Doin et al., 2009](#)). Other MT-InSAR methods such as the SBAS (e.g., [Berardino et al., 2002](#); [Cavalié et al., 2007](#); [López-Quiroz et al., 2009](#); [Lundgren et al., 2001](#); [Usai, 2003](#)) could be adopted to reduce tropospheric artefacts but they are also affected by seasonal atmospheric components ([Doin et al., 2009](#)). Three approaches that are more frequently employed in reducing tropospheric effects in InSAR interferograms are empirical and predictive methods ([Jolivet et al., 2014](#)) and spatio-temporal filtering of InSAR time series (e.g., [Berardino et al., 2002](#); [Ferretti et al., 2001](#); [Hooper et al., 2007](#)), which are summarised in the subsequent Subsections.

#### 3.3.2.1 The Empirical Approach

In the empirical approach, atmospheric path delay and topography are assumed correlated and the dependence of interferometric phase on elevation is modelled and estimated for interferograms (e.g., [Beauducel et al., 2000](#)). Low-order polynomial models have been utilised in atmospheric reduction applying the empirical approach with a linear function being applied in various studies in which the slope is a parameter that is estimated ([Cavalié et al., 2007](#); [Cavalié et al., 2008](#); [Elliott et al., 2008](#); [Wicks et al., 2002](#)). The relation between the phase delay due to tropospheric refraction ( $\phi_{i,j}^{tropo}$ ) and the elevation of the Earth's surface ( $Z$ ) is first identified from coherent pixels in each interferogram by which the slope parameter ( $S_{ij}$ ) is derived corresponding to the interferogram connecting the  $i^{th}$  and  $j^{th}$  images:

$$\phi_{i,j}^{tropo} = S_{ij}Z \quad (3.18)$$

Figure 3.1 shows an example of this relation derived from European Remote Sensing (ERS) satellite InSAR data applied in Nevada, USA, between January 5, 1997 and January 25, 1997, which is reproduced from [Cavalié et al. \(2007\)](#).

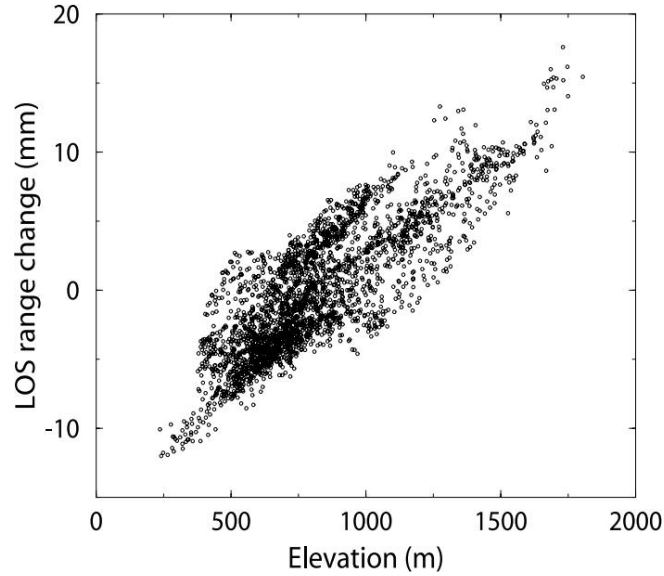


Figure 3.1. The correlation between InSAR LoS range change and topography from [Cavalié et al. \(2007\)](#).

The phase/elevation slopes of interferograms allow for the computation of the slopes of images by ([Cavalié et al., 2007](#)):

$$S_{ij} = S_j - S_i \quad (3.19)$$

where  $S_{ij}$  is the slope of the interferogram connecting the  $i^{th}$  and  $j^{th}$  images with the corresponding slopes  $S_i$  and  $S_j$ , respectively.

With an SBAS network of  $N$  interferograms formed by  $M + 1$  SAR images ( $N > M + 1$ ), the slopes of all images can be estimated in a network sense by solving ([Cavalié et al., 2007](#)):

$$\mathbf{d} = \mathbf{G} \cdot \mathbf{s} \quad (3.20)$$

where  $\mathbf{d}$  is a vector of  $N$  interferogram slopes,  $\mathbf{s}$  is a vector of  $M$  image slopes,  $\mathbf{G}$  is a  $N \times M$  matrix with elements of the  $k^{th}$  row corresponding to the  $k^{th}$  interferogram being 1 in the secondary (formerly slave) acquisition,  $-1$  in the primary (formerly master) acquisition, and 0 otherwise. Next is an example.

$$\mathbf{G} = \begin{bmatrix} +1 & 0 & 0 & 0 & \dots \\ \dots & \dots & \dots & \dots & \dots \\ 0 & -1 & +1 & 0 & \dots \\ 0 & -1 & 0 & +1 & \dots \\ \dots & \dots & \dots & \dots & \dots \end{bmatrix} \quad (3.21)$$

Finally, the interferogram slopes are re-estimated by Equation (3.19) based on the computed image slopes, which are then used for the atmospheric error reduction.

This approach is applied with a constant slope estimated for an interferogram and has worked well with most weather conditions, but some extraordinary cases exist, e.g., inverted or non-monotonic tropospheric stratifications (Lin et al., 2010). Additionally, the phase/elevation slopes described above may have a local trade-off that the slopes best describe global linear regression rather than the local one (Cavalié et al., 2007). To overcome these disadvantages, Lin et al. (2010) proposed a multiscale approach for tropospheric error reduction. In this, instead of applying a constant slope for an interferogram, a multiscale decomposition relying on a Gaussian filter with band-pass filtering is applied to both topography and phase changes.

Another method, which is based on wavelet transforms, can also be adopted to identify the components of topography-correlated unwrapped interferograms over different frequencies (Shirzaei & Bürgmann, 2012). Alternatively, in mountainous or steep topography areas, the above linear model may be inappropriate, so a non-linear model can be applied (e.g., Remy et al., 2003).

### 3.3.2.2 The Predictive Approach

The predictive approach works by utilising external data to generate tropospheric delay maps, which are then used for reducing interferograms. In this approach, numerous methods have been proposed applying local data assimilation, e.g., local atmospheric data (Delacourt et al., 1998), ZTD computed from GNSS (e.g., Williams et al., 1998; Yu, Li, & Penna, 2018; C. Yu et al., 2017), spectrometer measurements (Li, Muller, et al., 2006), moderate resolution imaging spectroradiometer (MODIS) data (Li et al., 2009; Li et al., 2005), radiosonde-balloon sounding measurements (Bekaert et al., 2015), utilising global or regional atmospheric models (e.g., Doin et al., 2009; Jolivet et al., 2011; Parker et al., 2015), or integrating a global atmospheric model and GNSS data to an atmospheric reduction model (Yu, Li, & Penna, 2018).

### 3.3.2.2.1 Reduction Using Local Atmospheric Data

In the method of applying local atmospheric data, a 1D model for reducing tropospheric excess path in InSAR interferograms can be applied (Delacourt et al., 1998). In relation to meteorological data, atmospheric artefacts can be divided into the hydrostatic (dry) component, which is dependent on pressure and temperature, and the wet component, which depends on temperature and water vapour content (Delacourt et al., 1998; Hanssen, 2001). It is reasonable to account for both components, and therefore, in this method, the excess InSAR path length between satellite and ground due to the delay caused by the propagation of SAR signal through the troposphere can be expressed as (Delacourt et al., 1998):

$$\Delta L^{tropo} = \frac{1}{\cos\theta} (\Delta L_h^{tropo} + \Delta L_w^{tropo}) \quad (3.22)$$

where  $\Delta L^{tropo}$  is the excess path,  $\theta$  is the look angle,  $\Delta L_h^{tropo}$  and  $\Delta L_w^{tropo}$  are the hydrostatic and wet components, respectively.

The hydrostatic and wet components are the functions of ground meteorological variables (i.e., pressure, temperature and humidity) with a given altitude  $Z_g$ , which are empirical or semi-empirical formulas (Delacourt et al., 1998). These variables in turn have linear or non-linear relations with the corresponding variables to a reference point with altitude  $Z_0$ . The parameters of these functions can then be derived by utilising meteorological measurements, e.g., from ground-based stations situated within the SAR scenes by which a given formula can be obtained to be applied for atmospheric reduction for all interferograms (Delacourt et al., 1998).

### 3.3.2.2.2 Reduction Using GNSS Data

Another predictive method is the application of GNSS-derived ZTD in InSAR tropospheric reduction (e.g., Webley et al., 2002; Williams et al., 1998). The tropospheric excess path is caused by the variations of meteorological variables, including temperature, pressure and water vapour in which the effect of water vapour is higher in magnitude, unevenly distributed in space, and highly variable in time (Goldstein, 1995; Zebker et al., 1997). In addition, the hydrostatic part is dependent on temperature and pressure, which can be estimated by using meteorological measurements observed on or near the Earth's surface (e.g., Webley et al., 2002).

In this method, the reduction of the wet contribution is usually investigated. ZTD is first derived from GNSS measurements prior to converting to zenith wet delay (ZWD), which is associated with the wet component shown in Equation (3.22), by:

$$ZWD = ZTD - ZHD \quad (3.23)$$

where  $ZHD$  is the zenith hydrostatic delay contribution, which is relevant to the hydrostatic component shown in Equation (3.22), and can be computed for each GNSS station by (Saastamoinen, 2013):

$$ZHD = \frac{0.0022768P_s}{1 - 0.00266\cos(2\varphi) - 0.00028h_s} \quad (3.24)$$

where  $P_s$  is the surface pressure which is derived from surface observations or using an atmospheric model, e.g., Saastamoinen or Hopfield,  $h_s$  is the surface altitude above the ellipsoid and  $\varphi$  is the geodetic latitude.

ZWD estimated from Equation (3.23) is subsequently used for tropospheric reduction in InSAR. Although GNSS networks are becoming spatially denser and are of a broader spatial coverage (e.g., Blewitt et al., 2018), their spatial resolution is not consistent with that of InSAR, and thus spatial interpolation is needed (Emardson & Johansson, 1998; Williams et al., 1998). The effectiveness of this method, therefore, depends on the accuracy of GNSS ZTD data, their spatial density, the interpolator, and the spatial variation of tropospheric effects (Williams et al., 1998).

Various methods have been adopted to interpolate GNSS-derived zenith delay (i.e., ZTD or ZWD) at InSAR pixels, including nearest neighbour, a weighted sum of delay from surrounding stations, a Best Linear Unbiased Estimator (BLUE) (Emardson & Johansson, 1998; Li, Fielding, et al., 2006), inverse distance weighted average, bilinear, polynomial, Kriging (Jarlemark & Emardson, 1998; Onn & Zebker, 2006; Webley et al., 2002; Williams et al., 1998), or splines (Buckley et al., 2003; Janssen et al., 2004). Of these, the statistical methods, e.g., BLUE, Kriging, rely on the spatial correlation between stations, which requires the covariance between GNSS stations as well as between GNSS stations and InSAR pixels. This is derived by the spatial structure function over spatial distances  $L$ , with assumptions of homogeneous, isotropic and ergodic random fields (Li, Fielding, et al., 2006; Williams et al., 1998):

$$D_x(L) = \langle [x(r_0, L) - x(r_0)]^2 \rangle \quad (3.25)$$

where the angle brackets  $\langle . \rangle$  indicate the ensemble average,  $r_0$  is the spatial coordinate,  $x(r_0)$  and  $x(r_0, L)$  are the zenith path delays of tropospheric reduction at  $r_0$  and at a point separated from  $r_0$  by the distance  $L$ , respectively.

The spatial structure function shown in Equation (3.25) is described as a power law process (e.g., [Bekaert et al., 2015](#); [Emardson & Johansson, 1998](#); [Li, Fielding, et al., 2006](#); [Treuhaft & Lanyi, 1987](#); [Williams et al., 1998](#)):

$$D_x(L) = cL^\alpha \quad (3.26)$$

where  $c$  indicates the roughness or scale of the process and  $\alpha$ —again not to be confused with azimuth—is the power index indicating the rate at which the spatial correlation is lost with increasing distance.

In the frequency domain, a power law process is of a power spectrum with the form ([Agnew, 1992](#); [Mandelbrot & Van Ness, 1968](#)):

$$P_x(f) = P_0 \left( \frac{f}{f_0} \right)^\kappa \quad (3.27)$$

where  $f$  is the spatial or temporal frequency,  $P_0$  and  $f_0$  are the normalising constants, and  $\kappa$  is the spectral index.

The relation between the power index  $\alpha$  in Equation (3.26) and the spectral index  $\kappa$  in Equation (3.27) is ([Li, Fielding, et al., 2006](#)):

$$\alpha + \kappa = -1 \quad (3.28)$$

The spectral index varies between  $-3$  and  $1$ , with  $-3 < \kappa < -1$  being a nonstationary process and  $-1 < \kappa < 1$  indicating a stationary process. Special cases exist with integer spectral indices: (Gaussian) white noise has a spectral index of  $0$ , flicker noise corresponds to a spectral index of  $-1$ , and random walk or Brownian noise has an index of  $-2$  ([Williams et al., 2004](#)).

[Treuhaft and Lanyi \(1987\)](#) estimated  $\alpha = 2/3$  ( $\kappa = -5/3$ ), corresponding to Kolmogorov turbulence ([Tatarskii, 1971](#)), for distances  $L$  up to  $3000$  km and  $\alpha = 5/3$  ( $\kappa = -8/3$ ) for  $L$  much smaller than one kilometre. A power law with a spectral index ( $\kappa$ ) of  $-8/3$  for spatial scales between  $0.4$  and  $6$  km was found from C-band radar interferograms recorded over the Mojave Desert, California by [Goldstein \(1995\)](#). Atmospheric effects studied from TanDEM interferograms over Groningen, The Netherlands, showed power law behaviour with spectral indices being  $-5/3$ ,  $-8/3$  and  $-2/3$  for spatial scales larger than  $2$  km, between  $0.5$  and  $2$  km, and smaller than  $0.5$  km, respectively ([Hanssen, 2001](#)). [Williams et al. \(1998\)](#) show that the tropospheric delay variations confirm the [Treuhaft and Lanyi \(1987\)](#) statistical model both in time and space, and suggest that an average spacing of  $10$  km is needed for an

accuracy of 5 mm in InSAR tropospheric reduction when a Kriging interpolator is applied.

The spatial structure function shown in Equation (3.26) represents the variance between two points depending solely on their distance, which works in areas with small variations in elevation (Li, Fielding, et al., 2006). However, in mountainous areas with large variations in elevation, the average variance ( $\sigma$ ) in water vapour is dependent on both the distances and the height differences ( $\Delta h$ ) between observations (Emardson et al., 2003), and thus a function is applied as (Emardson et al., 2003; Li, Fielding, et al., 2006):

$$\sigma = 2.8 L^{1.4} + 0.5 \Delta h \quad (3.29)$$

Regardless of whether or not the above spatial structure functions consider the dependence of the variance of tropospheric delay on topography (i.e., Equations (3.26) or (3.29)), the topography is not dealt with in the above-mentioned interpolators, which may suffer from large errors in highly variable topographic areas. Methods used to interpolate GNSS-derived tropospheric total delay accounting for topography dependence have therefore been proposed (Xu et al., 2011). A model incorporating both stratified and turbulent components from GNSS-derived total delay has been proposed (C. Yu et al., 2017):

$$ZTD_k = T(\mathbf{x}_k) + L_0 e^{-\beta \bar{h}_k} + \varepsilon_k \quad (3.30)$$

where  $ZTD_k$  is the ZTD at the location  $k$ ,  $T$  is the turbulent component,  $\mathbf{x}_k$  is the vector of GNSS station coordinates,  $L_0 e^{-\beta \bar{h}_k}$  is the stratified component represented by an exponential function with parameters  $L_0$  and  $\beta$ ,  $\varepsilon_k$  is the remaining unmodelled residual errors,  $\bar{h}_k$  is the scaled height, which can be computed by:

$$\bar{h}_k = \frac{h_k - h_{min}}{h_{max} - h_{min}} \quad (3.31)$$

where  $h_{min}$  and  $h_{max}$  are the minimum and maximum heights in the image.

The model shown in Equation (3.30) is solved iteratively to decompose the turbulent, stratified components and the remaining residual errors via a model termed iterative tropospheric decomposition (ITD), with outputs being the turbulent delay components and residuals at GNSS stations and exponential coefficients ( $L_0$  and  $\beta$ ). These are subsequently used to interpolate ZTD at a location of interest by employing an interpolator applied to the turbulent components and residuals derived at the GNSS

stations prior to adding the stratified component estimated from its height. This model was adapted and applied to InSAR tropospheric reduction by [Yu, Li and Penna \(2018\)](#).

### 3.3.2.2.3 Reduction Using Atmospheric Models

The use of atmospheric models in InSAR tropospheric reduction is yet another method (e.g., [Foster et al., 2006](#); [Foster et al., 2013](#); [Jolivet et al., 2014](#); [Jolivet et al., 2011](#); [Nico et al., 2011](#); [Parker et al., 2015](#)). The tropospheric delay is divided into a stratified delay and a turbulent delay, in which the spatial patterns of the latter are mostly random at each SAR acquisition, and can be reduced by stacking interferograms or through InSAR time series analysis (e.g., [Doin et al., 2009](#)). This method normally accounts for the stratified contribution (e.g., [Doin et al., 2009](#); [Jolivet et al., 2011](#)) by:

$$\Delta L_{LoS}^{tropo}(Z) = \frac{10^{-6}}{\cos(\theta)} \left\{ \frac{222.751}{g_m} [P(Z) - P(Z_{ref})] + \int_Z^{Z_{ref}} \left[ (0.716 - 0.483) \frac{e(Z)}{T(Z)} + 3750 \frac{e(Z)}{T(Z)^2} \right] dZ \right\} \quad (3.32)$$

where  $\Delta L_{LoS}^{tropo}(Z)$  is the total LoS single-path tropospheric delay,  $\theta$  is the local incidence angle,  $g_m$  is the weighted average of the gravity acceleration between surface elevation ( $Z$ ) and the elevation of the reference ( $Z_{ref}$ ),  $P$  is the dry air partial pressure in Pa,  $e$  is the water vapour partial pressure in Pa,  $T$  is the temperature in Kelvin.

$Z_{ref}$  in Equation (3.32) is the height above which the delay is assumed to be unchanged, which was chosen as 10,000 m by [Jolivet et al. \(2011\)](#) or 15,000 m by [Parker et al. \(2015\)](#). The first term in Equation (3.32) corresponds to the dry component, whilst the second term is related to the wet component. Various atmospheric models can be utilised for tropospheric reduction, which are listed in [Table 3.1](#).

Table 3.1. Atmospheric models utilised in InSAR tropospheric correction.

Model name	Provider	Reference
ERA40 reanalysis	European Centre for Medium-Range Weather Forecast	
ERA-Interim	European Centre for Medium-Range Weather Forecast	
MERRA	National Aeronautics and Space Administration	<a href="#">Rienecker et al. (2011)</a>
NARR	National Centre for Environmental Prediction	<a href="#">Mesinger et al. (2006)</a>
	National Centre for Atmospheric Research	
WRF	National Centre for Environmental Prediction	<a href="#">Skamarock et al. (2008)</a>
	National Centre for Atmospheric Research	
	Department of Defense's Air Force Weather Agency	
	Naval Research Laboratory	
	Center for Analysis and Prediction of Storms at the University of Oklahoma	
	Federal Aviation Administration	

The meteorological variables of temperature, dry air partial pressure and water vapour partial pressure are provided from atmospheric models on various pressure levels and are extracted at regular grids overlapping with the spatial coverage of SAR images. They can be interpolated vertically from the Earth's surface and the reference altitude ( $Z_{ref}$ ) by, e.g., spline interpolation (Jolivet et al., 2014; Jolivet et al., 2011; Parker et al., 2015; Walters et al., 2013). The delay map is generated for each acquisition by Equation (3.32). The tropospheric delay is then computed for each acquisition at InSAR pixels by spatial interpolation from grids in close vicinity. Finally, differential delay maps are created for interferograms by combining pairs of absolute delay maps of SAR scenes, which are then used to correct the interferograms. Various methods can be applied to spatially interpolate the absolute atmospheric delays from grids to SAR pixels and vertically interpolate meteorological variables, e.g., bilinear and spline (Jolivet et al., 2014; Jolivet et al., 2011; Parker et al., 2015; Walters et al., 2013).

Another method combining different data has also been studied, e.g., a combination of GNSS and the National Aeronautics and Space Administration (NASA) Moderate Resolution Imaging Spectroradiometer (MODIS) water vapour data (Li et al., 2005), an integration of GNSS and the European Centre for Medium-Range Weather Forecasts (ECMWF) data (Yu, Li, Penna, et al., 2018), or a combination of spectrometer data with an atmospheric model (Walters et al., 2013).

### 3.3.2.3 Spatio-temporal Filtering

Filtering methods are applied in InSAR at different stages with different aims. For example, the bandpass filtering method (Gatelli et al., 1994) or the Goldstein method (Goldstein & Werner, 1998) is applied before or after interferogram formation to reduce interferometric noise. The spectral filter method is applied to assist in selecting coherent pixels (Hooper, 2008). Filtering methods based on a sequential Monte Carlo framework are applied to reduce residual noise in InSAR deformation time series (Khaki et al., 2019). To reduce tropospheric error, spatio-temporal filtering (Berardino et al., 2002; Hooper, 2008; Hooper et al., 2007) can also be applied.

The spatio-temporal filtering method was developed relying on the relation between different components contributing to the interferometric phase in Equation (3.1), in which the deformation component, atmospheric and orbital errors are spatially-correlated. Spatial filtering is therefore applied to interferometric phase to

estimate the spatially correlated terms, which is then subtracted from the interferometric phase. The DSM error contribution is then modelled in the remaining component, i.e., after removing the spatially-correlated terms, for the time series by which the noise is estimated. With the assumption that the deformation is correlated in time, the atmospheric component is spatially correlated, and noise is uncorrelated, this spatio-temporal filtering can be applied to reduce the atmospheric contribution, which is mostly due to time- and space-variable turbulent tropospheric noise (Cao et al., 2018).

### 3.4 Digital Surface Model Error Reduction

A digital surface model (DSM) is used to remove the topographic component in InSAR interferograms. However, a DSM is not perfectly precise, which leads to the transmission of DSM uncertainties to InSAR results (Bombrun et al., 2009). Two methods can be applied to reduce DSM errors: working with wrapped interferograms (e.g., Ducret et al., 2011, 2014; Goel & Adam, 2014; Pepe & Lanari, 2017) or unwrapped interferograms (e.g., Berardino et al., 2002; Bombrun et al., 2009; Pepe et al., 2011; Samsonov, 2010).

#### 3.4.1 Reduction to Wrapped Interferograms

The interferometric phase of an interferogram connecting two SAR scenes is of the form shown in Equation (3.1), in which the residual topographic error component can be written in relation to the perpendicular baseline as (e.g., Bombrun et al., 2009; Ducret et al., 2014):

$$\phi^{top} = \frac{4\pi}{\lambda} \frac{B_{\perp,ij}}{r \sin\theta} \Delta Z^{top} \quad (3.33)$$

where  $\lambda$  is the radar wavelength,  $B_{\perp,ij}$  is the perpendicular baseline between the two SAR images,  $\theta$  is the pixel local incidence angle,  $\Delta Z^{top}$  is the local DSM error.

In the algorithm proposed by Ducret et al. (2014), SAR scenes are divided into various overlapping sub-windows then, in each sub-window, a reference pixel with the highest average coherence ( $\bar{\gamma}$ ) over all interferograms is selected. The interferometric phase difference of a pixel with respect to the reference pixel can be written by combining Equations (3.1) and (3.33) as:

$$\delta\phi_{ij} = \delta\alpha B_{\perp,ij} + \beta \quad (3.34)$$

where  $\beta$  is the phase offset, which should tend to the average deformation over all interferograms with respect to the reference pixel, providing that the atmospheric delay and the orbital error components are assumed to be negligible if the interest and reference pixel are located nearby, and  $\delta\alpha$  is the relative DSM error coefficient, which is defined as:

$$\delta\alpha = \frac{4\pi}{\lambda r \sin\theta} (\Delta Z^{top} - \Delta Z_{ref}^{top}) \quad (3.35)$$

where  $\Delta Z^{top}$  and  $\Delta Z_{ref}^{top}$  are the DSM errors of the interest pixel and the reference pixel, respectively.

A three-step procedure is then applied to reduce DSM errors relying on Equation (3.34) before they are mosaicked to derive the reduced DSM for the entire image (Ducret et al., 2014). The method of Ducret et al. (2014) considers the average velocities ( $\bar{V}$ ) of overlapping patches, neglecting local deformation gradients. A similar method, but considering the local gradients of deformation velocity and the local gradients of DSM error in range and azimuth directions, is proposed by Goel and Adam (2014), with the deformation model being:

$$\phi_{p,l}^{model} = kV_1 \delta V_x id_{x_p} + kV_1 \delta V_y id_{y_p} + kZ_1 \delta \Delta Z_x^{top} id_{x_p} + kZ_1 \delta \Delta Z_y^{top} id_{y_p} \quad (3.36)$$

where  $\phi_{p,l}^{model}$  is the phase model of deformation rates of the  $l^{th}$  interferogram at the pixel  $p$ , accounting for the local gradients of deformation velocity  $\delta V_x$ ,  $\delta V_y$  and the local gradients of DSM error  $\delta \Delta Z_x^{top}$ ,  $\delta \Delta Z_y^{top}$  in range  $x$  and azimuth  $y$  directions, respectively,  $id_{x_p}$  and  $id_{y_p}$  are the pixel indices in range and azimuth directions, respectively,  $kV_1$  and  $kZ_1$  are the velocity and height conversion factors, which are given by (Goel & Adam, 2014):

$$\begin{aligned} kV_1 &= \frac{4\pi}{\lambda} B_{T,l} \\ kZ_1 &= \frac{4\pi}{\lambda} \frac{B_{\perp,l}}{r \sin\theta} \end{aligned} \quad (3.37)$$

where  $B_{T,l}$  and  $B_{\perp,l}$  are the temporal and perpendicular baselines of the  $l^{th}$  interferogram.

Another method working with wrapped interferograms was proposed by Pepe and Lanari (2017). The scenes are divided into patches then coherent pixels are selected. However, instead of computing the relative phase of a pixel with respect to the chosen reference pixel, in this method, arcs connecting these coherent pixels are chosen, then their relative phases are computed as (Pepe & Lanari, 2017):

$$\delta\phi_{l,PQ} = \frac{4\pi}{\lambda} \frac{B_{\perp,l}}{r \sin\theta} (\Delta Z_P^{top} - \Delta Z_Q^{top}) + \frac{4\pi}{\lambda} B_{T,l} (V_P - V_Q) \quad (3.38)$$

where  $\delta\phi_{l,PQ}$  is the relative phase of the  $l^{th}$  interferogram between pixels  $P$  and  $Q$ ,  $\Delta Z_P^{top}$ ,  $\Delta Z_Q^{top}$  are the DSM errors and  $V_P$ ,  $V_Q$  are the ground deformation velocities at the two pixels, respectively.

The DSM errors ( $\Delta Z^{top}$ ) and deformation rates ( $V$ ) are then derived by solving the quasi-Newton limited-memory bounded Broyden-Fletcher-Goldfarb-Shanno (L-BFGS) (Byrd et al., 1995) algorithm based on Equation (3.38) before patches are mosaicked (Pepe & Lanari, 2017).

### 3.4.2 Reduction to Unwrapped Interferograms

Alternatively, reduction of DSM errors can be conducted with unwrapped interferograms. Bombrun et al. (2009) proposed a method to reduce DSM errors through analysing time series of unwrapped interferograms that is based on that the DSM error component is proportional to perpendicular baseline lengths. In this method, the phase difference between interferogram  $k$  linking image acquisitions  $k$ ,  $(k + 1)$  and the interferogram  $l$  connecting images acquired at dates  $l$ ,  $(l + 1)$  is defined as:

$$\delta\phi_{kl} = \delta\phi_{kl}^{def} + \delta\phi_{kl}^{top} + \delta\phi_{kl}^{atm} + \delta\phi_{kl}^n \quad (3.39)$$

where  $\delta\phi_{kl}^{def}$  is the phase component induced by the surface displacements from the two interferograms,  $\delta\phi_{kl}^{top}$  is the residual topographic phase,  $\delta\phi_{kl}^{atm}$  is the residual atmospheric artefacts, and  $\delta\phi_{kl}^n$  is the noise component.

With the aim of reducing DSM errors,  $\delta\phi_{kl}^{top}$  is considered as the “signal part” and the remaining terms, i.e., displacement, atmospheric artefacts and noise, are referred to as the “noise part” (Bombrun et al., 2009), with the signal part being:

$$\delta\phi_{kl}^{top} = \frac{4\pi}{\lambda} \frac{B_{\perp,k} - B_{\perp,l}}{r \sin\theta} \Delta Z^{top} \quad (3.40)$$

The residual topographic phase differences between two pixels  $P$  and  $Q$  is:

$$\begin{aligned} \delta\phi_{kl}^{top}(P, Q) &= \delta\phi_{kl}^{top}(P) - \delta\phi_{kl}^{top}(Q) \\ &= \frac{4\pi}{\lambda} \frac{B_{\perp,k} - B_{\perp,l}}{r \sin\theta} (\Delta Z_P^{top} - \Delta Z_Q^{top}) \end{aligned} \quad (3.41)$$

Finally, the DSM errors between pixels  $P$  and  $Q$  are:

$$\Delta Z^{top}(P, Q) = \Delta Z_P^{top} - \Delta Z_Q^{top} = \frac{\lambda}{4\pi} \frac{r \sin\theta}{B_{\perp,k} - B_{\perp,l}} \delta\phi_{kl}^{top}(P, Q) \quad (3.42)$$

Equation (3.42) indicates that the relative DSM error between two pixels ( $\Delta Z^{top}(P, Q)$ ) is a constant over all interferograms. The phase difference between two interferograms  $k$  and  $l$  from Equation (3.39) can be computed relatively between two pixels  $P, Q$ , which involves the term of DSM error as in Equation (3.41) and the remaining contributions, i.e., atmospheric artefacts, displacement and noise (see Equation (3.39)). The DSM component, as shown in Equation (3.42), is inversely proportional to relative perpendicular baseline lengths, whilst the remaining terms in Equation (3.39) are not. Equation (3.43) is therefore used as a hypothesis to test whether interferograms are affected by DSM errors:

$$K(P, Q) = \frac{\lambda}{4\pi} \frac{r \sin \theta}{B_{\perp,k} - B_{\perp,l}} \delta \phi_{kl}(P, Q) \quad (3.43)$$

The difference between Equations (3.42) and (3.43) in terms of the phase values used, which are  $\delta \phi_{kl}^{top}(P, Q)$  in Equation (3.41) and  $\delta \phi_{kl}$  in Equation (3.39). Equation (3.43) is then applied to different pairs of pixels  $P, Q$ . If  $K(P, Q)$  is a constant for all pixel couples and interferogram pairs then interferograms are affected by DSM errors. In this case, Equation (3.40) is applied to estimate DSM error ( $\Delta Z_i^{top}$ ) for each interferogram then the mean value is computed over  $N$  interferogram pairs by:

$$\Delta Z^{top} = \frac{1}{N} \sum_{i=1}^N \Delta Z_i^{top} \quad (3.44)$$

The new DSM is then derived by adding estimated DSM errors to the “old” DSM. In contrast, if estimated  $K(P, Q)$  is not a constant, i.e., the hypothesis shown in Equation (3.43) is rejected, then interferograms are affected by not only DSM errors but also other contributions, and nothing will be done.

### 3.5 Chapter Summary

This Chapter has reviewed sources of error and noise in InSAR interferograms, where the derived interferograms consist of not only the Earth’s deformation but also the contributions of DSM uncertainties, atmospheric artefacts, orbital error and other noise. The methods used to reduce these errors and noise in the literature are also reviewed.

Two approaches used in reducing interferometric orbital error are shown in this Chapter, which use a polynomial function, alternatively combined with other geodetic data, e.g., GNSS. In both approaches, least squares minimisation is employed to estimate orbital parameters by minimising the difference between interferometric

deformation, the contribution of the orbital errors from the polynomial function and the GNSS-derived deformation.

The methods used to reduce atmospheric error are divided into two groups, which are ionospheric and tropospheric reductions. Three methods of ionospheric reduction were reviewed in this Chapter. The first method is termed the multi-frequency split-spectrum technique, which works by dividing the bandwidth of the data into two sub-bands based on which the ionospheric component is estimated. In the second method, ionospheric reduction is conducted relying on the azimuth streaks, and the third method is based on co-registration.

The empirical, predictive, and spatio-temporal filtering approaches used to reduce tropospheric error are also reviewed. In the empirical approach, tropospheric path delay and topography are assumed correlated and low-order polynomial functions are utilised to reduce tropospheric artefacts. Alternatively, a multiscale method can also be applied, which works based on a multiscale decomposition on a Gaussian filter with band-pass filtering. Another method is based on wavelet transforms, which works by the estimation of the components of topography-correlated unwrapped interferograms over different frequencies. The predictive approach works by utilising external data to generate tropospheric delay maps to correct interferograms, which are local atmospheric data, GNSS-derived zenith wet delay, or meteorological variables from atmospheric models.

Spatio-temporal filtering applied in tropospheric error reduction relies on the relation between different components contributing to the interferometric phase, in which the deformation component, atmospheric and orbital errors are spatially correlated. Spatial filtering is applied to interferometric phase to estimate the spatially correlated terms, which is then subtracted from the interferometric phase. The DSM error contribution is then modelled in the remaining component for the time series by which the noise is estimated. With the assumption that the deformation term is correlated in time, the atmospheric component is spatially correlated, and noise is uncorrelated, spatio-temporal filtering can be applied to reduce the atmospheric contribution, which is mostly due to time- and space-variable turbulent tropospheric noise.

Two approaches working with wrapped and unwrapped interferograms in reducing topographic error are reviewed in this Chapter. In the first approach, a method proposed by [Ducret et al. \(2014\)](#) can be applied to reduce DSM errors relying on the

phase difference between a pixel with respect to a reference pixel, which is of the highest average coherence. A method proposed by [Goel and Adam \(2014\)](#) considers both the local gradients of deformation velocity and the local gradients of DSM error in range and azimuth directions can also be applied. Another method was proposed by [Pepe and Lanari \(2017\)](#), which uses arcs connecting these coherent pixels instead of working with the relative phase of a pixel with respect to a reference pixel. Alternatively, DSM error reduction can be conducted on unwrapped interferograms as proposed by [Bombrun et al. \(2009\)](#), in which the DSM error component is estimated based on its relationship with the perpendicular baseline.

## 4. AN OVERVIEW OF THE SMALL BASELINE SUBSET (SBAS) TECHNIQUE

Small baseline subset (SBAS) analysis is among the most commonly used methods in InSAR time series analysis, which is studied in this dissertation (Table 1.1). In this Chapter, the background of the SBAS method and its individual processing steps are reviewed. This starts with SBAS algorithms in Section 4.1, followed by the steps of selecting interferograms in Section 4.2, and the selection of coherent pixels in Section 4.3. The steps of reducing error and noise sources in InSAR SBAS are then provided in Section 4.4, including orbital error, atmospheric artefacts and DSM uncertainties (cf. Chapter 3). The inversion step, which is applied to invert interferometric time series to deformation time series, is subsequently described in Section 4.5. Section 4.6 summarises the Chapter.

### 4.1 SBAS Algorithms

As shown in Section 3.1, InSAR interferograms are contaminated by various error and noise sources such as errors induced by DSM uncertainties, orbital errors, atmospheric artefacts, temporal decorrelation, and other noise sources (Lee et al., 2012). Multi-temporal InSAR (MT-InSAR) methods were proposed to mitigate these errors and noise (e.g., Hooper, 2008), which work by analysing a network of multiple interferograms (e.g., Shanker et al., 2011). Two commonly-used sub-categories are 1) the persistent scatterer (PS) method, which is employed with an interferogram network of a single primary image usually formed at a high spatial resolution, e.g., using a single look (e.g., Ferretti et al., 2001; Hooper et al., 2007; Hooper et al., 2004), and 2) the small baseline (SB) method, which works with an interferogram network of multiple primary images normally generated at multi-looked (i.e., averaged with surrounding pixels) resolution (e.g., Berardino et al., 2002; Cavalié et al., 2007; López-Quiroz et al., 2009; Lundgren et al., 2001; Schmidt & Bürgmann, 2003; Usai, 2003).

In the SBAS method studied in this dissertation, multi-looking – although not compulsory – is used, which is of advantage in reducing the data volume being processed and noise reduction, and multiple primary images allow for many redundant interferograms (Shanker et al., 2011). Interferograms are normally chosen relying on spatial and temporal baseline thresholds to reduce the effects of topographic errors, geometric and temporal decorrelation (Berardino et al., 2002; Crosetto et al., 2016;

Shanker et al., 2011; Zebker & Villasenor, 1992). Coherent pixels are then filtered by a threshold utilising coherence (Berardino et al., 2002; Lanari, Mora, et al., 2004; López-Quiroz et al., 2009; Mora et al., 2003; Schmidt & Bürgmann, 2003), amplitude and phase stability (Hooper, 2008), or a statistical homogeneity test (Goel & Adam, 2014). A specific SBAS algorithm is subsequently applied to those selected coherent pixels to invert the phase signals of interferograms to phase time series by applying least squares (e.g., Schmidt & Bürgmann, 2003; Usai, 2003), singular value decomposition (SVD) (e.g., Berardino et al., 2002), or minimisation of the  $L_1$ -norm (Lauknes et al., 2011).

At a coherent pixel located at a radar coordinate  $(x, r)$ , the interferometric phase of an interferogram formed from two SAR images at acquisition times  $t_A$  and  $t_B$ , respectively, can be expressed as (Berardino et al., 2002; Lee et al., 2012):

$$\begin{aligned}\phi(x, r) &= \phi(t_A, x, r) - \phi(t_B, x, r) \\ &\approx \frac{4\pi}{\lambda} d_{LoS}(x, r) + \phi^{top}(x, r) + \phi^{atm}(x, r) + \phi^{orb}(x, r) \\ &\quad + \phi^{tmp}(x, r) + \phi^n(x, r)\end{aligned}\quad (4.1)$$

where  $\lambda$  is the radar wavelength,  $d_{LoS}$  is the Earth deformation in the line-of-sight (LoS) direction,  $\phi^{top}$ ,  $\phi^{atm}$ , and  $\phi^{orb}$  are the phase contributions induced by uncertainties in the DSM, atmospheric artefacts, and orbital error, respectively,  $\phi^{tmp}$  and  $\phi^n$  indicate phase components of temporal decorrelation and caused by various noise sources.

In subsequent Sections, various methods used to select SB interferograms and coherent pixels will be reviewed, which is followed by approaches used to reduce contributions shown in Equation (4.1). Finally, methods used to invert interferometric phase signal to phase time series corresponding to acquisitions will also be described.

## 4.2 Interferogram Selection

### 4.2.1 Selection Based on Baseline Thresholds

SBAS makes use of a network of interferograms from which temporal and perpendicular baselines are limited in time and length to reduce the effects of decorrelation Novellino et al. (2017). The temporal baseline threshold has been chosen varying from months to years (e.g., Lanari et al., 2007; López-Quiroz et al., 2009), while the perpendicular baseline threshold has been chosen ranging between hundreds

of metres and over one kilometre (e.g., [Berardino et al., 2002](#); [Chaussard et al., 2014](#)) (see [Table 4.1](#)).

These thresholds are chosen based on various factors, e.g., applications, the type and availability of InSAR data that is used, its time span, the area under investigation (e.g., urban or vegetated area) or the critical baseline, which in turn depends on the wavelength of the radar sensor, spatial resolution and incidence angle ([Gatelli et al., 1994](#); [Zebker & Villasenor, 1992](#)). For example, newer satellite generations (e.g., Sentinel-1 and TerraSAR (TSX)) frequently gather data in shorter time intervals (e.g., 6 days or 12 days with Sentinel-1, 11 days with TSX) and are available with fewer gaps compared to older SAR satellite missions (e.g., ERS, ENVISAT). Therefore, they are normally applied with smaller temporal and perpendicular baseline thresholds (see [Table 4.1](#) for this comparison). For older SAR missions, the perpendicular baselines vary within a wider range, compared to those from newer ones. To generate a network connecting all available scenes, a longer temporal baseline threshold is therefore usually adopted.

These thresholds are also dependent on the condition of the environment under investigation ([Gourmelen et al., 2010](#)). For example, in studies in vegetated areas, one would try to use temporal baseline threshold as small as possible to mitigate the effect of temporal decorrelation due to agricultural activities or existing vegetation, particularly in the case of using shorter wavelength data (e.g., C-band in ERS or Sentinel-1 data) (e.g., [Xu et al., 2017](#)). This higher temporal decorrelation effect on shorter wavelength missions is because it has been demonstrated that shorter radar wavelengths are prone to higher temporal decorrelation effects compared to longer wavelengths, which are able to better penetrate through vegetation (e.g., [Ebmeier et al., 2013](#); [Massonnet et al., 1996](#); [Rosen et al., 1996](#)).

Table 4.1. Examples of baseline thresholds used in several SBAS applications.

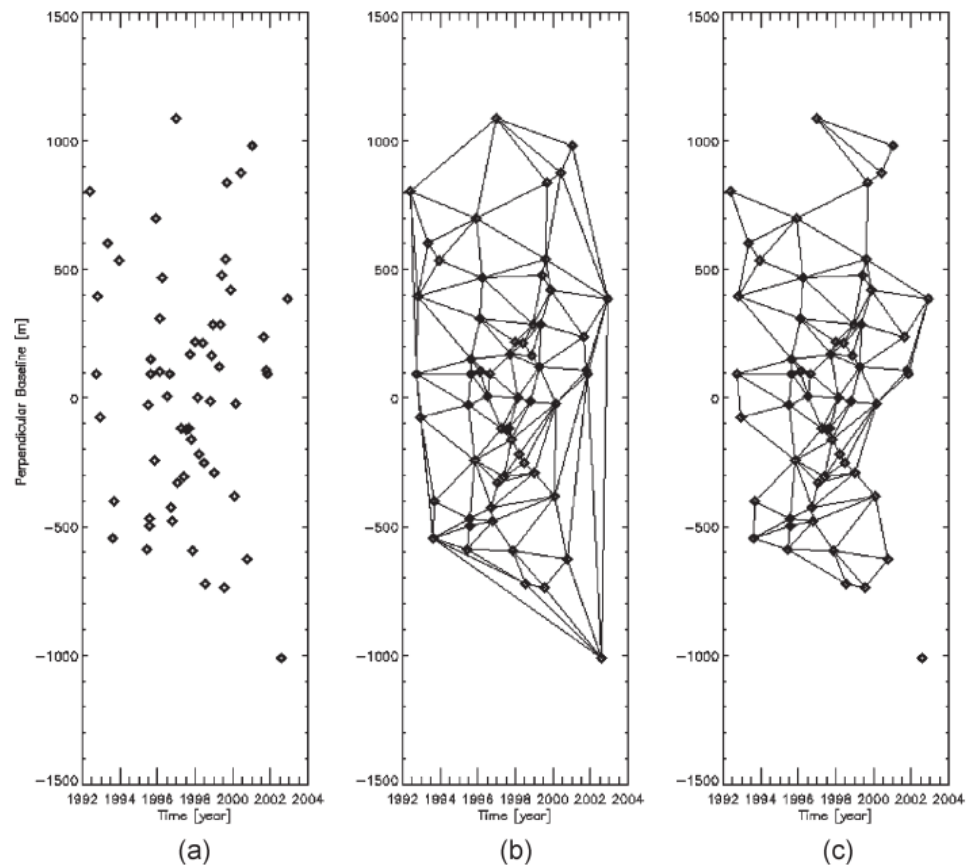
References	Data	Time span	Number of images	Temporal		Perpendicular		Number of interferogram
				baseline threshold	threshold	baseline threshold (m)	threshold (m)	
	TSX	10/2009-08/2010	12	110 days	180		33	
	ERS	06/1992-09/2000	44	-	130		70	
	ERS (area 1)	06/1992-05/2003	116	4 years	300		133	
	ERS (area 2)	1995-2002	42	4 years	300		102	
Cavalié et al. (2007)	ERS	06/1992-11/2001	43	-	300		241	
Chaussard et al. (2014)	ALOS	2007-2011	>600	1 year	1500		>3000	
Gong et al. (2016)	ERS (area 1)	04/1995-12/2000	48	5.5 years	600		149	
	ENV (area 2)	06/2003-07/2008	20	3.5 years	1000		87	
Guo et al. (2016)	ENV/ASAR	08/2007-09/2010	18	400 days	800		71	
Gourmelen et al. (2010)	ERS	1992-2000	44	1500 days	400		148	
Lanari, Lundgren, et al. (2004)	ERS	1995-2002	42	4 years	300		102	
Lanari et al. (2007)	ERS (area 1)	06/1992-05/2003	116	4 years	300		133	
	ERS (area 2)	Mid/1992-end/2000	45	4 years	300		109	
	ERS (area 3)	1992-2000	60	4 years	300		119	
Lauknes et al. (2010)	ERS	06/1992-09/1999	18	5 years	600		65	

Table 4.1. (Continued)

References	Data	Time span	Number of images	Temporal baseline threshold	Perpendicular baseline threshold (m)	Number of interferogram
	ERS	1992-2001	39	1500 days	350	196
	ENV	11/2002-03/2007	38	9 months	500	71
	SENT-1A,B	03/2015-12/2016	40	1 year	200	741
Pepe et al. (2005)	ERS	06/1992-02/2004	63	4 years	300	157
	ENV	11/2002-07/2004	12	4 years	300	24
Pepe et al. (2011)	ENV/ASAR	01/2003-09/2008	49	4 years	400	-
Schmidt and Bürgmann (2003)	ERS	06/1992-09/2000	47	-	200	115
Shirzaei and Bürgmann (2013)	ERS	1992-2010	52	4 years	400	401
	ENV	1992-2010	50	4 years	400	430
Sun et al. (2017)	TSX	02/2015-02/2016	27	99 days	400	157
Tizzani et al. (2007)	ERS	06/1992-10/2000	23	4 years	350	44
Xu et al. (2017)	SENT-1A (DES)	10/2014-07/2016	42	90 days	200	201
	SENT-1A (ASC)	10/2014-07/2016	36	90 days	200	183
L. Yu et al. (2017)	CSK	12/2013-03/2016	61	1000 days	800	155
	SENT-1A	02/2015-04/2017	33	1 year	-	368
Zhou et al. (2017)	SENT-1A	04/2015-04/2016	15	200 days	300	92

#### 4.2.2 Selection Based on Other Strategies

Besides using temporal and perpendicular baseline thresholds as described in subsection 4.2.1, interferograms in InSAR SBAS data processing can also be selected relying on other strategies. Delaunay triangulation (Lee & Schachter, 1980) is one of those strategies in which a Delaunay triangulation network is selected first from the entire set of SAR images, then the selected interferograms with long baselines are removed using selected thresholds. Delaunay triangulation is implemented in several open-access source codes such as the Stanford Method for Persistent Scatterers (StaMPS, [https://github.com/dbekaert/StaMPS/blob/master/matlab/sb\\_find\\_delaunay.m](https://github.com/dbekaert/StaMPS/blob/master/matlab/sb_find_delaunay.m)), the Miami InSAR time series software in Python (MintPy, <https://github.com/insarlab/MintPy/blob/main/mintpy/utils/network.py>). An example of such a Delaunay triangulation network is shown in Figure 4.1 by Pepe and Lanari (2006), which was formed from an ERS-1/2 SAR data set captured in the Central Apennines, Italy, covering the time between August 1992 and October 2002. A full Delaunay triangulation network (Figure 4.1, b) was formed from the entire SAR images (Figure 4.1, a), then interferograms with temporal and/or perpendicular baselines longer than the selected thresholds of 300 m and 1500 days, respectively were removed (Figure 4.1, c).



**Figure 4.1.** A Delaunay triangulation interferogram network from ERS-1/2 SAR data from [Pepe and Lanari \(2006\)](#). (a) SAR images distribution, (b) a full Delaunay triangulation network, (c) a Delaunay triangulation network after removing interferograms with temporal and/or perpendicular baselines longer than 300 m and 1500 days, respectively.

Another approach to select interferograms is the use of hierarchical thresholds. In this approach, instead of using a single pair of temporal and perpendicular baseline thresholds, a combination of multiple pairs can be applied. The hierarchical thresholds network approach is implemented in the MintPy open-source software. [Figure 4.2](#) shows an example of a hierarchical thresholds network by [Zhao \(2017\)](#), which was formed from a TSX SAR data set captured in the Brazoria and Galveston counties, Texas covering the time between January 27, 2012 and April 20, 2014. The interferograms were chosen by the pairs of temporal and perpendicular baseline thresholds of 22 days and 50 m, 33 days and 120 m, 44 days and 80 m, 55 days and 40 m, and 66 days and 20 m.

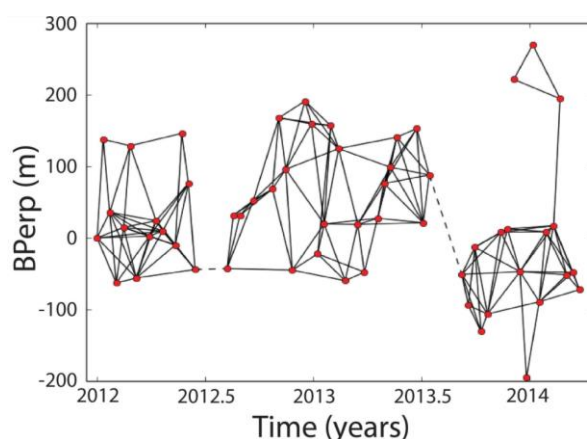


Figure 4.2. A hierarchical thresholds interferogram network from TSX SAR data from Zhao (2017).

A minimum spanning tree (Kruskal, 1956) is another strategy that can be applied to select interferograms in InSAR SBAS data processing. In this approach,  $N - 1$  interferograms are chosen from the entire set of  $N$  SAR images in a way that the sum of their user-defined edge weights, e.g., their coherence, is shortest. The minimum spanning tree network approach is implemented in several open-source code software such as MintPy, the Python tool for InSAR rate and time series estimation (PyRate, <https://github.com/GeoscienceAustralia/PyRate/blob/master/pyrate/core/mst.py>).

Figure 4.3 shows an example of a minimum spanning tree interferogram network from Refice et al. (2006), which was formed from an ERS-1/2 SAR data set gathered between 1992 and 2000. The network was chosen based on the edges (i.e., interferograms) weights defined by their coherence.

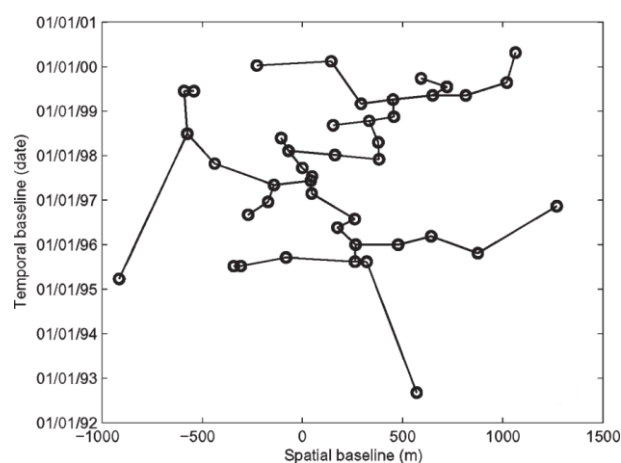


Figure 4.3. A minimum spanning tree interferogram network from ERS-1/2 SAR data from Refice et al. (2006). The network was formed by the weights of edges (i.e., interferograms) chosen as their coherence.

### 4.3 Coherent Pixels Selection

As mentioned in Section 4.1, pixels that are considered coherent are selected prior to error and noise reduction and inverting interferometric phase to time series. Here, several frequently-used criteria for pixel selection in SBAS methods are described.

#### 4.3.1 Selection Based on Interferometric Coherence

The most-used criterion for coherent pixel selection is the coherence (e.g., [Berardino et al., 2002](#); [Lanari, Lundgren, et al., 2004](#); [López-Quiroz et al., 2009](#); [Mora et al., 2003](#); [Schmidt & Bürgmann, 2003](#)), which can be used as a measure of the quality of an interferogram essential for InSAR signal processing ([Bamler & Hartl, 1998](#)). Generally, the coherence or correlation of an interferogram at a given pixel comprises four components expressed as ([Rosen et al., 2000](#); [Simons & Rosen, 2015](#)):

$$\gamma = \gamma_N \cdot \gamma_G \cdot \gamma_Z \cdot \gamma_T \quad (4.2)$$

where  $\gamma_N$  is the thermal noise correlation,  $\gamma_G$  denotes the geometric correlation,  $\gamma_Z$  refers to the volume correlation, and  $\gamma_T$  is the temporal correlation.

In some cases, it is convenient to consider the loss of coherence ( $\delta$ ), which is defined as the decorrelation of which the relation with coherence ( $\gamma$ ) is expressed as  $\delta = 1 - \gamma$  ([Simons & Rosen, 2015](#)). Like coherence, the loss of coherence is constituted of four components including thermal decorrelation resulting from uncorrelated noise sources from radar instruments, geometric decorrelation caused by the difference in the look angles between the two radar images used, volume decorrelation due to total volume of backscattering effects, and temporal decorrelation caused by the change in target environment over time ([Zebker & Villasenor, 1992](#)).

In InSAR signal processing, the coherence of an interferogram at a given pixel can be computed by the cross-correlation between the two SAR images that are used ([Bamler & Eineder, 1996](#); [Hanssen, 2001](#); [Lu & Dzurisin, 2014](#); [Rosen et al., 2000](#); [Simons & Rosen, 2015](#)):

$$\gamma = \frac{|\sum_{n=1}^N y_1^{(n)} y_2^{*(n)}|}{\sqrt{\sum_{n=1}^N (y_1^{(n)})^2 \sum_{n=1}^N (y_2^{(n)})^2}} \quad (4.3)$$

where  $N$  is the number of individual scatterers within the resolution cell considered,  $y_1^{(n)}$  and  $y_2^{(n)}$  are the complex-valued backscattering coefficients of the  $n^{th}$  scatterer from the primary and secondary SAR images, and  $y_2^{*(n)}$  is the complex conjugate of  $y_2^{(n)}$ .

The magnitude of coherence varies between 0 (completely incoherent) and 1 (completely coherent). The coherence threshold used to filter coherent pixels in SBAS methods in which pixels with coherence magnitudes larger than this threshold are considered as coherent and *vice versa* is used differently among studies. This depends on various factors such as the study area, applications, InSAR data that were used. For instance, the coherence threshold of 0.15 was used by [Biggs et al. \(2007\)](#), 0.25 was used by [Berardino et al. \(2002\)](#) and [Mora et al. \(2003\)](#); 0.35 was employed by [Lanari, Mora, et al. \(2004\)](#). The coherence threshold was adopted arbitrarily from studies in the literature. In [Berardino et al. \(2002\)](#), a pixel was defined as coherent if its coherence magnitude is higher than the threshold of 0.25 in at least 30% of interferograms, whilst in [Schmidt and Bürgmann \(2003\)](#), pixels with coherence magnitudes over the threshold in all interferograms are selected.

Conversely, in [Mora et al. \(2003\)](#), coherent pixels were selected by a two-step procedure which, in the first step, an initial subset of candidate pixels was selected based on mean coherence magnitude computed from the entire set of interferograms with a threshold of 0.25. The coherence of these selected candidates was then computed based on neighbouring pixels by applying a proposed model coherence function, then the final set of coherent pixels were selected relying on a threshold of 0.7. In [Lanari, Mora, et al. \(2004\)](#), only pixels with coherence values over the given threshold and highly correlated with surrounding targets are considered as coherent, whilst in [López-Quiroz et al. \(2009\)](#), pixels that are coherent in at least 40 interferograms out of the total 71 interferograms were chosen to be involved in subsequent steps.

[Figure 4.1](#) shows a coherence map over Perth, Western Australia derived using Equation (4.3) from an interferogram formed from two TSX images acquired on September 28, 2016 and October 9, 2016. The results were computed for the entire scene, in which within each pixel of one-arc-second size which is equivalent to that of SRTM DSM used, the coherence was estimated from all included individual scatterers. The estimated coherence was then geocoded from radar coordinates to geodetic coordinates in the WGS84 system.

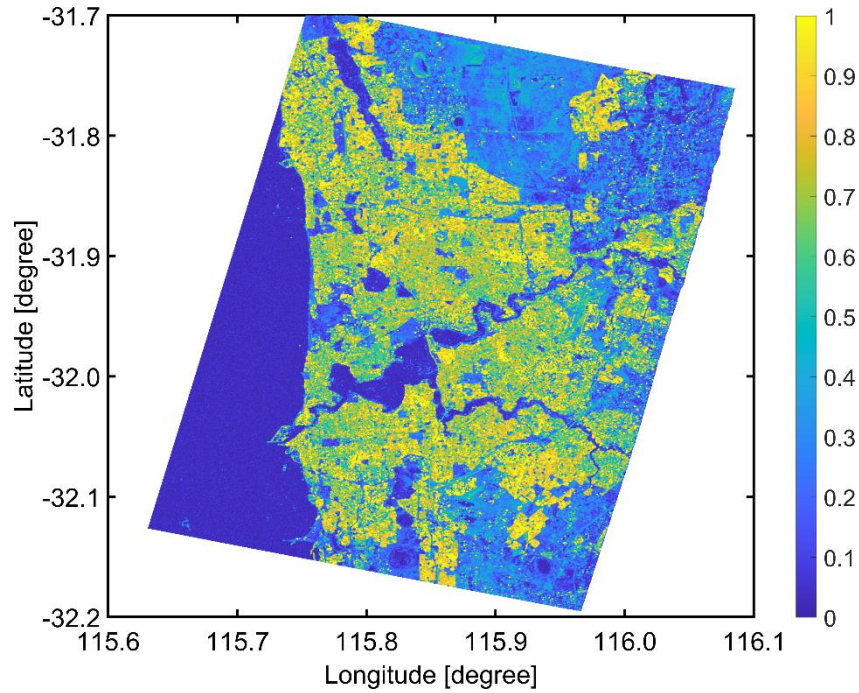


**Figure 4.4.** A coherence map generated by the ISCE software (Rosen et al., 2018) from TSX data over Perth, Western Australia. The map shows the coherence magnitude of an interferogram formed from two TSX SAR images captured on September 28, 2016 and October 09, 2016. TSX data were provided under the German Space Centre’s Science Project LAN1499 and Australian Research Council Linkage Projects LP110100284 and LP140100155.

#### 4.3.2 Selection Based on Amplitude and Phase Stability

Another approach that has been adopted in selecting coherent pixels in the SBAS methods is based on amplitude and phase stability, which is termed as slowly decorrelating filtered phase (SDFP) pixels (Hooper, 2008). Candidate pixels (or candidates) are selected first by the amplitude difference dispersion ( $D_{\Delta A}$ ), which is defined by the fraction between the standard deviation of the difference in amplitude between the primary and secondary images ( $\sigma_{\Delta A}$ ) and the mean amplitude ( $\mu_A$ ) as shown in Equation (4.4), with a given threshold.

$$D_{\Delta A} = \frac{\sigma_{\Delta A}}{\mu_A} \quad (4.4)$$

The spatially correlated phase part, which involves the phase relating to the surface displacement, the change in atmospheric delay, orbital errors, and spatially correlated topographic errors, is then computed via band-pass filtering of neighbouring pixels for all candidates. Next, the spatially uncorrelated phase part relating to the spatially uncorrelated topographic errors and the difference between the pixel’s phase

centre and its physical centre is estimated in a least squares sense via the correlation with perpendicular baseline for the selected candidate pixels (Hooper et al., 2004).

The estimated spatially correlated phase part ( $\tilde{\phi}_{x,i}$ ) at the pixel  $x$  of the  $i^{th}$  interferogram and the corresponding spatially uncorrelated phase part ( $\Delta\hat{\phi}_{\theta,x,i}^u$ ) are subsequently removed from the wrapped phase ( $\phi_{x,i}$ ) prior to calculating the mean value over the entire  $N$  interferograms, which results in the so-called decorrelation noise ( $\gamma_x$ ) as shown in Equation (4.5) (Hooper, 2008; Hooper et al., 2007):

$$\gamma_x = \frac{1}{N} \left| \sum_{i=1}^N \exp[\sqrt{-1}(\phi_{x,i} - \tilde{\phi}_{x,i} - \Delta\hat{\phi}_{\theta,x,i}^u)] \right| \quad (4.5)$$

A threshold ( $\gamma_x^{thresh}$ ), which is estimated relying on the fraction between the probability density function (PDF) of the random phase pixel and that of SDFP pixels (Hooper et al., 2007; Hooper et al., 2004). This is estimated in a way that the fraction is acceptable to a particular application (Hooper et al., 2007), which is defined by users (Hooper, 2008).

Alternatively, the statistical homogeneity test can be used for filtering coherent pixels in SBAS time series analysis (Massonnet & Feigl, 1998), which are termed homogeneous pixels. This starts by dividing the studied area into non-overlapping rectangular blocks (e.g., 40×40 pixels), then homogeneous pixels are detected by the Anderson-Darling statistical test (Pettitt, 1976) applied to the SAR amplitude within homogeneous patches of pixels with a minimum size of, e.g., 20×20 pixels.

#### 4.3.3 Selection Based on Interferometric Phase Misclosure

Another method applied in filtering coherent pixels relies on the interferometric phase misclosure (Cavalié et al., 2007). A sketch of an interferogram phase loop formed from three SAR image acquisitions is shown in Figure 4.5, in which the phase field is conservative, i.e., in theory,  $\phi_{ij} + \phi_{jk} + \phi_{ki} = 0$  (Biggs et al., 2007; Parker et al., 2017). This can be expanded to a loop with  $N$  acquisitions ( $N \geq 3$ ).

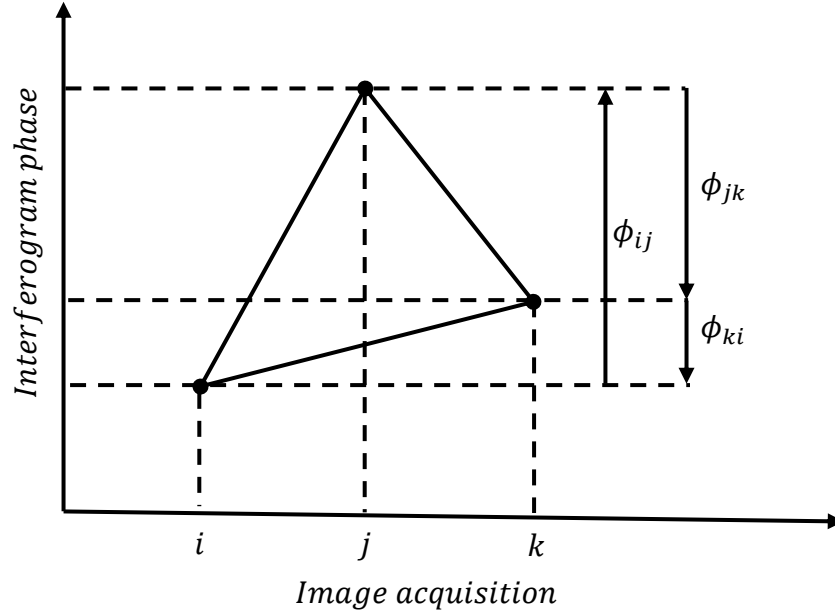


Figure 4.5. A sketch of an interferogram phase loop between three image acquisitions.

However, errors and noise in the interferograms leads to phase loop misclose, i.e., the sum of interferometric phases over a loop does not equal zero. In this method, the interferometric deformation misclosure is computed at each pixel for all selected interferograms, then its system misclosure is estimated by root mean square (RMS) of all derived interferometric deformation misclosure as (Cavalié et al., 2007):

$$\phi_{RMS} = \left[ \frac{1}{N} \sum_N \left( \phi_{ij} - \sum_{k=i}^{j-1} m_k \right)^2 \right]^{1/2} \quad (4.6)$$

where  $N$  is the number of selected interferograms,  $\phi_{ij}$  denotes the interferometric phase derived from the  $i^{th}$  and  $j^{th}$  images, respectively,  $\sum_{k=i}^{j-1} m_k$  refers to the sum of successive interferometric phase increments of the same image pair reconstructed from the inversion step in which the incremental phase change of successive images are inverted from the network of SBAS interferograms.

The idea of using interferometric phase loops can also be applied to detecting and masking phase unwrapping errors (Biggs et al., 2007; Parker et al., 2017). As described in Subsection 2.3.3, the interferometric phase is modulated by  $2\pi$ , i.e., wrapped module  $2\pi$ , ranging between  $-\pi$  and  $\pi$ . Its full phase value is then derived by computing the integer ambiguity, which is the number of multiple radar wavelengths, via the unwrapping step (e.g., Chen & Zebker, 2001, 2002; Hooper &

Zebker, 2007). However, residual unwrapping errors may still exist in unwrapped interferograms. As these errors do not follow the conservative rule described above, the phase misclosure over interferogram closed loops can be employed to detect and mask out these errors.

#### 4.4 Error and Noise Reduction in SBAS

Error and noise sources need to be mitigated either before (i.e., to interferometric phase) or after (i.e., to the time series of image phase or the deformation time series) applying SBAS inversion to invert interferometric phase to deform time series. In InSAR SBAS data processing, error reduction is applied to individual interferograms first, which has been described in Chapter 3. The estimated results are then applied to multiple interferograms in an SBAS network or to InSAR SBAS-derived deformation time series after SBAS inversion, which will be described in this Section. This mitigation includes orbital error reduction (Subsection 4.4.1), atmospheric error reduction (Subsection 4.4.2), and DSM error reduction (Subsection 4.4.3).

##### 4.4.1 Orbital Error Reduction in SBAS

Orbital error can be mitigated individually for each interferogram as described in Section 3.2 using a polynomial function, e.g., a planar function or a “twisted plane”, alternatively combined with other geodetic data, e.g., GNSS. In this way, orbital parameters  $a_{ij}$ ,  $b_{ij}$ ,  $c_{ij}$  (Equation (3.3)) and  $d_{ij}$  (Equation (3.4)) of the interferogram connecting the  $i^{th}$  and  $j^{th}$  images can be estimated by the least squares  $L_2$ -norm minimisation. Additionally, as in Section 4.2, SBAS methods work with a network of SB interferograms, chosen based on temporal and perpendicular baseline thresholds. Therefore, a network sense can be adopted to estimate image orbital parameters from interferometric orbital parameters (Agram et al., 2012).

With an interferogram joining the  $i^{th}$  and  $j^{th}$  SAR images, the relation between image orbital parameters and interferometric orbital parameters can be written as:

$$a_{ij} = a_i - a_j \quad (4.7)$$

$$b_{ij} = b_i - b_j \quad (4.8)$$

$$c_{ij} = c_i - c_j \quad (4.9)$$

$$d_{ij} = d_i - d_j \quad (4.10)$$

where  $a_i$ ,  $b_i$ ,  $c_i$ ,  $d_i$  and  $a_j$ ,  $b_j$ ,  $c_j$ ,  $d_j$  are the orbital parameters of the  $i^{th}$  and  $j^{th}$  images, respectively, which are estimated based on a system of equations formed from the

linear systems given in Equations (4.7) to (4.10) corresponding to the chosen interferogram SBAS network.

With this option, image orbital error parameters are estimated from interferometric orbital error parameters based on least squares minimisation before interferometric orbital error parameters are re-estimated based on which orbital error reduction maps are produced and used to correct interferograms. This network sense is applied to ensure the consistency of the interferogram network in which the image orbital error parameters are estimated first then they are used to correct the interferograms (Agram et al., 2012).

#### 4.4.2 Atmospheric Error Reduction in SBAS

Atmospheric artefacts can be reduced by applying the methods described in Section 3.3. The ionospheric reduction (Subsection 3.3.1) can be applied utilising either the multi-frequency split-spectrum technique (Subsection 3.3.1.1), using azimuth streaks (Subsection 3.3.1.2) or based on co-registration (Subsection 3.3.1.3). The tropospheric reduction (Subsection 3.3.2) can be employed by the empirical approach (Subsection 3.3.2.1), predictive approach (Subsection 3.3.2.2), or spatio-temporal filtering (Subsection 3.3.2.3).

#### 4.4.3 Digital Surface Model Error Reduction in SBAS

Three approaches can be used to reduce DSM errors in InSAR SBAS, which work with the interferometric phase (e.g., Bombrun et al., 2009; Ducret et al., 2011; Pepe & Lanari, 2017; Samsonov, 2010), the time series of image phase (Pepe et al., 2011), or with the deformation time series (Fattahi & Amelung, 2013).

##### 4.4.3.1 Reduction to Interferometric Phase

DSM uncertainties can be mitigated for the interferometric phase by working either with wrapped or unwrapped interferograms, which has been shown in Section 3.4. Alternatively, in the case of working with unwrapped interferograms, this can also be conducted in the SBAS inversion step (Berardino et al., 2002; Samsonov, 2010), which will be described in Section 4.5. The aim of the inversion step is to invert interferometric phase differences to the time series of image phase.

With  $M$  interferograms formed from  $N + 1$  SAR images ( $M > N$ ), the inversion equation can be written as (e.g., Berardino et al., 2002):

$$\mathbf{B}\mathbf{v} = \delta\phi \quad (4.11)$$

where  $\mathbf{B}$  is a  $M \times N$  matrix with elements being: in the  $k^{th}$  row corresponding to the  $k^{th}$  interferogram connecting the  $i^{th}$  and  $j^{th}$  images ( $j > i$ ), its elements from  $i^{th}$  to  $j^{th}$  columns are  $t_i - t_{i-1}$ ;  $t_{i+1} - t_i$ ; ...;  $t_j - t_{j-1}$  ( $t$  is the acquisition time), and elements at other locations are all zero,  $\delta\phi$  is the vector of  $M$  interferometric phase,  $\mathbf{v}$  is the vector of mean phase velocities between time-adjacent acquisitions, which is of the form:

$$\mathbf{v}^T = \left[ v_1 = \frac{\phi_1}{t_1 - t_0}, v_2 = \frac{\phi_2 - \phi_1}{t_2 - t_1}, \dots, v_N = \frac{\phi_N - \phi_{N-1}}{t_N - t_{N-1}} \right] \quad (4.12)$$

Equation (4.11) can be solved by least squares or singular value decomposition (SVD) to derive mean phase velocities ( $\mathbf{v}$ ) (Berardino et al., 2002). In case that the DSM error is estimated simultaneously with the mean phase velocities in the inversion step, the matrix  $\mathbf{B}$  can be modified by adding one more column to its right hand side with  $B_{\perp}/r\sin\theta$ , with  $B_{\perp}$ ,  $r$  and  $\theta$  being the perpendicular baselines of corresponding interferograms, the sensor-target distance and the look angle. The unknowns will then be a combination of mean phase velocities ( $\mathbf{v}$ ) and DSM error ( $\Delta Z^{top}$ ). Similarly, the modified inversion equation can be solved to simultaneously estimate mean phase velocities and residual DSM error terms (Berardino et al., 2002).

#### 4.4.3.2 Reduction to the Time Series of Image Phase

DSM errors can be corrected from the time series of image phase (Pepe et al., 2011). In this method, the image phase ( $\phi$ ) corresponding to  $N$  acquisitions is computed from mean phase velocities ( $\mathbf{v}$ ) estimated from SBAS inversion by Equation (4.12). DSM error reduction is then conducted based on the estimated image phase by a filter. Specifically, a low-pass filter in the time domain with a moving average operation is applied to derive the low-pass phase component ( $\phi^{LP}$ ). The high-pass component ( $\phi^{HP}$ ) is then calculated by removing the low-pass estimation from the image phase ( $\phi$ ) as:

$$\begin{aligned} H_i^{HP}(x, r) &= \phi_i(x, r) - \phi_i^{LP}(x, r) \\ &\approx \phi_i^{top}(x, r) + \phi_i^{atm}(x, r) + \frac{4\pi}{\lambda} d_i^{HP}(x, r) \end{aligned} \quad (4.13)$$

The high-pass phase estimated by Equation (4.13) consists of a DSM error contribution ( $\phi_i^{top}(x, r)$ ), atmospheric artefacts ( $\phi_i^{atm}(x, r)$ ) and high-pass

deformation signal ( $d_i^{HP}(x, r)$ ). Therefore, the DSM error component can then be estimated from this high-pass phase relying on Equation (4.14) by least squares:

$$\phi_i^{top}(x, r) = \frac{4\pi}{\lambda} \frac{B_{\perp,i} - B_{\perp,0}}{r \sin\theta} Z^{top}(x, r) \quad (4.14)$$

#### 4.4.3.3 Reduction to Deformation Time Series

In a method working on deformation time series proposed by [Fattahi and Amelung \(2013\)](#), DSM error reduction is conducted in a two-step procedure. In the first step, mean phase velocities as in Equation (4.12) are estimated from SBAS inversion following Equation (4.11). In the second step, a cubic temporal deformation is assumed ([Berardino et al., 2002](#)):

$$\phi_i^{def} = \bar{v}(t_i - t_0) + \frac{1}{2}\bar{a}(t_i - t_0)^2 + \frac{1}{6}\Delta\bar{a}(t_i - t_0)^3 \quad (4.15)$$

where  $\phi_i^{def}$  is the deformation phase at the time  $t_i$ ,  $\bar{v}$  is the mean velocity,  $\bar{a}$  is the mean acceleration and  $\Delta\bar{a}$  is the mean acceleration variation.

The phase value at time  $t_i$  ( $\phi_i$ ) among  $N$  acquisitions derived from SBAS inversion following Equation (4.11) includes deformation phase ( $\phi_i^{def}$ ) in Equation (4.15) and other sources, which can be written as:

$$\phi_i = \phi_i^{def} + \frac{4\pi}{\lambda} \frac{B_{\perp,i}}{r \sin\theta} \Delta Z^{top} + \psi_i \quad (4.16)$$

where  $\psi_i$  is the high-frequency components including atmospheric artefacts, orbital error, decorrelation noise and high-frequency deformation component.

Combining Equations (4.15) and (4.16), gives:

$$\begin{aligned} v_i &= \frac{\phi_i - \phi_{i-1}}{t_i - t_{i-1}} \\ &= \bar{v} + \frac{1}{2}\bar{a}(t_i + t_{i-1} - t_0)^2 + \frac{1}{6}\Delta\bar{a} \frac{(t_i - t_0)^3 - (t_{i-1} - t_0)^3}{6(t_i - t_{i-1})} \\ &\quad + \frac{4\pi}{\lambda} \frac{\dot{B}_{\perp,i}}{r \sin\theta} \Delta Z^{top} + \dot{\psi}_i \end{aligned} \quad (4.17)$$

where  $\dot{B}_{\perp,i}$  is the baseline velocity history defined as:

$$\dot{B}_{\perp,i} = \frac{B_{\perp,i} - B_{\perp,i-1}}{t_i - t_{i-1}} \quad (4.18)$$

where  $\dot{\psi}_i$  is the temporal gradient of  $\psi_i$ , which is considered as noise in this DSM reduction.

From (4.17), a linear system of equations can be formed:

$$\mathbf{v} = \mathbf{A}\mathbf{x} + \mathbf{N} \quad (4.19)$$

where  $\mathbf{v}$  is the vector of mean phase velocities estimated from SBAS inversion in the first step (Equation (4.11)),  $\mathbf{x}^T = [\bar{v}, \bar{a}, \Delta\bar{a}, \Delta Z^{top}]$  is the vector of unknowns,  $\mathbf{A}$  is a matrix of the form:

$$\mathbf{A} = \begin{bmatrix} 1 & \frac{t_1 - t_0}{2} & \frac{(t_1 - t_0)^2}{6} & \frac{4\pi}{\lambda} \frac{\dot{B}_{\perp,1}}{r \sin\theta} \\ 1 & \frac{t_2 + t_1 - 2t_0}{2} & \frac{(t_2 - t_0)^3 - (t_1 - t_0)^3}{6} & \frac{4\pi}{\lambda} \frac{\dot{B}_{\perp,2}}{r \sin\theta} \\ \dots & \dots & \dots & \dots \\ 1 & \frac{t_N + t_{N-1} - 2t_0}{2} & \frac{(t_N - t_0)^3 - (t_{N-1} - t_0)^3}{6} & \frac{4\pi}{\lambda} \frac{\dot{B}_{\perp,N}}{r \sin\theta} \end{bmatrix} \quad (4.20)$$

The solution  $\mathbf{x}$  can then be derived by solving the linear system of Equations (4.19) by least squares estimation in which DSM error is estimated and reduced (Fattahi & Amelung, 2013).

#### 4.5 Small Baseline Subset Inversion

In InSAR SBAS, after reducing errors and noise in interferograms, the inversion step is applied to convert reduced interferometric phase differences to deformation time series. Assuming that we have  $N + 1$  images acquired at times  $t_0, t_1, \dots, t_N$  of which the phase values are:

$$\boldsymbol{\phi}^T = [\phi_1, \phi_2, \dots, \phi_N] \quad (4.21)$$

where  $\phi_i$  ( $i = 1, \dots, N$ ) is the phase of  $i^{th}$  acquisition with respect to the first acquisition ( $t_0$ ).

In InSAR SBAS, the phase values, and thus the deformation, of acquisitions are relative to the super primary (formerly super master) scene, which is the first acquisition in many applications. In other words, there is no deformation assumed in the first image acquisition. Therefore,  $\phi_0$  is not included in Equation (4.21). These SAR images are then combined to form  $M$  interferograms:

$$\boldsymbol{\delta\phi}^T = [\delta\phi_1, \delta\phi_2, \dots, \delta\phi_M] \quad (4.22)$$

with the number of interferograms satisfying the below inequality (Berardino et al., 2002):

$$\frac{N + 1}{2} \leq M \leq \frac{N(N + 1)}{2} \quad (4.23)$$

In the inversion step,  $N$  unknown phase values ( $\phi$ ) are derived from  $M$  known interferometric phase values ( $\delta\phi$ ). A system of  $M$  equations with  $N$  unknowns can then be defined as (Berardino et al., 2002):

$$\mathbf{A}\boldsymbol{\phi} = \boldsymbol{\delta\phi} \quad (4.24)$$

where  $\mathbf{A}$  is the design matrix of dimension  $M \times N$  with values of elements being: in  $k^{th}$  row corresponding to  $k^{th}$  interferogram connecting  $i^{th}$  and  $j^{th}$  images, its values at  $i^{th}$  column is  $-1$ , at  $j^{th}$  column is  $+1$ , and are all zero otherwise. An example of  $\mathbf{A}$  is shown in Equation (4.25).

$$\mathbf{A} = \begin{bmatrix} +1 & 0 & 0 & 0 & \dots \\ \dots & \dots & \dots & \dots & \dots \\ 0 & -1 & +1 & 0 & \dots \\ 0 & -1 & 0 & +1 & \dots \\ \dots & \dots & \dots & \dots & \dots \end{bmatrix} \quad (4.25)$$

Generally, the number of interferograms ( $M$ ) is larger than the number of SAR images ( $N + 1$ ), and thus the solution ( $\boldsymbol{\phi}$ ) in Equation (4.24) can be solved in the least squares sense as (Berardino et al., 2002; Lundgren et al., 2001; Usai, 2003):

$$\widehat{\boldsymbol{\phi}} = (\mathbf{A}^T \mathbf{A})^{-1} \mathbf{A}^T \boldsymbol{\delta\phi} \quad (4.26)$$

Alternatively, Equation (4.24) can also be solved by SVD in which the design matrix  $\mathbf{A}$  can be decomposed by (Berardino et al., 2002):

$$\mathbf{A} = \mathbf{U}\mathbf{S}\mathbf{V}^T \quad (4.27)$$

where  $\mathbf{U}$  is a  $M \times M$  matrix with its columns being the left-singular vectors of  $\mathbf{A}$  which are the eigenvector of  $\mathbf{A}\mathbf{A}^T$ ,  $\mathbf{S}$  is a  $M \times N$  matrix of which the non-zero elements (the singular values  $\sigma_i$ ) are the square roots of the non-zero eigenvalues of  $\mathbf{A}\mathbf{A}^T$ , and  $\mathbf{V}$  is a  $N \times N$  matrix with its columns being the right-singular vectors of  $\mathbf{A}$  which are the eigenvectors of  $\mathbf{A}^T \mathbf{A}$ . The solution of Equation (4.24) can then be estimated as:

$$\widehat{\boldsymbol{\phi}} = \mathbf{V}\mathbf{S}^+ \mathbf{U}^T \boldsymbol{\delta\phi} \quad (4.28)$$

where  $\mathbf{S}^+ = \text{diag}\left(\frac{1}{\sigma_1}, \dots, \frac{1}{\sigma_{N-L+1}}, 0, \dots, 0\right)$  with  $L$  being the number of different subsets.

Alternatively, the inversion Equation (4.24) can be modified by replacing the unknowns in terms of phase values of acquisitions with respect to the first acquisition (i.e.,  $\phi_i$  in Equation (4.21)) by those in terms of the mean phase velocities between time-adjacent acquisitions by (Berardino et al., 2002; Schmidt & Bürgmann, 2003):

$$\mathbf{V}^T = \left[ v_1 = \frac{\phi_1}{t_1 - t_0}, v_2 = \frac{\phi_2 - \phi_1}{t_2 - t_1}, \dots, v_N = \frac{\phi_N - \phi_{N-1}}{t_N - t_{N-1}} \right] \quad (4.29)$$

The inversion equation corresponding to these new unknowns will be:

$$\mathbf{B}\mathbf{V} = \boldsymbol{\delta\phi} \quad (4.30)$$

where  $\mathbf{B}$  is a  $M \times N$  matrix with elements being: in the  $k^{th}$  row corresponding to the  $k^{th}$  interferogram connecting the  $i^{th}$  and  $j^{th}$  images ( $j > i$ ), its elements from  $i^{th}$  to  $j^{th}$  columns are  $t_i - t_{i-1}; t_{i+1} - t_i; \dots; t_j - t_{j-1}$ , and elements at other locations are all zero. An example of  $\mathbf{B}$  is shown in Equation (4.31).

$$\mathbf{B} = \begin{bmatrix} t_1 - t_0 & 0 & 0 & 0 & \dots \\ \dots & \dots & \dots & \dots & \dots \\ 0 & t_2 - t_1 & t_3 - t_2 & 0 & \dots \\ 0 & t_2 - t_1 & t_3 - t_2 & t_4 - t_3 & \dots \\ \dots & \dots & \dots & \dots & \dots \end{bmatrix} \quad (4.31)$$

Similarly, the solution ( $\mathbf{V}$ ) can be obtained by solving Equation (4.30) by SVD. Equation (4.24) or (4.30) is applied with a fixed design matrix ( $\mathbf{A}$  or  $\mathbf{B}$ ) for all pixels, which are selected based on a coherence threshold as shown in Subsection 4.3. This is an advantage in terms of convenience and reduced processing time, but may suffer from decorrelation, particularly in vegetated or snow-covered areas (Sowter et al., 2013). Alternatively, it can be applied in a more flexible way in which the inversion is applied differently to pixels. That is, different pixels have different number of interferograms and images (Cavalié et al., 2007; Sowter et al., 2013). This is due to different pixels are of different coherence over interferograms, and thus the number of interferograms used for inversion is not the same after selection relying on a coherence threshold (Cavalié et al., 2007).

## 4.6 Chapter Summary

This Chapter has reviewed the SBAS method in InSAR data processing. It started with the background of SBAS algorithms (Section 4.1), indicating the steps applied, including interferogram selection (Section 4.2), coherent pixel selection (Section 4.3), reduction of error and noise sources (i.e., orbital error, atmospheric artefacts and DSM uncertainties) (Section 4.4), and inversion of interferometric phase to image phase (Section 4.5).

In the first step of interferogram selection, temporal and perpendicular baseline thresholds are usually adopted to select interferograms with the aim of reducing the effects of decorrelation (Subsection 4.2.1). They have been chosen from months to years in the temporal baseline threshold and between hundreds of metres and over one kilometre in the perpendicular baseline threshold. They have been based on various

factors such as applications, the type and availability of data used, its time span, the wavelength of the radar sensor, spatial resolution and incidence angle. Alternatively, other strategies can be employed to select interferograms, such as Delaunay triangulations, hierarchical thresholds, or a minimum spanning tree (Subsection 4.2.2).

The subsequent steps of error and noise reduction and SBAS inversion are then applied to coherent pixels only. Therefore, high-quality pixels are selected based on coherence thresholds (Subsection 4.3.1), amplitude and phase stability (subsection 4.3.2), or interferometric phase misclosure (Subsection 4.3.3).

Error and noise reduction is the next step. The orbital error can be mitigated utilising one of the methods described in Chapter 3 using a polynomial function with or without other geodetic data, e.g., GNSS. Alternatively, with multiple interferograms selected, a network sense can be applied to ensure the consistency of the interferogram network (Subsection 4.4.1). Atmospheric artefacts can also be reduced utilising one of the methods provided in Chapter 3, in which the ionospheric reduction can be done utilising either the multi-frequency split-spectrum technique (Subsection 3.3.1.1), using azimuth streaks (Subsection 3.3.1.2) or based on co-registration (Subsection 3.3.1.3). The tropospheric reduction can be employed by either the empirical (Subsection 3.3.2.1) or predictive (Subsection 3.3.2.2) approach.

The influences of DSM uncertainties can be reduced by methods working with interferograms (Subsection 4.4.3.1), the time series of image phase (Subsection 4.4.3.2) or deformation time series (Subsection 4.4.3.3). Finally, the inversion step is applied to invert the interferometric phase to deformation time series by least squares or SVD (Section 4.5). Alternatively, for a physically sound solution, the inversion can be modified by replacing the unknowns in terms of phase values of acquisitions with respect to the first acquisition by those in terms of the mean phase velocities between time-adjacent acquisitions.

## 5. SIMULATED INFLUENCE OF RESIDUAL INTERFEROMETRIC NOISE AND DATA GAPS ON SBAS INSAR

In this Chapter, the influence of residual interferometric error and noise and data gaps on SBAS-derived rates are investigated. It is a more detailed description of the same results in [Bui et al. \(2020\)](#). Simulated InSAR datasets are generated with subsidence signals of linear rates with and without sinusoidal annual amplitudes contaminated by Gaussian residual interferometric noise. The influence of data gaps is investigated through simulations with percentages of missing data ranging from 5% to 50% that are selected randomly across the four-year time series, and for three-month windows to represent the northern winter season where snow cover may cause SAR decorrelation. The SBAS algorithm (e.g., [Berardino et al., 2002](#); [Cavalié et al., 2007](#); [López-Quiroz et al., 2009](#); [Schmidt & Bürgmann, 2003](#); [Usai, 2003](#)) incorporated in the open-source package GIANt ([Agram et al., 2013](#); [Agram et al., 2012](#)) is implemented for all the InSAR data processing presented in this Chapter.

### 5.1 InSAR Data Simulation

A time series of 1000 independent pixels that are reasonably representative of the range of Earth deformations detected by InSAR are simulated in this Chapter, these being: millimetres per year (e.g., [Elliott et al., 2010](#); [Furuya et al., 2007](#); [Jiang et al., 2011](#); [Schmidt & Bürgmann, 2003](#)), centimetres per year (e.g., [Amelung et al., 1999](#); [Cavalié et al., 2013](#); [Chaussard et al., 2014](#); [Lee et al., 2012](#)), and tens of centimetres per year (e.g., [Chaussard et al., 2014](#); [López-Quiroz et al., 2009](#); [Motagh et al., 2007](#); [Short et al., 2011](#)).

The simulated data cover a four-year time span with an 11-day sampling interval that corresponds to 133 equally time-spaced InSAR images. The baseline history of these 133 images, which is defined as the perpendicular baselines between images and the reference one (i.e., the first scene), is assumed to be within  $[-200, +200]$  m, which is the order of modern SAR missions such as C-band Sentinel-1 ([Yague-Martinez et al., 2016](#)) or X-band TerraSAR-X (TSX) (e.g., [Chen et al., 2016](#); [Lubitz et al., 2013](#)). The simulated baseline history of 133 images is generated randomly with ranges between  $-200$  m and  $+200$  m with that of the first scene being fixed to be zero (so leaving 132), and are shown as a scatter plot in [Figure 5.1](#).

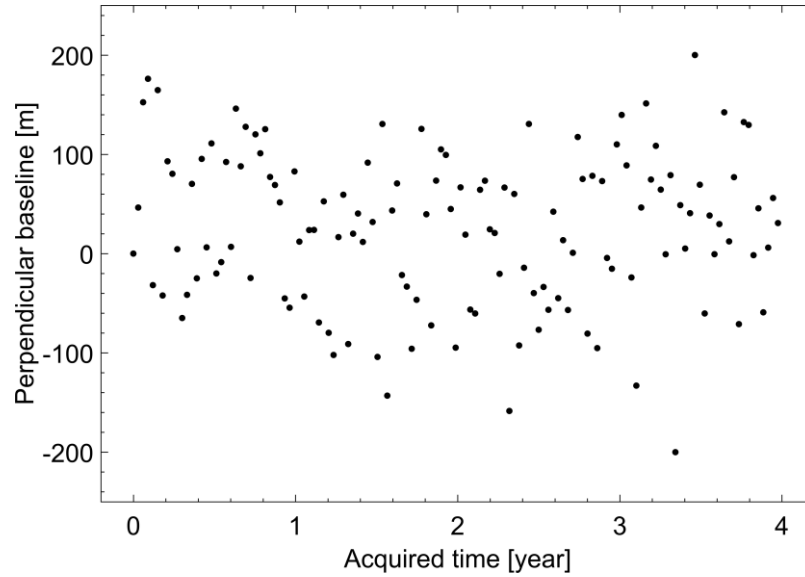


**Figure 5.1.** Scatter plot of simulated perpendicular baseline history. The perpendicular baseline history ranges between  $-200$  and  $200$  m, with the mean and standard deviation of  $24$  m and  $\pm 77$  m, respectively.

These simulated temporal and perpendicular baselines with respect to the first SAR scene will then be used to select image pairs to form small baseline interferograms. Though the difference in Doppler centroid between SAR images can also be applied as an alternative parameter to select interferograms (Hooper, 2008), applying temporal and perpendicular baselines with their thresholds is simple and efficient, which have been applied frequently in the literature (see Table 1.2). Therefore, Doppler centroid baselines are not simulated in this dissertation for the sake of simplicity. A land subsidence signal with both a linear trend and a superposed annual sinusoidal oscillation is of interest in this Chapter. All pixels are simulated to experience surface deformation in the LoS with linear plus annual periodic terms, which are expressed as:

$$d_{p,i} = v_p t_i + a_p \sin(2\pi t_i) \quad (5.1)$$

where  $d_{p,i}$  is the deformation of pixel  $p$  at the  $i^{\text{th}}$  image with corresponding acquired time  $t_i$ ,  $v_p$  and  $a_p$  are the linear rate (velocity) and annual amplitude of the same pixel, respectively. This model form is selected because time series analyses of other environmental phenomena do likewise (e.g., Davis et al., 2012; Didova et al., 2016).

The linear rates are chosen as  $-2$  mm/yr,  $-20$  mm/yr and  $-100$  mm/yr over the four-year period, which are representative of Earth deformation rates measured by InSAR (e.g., Cavalié et al., 2013; Chaussard et al., 2014; Elliott et al., 2010). The

sinusoidal annual amplitude of Earth surface deformation has been drawn from the literature, which can range from the order of millimetres to centimetres (e.g., Baldi et al., 2009; Bock et al., 2012; Davis et al., 2012; Dzurisin et al., 2009; Osmanoglu et al., 2011). For example, Osmanoglu et al. (2011) report annual amplitudes of surface deformation at GNSS stations ranging from several millimetres up to  $\sim 2.6$  cm. Murray and Lohman (2018) found seasonal deformation amplitudes up to  $\sim 5$  cm in California detected by InSAR and peak-to-peak amplitudes of  $\sim 6$  cm from GNSS in the Amazon Basin (cf. <http://geodesy.unr.edu/NGLStationPages/stations/NAUS.sta>).

While there can be large annual signals in various parts of the world, more conservative cases of simulated deformation signal with pairs of signal parameters of linear rate plus annual amplitude are simulated in this study (Table 5.1). A Monte Carlo simulation (Kroese et al., 2014) with 1000 pixels for each scenario is then applied. Fewer tested pixels are chosen to avoid prohibitive computation times for the simulation experiments. The deformation time series of the 1000 pixels are then computed for the 133 equally spaced 11-day acquisition times using Equation (5.1), and are termed herein the “simulated deformation time series”. These are considered to be the “true” or noise-free signal, and will be used to validate the SBAS InSAR data processing results later in this Chapter.

**Table 5.1.** The three cases of simulated signals showing linear rates and annual amplitudes.

Signal case	Linear rate [mm/yr]	Annual amplitude [mm]
1	-2	2
2	-20	5
3	-100	10

The maximum number of possible interferograms ( $M_{max}$ ) selected from all combinations of any two images can be computed from the number of InSAR images ( $N$ ) by (Berardino et al., 2002):

$$M_{max} = \frac{N(N + 1)}{2} \quad (5.2)$$

With 133 InSAR images, the maximum possible number of interferograms is 8778. These 8778 noise-free interferograms are then computed based on this simulated

deformation SAR time series: the phase difference of an interferogram connecting  $i^{th}$  and  $j^{th}$  images is computed by subtracting the simulated time series value at  $i^{th}$  time from that at  $j^{th}$  time.

The simulated residual errors and noise, herein called the “residual interferogram noise”, are then added to the noise-free interferograms. Three sets of assumed 8778 Gaussian noise values with zero mean are generated for each of the 1000 pixels and bounded within  $[-2; +2]$  mm,  $[-5; +5]$  and  $[-10; +10]$  mm, which correspond to standard deviations of approximately  $\pm 0.5$  mm,  $\pm 1.5$  mm and  $\pm 3.0$  mm, respectively (Table 5.2). Specifically, for each pixel, 8778 random samples of a Gaussian distribution with a zero mean and a standard deviation of one are first generated. These are subsequently rescaled so that their ranges lie exactly within the bounds set in Table 5.2. It is acknowledged that the residual errors and noise in real SAR data may not be Gaussian with zero mean (e.g., Agram & Simons, 2015; Dawson & Tregoning, 2007; Rocca, 2007), because they originate from a variety of sources as shown in Chapter 3. However, it would only ever be able to postulate the actual statistical distribution of real InSAR data errors, so instead make the simple assumption of Gaussian zero mean for these simulations.

Table 5.2. Simulated noise with various ranges and standard deviations.

Noise case	Range [mm]	Standard deviation [mm]
A	$[-2; +2]$	$\pm 0.5$
B	$[-5; +5]$	$\pm 1.5$
C	$[-10; +10]$	$\pm 3.0$

Note that not all 8778 interferograms will be analysed. The number of interferograms that will be used depends on the SBAS network under consideration. This simulated noise was added to noise-free interferograms to generate noisy interferograms. The simulated residual interferogram noise is generated in such a way that longer baseline lengths are assigned with noise of higher magnitude. Additionally, they have different ranges with the temporal baselines being from  $\sim 0.03$  years to  $\sim 3.97$  years, whilst the perpendicular baselines being between  $-376$  m and  $400$  m. Therefore, they are first “normalised” by (Pepe & Lanari, 2006):

$$\begin{aligned} norm\_btemp_i &= btemp_i \times \frac{\max(bperp) - \min(bperp)}{\max(btemp) - \min(btemp)} \\ norm\_bperp_i &= bperp_i \end{aligned} \quad (5.3)$$

where  $norm\_btemp_i$  and  $norm\_bperp_i$  are the “normalised” temporal and perpendicular baselines of the  $i^{th}$  interferogram, respectively, which correspond to their values before “normalisation”  $btemp$  and  $bperp$ ,  $\max(\cdot)$  and  $\min(\cdot)$  indicate the maximum and minimum values, respectively. The normalised baseline lengths of all interferograms are then computed with the  $i^{th}$  interferogram being (Pepe & Lanari, 2006):

$$norm\_bsln_i = \sqrt{norm\_btemp_i^2 + norm\_bperp_i^2} \quad (5.4)$$

In this dissertation, the 1000 studied pixels are of high quality, i.e., those after the coherent pixel selection step described in Chapter 4, and thus their coherence is high. Therefore, for the sake of simplicity, a coherence model is not simulated and the normalised baseline lengths computed from Equation (5.4) are used to assign the residual interferogram noise. Specifically, for each pixel with a corresponding noise set of 8778 samples, the noise is assigned to interferograms in a way that an interferogram with a longer normalised baseline length will be assigned with noise of larger magnitude.

It is acknowledged that the influences of temporal and perpendicular baselines on interferometric noise are different. While the influence of perpendicular baselines can be quantified via their relationship with DSM error (Lee et al., 2012), the influence of temporal baselines is more sophisticated, which is dependent on the change of atmosphere and target environment over time (Zebker et al., 1997; Zebker & Villasenor, 1992). Temporal decorrelation has also been described with models other than linear decay (e.g., exponential, see Rocca (2007)). Here, for the sake of simplicity, the two types of baseline are assumed to be equal in terms of their weights in calculating normalised baselines using Equation (5.4).

## 5.2 Interferogram Networks Chosen by Temporal and Perpendicular Baseline Thresholds

In order to assess the influence of residual noise and small baseline network configuration on SBAS-derived deformation rates, various interferogram networks were formed through the use of different thresholds for the temporal baselines. For the sake of simplicity initially, the perpendicular baseline length is restricted to 200 m and

only the temporal baseline varies. [Table 5.3](#) shows the temporal baseline thresholds that are applied with the resulting number of interferograms. The geometrical configurations of those networks are displayed in [Figure 5.2](#).

[Table 5.3](#). List of networks tested based on various temporal baseline thresholds. The perpendicular baseline threshold is set fixed at 200 m ([Figure 5.1](#)).

Temporal baseline threshold [days]	Number of interferograms
22	263
33	376
44	498
55	621
66	745
77	863
88	986

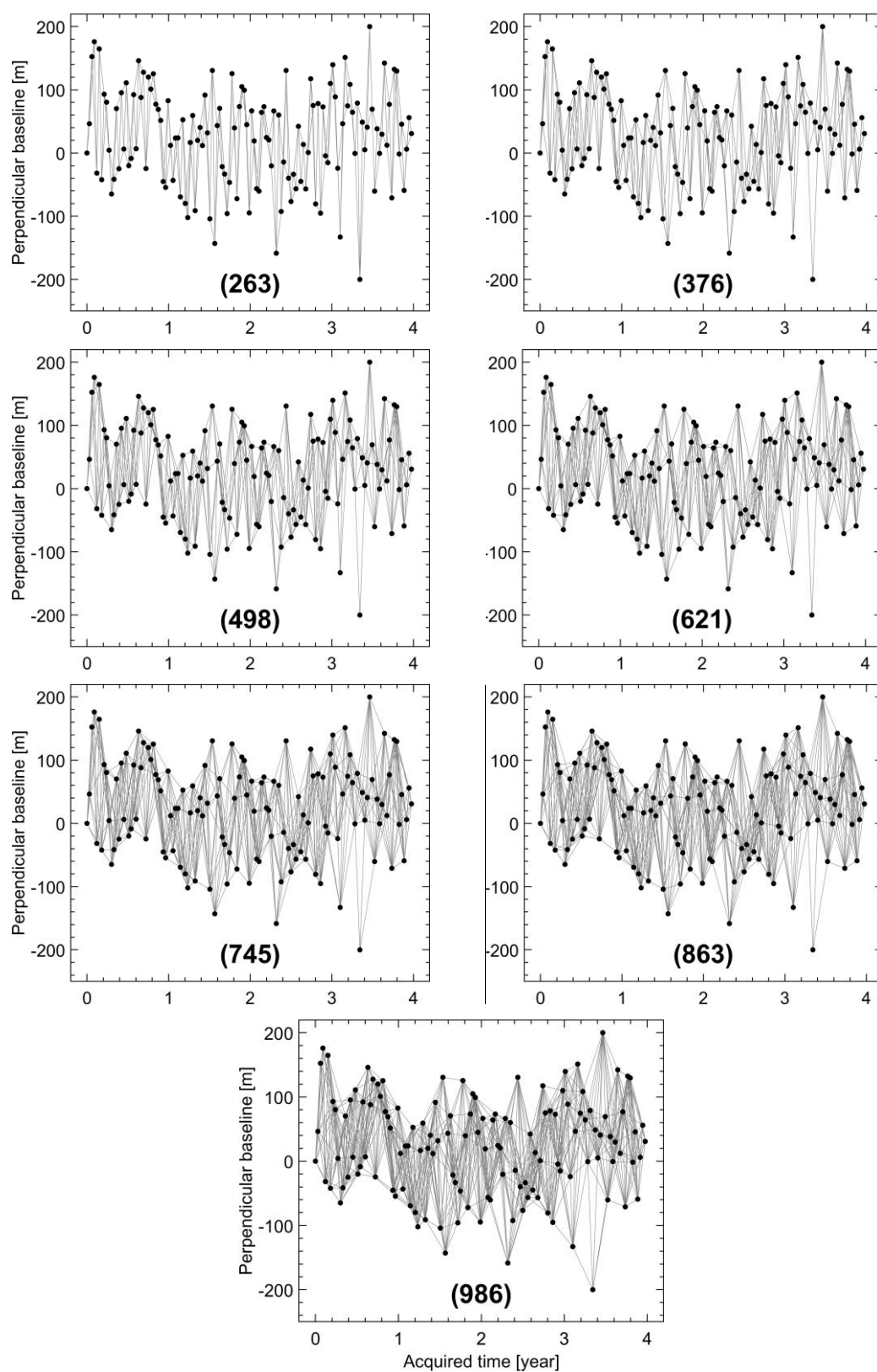


**Figure 5.2.** Different SBAS interferogram networks chosen relying on temporal baseline thresholds shown in [Table 5.3](#) and a fixed perpendicular baseline threshold of 200 m. The bracketed bold number under each network indicates the number of interferograms.

### 5.3 Influence of Residual Noise and Network Configuration

The SBAS approach is applied to subsets of the simulated noisy interferograms (Table 5.3) by using the Generic InSAR Analysis Toolbox (GIANt) package (Agram et al., 2013; Agram et al., 2012). GIANt incorporates most of the SBAS-based data processing methods mentioned in Chapter 1, including the “traditional” SBAS (e.g., Berardino et al., 2002; Cavalié et al., 2007; Schmidt & Bürgmann, 2003; Usai, 2003), the new SBAS (NSBAS) (Doin et al., 2011; López-Quiroz et al., 2009), and the Multiscale InSAR Time Series (MInTS) (Hetland et al., 2012); cf. Table 1.2.

Time series of deformation relative to the first-acquired SAR image time for each of the 1000 test pixels are generated assuming that there is no deformation in the first acquisition. Both unweighted linear regression and unweighted least squares (LS) are then applied to these SBAS time series in order to compute SBAS-derived linear rates and annual sinusoids, which are then compared with the simulated parameters listed in Table 5.1. The RMS of the difference between simulated deformation time series (the “true” signal) and SBAS-derived deformation time series is also computed in order to test dependence on the number of interferograms chosen.

#### 5.3.1 Influences on Simulated Linear Signals

A signal where Equation (5.1) is adopted solely with the linear rate components of  $-2$  mm/yr,  $-20$  mm/yr and  $-100$  mm/yr (Table 5.1) is examined first. Figure 5.3 shows results from different combinations of simulated deformation rates and residual interferogram error and noise. Here, the assumed simulated linear rates are considered as the “true” rates to which the SBAS-derived rates are compared and the differences between them are herein termed the “errors in rate determination”. The SBAS rates are derived by fitting a linear regression to the corresponding deformation time series, then the errors in rate determination are calculated.

The “errors” are shown in Figure 5.3, and are the same in both magnitude and sign among all three simulated linear rate cases from Table 5.1. Generally, the larger simulated residual interferogram noise (i.e.,  $[-10; +10]$  mm vs.  $[-5; +5]$  mm vs.  $[-2; +2]$  mm) leads to larger errors in the rate determination (cf. blue, green and black plotlines in Figure 5.3), whereas an increase in the number of chosen interferograms (by choosing a larger temporal baseline threshold) can reduce these errors.

Additionally, while their trends are in an agreement for the cases of larger signal rates (i.e.,  $-20$  mm/yr and  $-100$  mm/yr, Figure 5.3, top-right and bottom),

contradictory trends exist in the cases of small deformation (i.e.,  $-2$  mm/year, [Figure 5.3](#), top-left), particularly when networks of fewer interferograms are used together with higher residual noise of  $[-5; +5]$  mm and  $[-10; +10]$  mm. Importantly, the SBAS-derived deformation trends are affected by not only the magnitude of noise, but also its relation to the signal size (see [Figure 5.3](#), top-left). Thus, a low SNR is more likely to result in incorrect or even contradictory trend estimates. In essence, small deformation rates in the presence of proportionally large noise (i.e., low SNR) may lead to spurious results, which become exacerbated in the presence of significant data gaps (Section 5.4).

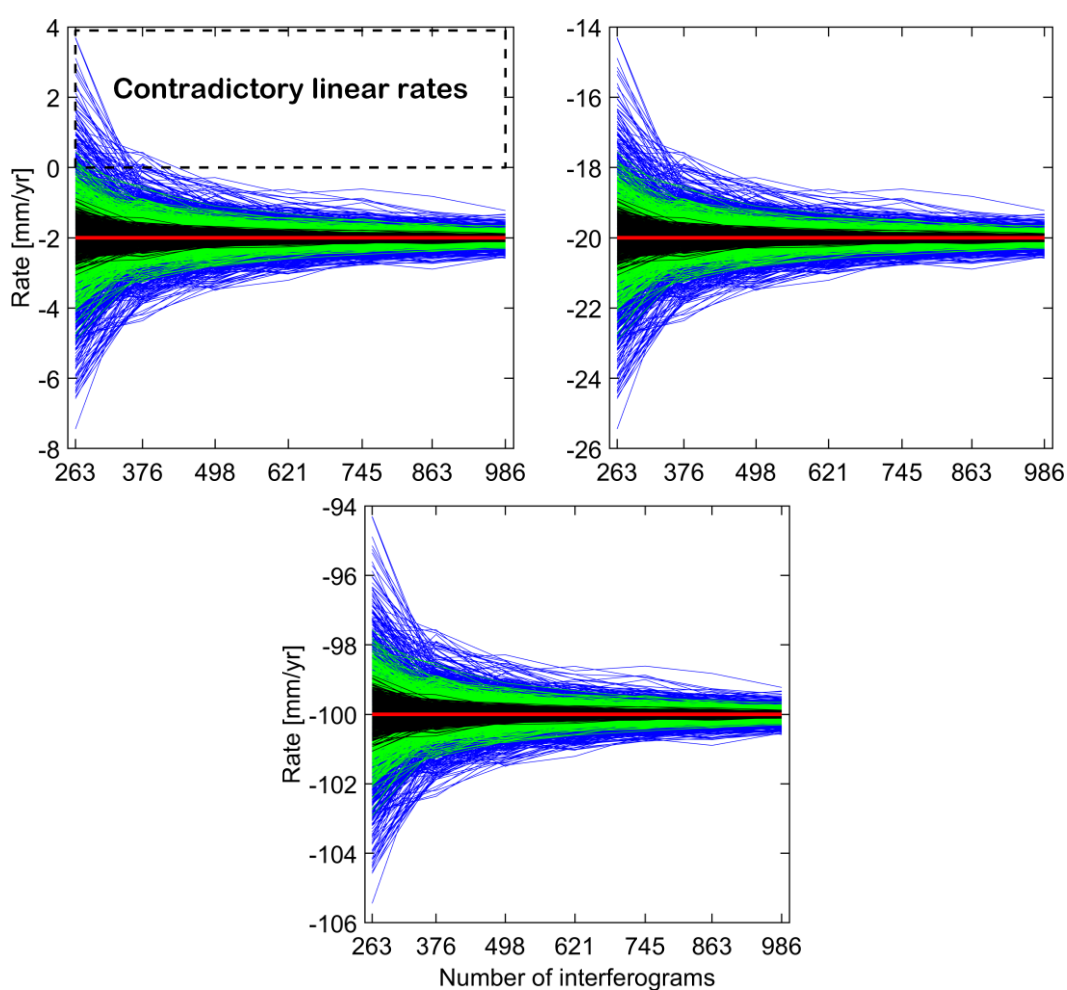


[Figure 5.3](#). Comparison of rates computed by unweighted linear fit from combinations of different deformation signals. The simulated linear rate cases 1 (top-left), 2 (top-right) and 3 (bottom) shown in [Table 5.1](#) are contaminated by simulated residual interferogram noise. Black, green and blue polylines are SBAS-derived rates computed from simulated data with simulated noise cases A to C, respectively ([Table 5.2](#)). Red horizontal lines represent the simulated rates. The black dashed box in the top-left panel is used to contrast between positive and negative rates that indicates contradictory trends.

The “errors in rate determination” are next compared for the networks listed in [Table 5.3](#) and shown in [Figure 5.4](#) for four example pixels. Within a specific network and pixel, the retrieved rate errors are identical when the same residual noise is applied regardless of the signal rates. In other words, if a specific network chosen from [Table 5.3](#) with corresponding interferogram noise set is applied, then its error in rate determination will not depend on the magnitude of simulated rate (cf. blue, orange and yellow bars in [Figure 5.4](#)). This is attributable to SBAS using the LS principle (e.g., [Schmidt & Bürgmann, 2003](#)) or the singular value decomposition (SVD) method (e.g., [Berardino et al., 2002](#)).

The results computed from applying the LS principle depend on redundant interferograms, together with residual interferogram error and noise that, in turn, depends on the configuration of the network specified by the design matrix ([Berardino et al., 2002](#)). Both the LS principle and SVD method result in the same InSAR-derived rates, except that the latter can better cope with disconnected subsets of interferogram networks, whereas the former cannot (cf. [Berardino et al., 2002](#); [Gong et al., 2016](#)). Consequently, the same error in rate determination will result if the same residual noise is applied to a network, regardless of the deformation rate.

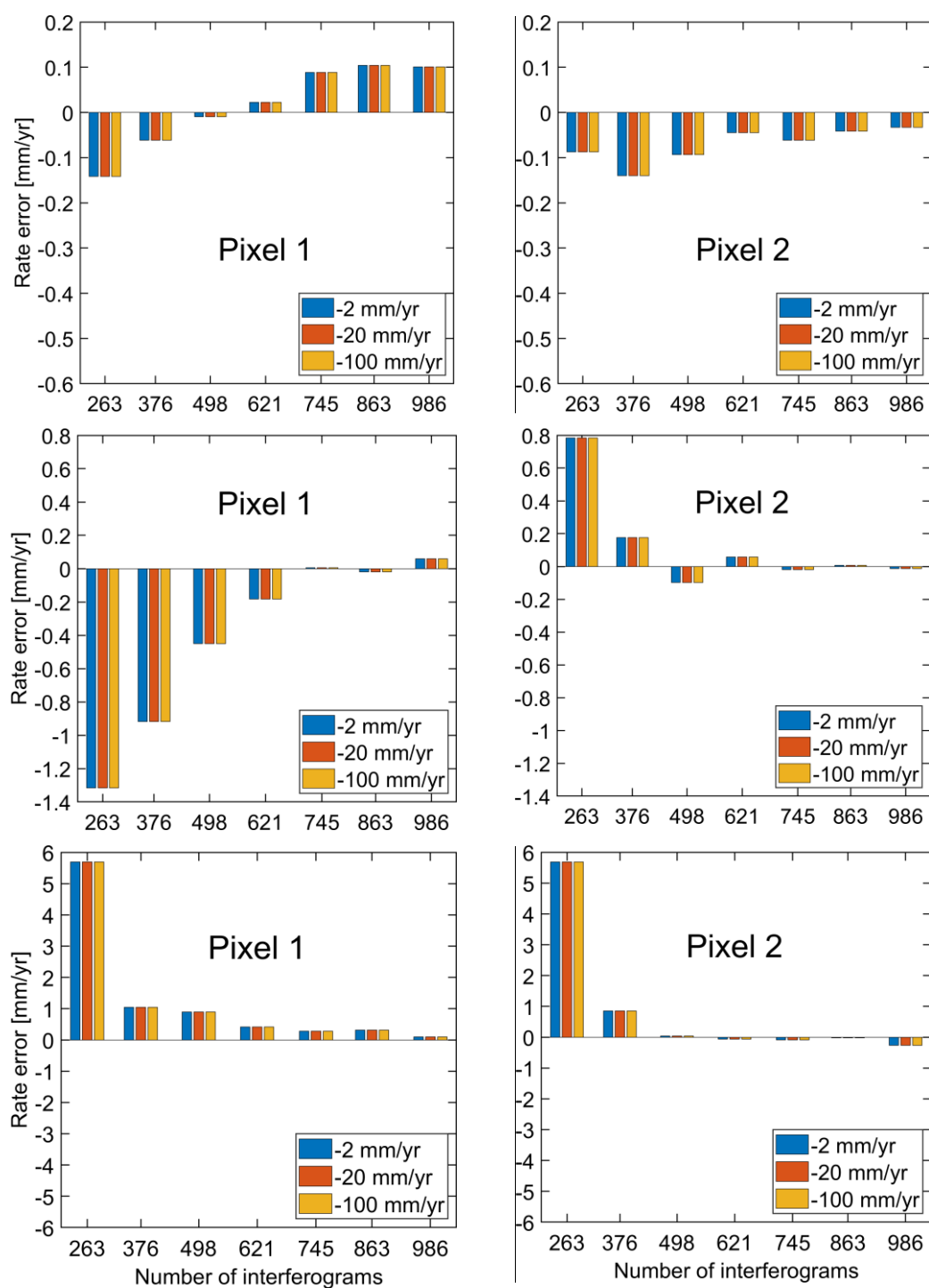


Figure 5.4. Comparison of rate errors computed from different networks for four example pixels. The top, centre and bottom rows correspond to simulated noise cases A, B and C (Table 5.2). Note the different scales on the y-axis for each noise case.

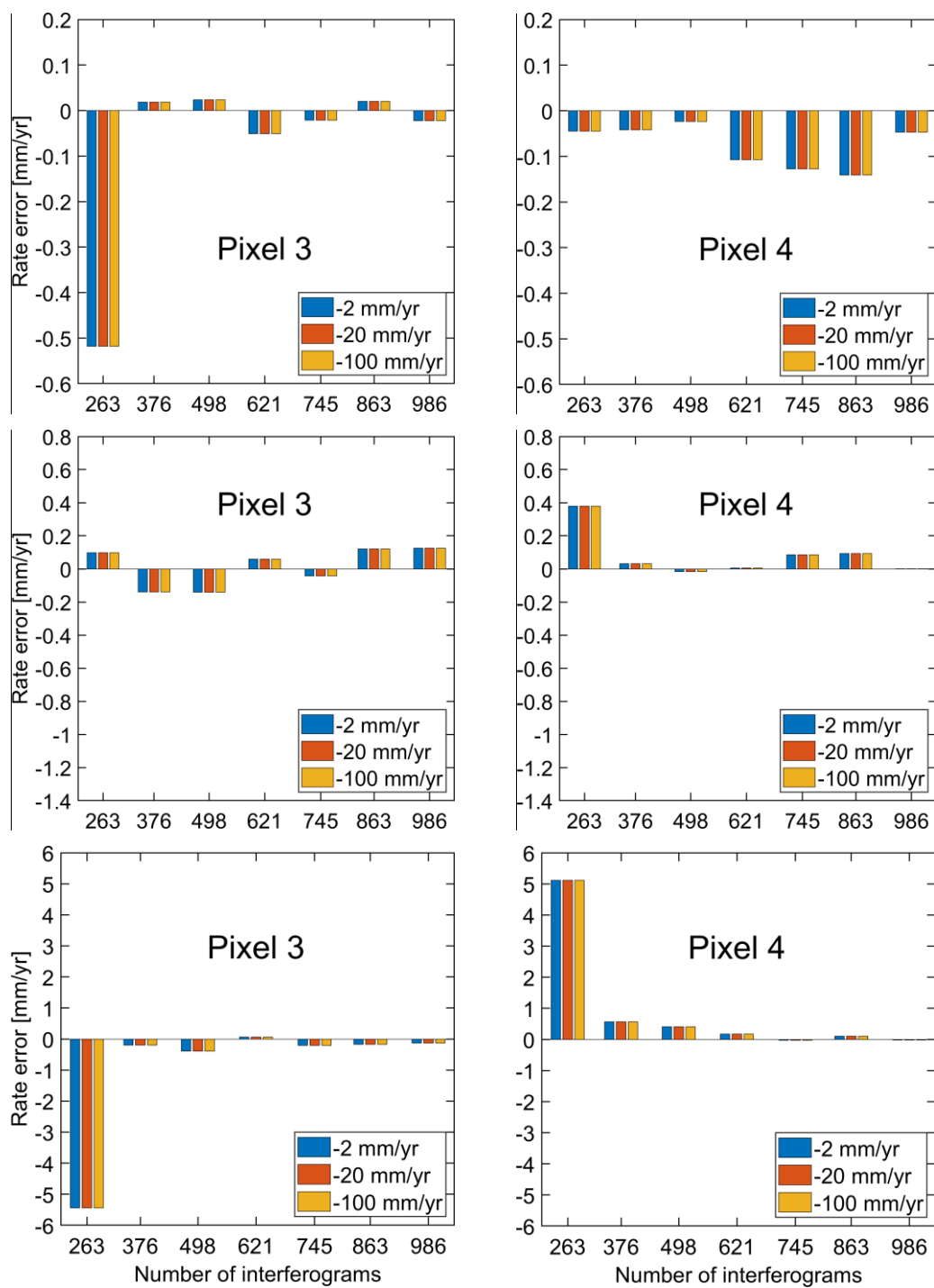


Figure 5.4. (Continued)

### 5.3.2 Influences on Simulated Non-linear Signals

The signal combining both a linear trend and a sinusoidal annual term is examined next. As mentioned in Section 5.1, pairs of signal parameters of linear rate plus annual amplitude are applied, which are  $-2$  mm/yr plus 2 mm,  $-20$  mm/yr plus 5 mm, and  $-100$  mm/yr plus 10 mm (Equation (5.1)) as listed in Table 5.3. Via this simulation, the influence of non-linearity of signal on unweighted linear fit rates will be tested, which are derived by fitting a linear regression to the simulated SBAS-derived deformation time series.

Like the previous test of a linear signal only, the simulated deformation time series is generated by first applying Equation (5.1) for all 1000 pixels prior to forming 8778 noise-free interferograms and applying simulated residual interferogram noise. The networks shown in Table 5.3 are then applied in sequence to select corresponding stacks of interferograms, which are then utilised with the SBAS method. Both the unweighted linear fit and unweighted LS methods are subsequently adopted to derive linear rates and annual amplitudes. Additionally, the RMSs between simulated and SBAS-derived time series are calculated.

Figure 5.5 shows unweighted linear-fit rates computed using the linear rates from Table 5.1 and the simulated noise in Table 5.2. These results in Figure 5.5 reflect the influence of signal non-linearity on linear-fit rates through biases in rate errors, particularly in the case of large annual amplitudes, i.e., strongly non-linear, (cf. Figure 5.5 between red lines and coloured polylines). This is due to the inappropriate functional model used here to derive the linear rates, i.e., linear regression, which is applied to the linear plus annual signal.

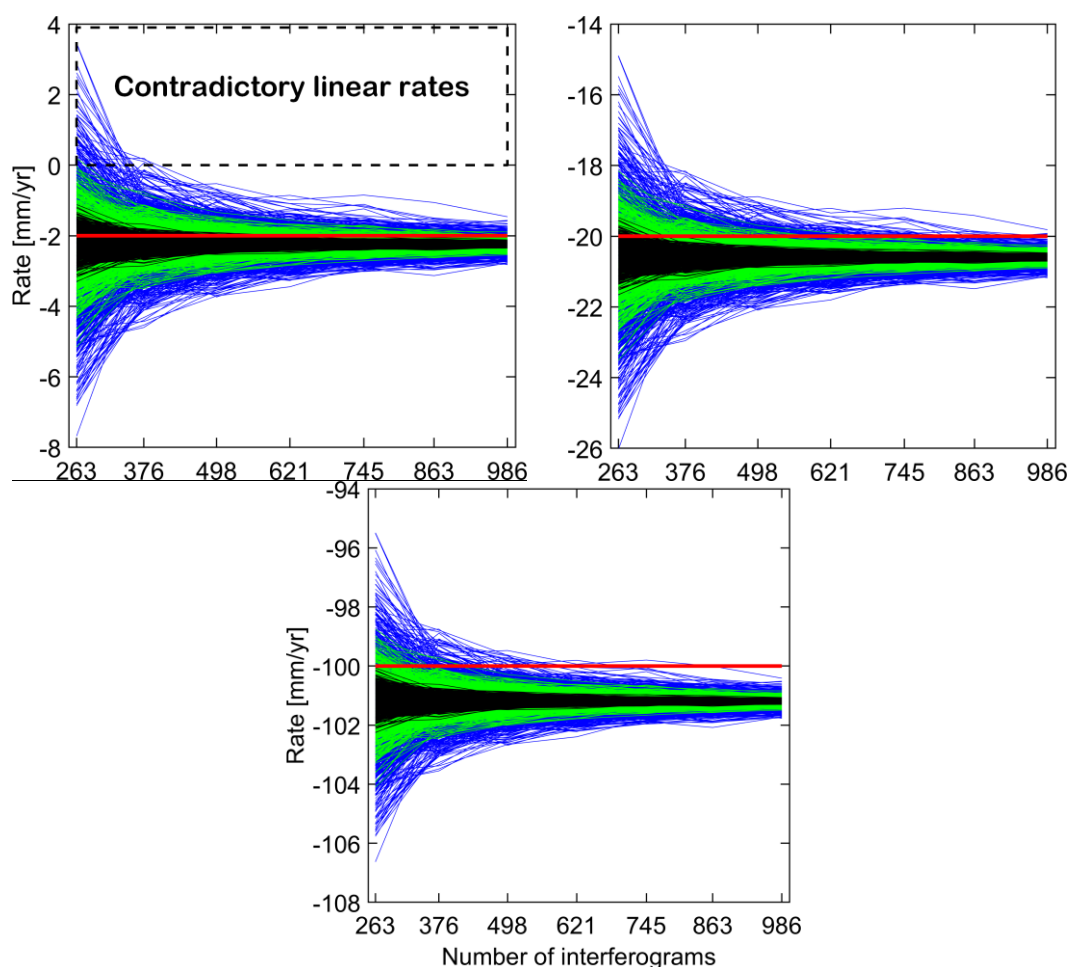


**Figure 5.5.** Comparison of unweighted linear-fit rates from linear plus annual signals. The simulated signal cases 1 (top-left), 2 (top-right) and 3 (bottom) shown in [Table 5.1](#) are contaminated by simulated residual interferogram noise. Black, green and blue polylines indicate the results computed from simulated data with noise cases A, B and C ([Table 5.2](#)). Red horizontal lines represent the simulated rates. The black dashed box in the top-left panel is used to contrast between positive and negative rates that indicates contradictory trends in some cases.

The simulated signal is known (Equation (5.1)), so this is adopted for estimating both rates and annual amplitudes utilising unweighted LS ([Figure 5.6](#)). The results indicate similar behaviour to that in the case of solely linear signals (cf. [Figure 5.6](#) (left) with [Figure 5.3](#)) and those with biases removed (cf. [Figure 5.6](#) (left) and [Figure 5.5](#)). Again, this is attributable to the SBAS method in which the results computed depend on the configuration of the network and residual interferogram noise, but not the deformation rate. Also, it is due to the more appropriate functional model used to obtain the linear rates where the influence of the signal non-linearity cancels out. It is therefore an important “warning” that a suitable functional model should be utilised to

calculate linear rates in case the Earth's surface experiences non-linear deformation, particularly in strongly non-linear cases.

In the case of applying LS estimation with an appropriate functional model, not only the linear rate but also its accompanying parameters, e.g., the annual amplitude in this study, will be obtained. This is shown in [Figure 5.6](#) (right), where the computed annual amplitudes indicate that more interferograms in the SBAS network result in more accurate LS estimation of the annual amplitude. In addition, the errors in those computed parameters are dependent on the SBAS network configuration and residual interferogram noise, but not the signal's magnitude.

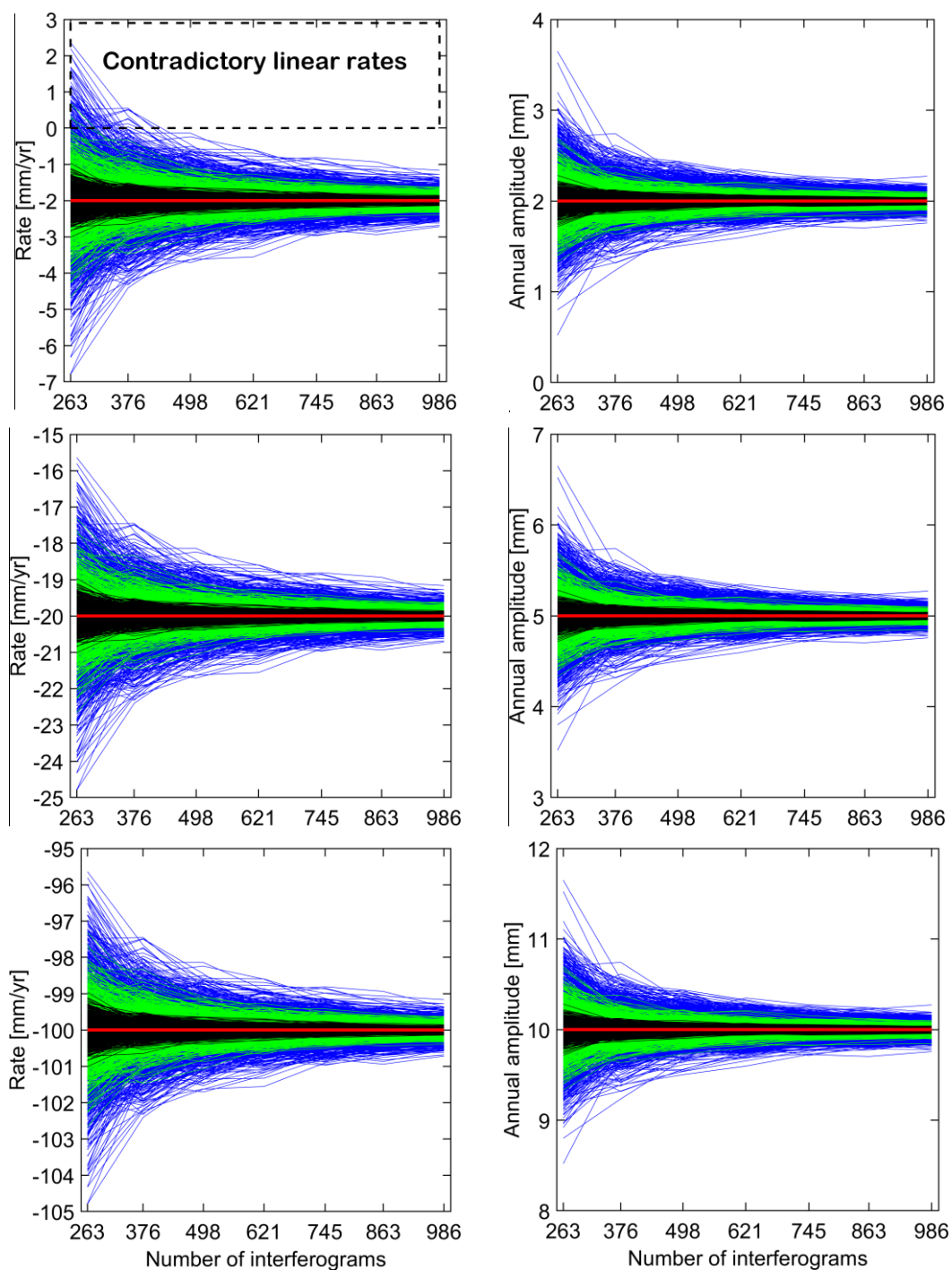


**Figure 5.6.** Comparison of unweighted least squares rates (left panel) and annual amplitudes (right panel) computed from linear plus annual signals. From top to bottom correspond to simulated signal cases 1 to 3 (Table 5.1) contaminated by various simulated residual interferogram noise. Black, green and blue polylines indicate the results computed from simulated data with noise cases A, B and C (Table 5.2). Red horizontal lines represent the simulated rates or annual amplitudes. The black dashed box in the top-left panel is used to contrast between positive and negative rates that indicates contradictory trends in some cases.

## 5.4 Influence of Data Gaps on SBAS-derived Rates

In this Subsection, the influence of SAR data gaps on SBAS-retrieved rates is studied. This is motivated by the likelihood of irregular temporal sampling of SAR data due to scheduling or other technical issues, such as decorrelation during winter snow cover in the Northern Hemisphere. Simulations with the network of 986 interferograms formed by applying a temporal baseline threshold of 88 days (approximately three months, [Table 5.3](#)) are conducted, with two scenarios of data gaps. In the first scenario, missing images are due to technical and/or scheduling issues, which are considered random, and, in the second scenario, missing images are chosen in the northern winter season that are assumed to have low coherence due to snow cover.

### 5.4.1 Random Data Gaps

In this Sub-subsection, it is assumed that there are, in turn, 5%, 10%, 15%, 20%, 25%, 30%, 35%, 40%, 45%, and 50% of acquisitions missing from the simulated time series. First, images that are assumed to be missing from the acquisition are chosen randomly then removed from the original list of 133 evenly-spaced acquired images. Interferograms having connections with those missing images are subsequently identified and eliminated from the original list of 986 interferograms.

The summary of these networks is listed in [Table 5.4](#) with column (2) indicating the percentages of missing images, columns (3) and (4) representing the number of removed and remaining images after randomly choosing gaps, and the corresponding number of interferograms listed in columns (5) and (6). The number of images reduces from 133 in the case of no gaps to 66 with 50% gaps. The corresponding number of remaining interferograms decreases from 986 to 235, for 50% gaps. [Figure 5.7](#) compares the network without gaps and those corresponding to various amounts of gaps in percentage.

**Table 5.4.** Number of images and interferograms removed after randomly choosing gaps.

No	Percentage of gaps (%)	Number of removed images	Number of remaining images	Number of removed interferograms	Number of remaining interferograms
1	0	0	133	0	986
2	5	7	126	106	880
3	10	13	120	193	793
4	15	20	113	278	708
5	20	27	106	370	616
6	25	33	100	436	550
7	30	40	93	503	483
8	35	47	86	592	394
9	40	53	80	652	334
10	45	60	73	706	280
11	50	67	66	751	235

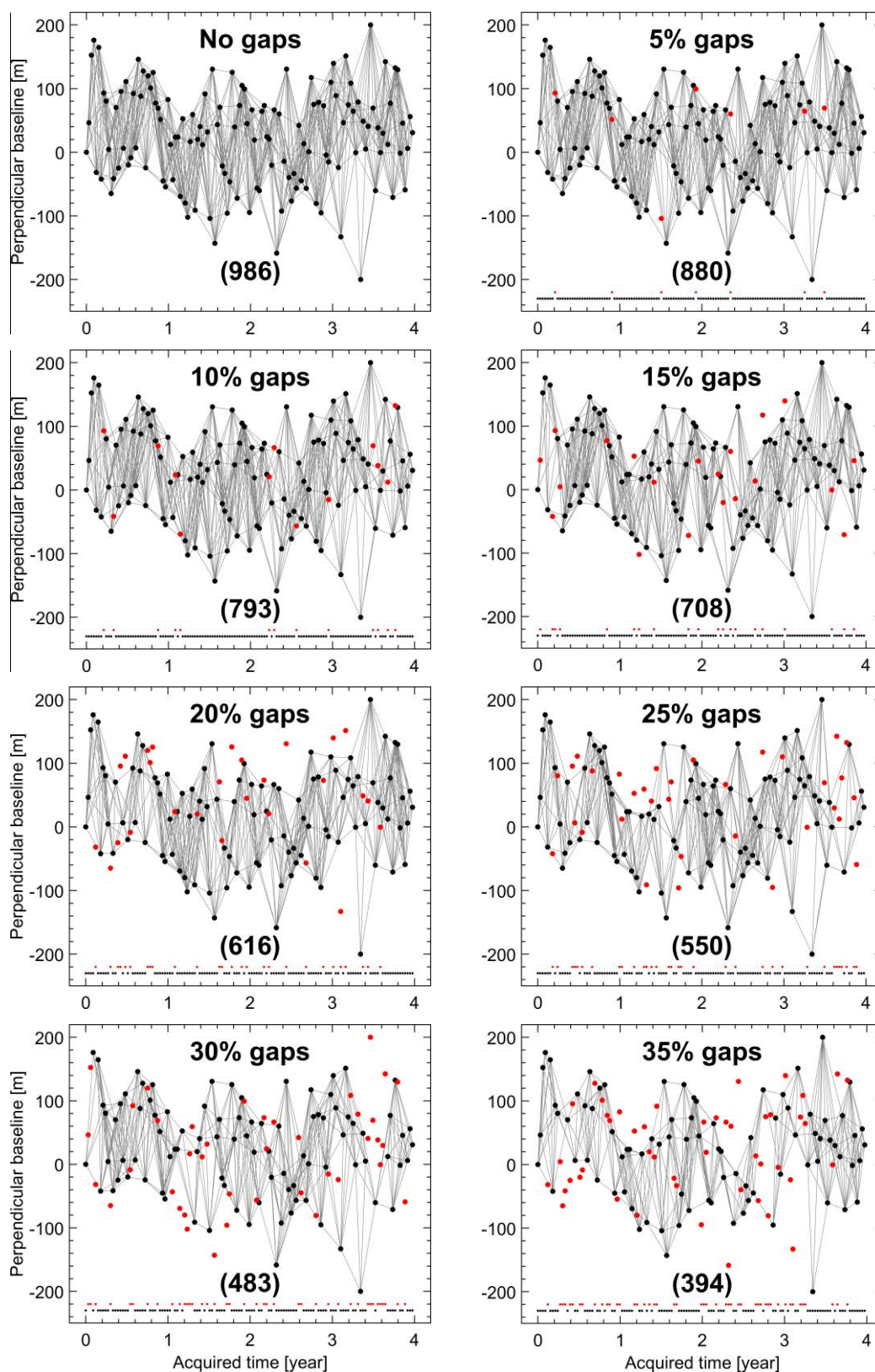


**Figure 5.7.** Comparison of the interferogram network gaps in percentage of image removed. Grey lines indicate InSAR interferograms connecting images denoted by black dots. Red dots indicate missing images. The bracketed bold number under each network refers to the number of interferograms.

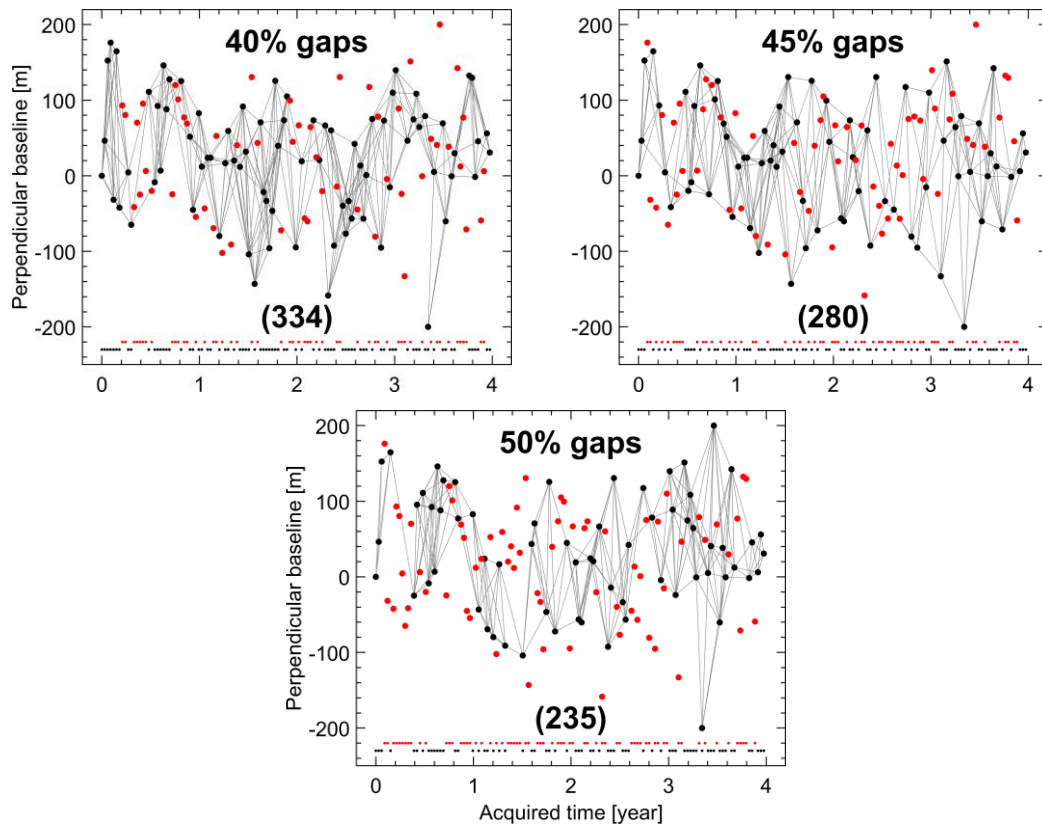
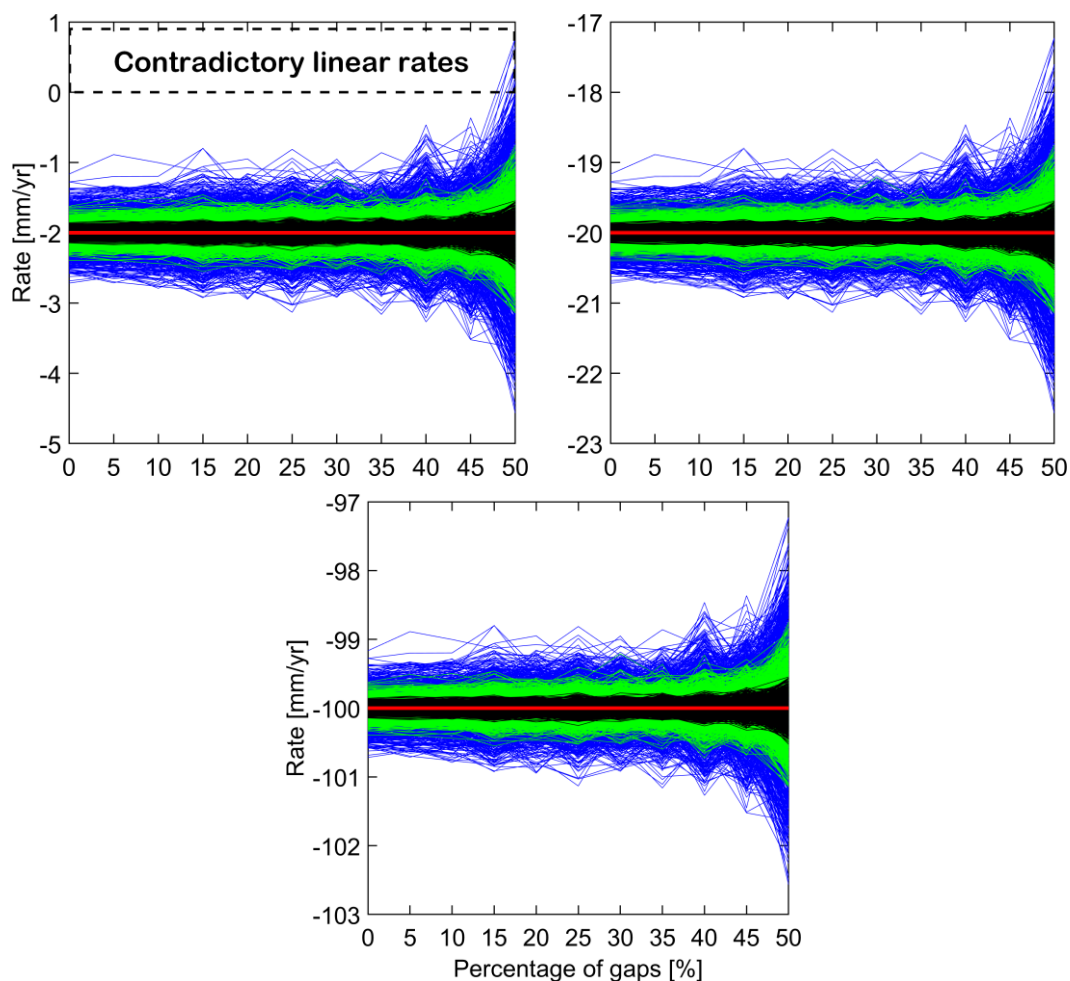


Figure 5.7. (Continued)

Here, the same linear plus annual signals as those used in Subsection 5.3.2 according to simulated signal cases shown in Table 5.1 is used. For each network shown in Figure 5.7, the SBAS approach in the GIANt software is applied to all 1000 pixels in which the deformation time series at each pixel is derived. Unweighted LS is then applied to calculate the deformation rates and the RMSs of the difference between simulated and SBAS-derived time series are then calculated.

Figure 5.8 compares SBAS-derived unweighted LS rates between the SBAS network with no gaps and those of different percentages of data gaps. Figure 5.9 shows the corresponding RMSs of the difference between simulated and SBAS-derived deformation time series. These RMSs are the same for all three cases of linear plus annual signal (Table 5.1). Figure 5.8 and Figure 5.9 confirm that data gaps have an effect on the retrieved rates and RMSs with a noticeably larger influence in cases of higher gap percentages, particularly the 50% case. Contradictory trends are obtained for some pixels in the case of large residual interferogram noise and low magnitude rates (i.e., low SNR) (Figure 5.8, top-left). This is likely to be caused by a weak SBAS network configuration (see Figure 5.7 with the 50% gaps case).



**Figure 5.8.** Comparison of unweighted least squares rates computed from linear plus annual signals between the interferogram network of no gaps and those with randomly chosen gaps of various percentages. The simulated signal cases 1 (top-left), 2 (top-right) and 3 (bottom) shown in [Table 5.1](#) are contaminated by simulated residual interferogram noise. Black, green and blue polylines indicate the results computed from simulated data with noise cases A, B and C ([Table 5.2](#)). Red horizontal lines represent the simulated rates. The black dashed box in the top-left panel used to contrast between positive and negative rates that indicates contradictory trends in some cases.

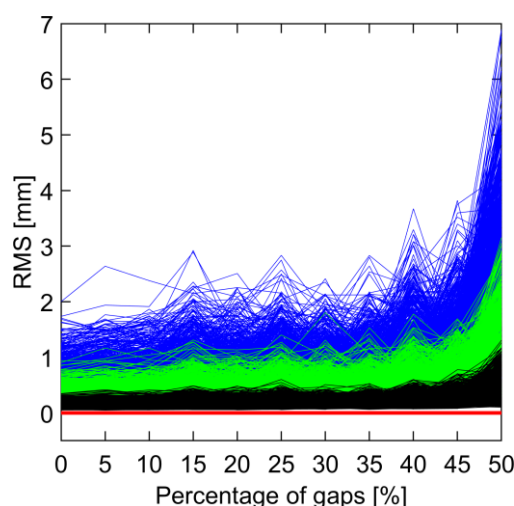


**Figure 5.9.** Comparison of RMSs of the difference between simulated and SBAS-derived deformation time series of all pixels between the SBAS interferogram network of no gaps and those with random gaps. Black, green and blue polylines indicate the results computed from simulated data with noise cases A, B and C (Table 5.2).

With the same temporal baseline threshold of 88 days that is used (Table 5.3), random gaps in SAR acquisitions lead to a change in network configuration (cf. Figure 5.7), which may be weak with independent interferograms, i.e., those do not link with any closed interferogram loops, as the network of 50% gaps shown in Figure 5.7 (bottom). This type of network with independent interferograms results in estimated rates that might be contradictory with the simulated rates in some pixels (see Figure 5.8, top-left). This is confirmed by the results shown in Figure 5.10 in which, with the same SAR acquisitions (i.e., the 50% gap case), a more robust network with all dependent interferograms is formed by the temporal baseline threshold of 99 days (Figure 5.10, left). The estimated rates from applying this network are shown in Figure 5.10 (right, 50% gaps) with no contradictory rates.

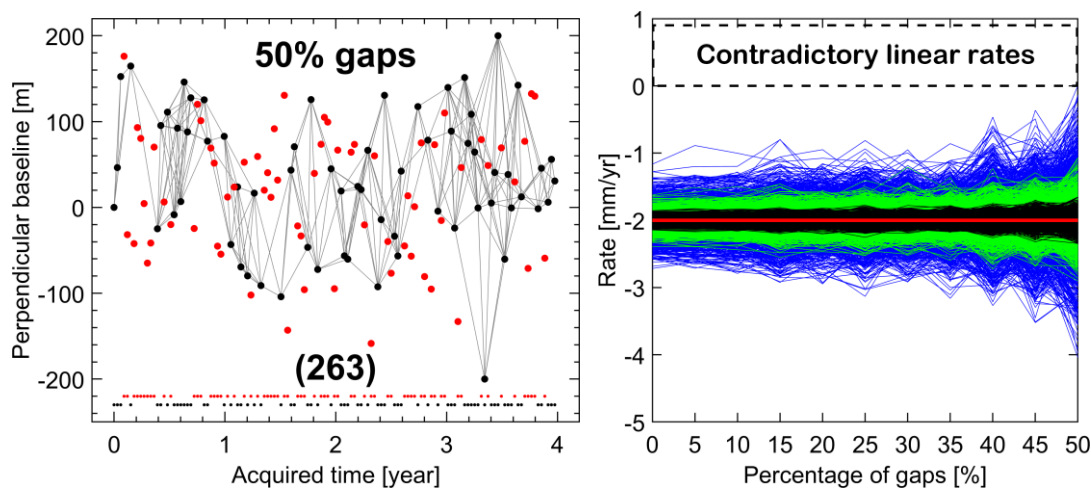


**Figure 5.10.** (left) A network of 50% random data gaps formed by the temporal baseline threshold of 99 days, (right) unweighted least squares rates computed from linear plus annual signals between the interferogram network of no gaps and those with randomly chosen gaps of various percentages, of which the results of the 50% gaps case are from the network in the left panel.

The influence of random data gaps on the errors in rate determination and the RMS of the difference between simulated and SBAS-derived deformation time series is caused by a reduction in the number of interferograms when the percentage of gaps increases. However, a reduction in interferograms in the SBAS network can be caused by random data gaps (Figure 5.8 and Figure 5.9) or by changing the temporal baseline thresholds (as shown in Section 5.3). Errors resulting from fewer interferograms in an SBAS network due to (1) random gaps and (2) temporal baseline thresholds are compared from Figure 5.11 to Figure 5.13 (cf. blue and green polylines). This demonstrates the role of the network configuration, where a network may have the same number of interferograms but will have larger errors depending upon which interferograms are selected. The networks used will be studied further in Chapter 6.

The random gap scenario results in more redundant interferograms, making the network more robust, especially in the case of noisier time series (bottom plots in Figure 5.11 to Figure 5.13). Therefore, in this case of randomly selected data gaps, mixed interferograms covering both short and long time spans make the network more robust in recovering the deformation signal compared to the case of no gaps in which only short-time interferograms are chosen, which are limited by the temporal baseline threshold.

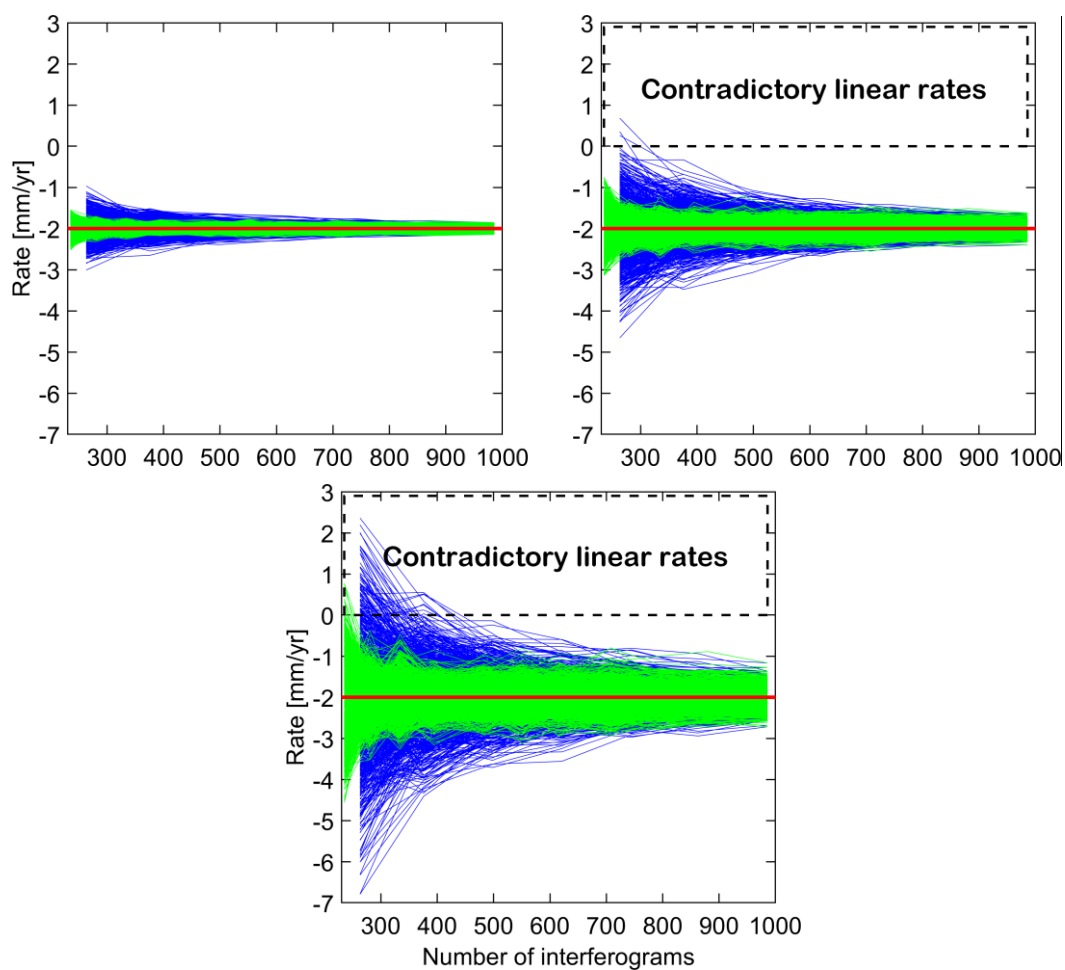


**Figure 5.11.** The influence of the change in number of interferograms chosen by various temporal baseline thresholds (blue) and due to random data gaps (green) on SBAS-derived unweighted least squares rates from simulated signal cases 1 (Table 5.1). The interferograms are contaminated by residual interferogram noise cases A (top-left), B (top-right) and C (bottom) as shown in Table 5.2. Black dashed boxes are used to contrast between positive and negative rates that indicate contradictory trends.

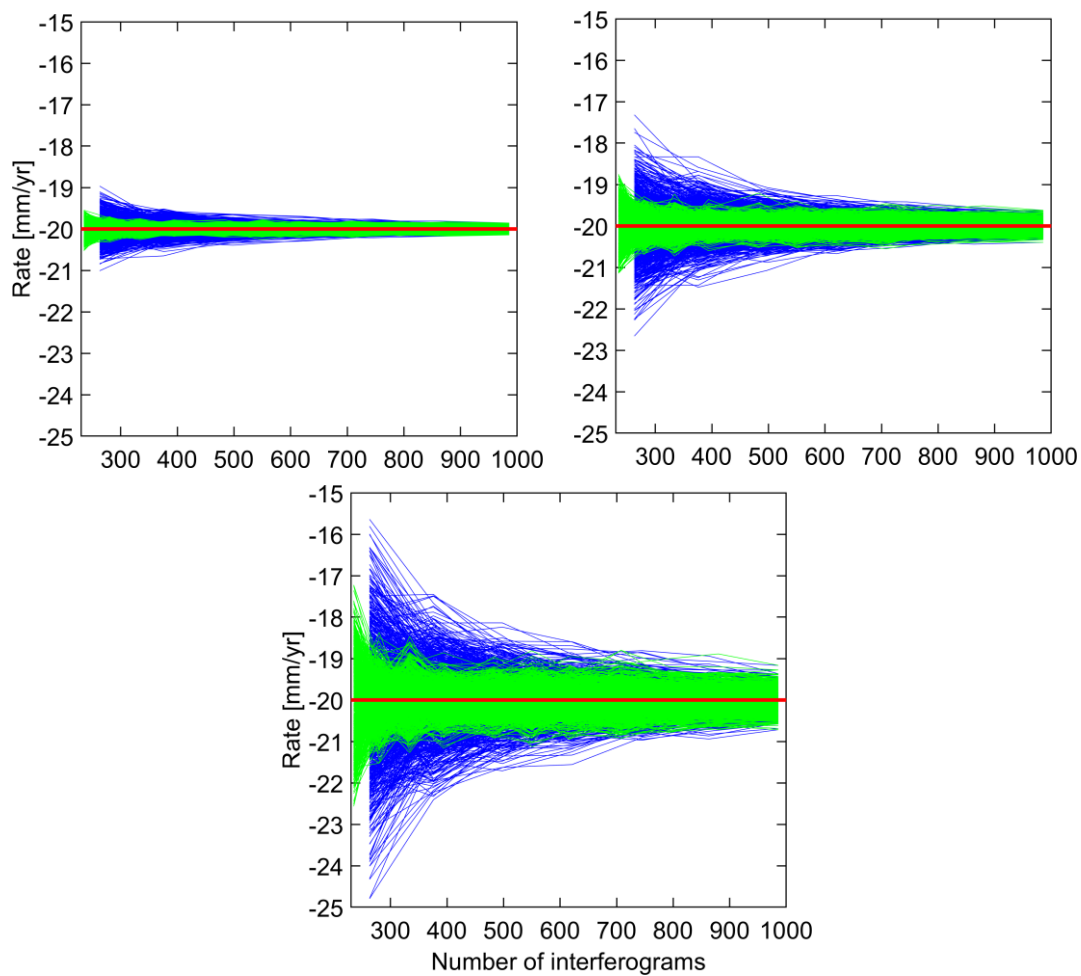
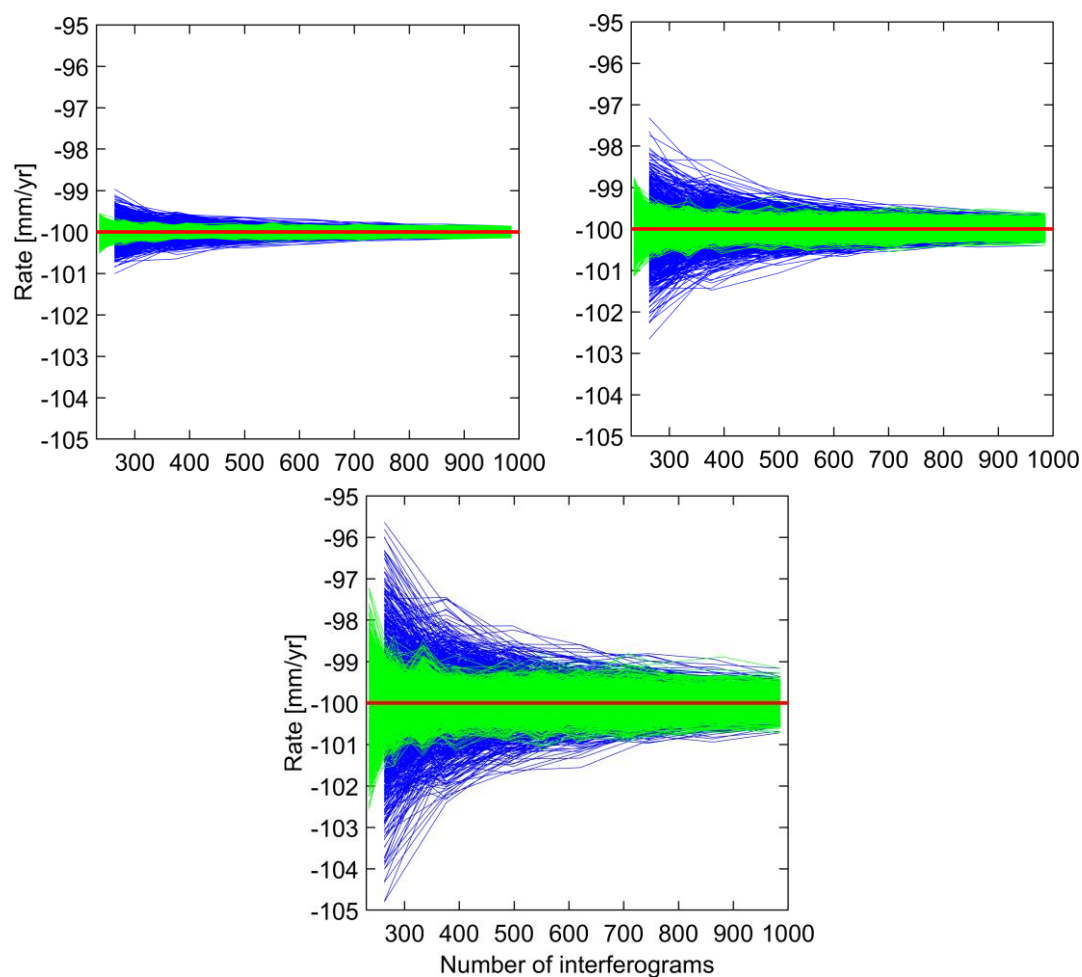


Figure 5.12. The influence of the change in number of interferograms chosen by various temporal baseline thresholds (blue) and due to random data gaps (green) on SBAS-derived unweighted least squares rates from simulated signal cases 2 (Table 5.1). The interferograms are contaminated by residual interferogram noise cases A (top-left), B (top-right) and C (bottom) as shown in Table 5.2.



**Figure 5.13.** The influence of the change in number of interferograms chosen by various temporal baseline thresholds (blue) and due to random data gaps (green) on SBAS-derived unweighted least squares rates from simulated signal cases 3 (Table 5.1). The interferograms are contaminated by residual interferogram noise cases A (top-left), B (top-right) and C (bottom) as shown in Table 5.2.

#### 5.4.2 “Winter” Data Gaps

The test on data gaps in Subsection 5.4.1 is based on SAR data that are missing sometimes due to technical and/or scheduling issues, which are considered random. There is an alternative situation where there may be “user-defined” data gaps in which data missing is due to, e.g., very low coherence caused, for instance, by snow cover. This situation is termed as “winter data gaps” where all images acquired in the winter season (December to February for the Northern Hemisphere are assumed) are removed (Figure 5.14). To avoid disconnection in the SBAS network, a network of 1340 interferograms is applied, which is formed by applying a temporal baseline threshold of 121 days (approximately four months), instead of approximately three months as in Subsection 5.4.1, and a perpendicular baseline threshold of 200 m. These networks of

no gaps, random gaps and winter gaps are shown in [Figure 5.14](#) with their summary listed in [Table 5.5](#).

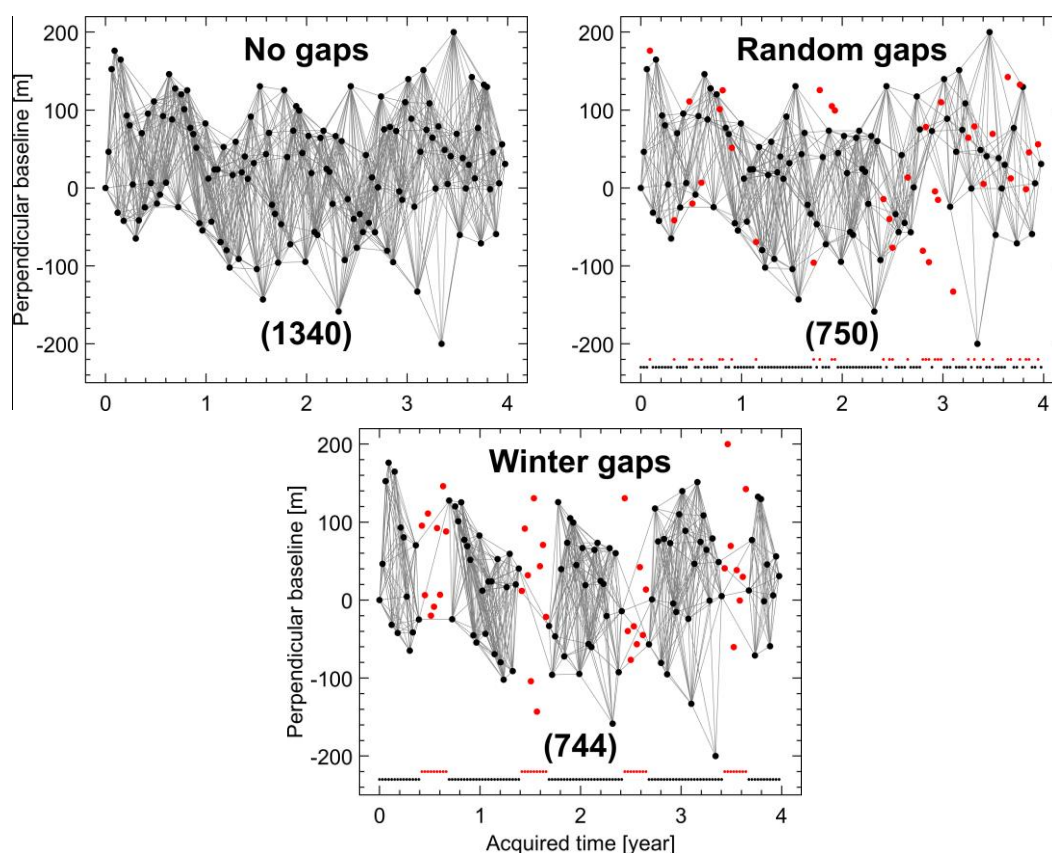


[Figure 5.14](#). Interferogram networks without (top-left) and with (top-right, bottom) missing images. The number of missing images is 34 out of 133 corresponding to about 25%, which are selected randomly (top-right) and in the northern winter season (bottom). The networks are formed using a temporal baseline threshold of four months and a perpendicular baseline threshold of 200 m. Grey lines indicate interferograms, with images denoted by black dots. Red dots indicate missing images (i.e., gaps). The bracketed bold number under each network refers to the number of interferograms.

[Table 5.5](#). Number of removed and remaining images and interferograms corresponding to random and winter gaps cases.

No	Gaps type	Number of removed images	Number of remaining images	Number of Removed interferograms	Number of remaining interferograms
1	No gaps	0	133	0	1,340
2	Random	34	99	590	750
3	Winter	34	99	596	744

The results of this simulation experiment are shown in [Figure 5.15](#). Unweighted LS rates and RMSs of the difference between simulated and SBAS-derived deformation time series are computed for networks with no gaps, random data gaps and winter data gaps, with the latter two having the same number of images (see [Figure 5.14](#) and [Table 5.5](#)). [Figure 5.15](#) compares unweighted LS rates for each network with RMSs between simulated and SBAS-derived deformation time series shown in [Figure 5.16](#). [Figure 5.14](#) shows the number of missing images, which is the same between the two cases of data gaps (34 out of 133) and, though the missing images are selected differently, the number of interferograms linking the remaining images are nearly the same; 750 for random gaps and 744 winter gaps (see [Figure 5.14](#) and [Table 5.5](#)). However, the influence of these two different data gap cases is distinct with the winter gaps having a larger influence, as confirmed by both retrieved rates in [Figure 5.15](#) and RMSs in [Figure 5.16](#).

This is caused by the strength of the network configuration, which is more robust with interferograms at regular intervals in the random gaps network but with “blocks” of gaps in the “winter” case, leading to a less robust network (cf. [Figure 5.14](#) (top-right) and (bottom)). This alerts users that, in addition to the effect of fewer interferograms and gap percentages, the strength of network configuration is another factor influencing the SBAS results, in which one should try to design an SBAS network that does not contain long gaps in the time series. The design of an SBAS network will be studied further in [Chapter 6](#).

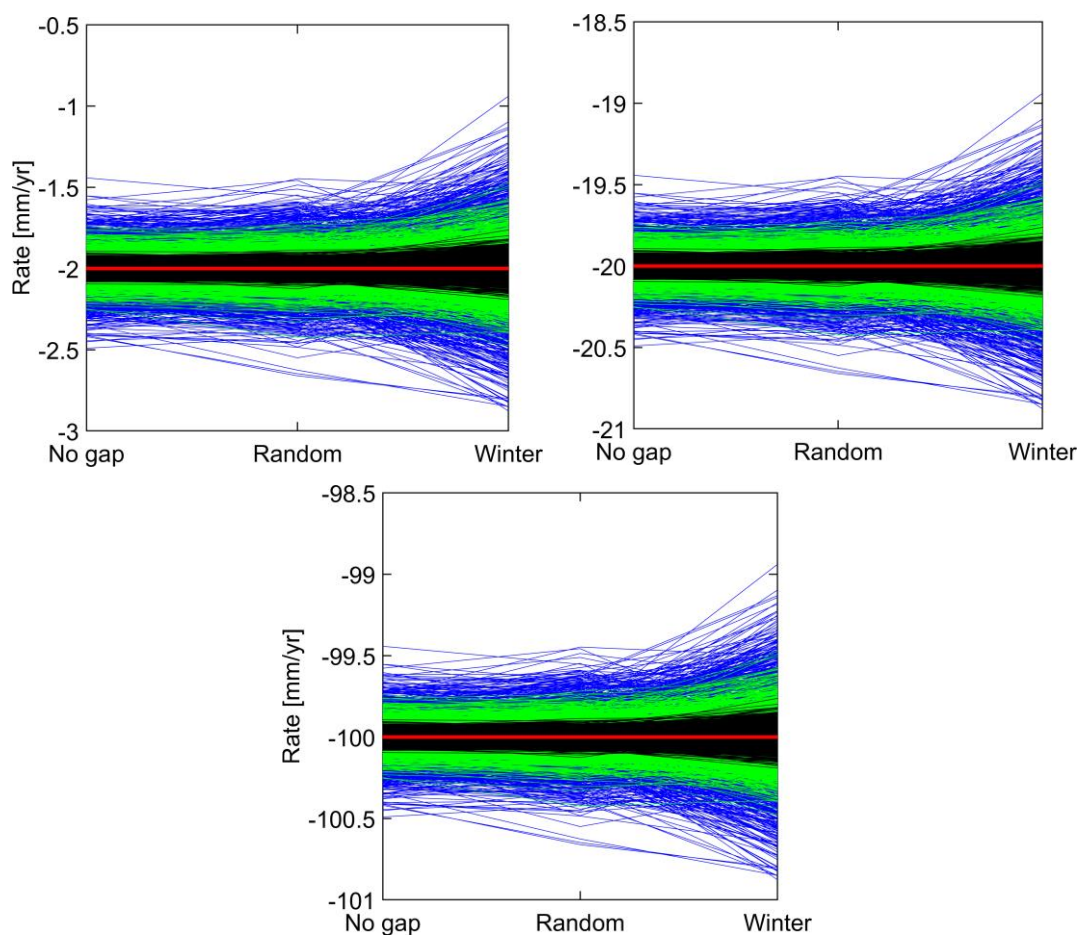


**Figure 5.15.** Comparison of unweighted least squares rates computed from linear plus annual signals according to interferogram networks with no gaps, random gaps and “winter” gaps. The networks adopt a temporal baseline threshold of four months and a perpendicular baseline threshold of 200 m. The results correspond to simulated signal cases 1 (top-left), 2 (top-right) and 3 (bottom) as shown in [Table 5.1](#). Black, green and blue polylines indicate the results computed from simulated data with noise cases A, B, and C ([Table 5.2](#)). Red horizontal lines represent the simulated rate.

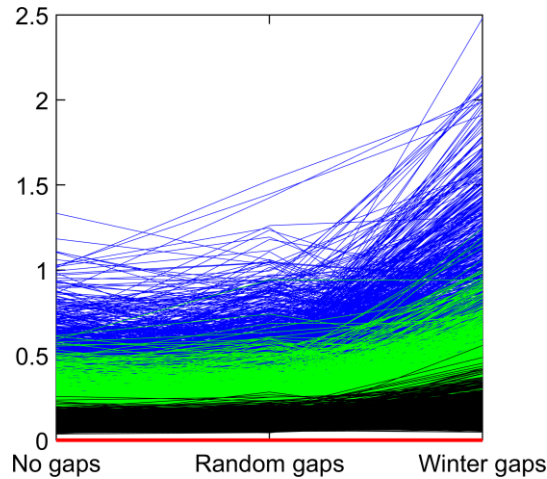


**Figure 5.16.** Comparison of RMSs of the difference between simulated and SBAS-derived deformation time series for all pixels between the interferogram networks of no gaps and those with randomly chosen gaps and “winter” gaps corresponding to  $\sim 25\%$  missing images. Black, green and blue polylines indicate the results computed from simulated data with noise cases A, B and C (Table 5.2).

## 5.5 Comparison With Other Network Types

In this Section, a comparison between results from SBAS networks selected by temporal baseline thresholds (SBAS networks hereinafter) with those from Delaunay triangulations, hierarchical thresholds networks, and a minimum spanning tree shown in Subsection 4.2.2 is conducted.

### 5.5.1 Interferogram Network Formation

A Delaunay triangulation network of 384 interferograms is selected first from 133 images. Temporal baseline thresholds shown in Table 5.6 are then used to filter interferograms. As a result, a total of 32 networks are formed among which the first six networks are disconnected (see Table 5.6). A study on disconnected interferogram networks is beyond the scope of this dissertation, and thus, the remaining 26 connected interferogram networks are employed. The last network in Table 5.6 corresponds to the full Delaunay network, i.e., the Delaunay network without applying baseline thresholds. Some of these networks are shown in Figure 5.17 as examples.

**Table 5.6.** List of Delaunay networks based on various temporal baseline thresholds. The perpendicular baseline threshold is set fixed at 200 m (Figure 5.17). Underline and bold numbers indicate disconnected networks and the full network, respectively.

Temporal baseline threshold [days]	Number of interferograms	Temporal baseline threshold [days]	Number of interferograms
<u>22</u>	<u>76</u>	198	354
<u>33</u>	<u>104</u>	209	358
<u>44</u>	<u>139</u>	220	362
<u>55</u>	<u>172</u>	231	366
<u>66</u>	<u>200</u>	242	369
<u>77</u>	<u>226</u>	264	372
88	251	275	373
99	270	286	374
110	290	330	376
121	301	341	377
132	308	374	379
143	319	462	380
154	329	528	381
165	335	649	382
176	341	704	383
187	345	<b>1243</b>	<b>384</b>

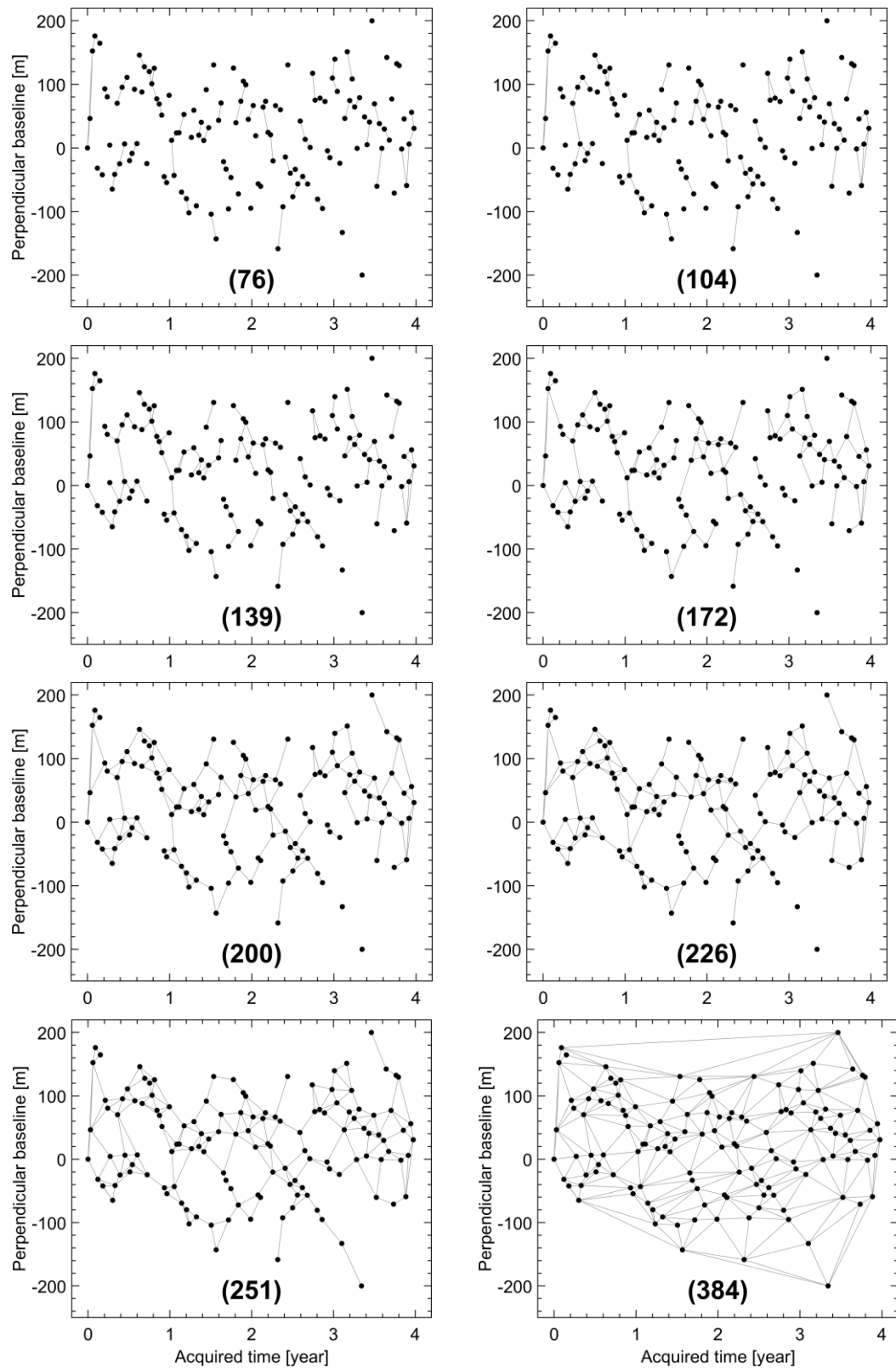


**Figure 5.17.** Examples of disconnected, connected, and full Delaunay interferogram networks chosen based on different temporal baseline thresholds in [Table 5.6](#). The bracketed bold number under each network indicates the number of interferograms.

The hierarchical thresholds approach is applied to select interferograms relying on different combinations of temporal and perpendicular baseline thresholds shown in [Table 5.7](#) with corresponding networks shown in [Figure 5.18](#).

[Table 5.7](#). List of hierarchical thresholds networks based on various combinations of temporal and perpendicular baseline thresholds.

Temporal/perpendicular baseline threshold [days/metres]	Number of interferograms
[22/200]	245
[22/200], [33/180]	367
[22/200], [33/180], [44/160]	474
[22/200], [33/180], [44/160], [55/140]	582
[22/200], [33/180], [44/160], [55/140], [66/120]	675

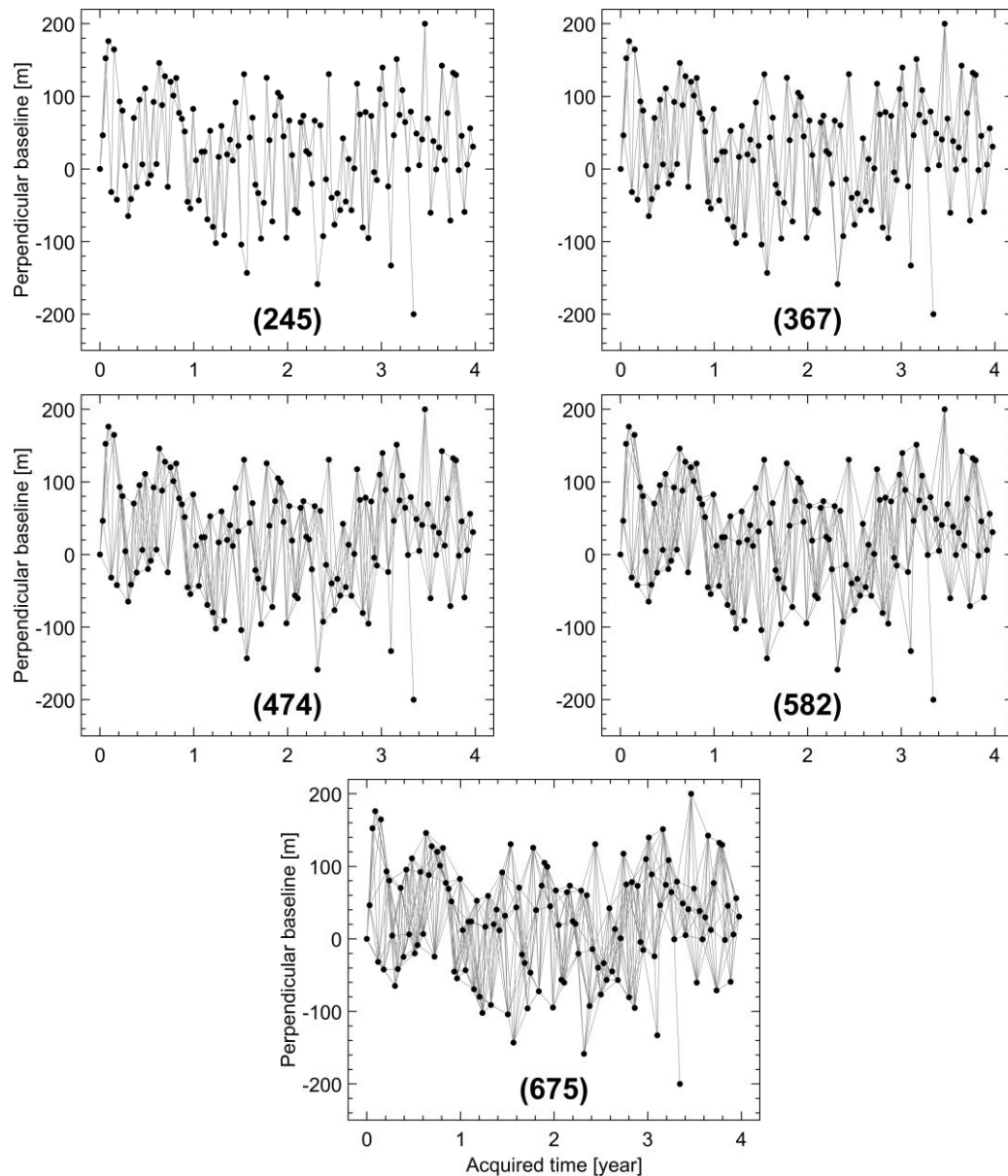


**Figure 5.18.** Hierarchical thresholds interferogram networks formed by multiple pairs of temporal and perpendicular baseline thresholds listed in [Table 5.7](#). The bracketed bold number under each network indicates the number of interferograms.

Finally, a minimum spanning tree network is formed by weights of normalised baseline lengths computed by Equations (5.3) and (5.4). The interferograms are selected so that the sum of their edges' weights, i.e., interferogram normalised baseline lengths, is minimum. As a result, a network of 132 interferograms is generated from 133 images, which is shown in [Figure 5.19](#).

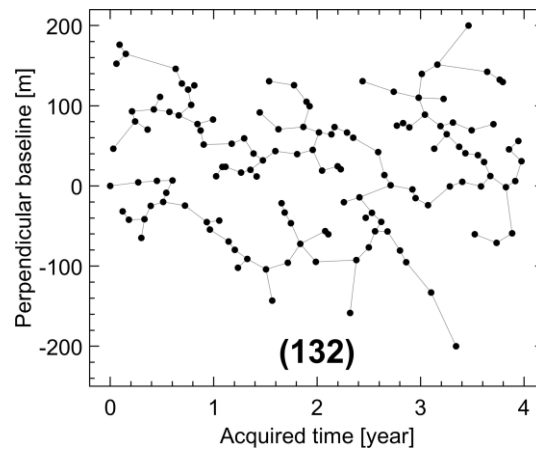


**Figure 5.19.** A minimum spanning tree interferogram network selected by the weights of normalised baseline lengths. The bracketed bold number under each network indicates the number of interferograms.

### 5.5.2 Results of Comparison

**Figure 5.20** compares linear-fit rates between SBAS interferogram networks and those from Delaunay triangulations, hierarchical thresholds networks, and a minimum spanning tree in the case of simulated linear signals of  $-2$  mm/year,  $-20$  mm/yr, and  $-100$  mm/yr. This is compared relying on the number of interferograms that are selected. The results are relatively identical between SBAS networks and hierarchical thresholds networks (cyan elements in **Figure 5.20**). However, a minimum spanning tree (magenta elements in **Figure 5.20**) and Delaunay triangulations (orange elements in **Figure 5.20**) show good results of estimated linear-fit rates even with a small number of interferograms, particularly the minimum spanning tree network of 132 interferograms. This is because it is assumed in this simulation that smaller normalised baselines are of smaller interferometric noise, and thus they have been assigned with smaller noise.

The minimum spanning tree network applied in this dissertation works by choosing interferograms of the smallest baseline lengths. Therefore, all selected interferograms have the smallest noise. Though the minimum spanning tree results are promising, it has a limitation that its network of independent interferograms cannot be used to detect unwrapping errors based on the sum of interferogram loops as described in Subsection 4.3.3 (Biggs et al., 2007; Parker et al., 2017).

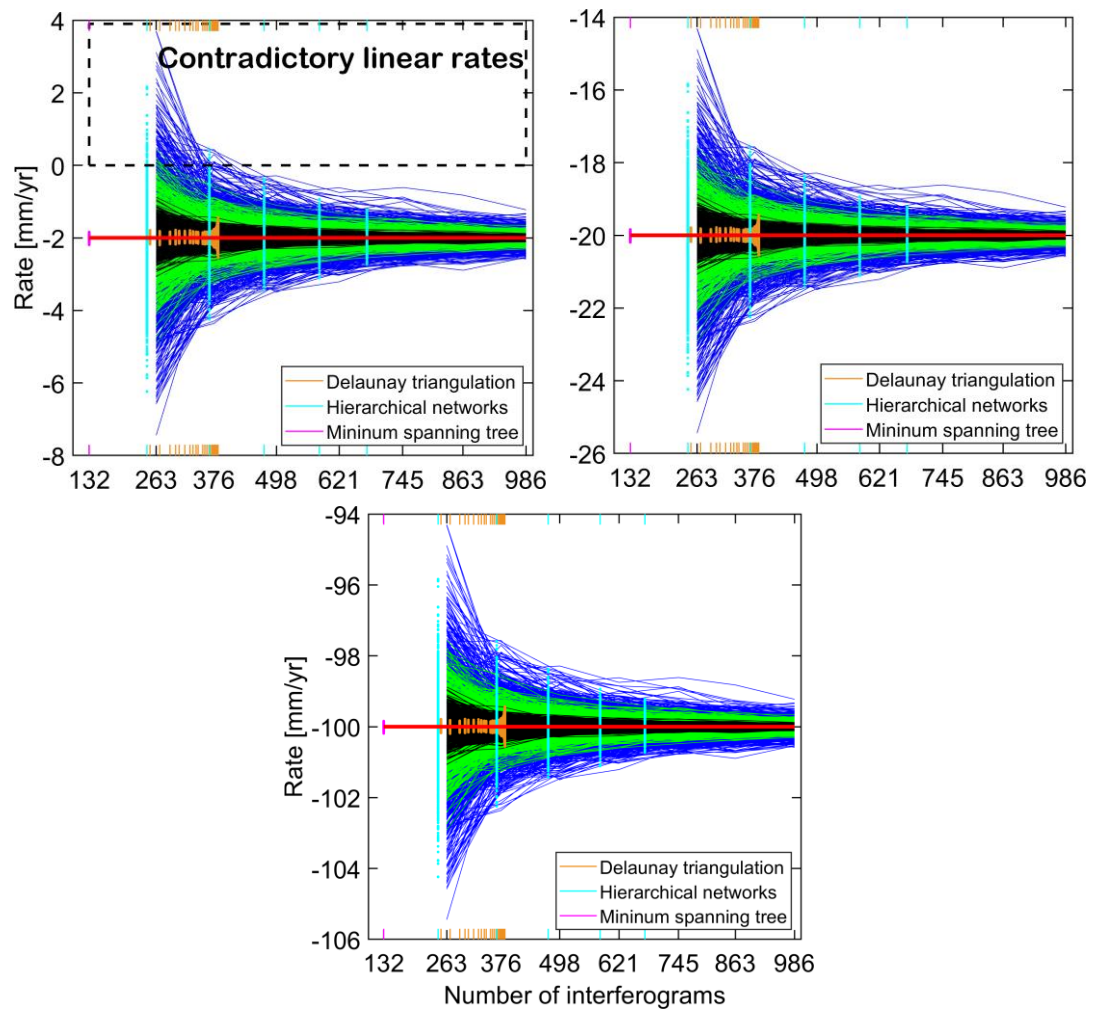


**Figure 5.20.** Comparison of unweighted linear-fit rates between SBAS networks, Delaunay triangulations, hierarchical thresholds networks, and a minimum spanning tree in the cases of simulated linear signals of  $-2$  mm/yr (top-left),  $-20$  mm/year (top-right), and  $-100$  mm/yr (bottom).

Similar promising results of estimated linear-fit rates can be found from Delaunay triangulations as shown in [Figure 5.20](#) (orange elements) for the same reason as that of the minimum spanning tree network, i.e., interferograms with small noise have been selected to form the networks. [Figure 5.21](#) compares SBAS networks and Delaunay triangulations in the estimated linear-fit rates and the number of selected interferograms applying the same temporal baseline thresholds. This indicates the advantage of the Delaunay triangulations with thresholds approach that with the same thresholds as those used in the SBAS approach, fewer interferograms are chosen but similar or even better estimated linear-fit rates are derived. However, a disadvantage of Delaunay triangulations is that disconnected networks will be formed if small temporal baseline thresholds are applied, which is 77 days or less in this study (see [Table 5.6](#) and [Figure 5.21](#), bottom).

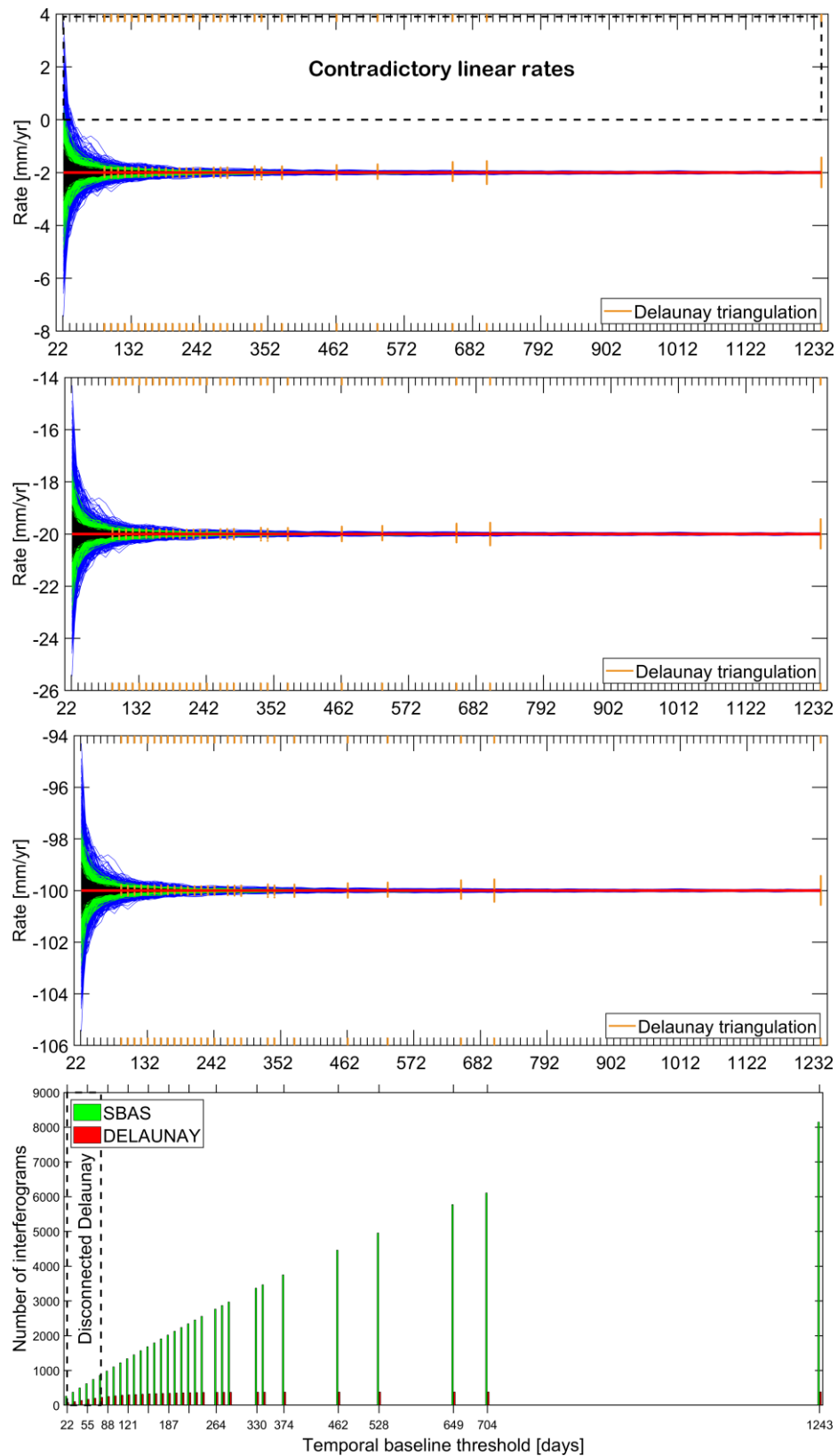


**Figure 5.21.** Comparison between SBAS networks and Delaunay triangulations in estimated linear-fit rates and the number of selected interferograms applying the same temporal baseline thresholds. The simulated linear rate of  $-2$  mm/yr (top panel),  $-20$  mm/yr (second panel), and  $-100$  mm/yr (third panel) are shown in [Table 5.1](#).

The same networks of SBAS, Delaunay triangulations, hierarchical thresholds and a minimum spanning tree are applied to the nonlinear simulated signals of which the results are compared in [Figure 5.22](#). It is shown that the non-linearity in the simulated signal affects all types of networks in that biases in rate errors are existent if unweighted linear-fit rates are computed, particularly the case of strong non-linearity (cf. left panels in [Figure 5.22](#)). However, the biases are removed if LS is applied with the appropriate functional model, i.e., linear plus annual in this dissertation (cf. left and right panels in [Figure 5.22](#)). Again, this is attributable to the SBAS method in which the results computed depend on the configuration of the network and residual interferogram noise but not the deformation rate. In addition, the error in rate determination is dependent on the suitability of the functional model that is used for rate estimation.

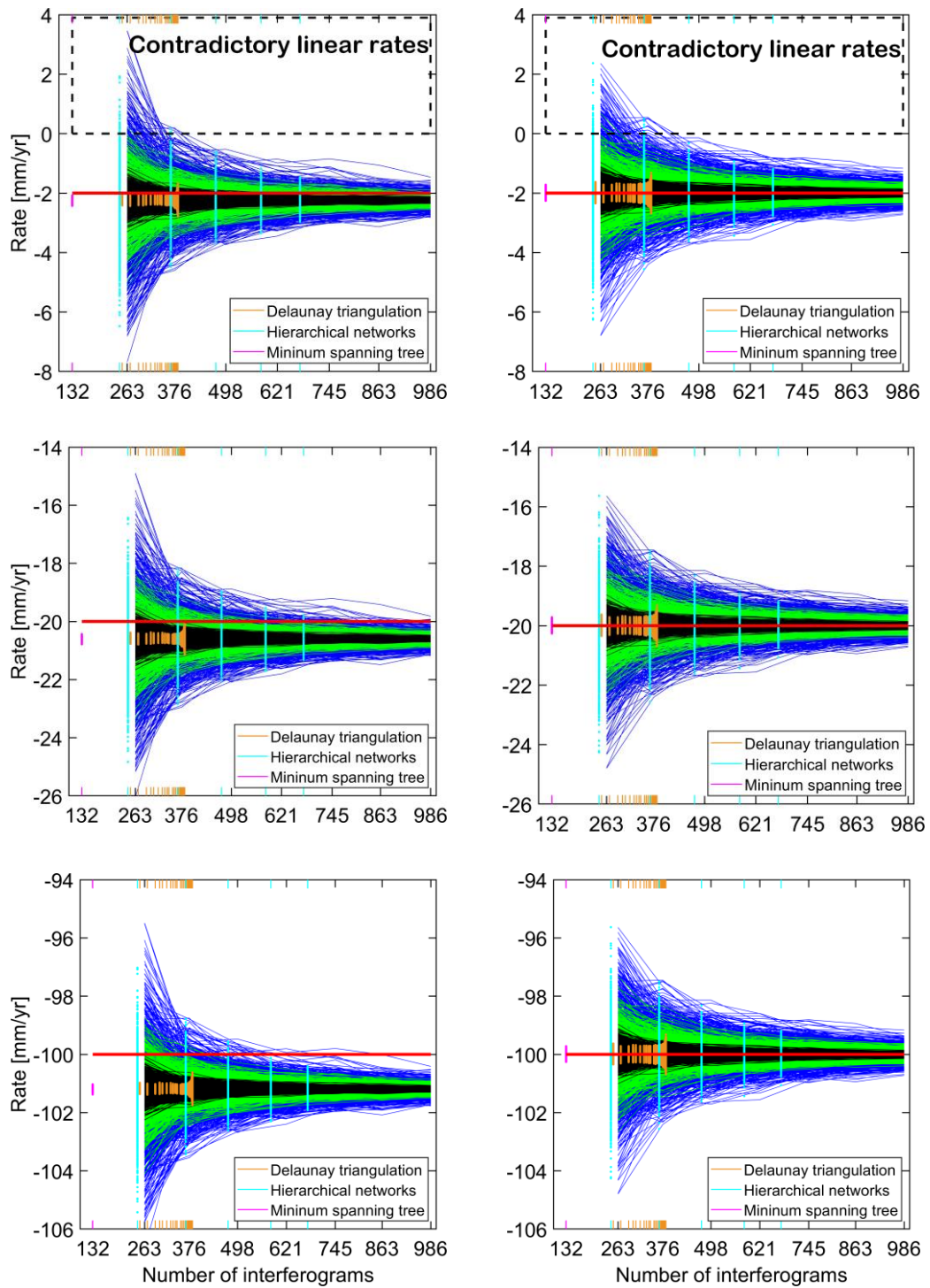


**Figure 5.22.** Comparison of unweighted linear-fit rates and unweighted least squares rates from linear plus annual signals between four types of interferogram networks of SBAS, Delaunay triangulations, hierarchical thresholds, and a minimum spanning tree. The simulated signal cases 1 (top), 2 (middle), and 3 (bottom) shown in [Table 5.1](#) are contaminated by simulated residual interferogram noise.

## 5.6 Chapter Summary

This Chapter has used simulated Gaussian noise with zero mean applied to interferograms computed from simulated linear trends and annual sinusoids to demonstrate the effects of residual interferometric noise on InSAR-SBAS-derived deformation. This extends to how different SBAS network configurations may influence the estimated deformation rates. Different simulated rates are tested, including the addition of annual periodic amplitudes so as to represent a range of real SAR data (Table 5.1). A Monte Carlo simulation with 1000 pixels for each scenario was adopted.

Firstly, only a linear deformation signal was investigated, finding that the SBAS linear-fit deformation trends were sensitive to both the magnitude of interferometric noise and signal size. The unweighted linear-fit rate error was the same in both magnitude and size for all rates if the same residual noise is applied to a given network. However, the trend may become contradictory for small-magnitude deformation where, for example, a  $-2$  mm/yr rate could be estimated from the SBAS LS or SVD method as a spurious uplift. This contradictory result was shown when small temporal thresholds of 33 days or fewer were used, which resulted in a less robust SBAS network configuration with fewer interferograms.

When the linear plus annual periodic signal with interferometric noise was tested, the linear-only-fit rates were biased (from the 1000 pixels) compared to the simulated rate. Alternatively, when the rates are estimated using a more suitable linear and periodic functional model, rather than just linear regression in the presence of non-linear terms, the estimated linear rates were not biased. This demonstrates the potential for errors to be introduced by using simple linear regression when non-linear deformation may also be occurring.

Because one of the strengths of the SBAS method is to provide redundant small interferogram baselines (in space and time), the effect of missing SAR acquisitions in the time series was tested. It is presumed that these gaps in the time series would be (1) random that may be due to satellite mission scheduling issues, or (2) blocks of missing interferograms over, for example, a northern winter with snow covered ground that causes decorrelation. The simulation results indicate that “winter gaps” causes a larger error in the estimated rates and in the RMSs of the differences between simulated and SBAS-derived deformation time series than for random gaps resulting from missed acquisitions.

However, the RMS for both random gaps and no gaps were mostly 1 mm, while the winter gaps RMS was generally  $<2$  mm, suggesting that random gaps have lesser influence. This is highlighted when random gaps are compared to temporal threshold limits, showing that for the same number of interferograms, limiting temporal thresholds can cause errors of up to 6 mm/yr with noisy simulated data, compared to  $\sim 3$  mm/yr for random gaps when using similar interferogram numbers. This suggests that it is the configuration of the SBAS network that is more important than the number of interferograms selected based on baseline thresholds, to the point that caution should be exercised when reducing the temporal baseline to increase the coherence of the interferograms. This is because the trade-off may be a geometrically weak SBAS network that is vulnerable to incorrect rate estimation in the presence of noisy data and non-linear deformation.

In a comparison between SBAS networks selected by temporal and perpendicular baseline thresholds and other types of interferogram networks, it was shown that whilst linear-fit rates from SBAS networks and hierarchical thresholds networks are identical, the results from Delaunay triangulations and a minimum spanning tree are better. This is because it is assumed in this dissertation that interferograms with smaller baseline lengths are of smaller noise, and thus the Delaunay triangulation and minimum spanning tree networks incorporate interferograms with the smallest simulated noise. However, these two types of networks have their limitations. The minimum spanning tree network involves independent interferograms only, and thus it is impossible to detect unwrapping errors via computing the sum of the interferogram loop. The Delaunay triangulation networks will become disconnected if small baseline thresholds are employed.

Finally, like the SBAS networks, the networks of Delaunay triangulation, hierarchical thresholds and a minimum spanning tree are all affected by the nonlinearity of deformation signal that biases in rate errors are existent if the linear-fit rates are estimated. However, these biases will be removed if LS is applied with the appropriate functional model.

## 6. GEODESY-BASED DESIGN OF SBAS INTERFEROGRAM NETWORKS

In this Chapter, the theory of optimal design of geodetic networks is described in terms of both mathematical models and their classification. The results here were published in shorter form in [Bui et al. \(2020\)](#). The same simulated InSAR datasets as those used in Chapter 5 are now tested with SBAS networks formed by different temporal and perpendicular baseline thresholds for which redundancy numbers are computed. The changes in the redundancy numbers and RMSs of the difference between simulated and SBAS-derived deformation time series are compared, where the range of the redundancy numbers between  $\sim 0.8$  and  $\sim 0.9$  are suggested to be used as an optimal design for InSAR SBAS networks.

### 6.1 Background on Design of Geodetic Networks

Geodetic surveying network “optimisation” aims at finding a geometric configuration and a set of observations of sufficient precision to satisfy some desired positional quality criteria with lower financial and logistical costs ([Kuang, 1993](#)). This aids surveyors in avoiding unnecessary observations, and thus may lead to saving considerable time and effort in the field ([Kuang, 1993](#)). In optimisation of a geodetic network, one seeks to minimise or maximise an objective function that represents a criterion defining the quality of the network. These criteria consist of precision, reliability and economy or price-cost of the network ([Schmitt, 1985a](#)). By minimising or maximising a single objective function or multiple objective functions, the optimised network should satisfy the prior criteria in a way that: (i) the postulated precision of the network measurements can be realised, (ii) it is sensitive to, e.g., detect outliers existent in the measurements, or to detect the movement of Earth or man-made structures in deformation monitoring applications, and (iii) the marking of the network points and the observations can be carried out in satisfying some price-cost criteria ([Schmitt, 1985a](#)).

The optimisation problem is traditionally divided into the zero-, first-, second- and third-order problems ([Grafarend & Sansò, 1985](#)). The zero-order design (ZOD) can be found in, e.g., [Teunissen \(1985b\)](#), which is adopted for designing an optimal reference system and is also called “datum problem”. In the first-order design (FOD), an optimal network configuration is adopted by choosing the best locations of ground

points in a geodetic network. This can be done by applying some small changes in the positions of the network points that in turn relates to the changes in the design matrix  $\mathbf{A}$  (Berné & Baselga, 2004; Koch, 1985).

The objective of second-order design (SOD) is to select optimal weights for the observations. Schmitt (1985a) showed that three approaches can be utilised for dealing with this problem, including (i) direct approximation of the criterion matrix, (ii) iterative approximation of the criterion matrix, and (iii) direct approximation of the inverse criterion matrix. By applying this approach, one seeks to obtain an optimum network in high precision sense (Amiri-Simkooei, 2004). In the third-order design (TOD), an existing network is improved, extended or densified in an optimal way by introducing new points and/or additional measurements (Schmitt, 1985b). This is also called densification problem and can be understood to be a mixed FOD and SOD. A combined design problem introduced by Vaníček and Krakiwsky (1986) is referred to the case where FOD and SOD problems are solved simultaneously.

The quality of a geodetic network under optimisation is defined by criteria that are represented by an objective function. These criteria include precision, reliability and economy or price-cost. The observational precision and network geometry are two crucial factors influencing the precision of a network. The variance-covariance (VCV) matrix is normally adopted to represent the network's precision. With the assumption of a minimum constraint, the VCV matrix is expressed as (Kuang, 1996):

$$\mathbf{C}_x = \sigma_0^2 \left[ (\mathbf{A}^T \mathbf{P} \mathbf{A} + \mathbf{D} \mathbf{D}^T)^{-1} - \mathbf{H} (\mathbf{H}^T \mathbf{D} \mathbf{D}^T \mathbf{H})^{-1} \mathbf{H}^T \right] \quad (6.1)$$

where  $\sigma_0^2$  is the a priori variance factor,  $\mathbf{A}$  and  $\mathbf{P}$  are the design and weight matrices of observations,  $\mathbf{D}$  and  $\mathbf{H}$  are the minimum and inner constraint datum information matrices, respectively.

The reliability of geodetic networks, as defined classically by Baarda (1968), is the ability of a network to detect and resist against gross errors in a series of observations. It is further divided into internal and external reliability as follows.

1) The internal reliability is defined as the ability of a network to detect gross errors, referring to the lower bounds of detectable gross errors (aka. the minimal detectable bias, MDB) that is expressed as (e.g., Baarda, 1968):

$$\nabla_0 l_i = \frac{\delta_0 \sigma_{l_i}}{\sqrt{r_i}} \quad (6.2)$$

where  $\delta_0$  is the lower bound for the non-centrality parameter,  $\sigma_{l_i}$  and  $r_i$  are the standard deviation and the redundancy or  $r$ -number of the  $i^{th}$  observation, respectively. The  $r$ -numbers of the observations are the diagonal elements of the matrix  $\mathbf{R}$  that are: (Amiri-Simkooei et al., 2012):

$$\mathbf{R} = \mathbf{I} - \mathbf{A}(\mathbf{A}^T \mathbf{P} \mathbf{A})^{-1} \mathbf{A}^T \mathbf{P} \quad (6.3)$$

where  $\mathbf{I}$  is the identity matrix,  $\mathbf{A}$  is the design matrix, and  $\mathbf{P}$  is the weight matrix of the observations.

2) The external reliability refers to the maximum effect of an undetectable gross error ( $\nabla_0 l_i$ ) on the estimates of unknown parameters as:

$$\nabla_{0,i} \hat{\mathbf{x}} = (\mathbf{A}^T \mathbf{P} \mathbf{A})^{-1} \mathbf{A}^T \mathbf{P} \nabla_{0,i} l \quad (6.4)$$

The internal reliability criterion is generally used as the measure for an “optimal” design of geodetic networks aiming at high reliability (Amiri-Simkooei, 2001a), as shown in Equation (6.3). In addition to the reliability criterion, there is an alternative criterion named the geometrical strength that is implemented in the robustness analysis technique via rotation, shear and scale (Amiri-Simkooei, 2001a, 2001b; Vaníček et al., 2001; Vaníček et al., 1991). These two criteria, i.e., the reliability and the geometrical strength, have been claimed to be strongly correlated (Amiri-Simkooei, 2004).

The third criterion in optimisation is the price-cost of a project that is minimised depending on the type of the project including the type of measurements, e.g., GNSS, levelling, transportation, the number of observations that is required, and so on. In general, the higher the accuracy and the better the reliability of a network, the more expensive it will be (Schmitt, 1985a). It is practically unfeasible to look forward to a solution providing the highest precision and reliability with the lowest price-cost. Therefore, the problem of optimisation can be understood as the problem of designing a network that is precise and reliable enough and can be realised in an effective way in an economic sense (Teunissen, 1985a).

Depending on the approach of using solely one objective function, two objective functions or more, we have a Single-Objective Optimisation Model (SOOM), a Bi-Objective Optimisation Model (BOOM) or a Multi-Objective Optimisation Model (MOOM), respectively (e.g., Bagherbandi et al., 2009; Eshagh & Alizadeh-Khameneh, 2015; Eshagh & Kiamehr, 2007; Xu, 1989, 1990; Xu & Grafarend, 1995).

Two strategies frequently utilised for optimal design problems include the computer simulation method and analytical method of which the latter method is

subsequently divided into linear and non-linear programming (Cross, 1985). In the computer simulation, a solution to the design problem is postulated and the design and price-cost criteria are computed. Should either of these criteria not be fulfilled, a new solution is postulated by slightly altering the original postulate and the criteria are recomputed. The procedure is repeated until a “satisfactory” network is found. In the analytical method, specific algorithms for a particular design problem are offered. The algorithm will automatically produce a network that will satisfy the quality requirements and that will be optimum in some mathematical sense.

In InSAR SBAS data processing, the objective is to find an “optimal” network of interferograms to be generated and then used in time series analysis. This allows one to keep the network as small as possible in terms of the number of interferograms that results in minimising data processing time, i.e., computational costs and disk storage requirements. In this Chapter, the redundancy number ( $r$ -number) is examined as a diagnostic metric to determine the likely effectiveness of the SBAS network design and verify this with simulation experiments. Specifically, for a given SBAS network with a corresponding design matrix  $\mathbf{A}$ , the  $r$ -number is computed using Equation (6.3) with the weights  $\mathbf{P}$  of interferograms computed as the inverse of normalised (perpendicular and temporal) baseline lengths, which has been described in Section 5.1 of Chapter 5.

## 6.2 A Review of Design of Geodetic Networks

This Section aims at reviewing previous studies on optimal design of geodetic networks. As has been described in Section 6.1, the problem of optimal design of geodetic networks can principally be classified into different categories based on the objective function used, including the precision, the reliability and the cost; their orders involving the zero-, first-, second-, and third-order optimisation; the mathematical models used in programming including linear and quadratic programming. In addition, other ways can be adopted for classifying these problems including that based on the method of simulation, which consists of computer simulation and analytical simulation, and the one based on the number of objective functions that are implemented, such as SOOM, BOOM, and MOOM. In this Section, previous studies on the optimal design of geodetic networks in the literature are summarised based upon different classes of objective function. These studies are listed in Table 6.1.

Table 6.1. A number of studies on the optimal design of networks from the geodetic literature

References	Type of network	Design order	Criteria	Method
	Levelling	First	Precision	Analytical
	Simulated quadrilateral	Second	Precision	Analytical
	2D network	Second	Precision	Analytical
Amiri-Simkooei et al. (2012)	Open traverse	Zero	Precision	Analytical
	Intersection	First	Precision	Analytical
	GNSS	First	Precision	Analytical
Berné and Baselga (2004)	GNSS	First	Precision	Computer simulation
Alizadeh-Khameneh et al. (2016)	GNSS	Second	Precision	Analytical
Amiri-Simkooei (2001a)	Trilateration	First, Second	Reliability	Analytical
Amiri-Simkooei (2001b)	2D network	First, Second	Reliability	Analytical
Amiri-Simkooei (2004)	Quadrilateral	Second	Reliability	Analytical
	Trilateration	Second	Reliability	Analytical
Xu (1989)	Levelling	Second	Bi-objective	Analytical
Xu and Grafarend (1995)	3D network	Second	Multi-objective	Analytical
Alizadeh-Khameneh et al. (2015)	GNSS	Second	Single-objective	Analytical
	GNSS	Second	Bi-objective	Analytical
	GNSS	Second	Multi-objective	Analytical
Eshagh and Alizadeh-Khameneh (2015)	Trilateration	First, Second	Bi-objective	Analytical

In the first category of optimal design of geodetic networks that relies on the criterion of precision, the target is to find an optimum network that meets a specific precision requirement. An example of this type of optimal design can be found in [Kuang \(1993\)](#) in which the optimal design problem of quadratic programming was applied to differential levelling networks. In his study, a required precision in height difference was priorly provided and an optimum set of measurements was chosen. With a real levelling network, all possible measurements, i.e., height differences between nearby levelling points were validated and the objective of the experiment is to find an optimal set of levelling routes that satisfies the required precision but with the minimum price-cost. The minimum cost criterion means finding out which measurements can be removed in order to have a minimum effect on the final precision.

In [Amiri-Simkooei and Sharifi \(2004\)](#), the SOD problem was applied to derive an optimum network of which measurements of various types are equivalent in their precision. This was conducted in a way that the observations' weights are amended so that different groups of observations have the same average  $r$ -numbers. Though the design was carried out based on  $r$ -numbers, the objective function is the precision as it targets to have the same average precision, together with the same average  $r$ -numbers, for all types of observations. An analytical equation was derived for applying to this special design problem through an iterative solution. The analytical approach proposed in their study was numerically validated by applying to a synthetic regular quadrilateral network and a real deformation network in Iran.

Another optimal design of geodetic network from the point of view of precision can be found in [Amiri-Simkooei et al. \(2012\)](#), in which a desired precision of the last point of an open traverse is obtained. Specifically, in their study, the design was applied to an open traverse in the ZOD problem with an objective to find the best position (i.e., the netpoint) where the azimuth measurement should be gathered so that the position error of the last point is minimum. The result shows that the best location for this azimuth measurement in an open traverse should be in the middle of the network. In the same study, the authors applied the FOD design problem in an intersection to find the best location of the intersection point so that its absolute error ellipse becomes a circle.

Their experiment was implemented with an assumption that the two measurements are uncorrelated and measured to the same precision. As a result, an

analytical equation was derived that can be used for determining the optimum location of the intersection point. Finally, the optimal design was applied to a GPS network to optimally choose a GPS satellite configuration in a way that the smallest value for geometrical dilution-of-precision (GDOP) is met. This was treated so because GDOP has the same interpretation as the precision criterion in a traditional geodetic network in a way that the minimal GDOP is equivalent to the maximal precision in positioning.

In another work carried out by [Alizadeh-Khameneh et al. \(2016\)](#), a GPS network created for deformation monitoring was validated by applying the SOD problem. In their study, more precise GPS data are assumed to be gathered in the second epoch compared to the first. This assumption corresponds to a longer observation time for data gathering and/or using forced centring pillars and/or the use of GPS together with other satellite systems, e.g., Europe's Galileo, Russia's Global Navigation Satellite System, China's BeiDou Navigation Satellite System. By this approach, a larger accuracy of GNSS observations is assumed in the second epoch that results in a drop in the number of baselines to be measured. Another study on the optimal design of geodetic networks based on the precision criterion can be found to apply the simulated annealing method in the FOD problem by minimising the hypervolume of the hyperellipsoid defined by an unknown covariance matrix ([Berné & Baselga, 2004](#)).

In the second category of the optimal design of geodetic networks based on reliability, the objective is to maximise the ability of the optimal network in detecting and resisting against possible gross errors in measurements. This is implemented by utilising the internal reliability and the external reliability. The former is relevant to the ability in detecting gross errors, which is normally represented by  $r$ -numbers, and the latter relates to the maximum effect of the undetectable gross error. Generally, the internal reliability criterion is used as a measure for the optimal design of geodetic networks in the high-reliability sense. An alternative criterion is the geometrical strength that is implemented in the robustness analysis technique via rotation, shear and scale. These two criteria of the reliability and the geometrical strength have been claimed to be strongly correlated ([Amiri-Simkooei, 2004](#)).

In [Amiri-Simkooei \(2001a\)](#), the author contrasts theoretically the concepts of the reliability represented by the  $r$ -numbers and the geometrical strength denoted by robustness parameters via robustness analysis. It is concluded, in his study, that the robustness parameters were affected by  $r$ -numbers, and the largest robustness parameters were caused by the observations with the minimum  $r$ -number. A

trilateration network of 17 netpoints with 66 distance measurements was used for testing the optimal design. FOD was used to choose the optimal positions of four netpoints (i.e., the optimal configuration of the network), and SOD was implemented to derive the optimal standard deviation of all observations. Both of these problems were implemented aiming at a high reliability that were carried out with both the  $r$ -number as well as the robustness parameters in rotation, shear and scale, which show a good correlation. [Amiri-Simkooei \(2001b\)](#) suggested a strategy that can be used for designing a geodetic network to meet a high reliability and geometrical strength. In his study, a 2D geodetic network used for deformation monitoring was used to validate the proposed strategy in which both FOD and SOD problems were implemented.

A similar design to obtain an optimum network with a high reliability is an idea that all observations have the same  $r$ -numbers was carried out and discussed in [Amiri-Simkooei \(2004\)](#). This idea of the same  $r$ -numbers for all observations has been referred to as “balanced observations” in other studies (e.g., [Kampmann & Krause, 1996](#)). In [Amiri-Simkooei \(2004\)](#), the design was applied to the SOD problem of which the optimum weights of observations are achieved. The proposed algorithm was tested over two simulated networks, 1) a quadrilateral network with six distance and eight angle observations constituted from four netpoints, and 2) a trilateration network of ten netpoints with 45 distance observations. For obtaining the optimum weights for all observations that have the same  $r$ -numbers, different linear, quadratic and cubic functions were implemented. Another study focusing on the reliability criterion can be found in [Rofatto et al. \(2018\)](#), which is based on the power of a data snooping testing procedure using Monte Carlo simulations.

Other than the single-objective design problem, the one combining various criteria named multi-objective optimal design has also been researched. The bi-objective second-order optimisation combining the precision and reliability criteria was investigated by [Xu \(1989\)](#). In his study, the non-linear programming method was applied and the proposed algorithm was tested on a levelling network located in an earthquake area in China. In [Xu \(1993\)](#), an approach incorporating a multi-objective function of criterion matrix designed for homogeneous, isotropic and reliable geodetic networks is described. [Xu and Grafarend \(1995\)](#) applied the SOD problem to deforming networks based on a multi-objective solution combining the accuracy, the reliability and the character of a deformation model.

In [Alizadeh-Khameneh et al. \(2015\)](#), the authors compared results of applying the SOOM, the BOOM and the MOOM designs to an existing GNSS network used for deformation monitoring in order to choose an optimum baseline configuration. [Eshagh and Alizadeh-Khameneh \(2015\)](#) applied the BOOM of the precision and the reliability and investigated the effect of the controlling constraints on a 2D simulated network. The investigations were conducted with both constrained BOOM and unconstrained BOOM, and the latter one showed a result that satisfies the demand on precision and reliability.

### 6.3 Design of InSAR SBAS Networks Using Redundancy Numbers

Increasing the number of interferograms in InSAR SBAS data processing will increase the network's reliability, but will also reduce the cost effectiveness as a longer time and larger data storage are required in the data processing stage. Therefore, the balance between two criteria, i.e., the reliability and the cost, is necessary. It is reasonable if a threshold of the  $r$ -number is available to assign temporal and perpendicular baseline thresholds in selecting interferograms to be subsequently processed. The objective of this design is thus to increase the  $r$ -number of the network while keeping the number of interferograms as small as possible. In this Section, the same simulated datasets as those in Chapter 5 are used in which different scenarios are tested to observe the relation between the  $r$ -numbers, which are relevant to networks selected by various thresholds, and errors in SBAS-derived rates as well as RMSs of the difference between simulated and SBAS-derived deformation time series.

The objective of this study is to seek an  $r$ -number that can be considered as a threshold used in designing an SBAS interferogram network. Equation (6.3), used for computing the  $r$ -number, is thus applied to networks that are chosen based on various thresholds. In InSAR SBAS data processing, the super primary (formerly super master) scene, which is the first scene in many applications, is assumed to be stable (i.e., without any deformation within the acquired time period), and this assumption can be understood as an inner constraint in datum in geodesy. As a result, the ZOD problem is not implemented for InSAR. In addition, it is impractical to define accurately or even relatively accurately predict the precision of interferograms as this is dependent on so many complex factors, such as temporal and perpendicular baselines, DSM uncertainties, orbital error of InSAR ephemeris, the variation of atmospheric conditions between two acquired times, the change in Earth surface

properties such as those of vegetation or artificial structures (Chapter 3). This is opposed to traditional geodetic networks of which precision of their measurements can be pre-defined by, e.g., choosing suitable measuring instruments such as a total station, a level or GNSS receivers.

The precision of Earth deformation retrieved from InSAR cannot be controlled by precision constraint of their measurements, which is implemented frequently in optimisation of geodetic networks by a precision criterion. In some studies on the optimisation of geodetic networks, weights of measurements are chosen starting from an assumed standard deviation. This can be done in some types of geodetic networks such as GNSS, levelling, triangulation or trilateration networks. These standard deviations are initially adopted based on equipment precision. For example, the standard deviation of angular observations can be assumed based on the type of total station that is used. Similarly, measurements of distances can be assumed according to the precision of electronic distance meter used. This assumption will bring about initial weights and the optimal ones can be obtained by the procedure of optimisation. However, as has been mentioned, the precision of InSAR measurements cannot be predicted well, and the optimisation of InSAR network by optimally choosing their weights is thus not applicable.

Two scenes will be selected to be paired for interferogram formation only if their temporal and/or perpendicular baselines are smaller than the chosen thresholds. For designing a network, if we consider “locations” of InSAR scenes by their “coordinates” represented by temporal and perpendicular baselines with respect to the first scene (see [Figure 6.1](#) as an example), then these “coordinates” are fixed, i.e., the interferogram configuration has been given. This is because these “coordinates” are dependent on the “locations” of images acquired by InSAR platforms and cannot be optimised. This is again opposed to traditional geodetic networks, e.g., triangulation, levelling or GNSS, of which locations of ground points, benchmarks or monuments are located on the Earth’s surface and are frequently chosen in suitable locations for a good geometrical configuration and intervisibility.

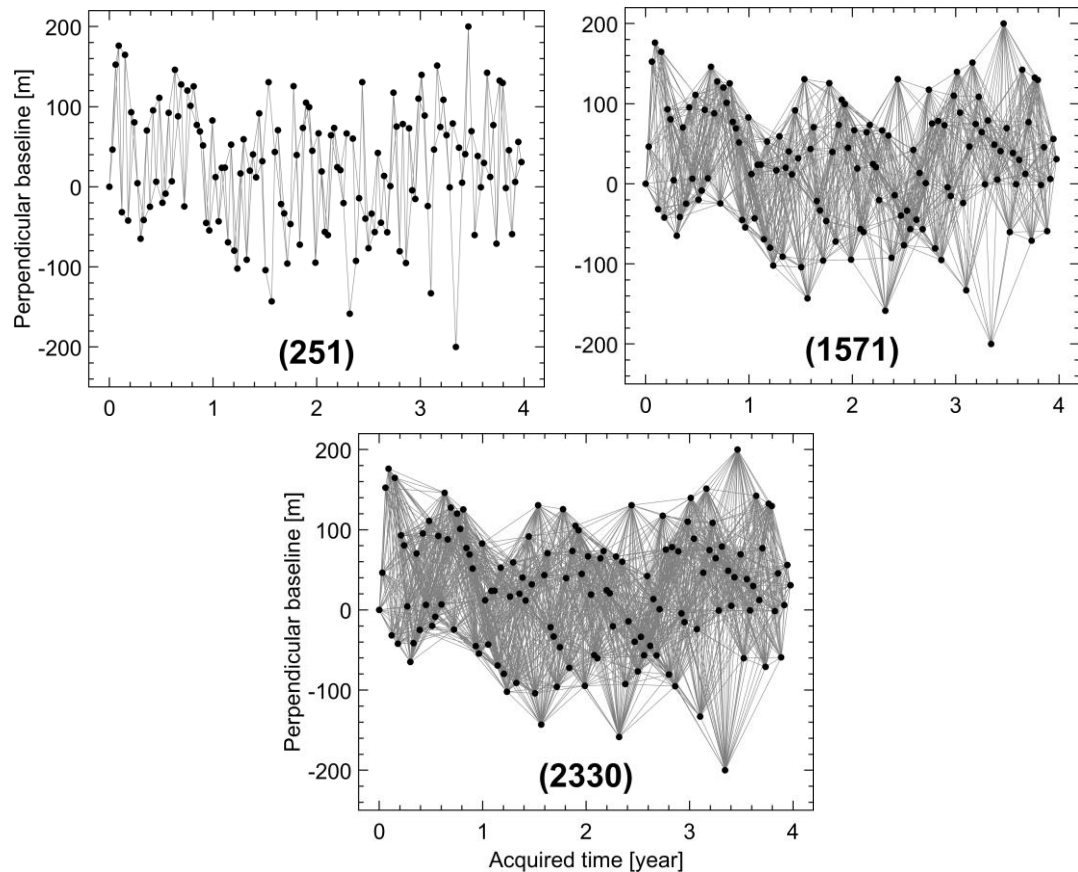


**Figure 6.1.** Examples of interferogram networks chosen based on different temporal and perpendicular baseline thresholds.  $r$ -numbers computed corresponding to these networks are  $\sim 0.2$  (top-left),  $\sim 0.8$  (top-right) and  $\sim 0.9$  (bottom). The bracketed bold number under each network refers to the number of interferograms.

The InSAR network configuration is therefore optimised only by choosing appropriate pairs of images to be combined for interferogram formation. As has been mentioned in Section 4.2, this is normally carried out by using temporal and/or perpendicular baseline thresholds, or by using a model based on temporal, perpendicular and Doppler baselines. However, these thresholds are chosen differently between studies in the literature. Here, the relation between the  $r$ -numbers and errors in rates determined by the InSAR SBAS approach applied in the simulated data with networks defined by various thresholds is explored. Therefore, the optimal design of InSAR interferogram network investigated in this study means choosing an optimal subset of interferograms to be subsequently processed among all possible interferograms.

The objective of this design is thus to identify an optimal series of interferograms based on temporal and perpendicular baseline thresholds that meet a high reliability,

defined by the  $r$ -number, but with a minimal number of interferograms as possible in order to save processing time and disk storage required. Here, interferogram networks determined by combinations of temporal baseline thresholds, from one month to four years long, with a one-month increment, and perpendicular baseline thresholds of 100 m, 200 m and 300 m are tested. As a result, 144 networks are formed with the minimum and maximum number of interferograms being 251 and 8778, respectively.

Equation (6.3) is then applied to each of these networks to compute the reliability matrix  $\mathbf{R}$  with the  $r$ -numbers located on its diagonal ( $r_i$ ). The objective of this optimisation is to maximise these  $r$ -numbers by using their minimum value to represent the reliability of a network so that the  $r$ -numbers of all measurements in that network are larger or equal to this minimum value. The  $r$ -number of a network is thus defined as:

$$r = \min(r_i) \quad (6.5)$$

By applying Equation (6.3) then Equation (6.5), the  $r$ -numbers are computed for 144 interferogram networks. Examples of these networks are shown in [Figure 6.1](#), corresponding to those with computed  $r$ -numbers being  $\sim 0.2$  (251 interferograms),  $\sim 0.8$  (1571 interferograms) and  $\sim 0.9$  (2330 interferograms), respectively. These networks are formed based on temporal and perpendicular baseline thresholds of one month and 200 m, five months and 200 m, and seven months and 300 m, respectively. The statistics, including temporal and perpendicular baseline thresholds applied, number of interferograms, minimum and maximum values of the  $r$ -numbers of all 144 interferograms, are shown in [Table 6.2](#).

**Table 6.2.** Results of  $r$ -numbers computation according to networks defined by various temporal and perpendicular baseline thresholds. Temp and Perp indicate temporal and perpendicular baseline thresholds applied, IFGs stands for the number of interferograms chosen.

Temp [month]	Perp [metre]	IFGs	$min(r_i)$	$max(r_i)$	Temp [month]	Perp [metre]	IFGs	$min(r_i)$	$max(r_i)$
1	200	251	0.22	0.55	24	300	6486	0.97	0.98
1	300	263	0.38	0.55	24	400	6486	0.97	0.98
1	400	263	0.38	0.55	27	200	6658	0.96	0.98
2	200	621	0.45	0.82	25	300	6684	0.97	0.98
2	300	649	0.69	0.82	25	400	6684	0.97	0.98
2	400	649	0.69	0.82	26	300	6811	0.97	0.98
3	200	986	0.70	0.88	26	400	6811	0.97	0.98
3	300	1026	0.79	0.88	28	200	6818	0.96	0.98
3	400	1026	0.79	0.88	29	200	6974	0.96	0.98
4	200	1223	0.77	0.90	27	300	6993	0.97	0.98
4	300	1272	0.83	0.90	27	400	6993	0.97	0.98
4	400	1272	0.83	0.90	30	200	7069	0.96	0.98
5	200	1571	0.82	0.93	28	300	7165	0.97	0.98
5	300	1633	0.86	0.93	28	400	7165	0.97	0.98
5	400	1633	0.86	0.93	31	200	7206	0.96	0.98
6	200	1911	0.86	0.94	29	300	7330	0.98	0.98
6	300	1985	0.89	0.94	29	400	7330	0.98	0.98
6	400	1985	0.89	0.94	32	200	7341	0.96	0.98
7	200	2239	0.88	0.95	30	300	7435	0.98	0.98
7	300	2330	0.90	0.95	30	400	7435	0.98	0.98
7	400	2330	0.90	0.95	33	200	7466	0.96	0.98
8	200	2455	0.89	0.95	34	200	7545	0.97	0.98
8	300	2554	0.91	0.95	31	300	7584	0.98	0.98
8	400	2554	0.91	0.95	31	400	7584	0.98	0.98
9	200	2768	0.90	0.96	35	200	7658	0.97	0.98
9	300	2884	0.92	0.96	32	300	7724	0.98	0.98
9	400	2884	0.92	0.96	32	400	7724	0.98	0.98
10	200	3076	0.91	0.96	36	200	7762	0.97	0.98
10	300	3205	0.93	0.96	37	200	7827	0.97	0.98
10	400	3205	0.93	0.96	33	300	7854	0.98	0.98
11	200	3371	0.92	0.97	33	400	7854	0.98	0.98
11	300	3516	0.94	0.97	38	200	7916	0.97	0.98
11	400	3516	0.94	0.97	34	300	7937	0.98	0.98
12	200	3565	0.93	0.97	34	400	7937	0.98	0.98
12	300	3719	0.94	0.97	39	200	7996	0.97	0.98

Table 6.2. (Continued)

Temp [month]	Perp [metre]	IFGs	$\min(r_i)$	$\max(r_i)$	Temp [month]	Perp [metre]	IFGs	$\min(r_i)$	$\max(r_i)$
12	400	3719	0.94	0.97	35	300	8053	0.98	0.98
13	200	3846	0.93	0.97	35	400	8053	0.98	0.98
13	300	4016	0.95	0.97	40	200	8068	0.97	0.98
13	400	4016	0.95	0.97	41	200	8111	0.97	0.98
14	200	4118	0.94	0.97	36	300	8161	0.98	0.98
15	200	4289	0.94	0.98	36	400	8161	0.98	0.98
14	300	4303	0.95	0.97	42	200	8169	0.97	0.98
14	400	4303	0.95	0.97	43	200	8219	0.97	0.98
15	300	4490	0.95	0.98	37	300	8228	0.98	0.98
15	400	4490	0.95	0.98	37	400	8228	0.98	0.98
16	200	4551	0.94	0.98	44	200	8260	0.97	0.98
16	300	4763	0.96	0.98	45	200	8281	0.97	0.98
16	400	4763	0.96	0.98	46	200	8307	0.97	0.98
17	200	4799	0.94	0.98	38	300	8321	0.98	0.98
17	300	5027	0.96	0.98	38	400	8321	0.98	0.98
17	400	5027	0.96	0.98	47	200	8323	0.97	0.98
18	200	5035	0.95	0.98	48	200	8330	0.97	0.98
19	200	5194	0.95	0.98	39	300	8404	0.98	0.98
18	300	5281	0.96	0.98	39	400	8404	0.98	0.98
18	400	5281	0.96	0.98	40	300	8477	0.98	0.98
20	200	5421	0.95	0.98	40	400	8477	0.98	0.98
19	300	5446	0.96	0.98	41	300	8522	0.98	0.98
19	400	5446	0.96	0.98	41	400	8522	0.98	0.98
21	200	5638	0.95	0.98	42	300	8582	0.98	0.98
20	300	5685	0.96	0.98	42	400	8582	0.98	0.98
20	400	5685	0.96	0.98	43	300	8633	0.98	0.98
22	200	5844	0.95	0.98	43	400	8633	0.98	0.98
21	300	5916	0.97	0.98	44	300	8675	0.98	0.98
21	400	5916	0.97	0.98	44	400	8675	0.98	0.98
23	200	5982	0.96	0.98	45	300	8698	0.98	0.98
22	300	6137	0.97	0.98	45	400	8698	0.98	0.98
22	400	6137	0.97	0.98	46	300	8725	0.98	0.98
24	200	6174	0.96	0.98	46	400	8725	0.98	0.98
23	300	6280	0.97	0.98	47	300	8743	0.98	0.98
23	400	6280	0.97	0.98	47	400	8743	0.98	0.98
25	200	6363	0.96	0.98	48	300	8750	0.98	0.98
26	200	6483	0.96	0.98	48	400	8750	0.98	0.98

The SBAS method is applied to derive deformation time series for each of 1000 pixels for all 144 interferogram networks, then unweighted LS is applied to these time series to obtain its parameters in terms of linear rates and annual sinusoids. The estimated deformation linear rates are subsequently compared with simulated rates, which are  $-2$  mm/yr,  $-20$  mm/yr and  $-100$  mm/yr (Table 5.1), with the differences between these two rates referred to as errors in rate determination. The GIAN-T package (Agram et al., 2013; Agram et al., 2012) incorporating the SBAS algorithm is again utilised in this experiment for InSAR SBAS data processing.

The dependence of computed  $r$ -numbers and SBAS-retrieved annual rates on the number of selected interferograms are shown in Figure 6.2, where the change in SBAS-derived unweighted LS rates presents the same patterns among the three cases (Table 5.1) of simulated signals. Furthermore, the higher the  $r$ -number, the closer the agreement between simulated and SBAS-retrieved rates. The two rates are, in particular, nearly identical when the  $r$ -numbers are greater than  $\sim 0.9$ .

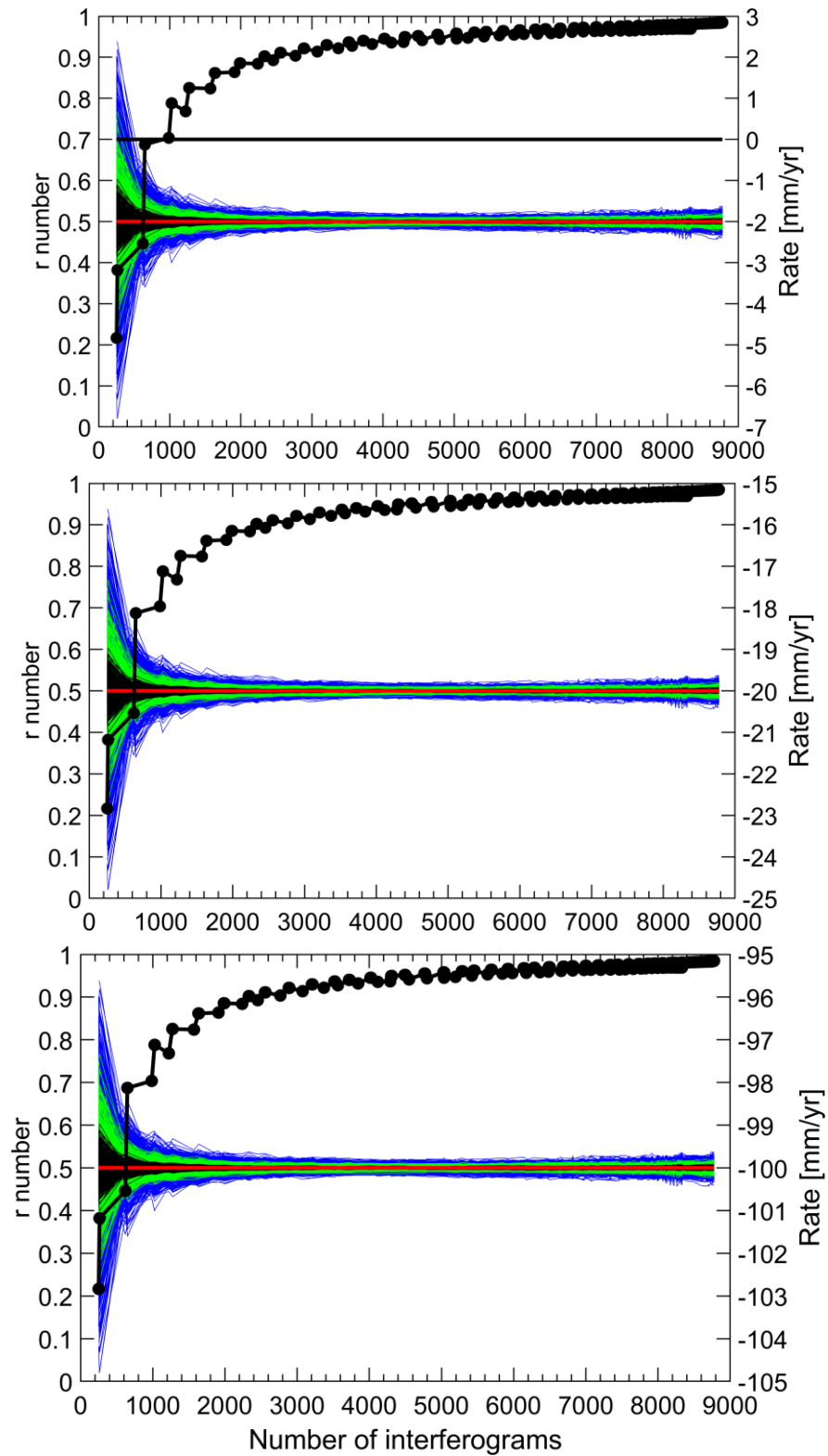


Figure 6.2. Dependence of the  $r$ -numbers and SBAS-derived unweighted LS rates for 1000 pixels on the number of chosen interferograms with various linear plus annual signals. From top to bottom are simulated signal cases 1 to 3 (Table 5.1). Black, green and blue polylines show the results for noise cases A, B and C (Table 5.2). Red horizontal lines represent the simulated rates.

The dependence of the RMSs of the difference between simulated and SBAS-retrieved deformation time series on the number of chosen interferograms is shown in Figure 6.3 (top) for all three cases of simulated noise (Table 5.2). The  $r$ -number increases as the number of interferograms increases, constrained by temporal baseline thresholds, and a reduction in the RMSs. The RMSs decrease from a small  $r$ -number until  $\sim 0.8$ , after which the change becomes negligible.

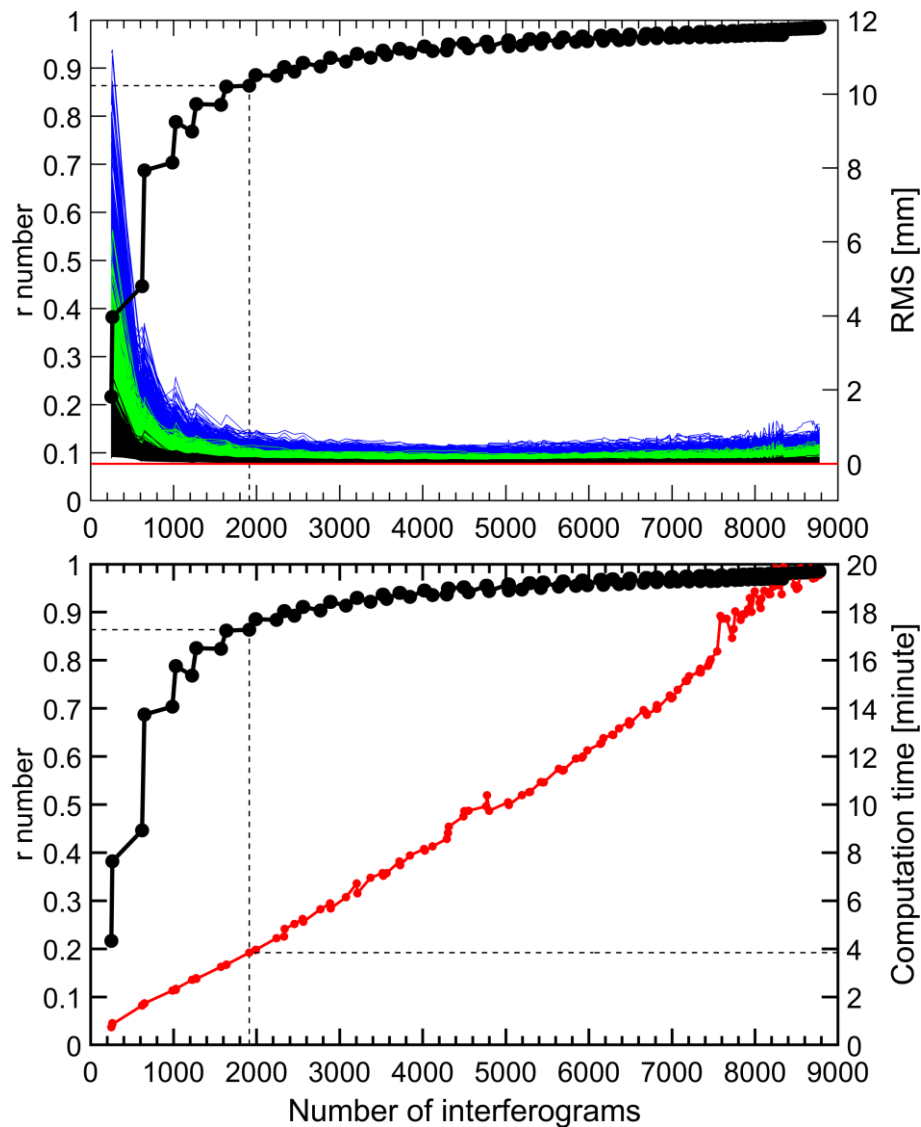
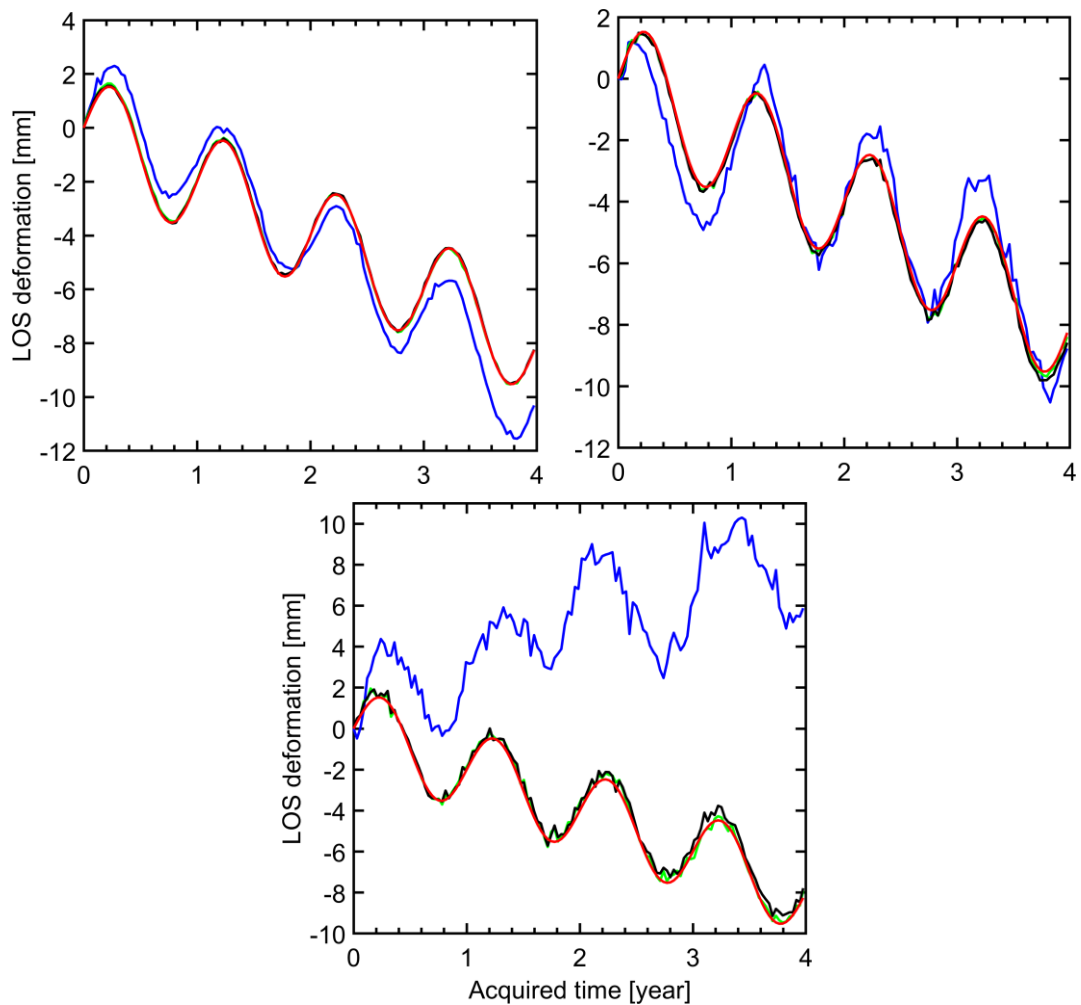


Figure 6.3. (top): Comparison of the change in the  $r$ -numbers and the RMSs of the difference between simulated and SBAS-derived deformation time series, (bottom): Comparison of the change in the  $r$ -numbers according to SBAS network interferogram numbers and computation time. Black, green and blue polylines in the top panel indicate the results computed from simulated data with noise cases A, B and C (Table 5.2). Dashed lines indicate the “optimal”  $r$ -numbers corresponding to the networks with interferograms chosen with all RMSs being smaller than the chosen trade-off values of 1/10 of the residual interferogram noise (Table 5.2).

A 1/10 ratio RMS criterion is then applied as a trade-off value to identify the “optimal”  $r$ -number in which a network with a minimal number of interferograms selected and with all RMSs smaller than 1/10 noise range, which are 0.2 mm, 0.5 mm and 1.0 mm for the simulated residual interferogram noise ranges shown in [Table 5.2](#). As shown in [Chapter 5](#), the RMSs are dependent on the SBAS network and residual interferogram noise but not signal magnitude. Thus, [Figure 6.3](#) indicates an “optimal”  $r$ -number being  $\sim 0.86$  for an SBAS network of 1911 interferograms derived from the 1/10 ratio RMS criterion, suggesting  $r$ -numbers between  $\sim 0.8$  and  $\sim 0.9$  to be a suitable range for the “optimal” design of SBAS networks.

The efficiency of the obtained “optimal”  $r$ -numbers are confirmed by not only the RMS trade-off but also the computation time as shown in [Figure 6.3](#) (bottom), where the network of 1911 interferograms (for the “optimal”  $r$ -number) runs for less than four minutes compared to nearly 20 minutes for the largest network of 8778 interferograms. This shows efficiency in processing time for the SBAS inversion step only. In reality, SBAS data processing with a full workflow, which comprises additional steps of interferogram formation and error reduction as described in [Chapter 3](#) and [Chapter 4](#), the time difference between processing all 8778 interferograms and the optimal 1911 interferograms can be substantial. Additionally, this “optimal” design of SBAS networks keeps the number of interferograms to a minimum, which limits the disk storage space required.

[Figure 6.4](#). shows an example of the SBAS-derived deformation time series of a pixel compared with a simulated linear plus annual signal of  $-2$  mm/yr plus 2 mm (i.e., the simulated signal case 1 in [Table 5.1](#)) according to selected cases of computed  $r$ -number of  $\sim 0.2$ ,  $\sim 0.8$  and  $\sim 0.9$ . The results of applying residual noise cases A, B, and C ([Table 5.2](#)) are shown in [Figure 6.4](#). . In all cases, the results corresponding to the computed  $r$ -numbers of  $\sim 0.8$  and  $\sim 0.9$  show close agreement with the simulated signal. In contrast, however, large differences between simulated and SBAS-derived deformation time series are shown in the case when the  $r$ -number is  $\sim 0.2$  (251 interferograms), particularly in the case of large residual interferogram noise (i.e., bounded within  $[-10; +10]$  mm) where the difference in both its trend (i.e., deformation or uplift) and magnitude is shown (cf. [Figure 6.4](#). (bottom) between the blue and red polylines).



**Figure 6.4.** An example of simulated and SBAS-derived deformation time series of simulated signal case 1 in Table 5.1 contaminated by residual interferogram noise cases A (top-left), B (top-right) and C (bottom) as listed in Table 5.2. The results are computed from applying various SBAS interferogram networks shown in Figure 6.1, corresponding to computed  $r$ -numbers of  $\sim 0.2$  (blue),  $\sim 0.8$  (green), and  $\sim 0.9$  (black), respectively. Red polylines indicate the simulated deformation time series. The blue line in the bottom panel shows the extreme case where spurious uplift is indicated, whereas subsidence is simulated.

Figure 6.4. shows that if the  $r$ -number is too small ( $< 0.2$ ), spurious or even contradictory rates can result, as was shown similarly in Section 5.3. Therefore, caution must again be exercised when using InSAR to detect small rates of deformation in the presence of large noise (low SNR). This is where the redundancy number may be of assistance in gauging the reliability of the estimated rates. This also shows that, though the reliability of a network is relevant to its ability to detect and resist against gross errors, in this specific case of InSAR SBAS networks, a good

agreement between the  $r$ -numbers and errors in rate determination is present that is useful for “optimal” design of InSAR SBAS networks.

#### 6.4 Tests With Other Network Types

In this Section, the  $r$ -numbers are calculated for networks of Delaunay triangulations, hierarchical thresholds and a minimum spanning tree as in Chapter 5 (Section 5.5). This is to test whether this  $r$ -number-based optimal design approach works with these other types of interferogram networks.

The  $r$ -numbers are first computed for the 32 Delaunay triangulation networks listed in Table 5.6. The results associated with the networks with independent interferograms and several networks with dependent interferograms (as examples) are shown in Figure 6.5 and Figure 6.6, respectively, in which the bottom-right panel in Figure 6.6 corresponds to the full Delaunay triangulation network. As shown in Chapter 5 (Section 5.5), low rate errors have been derived from applying the Delaunay triangulation networks even with a small number of interferograms with the reason that is recalled here that, interferograms with small noise are selected. However, the  $r$ -numbers associated with those networks are small as shown in Figure 6.5 and Figure 6.6. Therefore, this  $r$ -number-based optimal network design approach does not work with this type of Delaunay triangulation interferogram networks in terms of the precision represented by errors in rate determination.

This is useful in the other geodetic point of view in terms of the ability of the networks in gross error detection. Specifically, with those networks with independent interferograms shown in Figure 6.5, regardless of how many independent interferograms are included in the networks, the minimum  $r$ -number is zero, which is also the  $r$ -number of the network defined by Equation (6.5). These zero  $r$ -numbers are coincident with those independent interferograms in which if gross errors occur, they cannot be detected. Also, as shown in Chapter 5 (Section 5.5), phase unwrapping error detection based on interferogram loops (Biggs et al., 2007; Parker et al., 2017) also cannot be applied. Therefore, even with promising results in rate errors as shown in Chapter 5 (Section 5.5), these networks with independent interferograms are not recommended due to their inability in gross error detection as well as applying interferogram loops in unwrapping error detection.

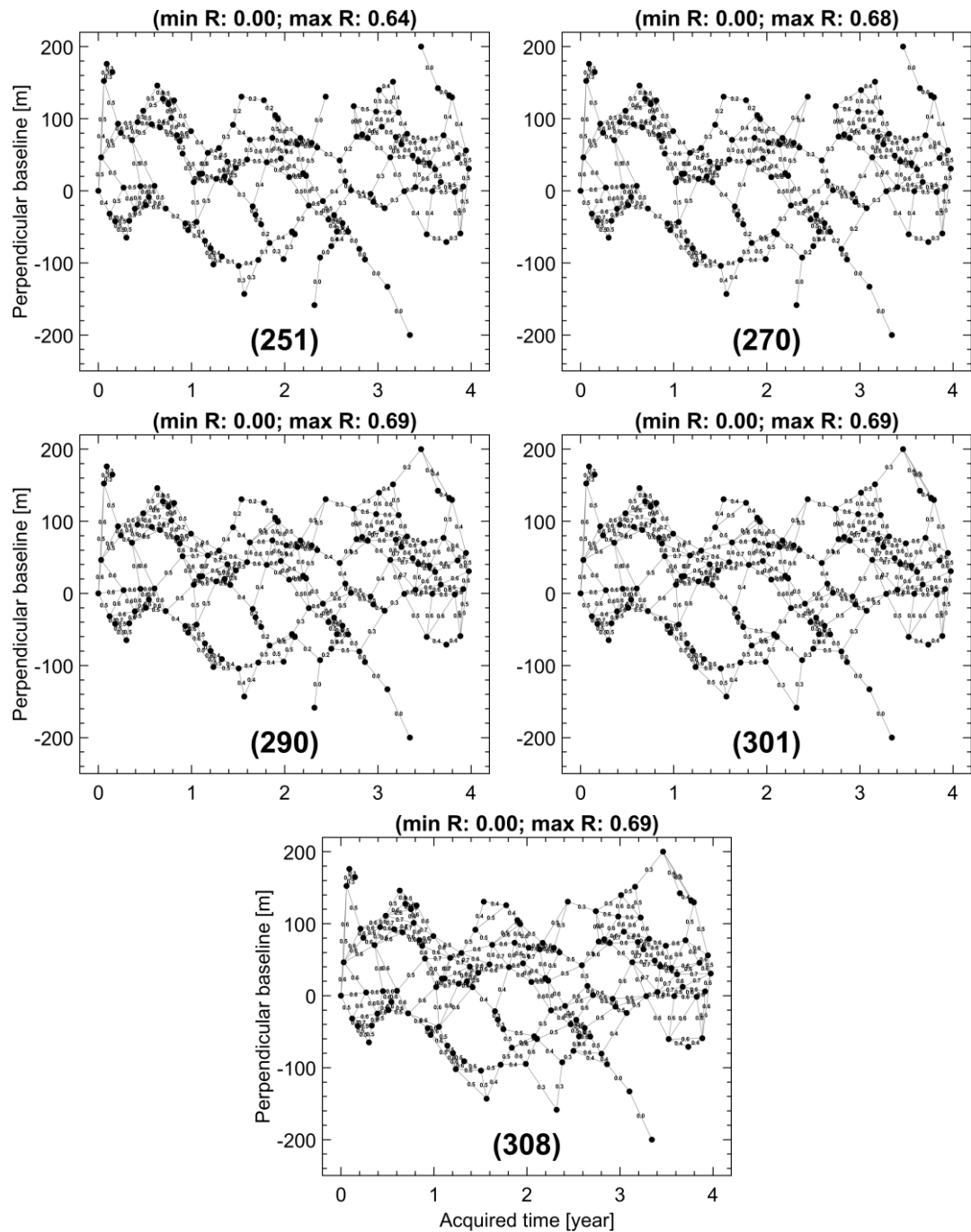


Figure 6.5.  $r$ -numbers computed for the Delaunay triangulation networks with independent interferograms. The minimum and maximum  $r$ -numbers are displayed on top of each network. The bracketed bold number under each network refers to the number of interferograms.

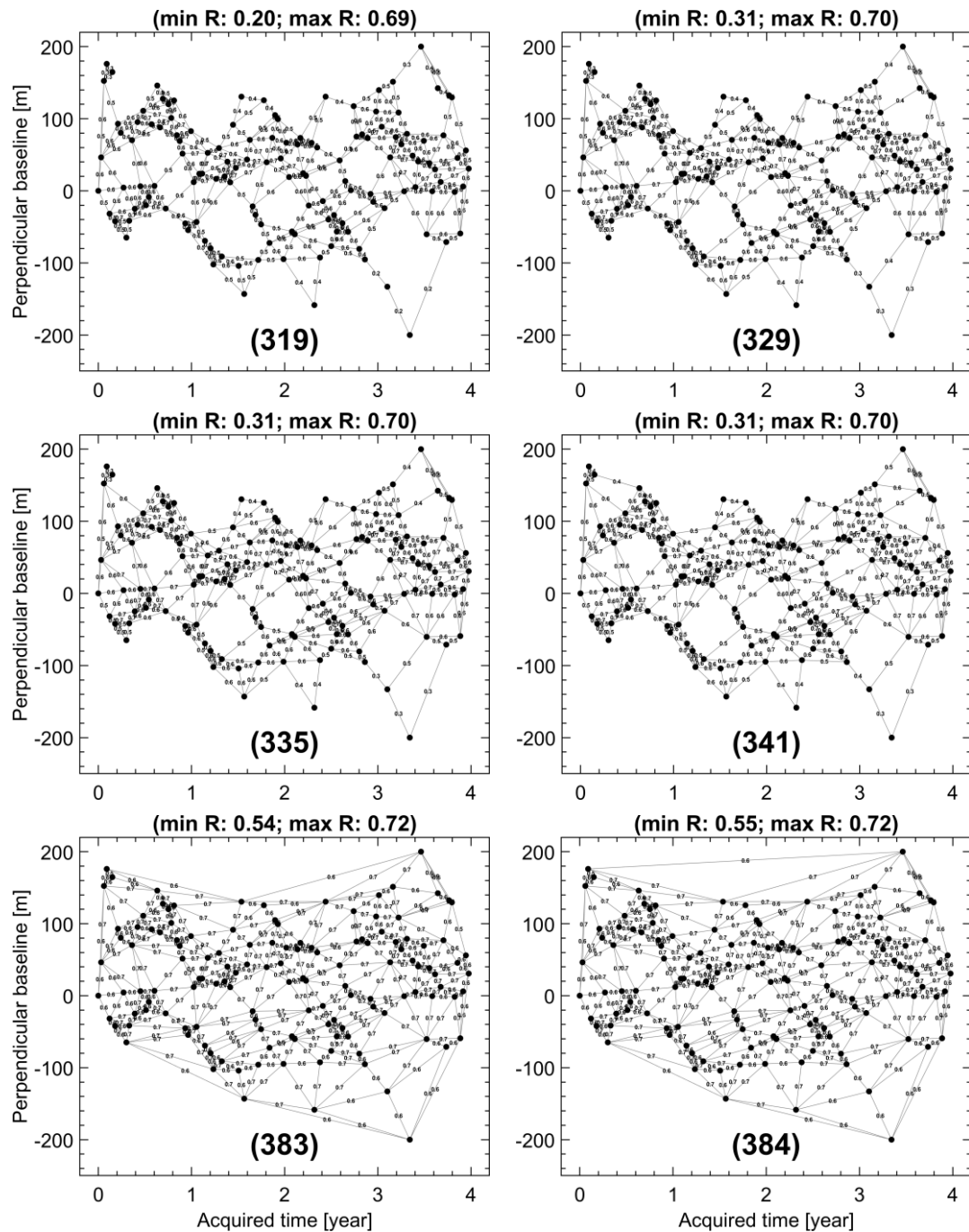


Figure 6.6.  $r$ -numbers computed for several Delaunay triangulation networks with dependent interferograms. The minimum and maximum  $r$ -numbers are displayed on top of each network. The bracketed bold number under each network refers to the number of interferograms.

The  $r$ -numbers estimated for the hierarchical thresholds and minimum spanning tree networks are shown in Figure 6.7 and Figure 6.8, respectively. In the hierarchical thresholds network case, the linear-fit and LS rates identical with those from the SBAS networks applying temporal and perpendicular baseline thresholds were found, which have been explained in Chapter 5 (Section 5.5). However, their associated  $r$ -numbers

are all zero as shown in Figure 6.6, which is due to the independent interferograms that are incorporated in the networks, even with the relatively dense network of 675 interferograms (Figure 6.7, bottom panel). Therefore, following the geodetic point of view of gross error detection, these networks are also not recommended.

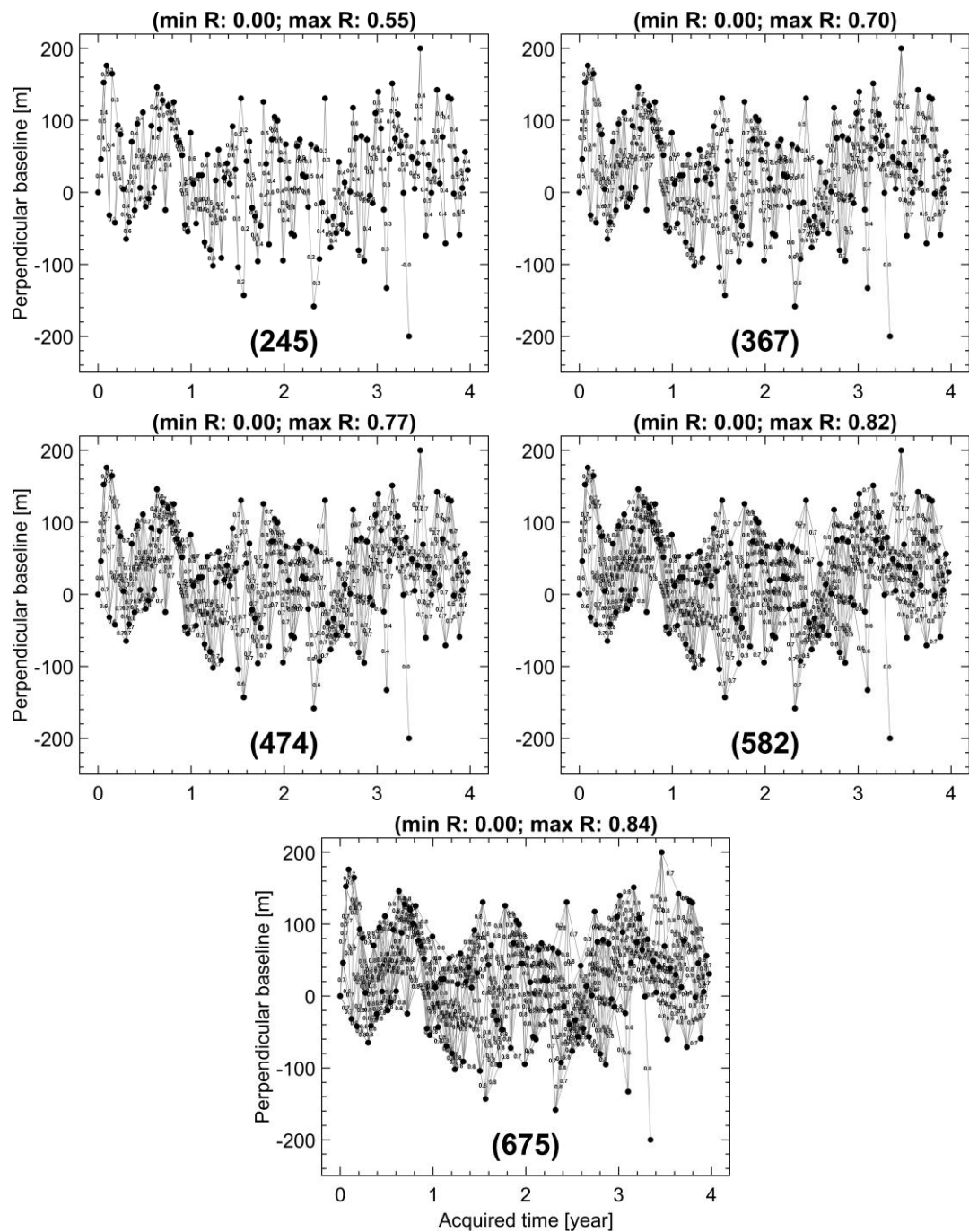
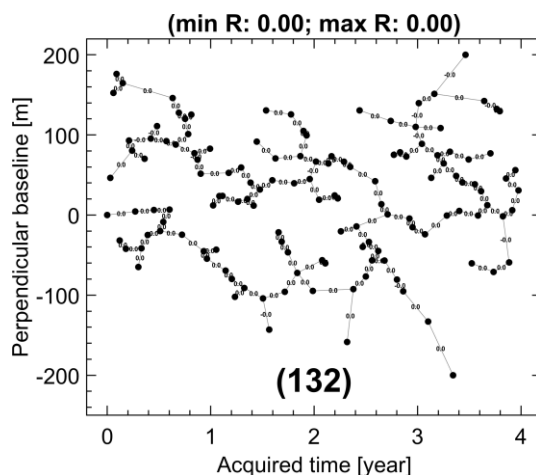


Figure 6.7.  $r$ -numbers computed for hierarchical thresholds networks. The minimum and maximum  $r$ -numbers are displayed on top of each network. The bracketed bold number under each network refers to the number of interferograms.



**Figure 6.8.**  $r$ -numbers computed for the minimum spanning tree network. The minimum and maximum  $r$ -numbers are displayed on top of each network. The bracketed bold number under each network refers to the number of interferograms

## 6.5 Chapter Summary

In this Chapter, the design of geodetic networks has been reviewed and applied to designing InSAR SBAS networks. The relation between the  $r$ -numbers from geodetic network design and errors in rate determination as well as the RMSs of the difference between simulated and SBAS-derived deformation time series was investigated. The reliability of a network is relevant to its ability to detect and resist measurements with gross errors. In this specific case of InSAR SBAS networks, a good agreement between the  $r$ -numbers and rate errors as well as the RMSs is present. In particular, the two rates, i.e., simulated and SBAS-derived, are nearly identical for an  $r$ -number larger than  $\sim 0.9$ .

The simulation results suggest that  $r$ -values greater than  $\sim 0.8$  or  $\sim 0.9$  indicate a robust SBAS network design, and that including more interferograms beyond this provided little improvement in the accuracy of the rate estimation. Notably, an alarming artefact in a couple of different simulation scenarios was found, where uplift was indicated by the SBAS results rather than the simulated subsidence. Furthermore, it was shown that the configuration (network design) is more important than simply the number of interferograms used, which is important given any limits on computing resources. For this reason, the use of redundancy numbers to help optimise SBAS network design is recommended.

The  $r$ -numbers were also tested with other types of interferogram networks of Delaunay triangulation, hierarchical thresholds and a minimum spanning tree. The

results indicate that the  $r$ -number-based optimal network design approach does not work with these network types in terms of the precision represented by errors in rate determination. This is because low rate errors were found but low  $r$ -numbers were also estimated. However, this approach is useful in the other geodetic point of view of gross error detection that even good results of linear-fit and LS rates were achieved, most of these networks were of zero  $r$ -numbers due to some or all independent interferograms are included. The networks with independent interferograms should not be employed because if gross errors occur in those independent interferograms, they cannot be detected. Also, the method of detecting unwrapping errors based on the interferogram close loop is inapplicable.

## 7. SIMULATED NOISE ANALYSIS OF INSAR SBAS DEFORMATION TIME SERIES

In this Chapter, the analysis of InSAR SBAS-derived deformation time series is presented, again relying on simulated data. These are slightly differently simulated data to those used in Chapters 5 and 6. The simulated data consist of surface deformation of linear plus annual sinusoidal signals contaminated by various interferometric noise and errors, including errors induced by DSM uncertainties, atmospheric artefacts, orbital error and temporal decorrelation. The noise analysis is employed utilising maximum likelihood estimation (MLE) incorporated in the CATS software (Williams, 2008). The Chapter starts with the background of correlated noise studies in geodesy in Section 7.1, which is followed by data simulation in Section 7.2 and InSAR data processing in Section 7.3. The results of the noise analysis is provided in Section 7.4, and Section 7.5 summarises the Chapter.

### 7.1 Correlated Noise

Errors in geodetic measurements are, in many cases, assumed to be statistically independent of each other and the rate of deformation is assumed to be constant over the duration of the observations. However, any temporal correlation between measurements can substantially affect the uncertainty in the velocity estimate when it is determined from the time series (Johnson & Agnew, 1995). In other words, a better understanding of the noise model in geodetic deformation time series allows more realistic uncertainty of estimated rate to be derived (Langbein, 2004). Measurements conducted using different methods are also affected by various types of errors and noise. Langbein and Johnson (1997) show that geodetic data are normally degraded by at least two noise sources, including the one caused by the instrument precision and that from localised motion of the geodetic monument.

For example, global navigation satellite system (GNSS) measurements are affected by errors in the phase measurement, satellite orbital information, noise brought about by atmospheric delays and several others (e.g., Langbein & Johnson, 1997; Mao et al., 1999). Temporally correlated errors from GNSS observations have been found in some global and regional data (e.g., Langbein, 2008; Mao et al., 1999; Williams et al., 2004; Zhang et al., 1997). Other temporally correlated errors have been detected in trilateration observations (e.g., Langbein, 2004; Langbein & Johnson,

1997). Among these studies, some were based on simulated data (e.g., [Johnson & Agnew, 1995](#); [Langbein, 2004](#); [Langbein & Johnson, 1997](#); [Mao et al., 1999](#); [Williams, 2003](#); [Williams et al., 2004](#)). GNSS, levelling and electronic distance meter are three methods where measurements are carried out on monuments (pillars or ground marks). Depending on how the monuments are made and attached to the Earth, the motion of the monument is possibly a source of temporal correlation ([Johnson & Agnew, 1995](#)).

Geodetic time series have been demonstrated to be correlated (e.g., [Johnson & Agnew, 1995](#); [Langbein, 2004, 2008](#); [Langbein & Johnson, 1997](#); [Mao et al., 1999](#); [Williams et al., 2004](#); [Zhang et al., 1997](#)), leading to the case that the assumption on statistically independent measurements is wrong. Geodetic research on Earth surface deformation requires precise estimation in both deformation functional parameters and time series error ([Mao et al., 1999](#)). Noise analysis is therefore essential so that an appropriate stochastic model can be applied in deformation parameter estimation and their computed uncertainties. This kind of approach can be found applied to GNSS data (e.g., [Langbein, 2008](#); [Mao et al., 1999](#); [Williams, 2003](#); [Zhang et al., 1997](#)) or electronic distance measurements (e.g., [Johnson & Agnew, 1995](#); [Langbein, 2004](#); [Langbein & Johnson, 1997](#)).

In InSAR data processing, noise models have been developed as the a priori precision of InSAR observations, i.e., individual interferograms to estimate earthquake source parameters ([Dawson & Tregoning, 2007](#)) or to understand the noise behaviour of tropospheric delay in interferograms ([Emardson et al., 2003](#)). This has also been developed with an interferogram network, which can be applied to SBAS inversion to estimate unknown parameters, i.e., deformation phase of acquisitions and DSM error ([Agram & Simons, 2015](#); [Cao et al., 2018](#); [González & Fernández, 2011](#); [Guarnieri & Tebaldini, 2007](#); [Hanssen, 2001](#); [Rocca, 2007](#)). However, in the further step of deformation parameter estimation, e.g., annual rate and (sinusoidal) periodic coefficients, a stochastic noise model is also needed, which can be derived via noise analysis, but has not been investigated to date. For example, [Filmer et al. \(2020\)](#) conducted the noise analysis of TerraSAR-X (TSX) derived deformation time series over Perth, Australia, but with a short time period of five years with 141 time series points, and limited to only a power-law model.

Annual velocities computed from InSAR SBAS-derived deformation time series are simply determined by fitting a linear regression to the time series or by applying a

library of canonical functions (Chang & Hanssen, 2016). This implicitly assumes that the errors and noise in InSAR SBAS-derived deformation time series are normally (Gaussian) distributed and statistically uncorrelated between each other, i.e., pure white noise. However, this assumption will be incorrect if the noise is of a type other than just white noise, e.g., coloured noise or a combination of coloured and white noise. The calculation of annual rates and their uncertainties in geodetic time series is commonly conducted in two steps, which are the estimation of the noise type and amplitude, and the estimation of the rates and their uncertainties (Williams, 2003). This two-stage work-flow can be extended to a more complicated functional model, rather than the linear function with just one parameter of an annual rate. The rate's uncertainty derived from geodetic time series depends on the assumed error model, e.g., white and/or coloured noise model (Williams, 2003).

This statement can be extended to parameters of other functional models, i.e., the uncertainties of those models' parameters are dependent on the noise model that is assumed. The noise analysis can be carried out in order to identify the type and quantify the amplitude of noise in geodetic time series. The objective of this part of the study is to identify the type and quantify the amplitude as well as the spectral index of noise in the simulated InSAR deformation time series. As the requirement of long time span or large number of points in geodetic deformation time series (e.g., Johnson & Agnew, 1995; Mao et al., 1999; Williams et al., 2004) is not yet available in real InSAR data so far, the analysis will be based on simulated InSAR data. For example, a minimum number of 256 data points were used by Williams et al. (2004) that is equivalent to ~8.4 years of Sentinel-1 (single platform with 12-day interval) or ~7.7 years of TSX.

Spectral estimation and maximum likelihood estimation (MLE) are two of the most popular methods that can be used for noise analysis in geodetic time series (e.g., Williams, 2008). Spectral estimation relies on a power spectrum and requires data taken at equally spaced time intervals (Langbein, 2004). This technique can be done either by the discrete Fourier transform (DFT) technique or the Scargle periodogram (Scargle, 1982). On the other hand, in MLE, the probability function of post-fit residuals between measurements and those computed from the functional model parameters is maximised by applying a Monte Carlo search or a downhill simplex algorithm, in which evenly sampled data are not required (Langbein & Johnson, 1997; Mao et al., 1999; Zhang et al., 1997). In this way, the amplitudes of noise sources,

corresponding to white and/or coloured noise, can be estimated so that an estimation of the covariance matrix can be achieved (Williams, 2008).

Spectral estimation is much faster but less precise and has fewer noise model options than MLE (Langbein & Johnson, 1997; Mao et al., 1999; Pilgram & Kaplan, 1998; Williams, 2008). In addition, spectral estimation does not estimate functional model parameters and their uncertainties (Williams, 2008). MLE, on the other hand, simultaneously estimates covariance matrix elements and functional model parameters (Langbein, 2004). In this study, therefore, MLE will be applied to noise analysis in simulated InSAR data by employing the public-domain Create and Analyse Time Series (CATS) software package authored by Williams (2008).

## 7.2 InSAR Data Simulation

As described in Section 3.1, an interferogram is generated from two InSAR scenes and is contaminated by various sources of errors and noise (e.g., Berardino et al., 2002; Lee et al., 2012):

$$\begin{aligned}\phi_{ij}(x, r) &= \phi(t_i, x, r) - \phi(t_j, x, r) \\ &\approx \frac{4\pi}{\lambda} d_{ij}(x, r) + \phi_{ij}^{top}(x, r) + \phi_{ij}^{atm}(x, r) + \phi_{ij}^{orb}(x, r) \\ &\quad + \phi_{ij}^{tmp}(x, r) + \phi_{ij}^n(x, r)\end{aligned}\quad (7.1)$$

where  $\phi_{ij}(x, r)$  indicates the InSAR phase measurement at a pixel with the coordinates in azimuth and range directions  $(x, r)$ , between two acquired times  $t_i$  and  $t_j$ ,  $\lambda$  is the radar wavelength,  $d_{ij}$  is the Earth deformation in the line-of-sight (LoS) direction to the satellite,  $\phi_{ij}^{top}$  is the phase component caused by the error in the DSM,  $\phi_{ij}^{atm}$  is the phase contribution due to the difference in atmospheric delay between two acquired times,  $\phi_{ij}^{orb}$  is the orbital error,  $\phi_{ij}^{tmp}$  represents temporal decorrelation, and  $\phi_{ij}^n$  represents the error in phase caused by various other noise sources.

In this Chapter, the simulated data are generated comprising linear and annual sinusoidal crustal deformation contaminated by various error and noise sources as shown in Equation (7.1), which are different from those in Chapters 5 and 6.

### 7.2.1 Simulation of Surface Deformation and Noiseless Interferograms

In this next simulation study, multiple InSAR interferograms without noise and various error and noise sources shown in Equation (7.1) are simulated, which will subsequently be used in InSAR data processing as well as noise analysis. An image of

500×500 pixels at one-arc-second spatial resolution is generated setting that, in each pixel, the Earth’s surface experiences a deformation with a linear trend plus annual sinusoidal trend. With this functional model of deformation, the annual rates and amplitudes for that image are first simulated for all pixels from which the cumulative LoS deformation at one pixel can be expressed as:

$$d(t_i, x, r) = v(x, r)t_i + A(x, r)\sin(2\pi t_i) \quad (7.2)$$

where  $d(t_i, x, r)$  is the cumulative deformation of the pixel located at radar coordinates  $(x, r)$  at the time  $t_i$ ,  $v(x, r)$  and  $A(x, r)$  represent the annual velocity and amplitude of that pixel. The pixels’ annual velocities are assumed to be limited between  $-40$  mm/yr and  $+40$  mm/yr, while amplitudes at annual period are limited within a range bounded by  $[10, 20]$  mm .

A simulated dataset spanning a 10-year period with a 12-day interval is generated. As a result, 332 InSAR images have been generated so as not to violate the limit of 256 set by Williams et al. (2004). It is assumed that perpendicular baselines of 331 images relative to the first one vary between  $-200$  metres and  $+200$  metres. These values of perpendicular baselines are simulated following a Gaussian distribution that is shown in Figure 7.1. Interferograms are then chosen based on a temporal baseline threshold that is 90 days ( $\sim 3$  months) and a perpendicular baseline threshold of 200 m. As a result, a network of 2510 interferograms has been generated that is shown in Figure 7.2.

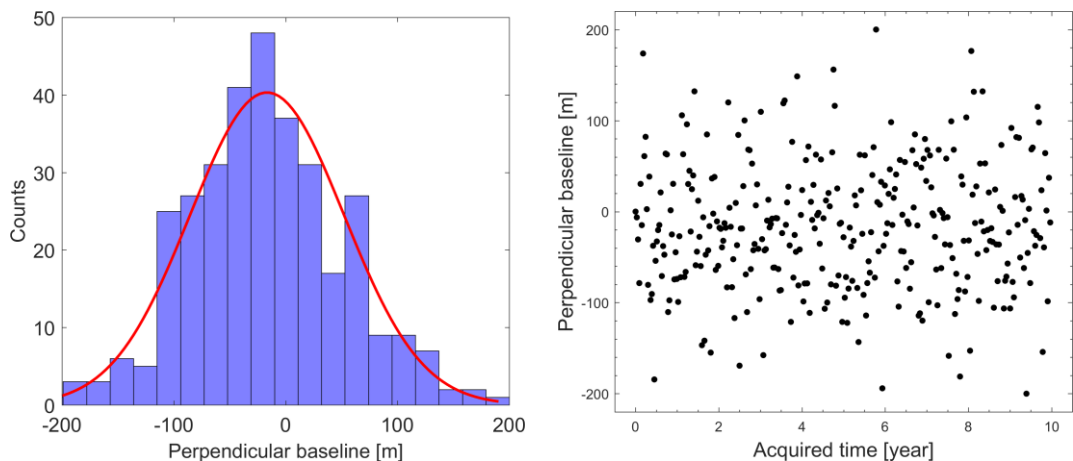
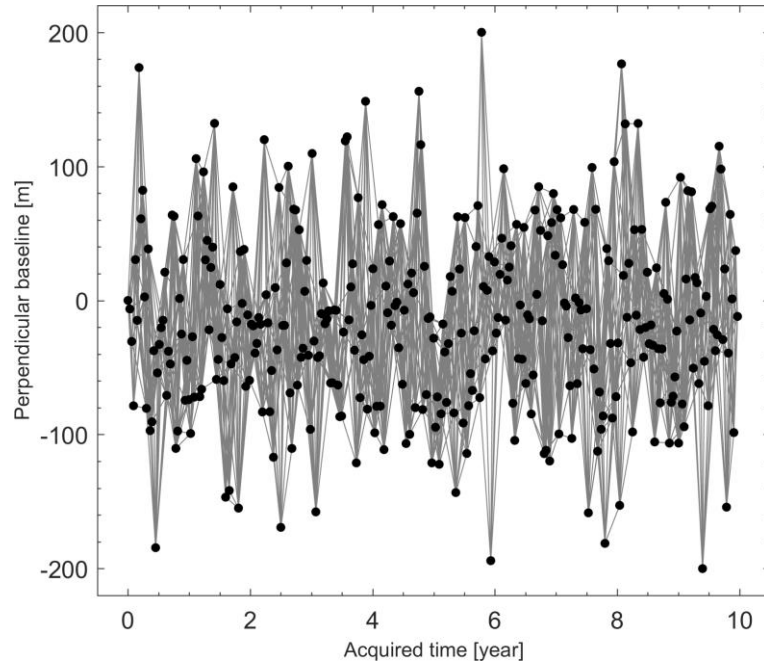


Figure 7.1. Histogram (left) and scatter plot (right) of 332 images of which locations are represented by temporal and perpendicular baselines. Both types of baselines are plotted as values relative to the first image.



**Figure 7.2.** Network of interferograms chosen based on temporal and perpendicular baseline thresholds of 90 days and 200 m, respectively. Filled dots indicate InSAR images. Grey lines denote interferograms that are chosen.

For each pixel located at radar coordinates  $(x, r)$ , 2510 phase interferograms are calculated by applying:

$$\phi_k^{def}(x, r) = \frac{4\pi}{\lambda} [d(t_i, x, r) - d(t_j, x, r)], \quad k = 1, \dots, 2510 \quad (7.3)$$

where  $\phi_k^{def}(x, r)$  is the phase of the  $k^{th}$  interferogram at a pixel located at radar coordinates  $(x, r)$  connecting two images captured at times  $t_i$  and  $t_j$ ,  $d(t_i, x, r)$  and  $d(t_j, x, r)$  are cumulative deformations in the LoS direction at that pixel corresponding to two captured times  $t_i$  and  $t_j$  that are calculated by using Equation (7.2), and  $\lambda$  is the radar wavelength that is the same as that in previous equations.

These interferograms are calculated from simulated deformations without adding any noise, so-called “noiseless interferograms”. As a consequence, a dataset of  $2510 \times 500 \times 500$  noiseless interferograms has been generated.

### 7.2.2 Simulation of Interferogram Error due to DSM Uncertainty

The second component  $\phi_{ij}^{top}(x, r)$  on the right hand side in Equation (7.1) is the phase contribution caused by error in the DSM. This component is proportional to the

perpendicular baseline history in the set of InSAR scenes (Fattahi & Amelung, 2015), and can be expressed as (Lee et al., 2012):

$$\phi_{ij}^{top}(x, r) = \frac{4\pi}{\lambda} \frac{B_{\perp,ij}}{r \sin\theta} \Delta Z^{top}(x, r) \quad (7.4)$$

where  $B_{\perp,ij}$  is the perpendicular baseline of InSAR scenes acquired at two times  $t_i$  and  $t_j$ ,  $r$  is the range between the reflecting target and the InSAR antenna,  $\theta$  is the look angle,  $\Delta Z^{top}(x, r)$  is the DSM error at the  $(x, r)$  location.

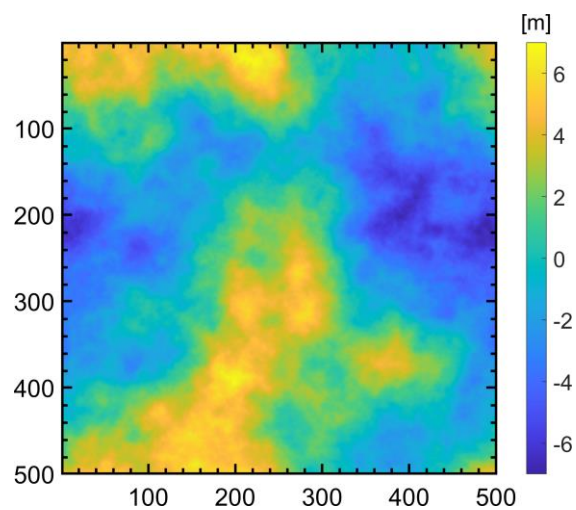
In InSAR data processing, an SRTM-derived (Farr & Kobrick, 2000) DSM is normally used of which vertical absolute error, linear vertical relative error, circular absolute geolocation error, and circular relative geolocation error have been reported less than 16 m, 10 m, 20 m and 15 m, respectively (Farr et al., 2007; Gesch et al., 2006; Smith & Sandwell, 2003). The 90% absolute error of SRTM has been reported to be better than 9 m that is based on a validation using available ground truth data (Farr et al., 2007; Rodríguez et al., 2005; Rodríguez et al., 2006). This assessment was carried out over six areas, including Africa, Australia, Eurasia, Islands, North America and South America, with the average value of 90% absolute error from those areas is 6.8 m (maximum of 9.0 m found in North America and minimum of 5.6 m found in Africa) (Farr et al., 2007; Rodríguez et al., 2005; Rodríguez et al., 2006). With validations carried out solely over Australia, similar results were derived (Hirt et al., 2010; Rexer & Hirt, 2014).

Table 7.1 shows examples of errors in InSAR interferograms caused by an assumed SRTM DSM error and other parameters corresponding to TSX and Sentinel-1 configurations. In Table 7.1, the satellites' altitudes have been used as examples for the range between the Earth's surface and satellite antenna positions. With a perpendicular baseline of 100 m and assumed SRTM DSM error of 10 m, the error in InSAR measurements caused by DSM error reaches the value of  $\sim 3$  mm. In InSAR SBAS, this type of error can be reduced by applying the methods as described in Section 3.3.2.3 and Subsection 4.4.3.

**Table 7.1.** Examples of error in InSAR interferograms caused by DSM uncertainties.

	TSX		Sentinel-1	
	example	range	example	Range
$B_{\perp}$ (m)	100		100	
$r$ (km)	515	505-533	700	697-726
$\theta$ (degree)	45	15-60	30	20-45
$\Delta Z^{top}$ (m)	10	$\pm 16$	10	$\pm 16$
$\phi^{top}$ (m)	0.0027		0.0029	

The Earth's topography behaves according to fractal statistics (Huang & Turcotte, 1989; Mandelbrot, 1982). The fractal surface theory is therefore applied to simulate topography that has been reported to be realistic (e.g., Mandelbrot, 1982; Massopust, 1990). DSM errors for 500×500 pixels was simulated from the aforementioned image ranging between  $-7$  m and  $+7$  m, corresponding to mean absolute height error computed over six areas of Africa, Australia, Eurasia, Islands, North America and South America (Farr et al., 2007; Rodríguez et al., 2005; Rodríguez et al., 2006). They are generated using fractal surface theory with the first step being the definition of an input sample set that will be used in the second step to construct the basic structure of the DSM uncertainty model. The fractal theory is then applied to interpolate DSM uncertainties to one-arc-second grids. These simulated uncertainties are shown in Figure 7.3.

**Figure 7.3.** Map of fractal surface simulated DSM error.

As described in Chapter 3, DSM uncertainties reflect the inaccuracy of the DSM model and other possible local effects, e.g., a significant change of height in the study area between the time the DSM was generated and the time the SAR scenes were acquired, e.g., due to open-cut mining or a building constructed after DSM acquisition. Also, this may be affected by the difference between the height of the pixel in the DSM model and that of the SAR reflection point, which is located in, e.g., a skyscraper. However, local effects are not considered in this study. Instead, interferogram errors due to DSM inaccuracy only are computed by applying Equation (7.4). For the sake of simplicity, it is assumed that the slant range ( $r$  in Equation (7.4)) equals 700 km and the look angle ( $\theta$  in Equation (7.4)) is 30 degrees. These values are assumed identical for all  $500 \times 500$  pixels. The maximum and minimum values of interferogram errors due to DSM uncertainties are +4 mm and -4 mm, respectively. An example of interferometric errors caused by simulated DSM uncertainties is shown in Figure 7.4.

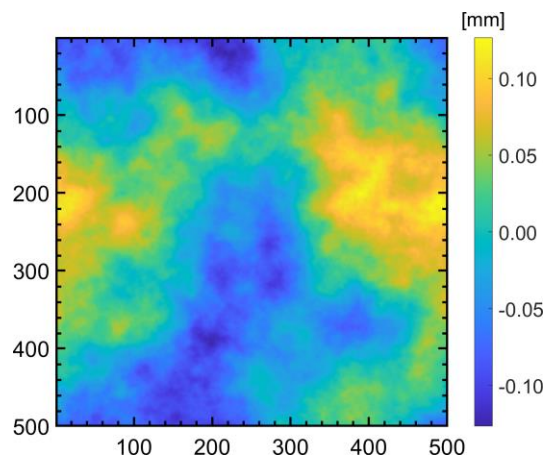


Figure 7.4. Interferogram errors caused by simulated DSM uncertainties in Figure 7.3 of the first interferogram.

### 7.2.3 Simulation of Atmospheric Artefacts

An atmospheric artefact is an error in phase delay caused when the InSAR signal propagates through the atmosphere. This is mainly attributable to the interaction of the signal with the ionosphere and troposphere (Gray et al., 2000; Hanssen, 2001; Mattar & Gray, 2002), and is considered to be one of the prominent error sources in InSAR (e.g., Zebker et al., 1997). For the sake of simplicity for this simulation, the simulated atmospheric artefact is assumed to be in homogeneous conditions and has a radially

symmetric property within the interferograms (Hanssen, 2001). The 1D covariance function proposed by Biggs et al. (2007) is applied that is expressed as:

$$C_{ij} = \sigma^2 e^{-\frac{d_{ij}}{\lambda}} \quad (7.5)$$

where  $C_{ij}$  and  $d_{ij}$  represent the covariance of the atmospheric artefact and the distance between two pixels  $i$  and  $j$ ,  $\sigma^2$  and  $\lambda$  are the variance and the wavelength of atmospheric delay, respectively.

2510 pairs of  $\sigma$  and  $\lambda$ , corresponding to 2510 interferograms, are simulated assuming that  $\sigma$  is within 5 mm and 15 mm and  $\lambda$  is within 5 km and 15 km following results from previous studies (e.g., Biggs et al., 2007; Hanssen, 2001; Lee et al., 2012; Lyons & Sandwell, 2003). Distributions of these values are shown in Figure 7.5 by histogram plots.

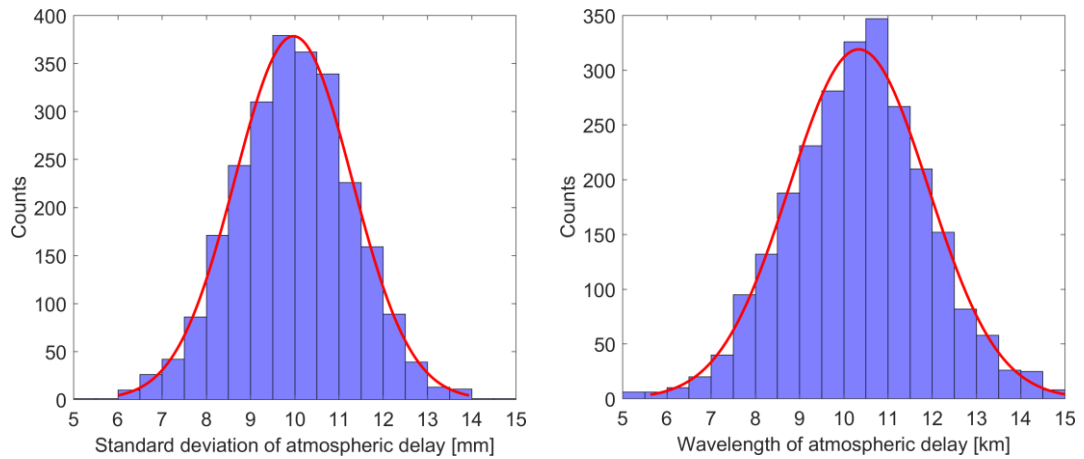
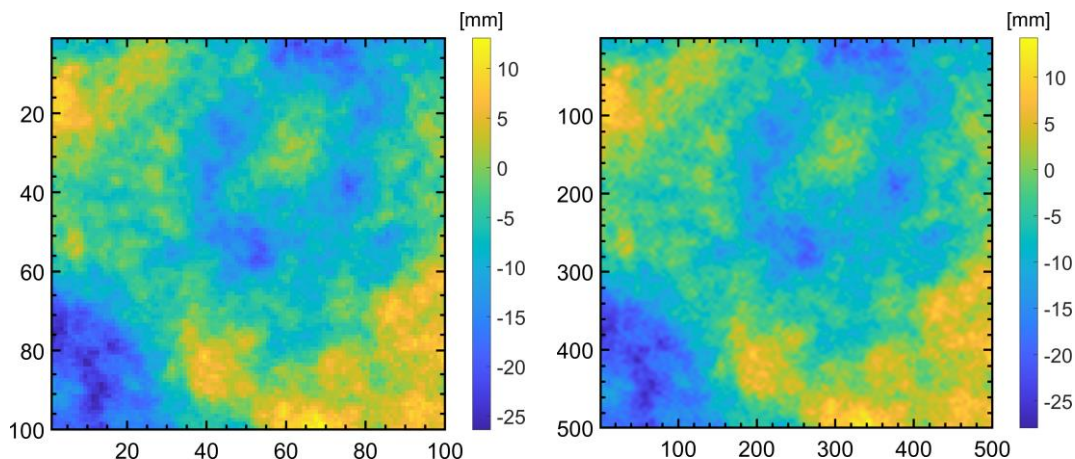


Figure 7.5. Histograms of standard deviation ( $\sigma$ ) (left) and wavelength ( $\lambda$ ) (right) of simulated atmospheric delays of 2510 interferograms.

For each interferogram, a matrix of  $2500 \times 2500$  in dimensions is required for the covariance matrix, resulting in a requirement on very large size of random-access memory (RAM). To avoid this, the image was down-sampled to  $100 \times 100$  pixels, i.e., with a five-arc-second resolution, for computation of covariances, then Cholesky decomposition (e.g., Dereniowski & Kubale, 2003; Golub & Van Loan, 1996) is applied to simulate the atmospheric artefacts. Interpolation by cubic splines (Hou & Andrews, 1978; Lam, 1983) was subsequently carried out to up-sample the image back to the one-arc-second resolution. The maximum and minimum values of interferograms atmospheric artefact are  $\sim 52$  mm and  $\sim -60$  mm, respectively. Figure

7.6 shows examples of atmospheric artefacts of the first interferogram at the down-sampled resolution of  $100 \times 100$  pixels (left) and at the full resolution of  $500 \times 500$  pixels (right).



**Figure 7.6.** Simulated atmospheric artefacts of the first interferogram at the down-sampled resolution of  $100 \times 100$  pixel (left) and at the full resolution of  $500 \times 500$  pixels (right).

#### 7.2.4 Simulated Orbital Error

Two InSAR images, which are chosen to generate an interferogram, are normally captured at different locations leading to a so-called baseline separation, and its effect needs to be removed in InSAR data processing. For this removal, the locations of InSAR images are used that can normally be accessed from a precise orbital ephemeris. However, even in case this precise information on satellite orbit has been used to reduce the baseline separation effect, baseline errors are still present (Biggs et al., 2007; Lee et al., 2012). For example, the best orbital products for European Remote Sensing (ERS) missions are of the precision of 50–70 mm in the radial component and 100–150 mm in the across track component (Scharroo & Visser, 1998). Sentinel-1 has been reported to have a more precise orbit ephemerides of 50 mm in 3D one-sigma RMS of position precision (Calero, 2018). A similar precision of 50 mm in precise orbit products was reported for TSX (Wermuth et al., 2012).

In InSAR data processing, a polynomial model can be used to model this orbital error (e.g., Fournier et al., 2011; Pritchard et al., 2002). An alternative method to account for this error is using other available data, e.g., GNSS (Gourmelen et al.,

2010). In this simulation study, the orbital error is simulated by applying the first-order polynomial (Biggs et al., 2007; Lee et al., 2012):

$$\phi^{orb}(x, r) = ux + vr + w \quad (7.6)$$

where  $\phi^{orb}(x, r)$  is the orbital error at a pixel located at radar coordinates  $(x, r)$ ,  $u$  and  $v$  are gradient parameters,  $w$  is the intercept (offset) parameter.

The first gradient parameter  $u$  is set at the range of  $[-2, +2]$  mm/km and the second one  $v$  is limited to  $[-1, +1]$  mm/km. The offset parameter is simulated with the range  $[-10, +10]$  mm following the results from Biggs et al. (2007). A dataset of 332 values for each parameter  $u$ ,  $v$  or  $w$ , corresponding to 332 InSAR images, is simulated following a Gaussian distribution with zero-mean. The orbital error of the interferogram connecting  $i^{th}$  and  $j^{th}$  SAR images is then calculated by:

$$\phi_{ij}^{orb}(x, r) = \phi^{orb}(t_i, x, y) - \phi^{orb}(t_j, x, y) \quad (7.7)$$

where  $\phi^{orb}(t_i, x, y)$  and  $\phi^{orb}(t_j, x, y)$  are the orbital errors of a pixel located at radar coordinates  $(x, r)$  from InSAR images acquired at times  $t_i$  and  $t_j$ , respectively. The maximum and minimum values of orbital error for interferograms are  $\sim 34$  mm and  $\sim -38$  mm. An example of simulated interferometric orbital errors is shown in Figure 7.7.

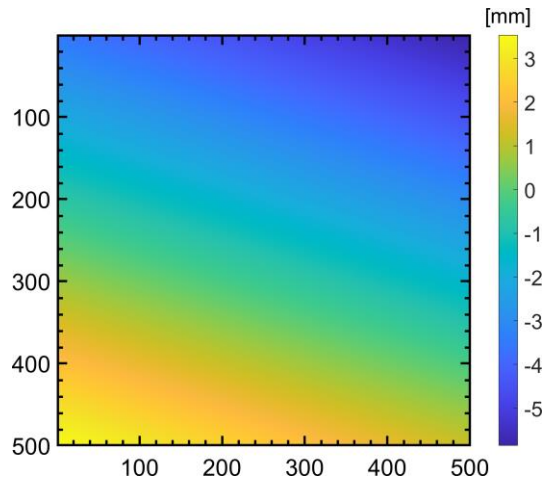


Figure 7.7. Simulated orbital errors of the first interferogram.

### 7.2.5 Simulation of Temporal Decorrelation

The temporal decorrelation shown in Equation (7.1) is the loss of interferometric coherence with time resulting from physical changes in the surface reflectivity due to various causes, such as vegetation growth, precipitation, snow, soil moisture and other

environmental factors between two SAR image acquisitions (Santoro et al., 2010). This decorrelates the InSAR measurements resulting in reduced quality of the InSAR data. This particularly reduces the reliability of InSAR data over vegetated areas caused by the change in relative positions of scatters in pixels (Zebker & Villasenor, 1992). In order to simulate temporal decorrelation, an approximation of InSAR phase variance resulting from temporal decorrelation suggested by Rodríguez and Martín (1992) is applied, which is expressed as:

$$\sigma_{\phi}^2 = \frac{1 - \gamma_T^2}{2N\gamma_T^2} \quad (7.8)$$

where  $\sigma_{\phi}^2$  is the phase variance caused by temporal decorrelation,  $N$  is the number of looks used in multi-looking technique to reduce speckle noise in interferograms,  $\gamma_T$  is the temporal correlation that can be simulated following Lee et al. (2012) as:

$$\gamma_T = e^{-3 \times 10^{-4} \Delta t} \quad (7.9)$$

where  $\Delta t$  is the time separation of the two InSAR images used to generate the interferogram. In this study, the maximum value of  $\Delta t$  is  $\sim 90$  days, which is equivalent to the temporal baseline threshold used for interferogram selection, while the minimum value is  $\Delta t = 12$  days, which is the time sampling interval of the simulated imagery.

A dataset of 2510 values of temporal correlation is computed first by applying Equation (7.9), with maximum and minimum values of 1.00 and 0.97. For each interferogram, Equation (7.8) is then applied to calculate the phase variance, with an assumption of the radar wavelength to be  $\lambda = 0.055$  m, which is equivalent to that of Sentinel-1. The maximum and minimum values of deformation variance are  $\sim 0.25$  mm and  $\sim 0.72$  mm. Finally, temporal decorrelation is randomly simulated following a Gaussian distribution with zero-mean and variance from the above computation. The maximum and minimum values of temporal decorrelation are  $+4$  mm and  $-4$  mm, respectively. An example of interferometric temporal decorrelation is shown in Figure 7.8.

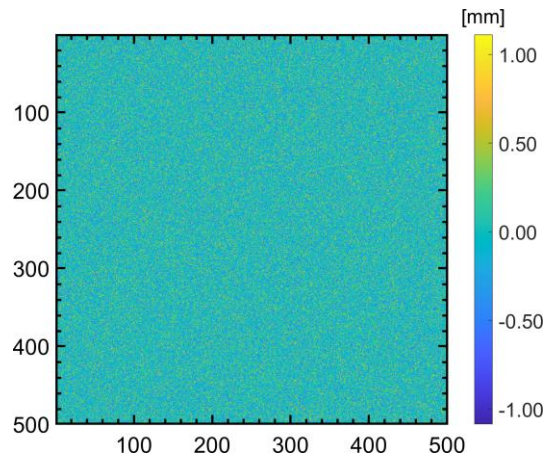


Figure 7.8. Simulated temporal decorrelation of the first interferogram.

### 7.3 InSAR Data Processing

The simulated error and noise sources in interferograms, comprising DSM-induced errors, atmospheric artefacts, orbital errors, and temporal decorrelation are algebraically summed up (assuming independence) and added to the noiseless interferograms described in Subsection 7.2.1 to create 2510 “noisy” interferograms by Equation (7.1). Figure 7.9 shows the first noisy interferograms as an example. The SBAS method incorporated in the GIANt software is applied to InSAR time series analysis for the whole image on a pixel-by-pixel basis.

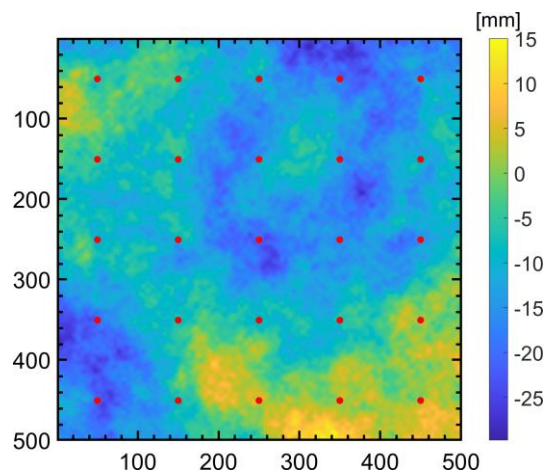


Figure 7.9. Noisy deformation map of the first interferogram. Red dots are 25 pixels that are selected to be regularly distributed over the whole image used for displaying results at individual pixels as examples in the following sections.

Deformation time series in the LoS direction are then derived for all 500×500 pixels. The noise analysis of deformation time series will then be conducted using the CATS package.

## 7.4 Noise Analysis of Simulated Deformation Time Series

In this Section, the noise in deformation time series derived from simulated InSAR data is analysed by the MLE method incorporated in the CATS package. In CATS, the functional model can be a combination of various types including an intercept, a slope, abrupt steps and periodic terms. Additionally, different noise models are also incorporated in CATS that have been listed and described in [Williams \(2008\)](#), including white, variable white, step-variable white, time-variable white, power-law, first-order Gauss Markov, generalised Gauss Markov and band-pass.

### 7.4.1 Deformation Rates, Amplitudes and Their Uncertainties Computed by CATS

Deformation time series of the 500×500 pixels are analysed for their noise patterns as well as functional model parameters. Those pixels cover a 10-year time span with a 12-day interval, indicating that there are 332 data points in each pixel which is larger than the limit of 256 set by [Williams et al. \(2004\)](#). A functional model combining linear and annual terms, which is consistent with the assumed model in the simulation stages (Equation (7.2)), is used that can be expressed as (e.g., [Bock et al., 2012](#); [Didova et al., 2016](#); [Langbein, 2004](#)):

$$d(t_i, x, r) = \alpha(x, r) + v(x, r)t_i + s(x, r)\sin(2\pi t_i) + c(x, r)\cos(2\pi t_i) \quad (7.10)$$

where  $\alpha(x, r)$  and  $v(x, r)$  are an intercept and a slope that constitute a linear trend in the model,  $s(x, r)$  and  $c(x, r)$  are annual term coefficients. By running CATS, these functional model parameters are estimated together with other parameters relating to the white and coloured noise model that will be shown and discussed in the following Subsection 7.4.2. For each pixel, the annual rate or velocity is represented by a slope  $v(x, r)$ , while the annual amplitude can be estimated by (e.g., [Davis et al., 2012](#)):

$$A(x, r) = \sqrt{[s(x, r)]^2 + [c(x, r)]^2} \quad (7.11)$$

[Figure 7.10](#) compares deformation rates (top panel) and amplitudes (bottom panel) over 500×500 pixels estimated by the CATS software (left panel) with simulated ones (right panel). The results indicate identical patterns between the two data sets, which include both the trends (i.e., deformation or uplift) and the magnitudes of deformation rates and amplitudes of annual sinusoids. A positive rate represents uplift while a negative one indicates subsidence.

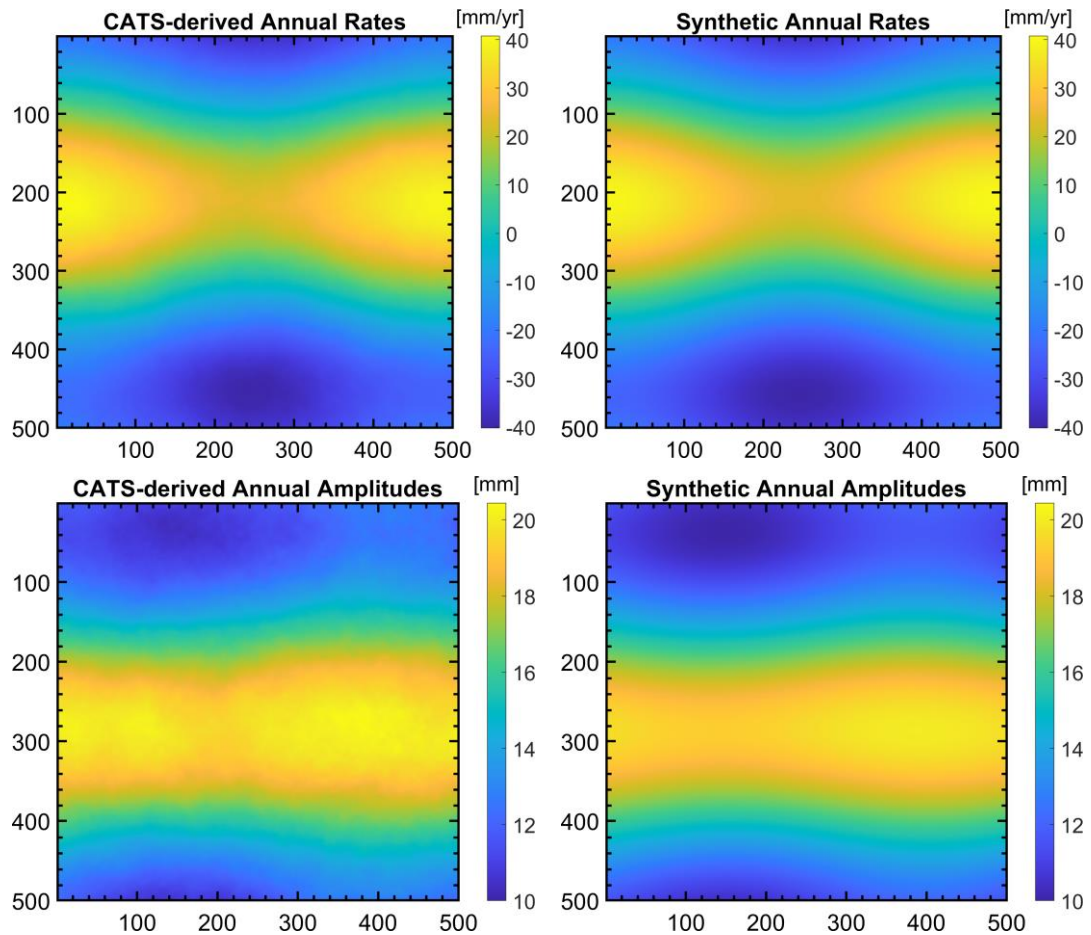


**Figure 7.10.** Comparison between CATS-derived and simulated deformation rates and annual sinusoidal amplitudes. CATS-derived annual rates (top-left) and amplitudes (bottom-left) are compared with corresponding synthetic parameters (right panel).

The statistics of the errors in rate and amplitude determinations are shown in [Table 7.2](#). Here, the errors are defined by the difference between simulated values and those derived by CATS. The rate errors indicate maximum and minimum values of 2.7 mm/yr and  $-2.8$  mm/yr with a standard deviation of  $\pm 0.9$  mm/yr. The rates have been simulated within the range of  $[-40, +40]$  mm/yr. Maximum and minimum values and standard deviation of the amplitude errors are 0.2 mm,  $-1.3$  mm, and  $\pm 0.2$  mm. The amplitudes have been simulated between 10 mm and 20 mm.

**Table 7.2.** Statistics of the errors in rate and amplitude determinations. Errors are the subtraction of simulated quantities derived by CATS from simulated ones.

Statistics	Annual rate error [mm/yr]	Annual amplitude error [mm]
Max	2.7	0.2
Min	-2.8	-1.3
Mean	0.0	-0.4
STD	$\pm 0.9$	$\pm 0.2$

Functional parameters retrieved from CATS are used to reconstruct deformation time series using Equation (7.10) from which simulated, SBAS-derived and CATS-retrieved time series are compared and shown in [Figure 7.11](#) for 25 pixels selected from [Figure 7.9](#) as examples.

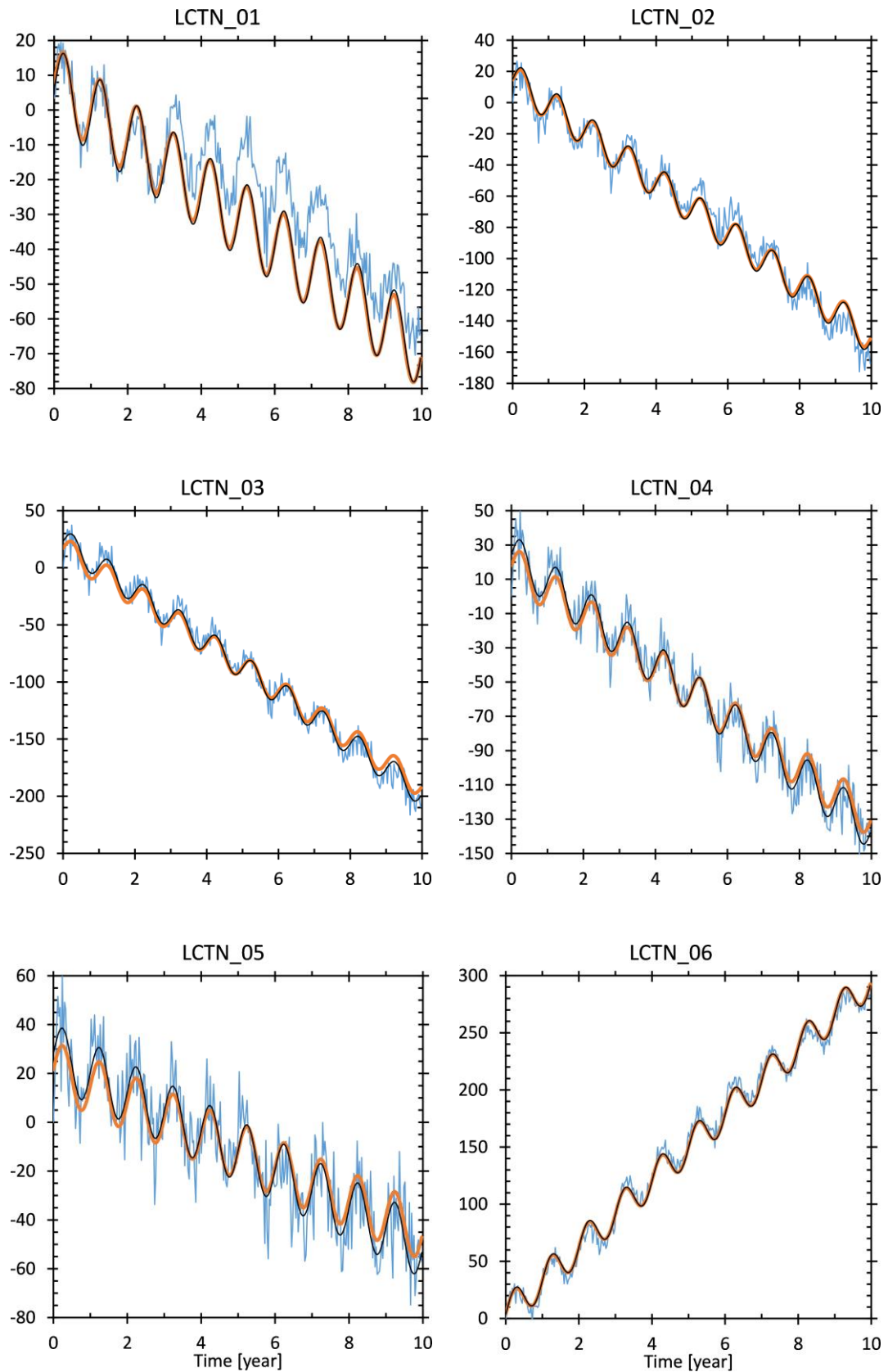


Figure 7.11. Synthetic (yellow lines), SBAS-retrieved (blue lines) and CATS-derived (black lines) deformation time series for 25 pixels regularly distributed over the image in Figure 7.9. (unit: mm).

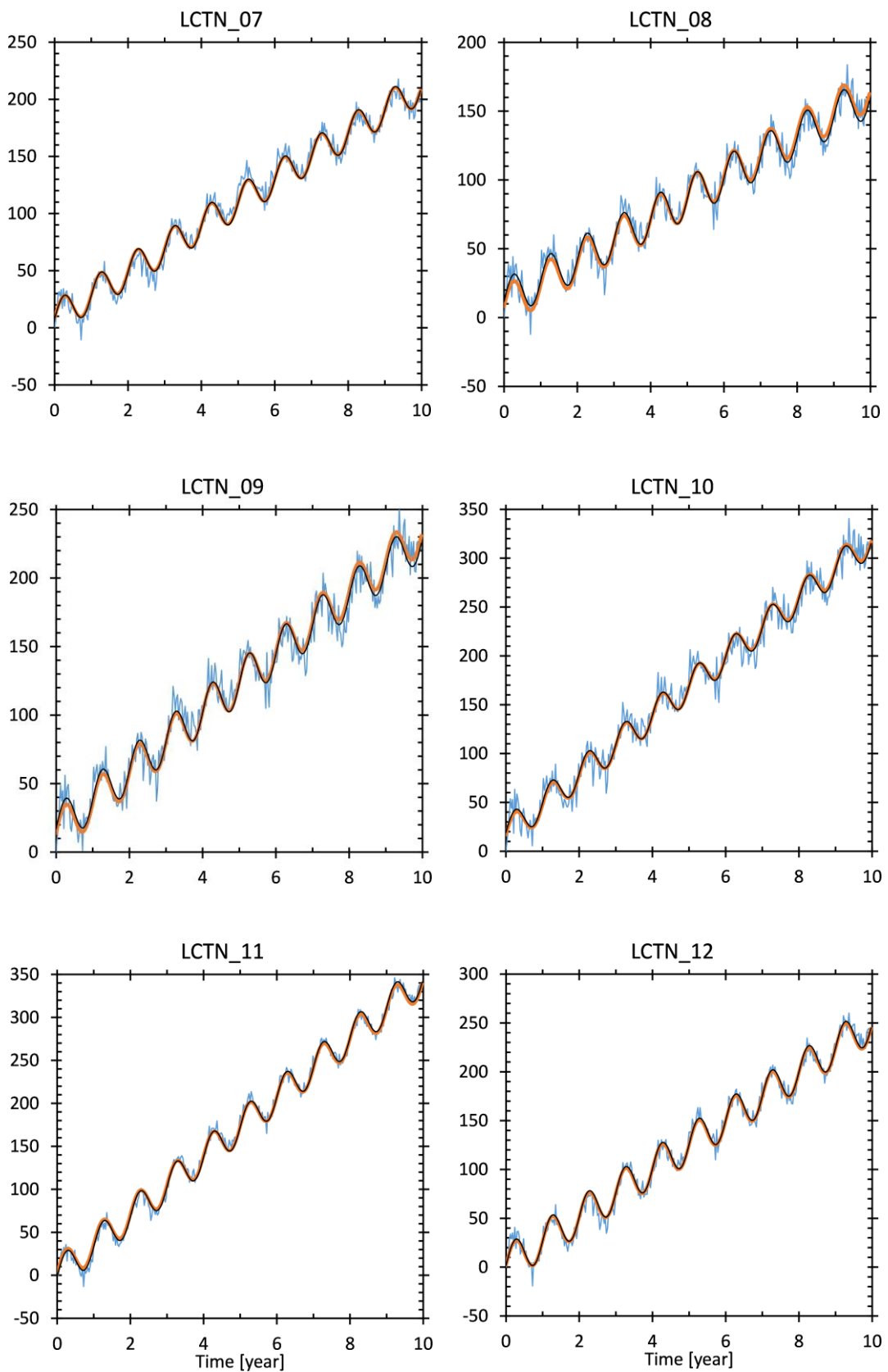


Figure 7.11. (Continued).

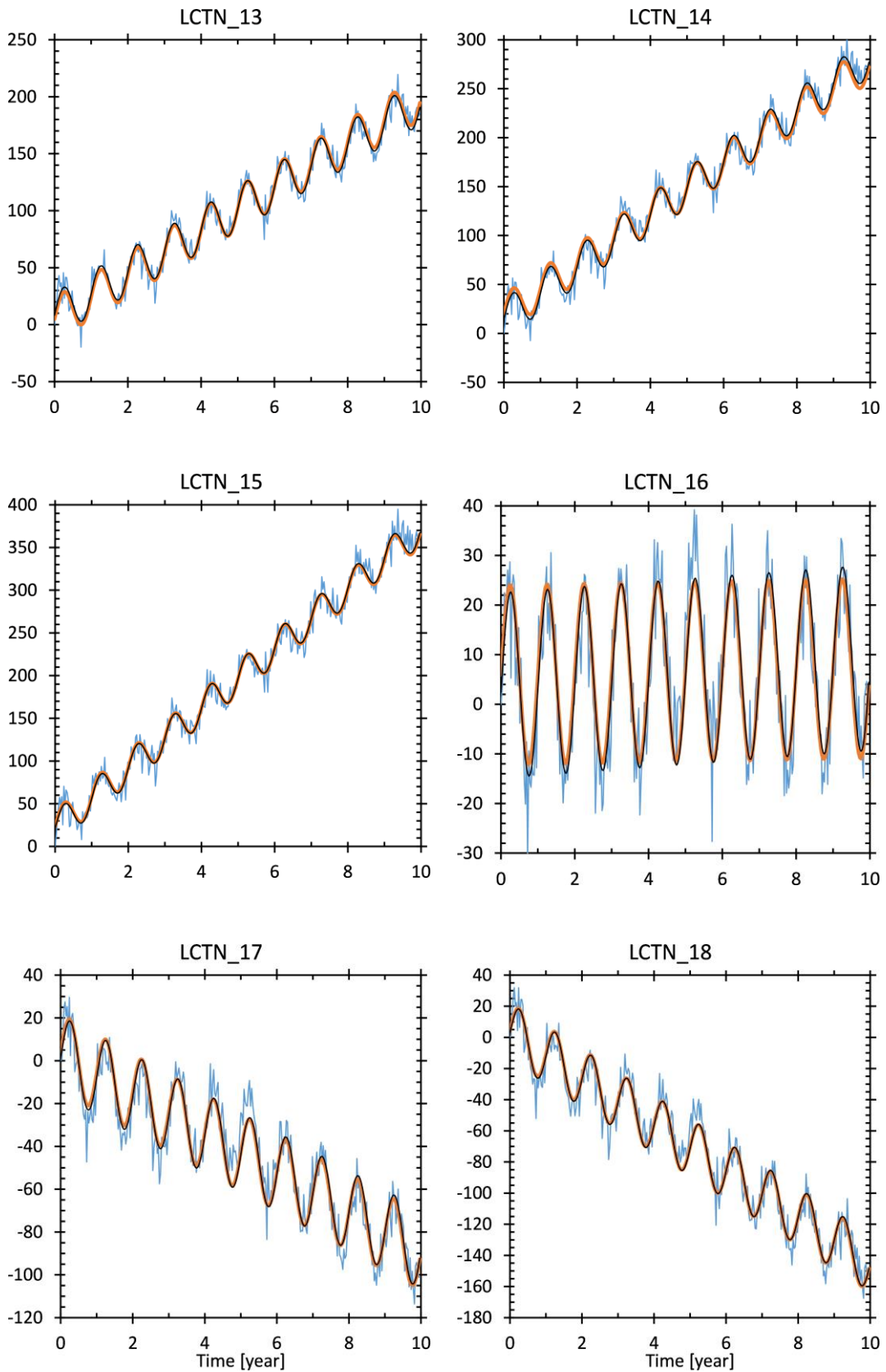


Figure 7.11. (Continued).

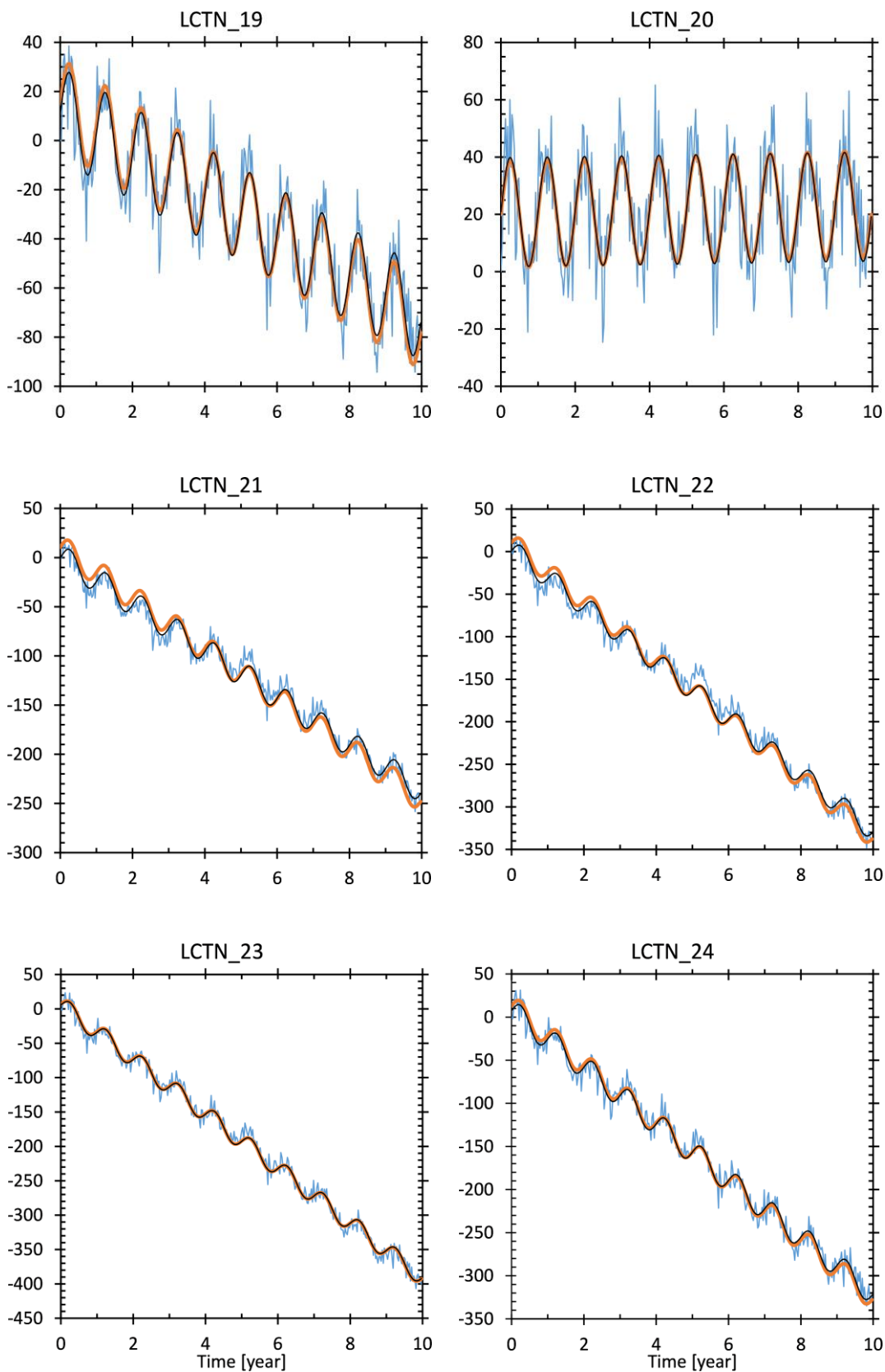


Figure 7.11. (Continued).

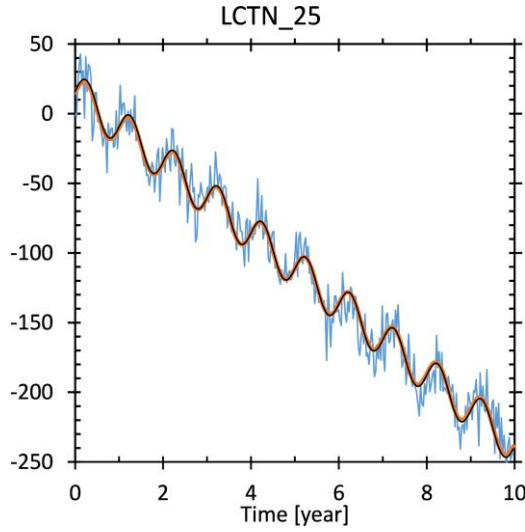


Figure 7.11. (Continued).

#### 7.4.2 Noise Amplitude and Spectral Indices

Noise analysis is conducted in this study by applying MLE incorporated in the CATS package. The reasons for utilising this method are the advantages described in Section 7.1 that, by applying MLE, the time-dependent functional model parameters, introduced in Subsection 7.4.1, and the noise parameters are estimated simultaneously. The noise model applied in this study is white plus coloured noise of which non-integer spectral index and amplitude of power law noise are estimated by CATS. The reason for applying this noise model is that it is a more general case than just fixing the spectral index to be an integer, e.g., in the white plus flicker noise or white plus random-walk noise models (Williams, 2003).

The statistics of those quantities estimated by running CATS for the entire set of  $500 \times 500$  pixels, including white and coloured noise amplitudes and spectral indices are summarised in Table 7.3. These results are derived from noise analysis applying to the post-fit residuals, i.e., the data after eliminating linear plus annual signal, by maximising their likelihood values computed by (e.g., Williams et al., 2004):

$$lik(\hat{\mathbf{v}}, \mathbf{C}) = \frac{1}{(2\pi)^{N/2} (\det \mathbf{C})^{1/2}} \exp(-0.5 \hat{\mathbf{v}}^T \mathbf{C}^{-1} \hat{\mathbf{v}}) \quad (7.12)$$

where  $\hat{\mathbf{v}}$  are the post-fit residuals between original time series and that computed from the functional model combining linear and annual signals,  $\mathbf{C}$  is the covariance matrix,  $N$  is the number of points in the time series corresponding to the number of images in

this study. In this research,  $\mathbf{C}$  is of the form that combines white and coloured noise components expressed as (e.g., Williams, 2003):

$$\mathbf{C} = a_w^2 \mathbf{I} + b_\kappa^2 \mathbf{J}_\kappa \quad (7.13)$$

where  $a_w$  and  $b_\kappa$  are the amplitudes of white and coloured noise,  $\mathbf{I}$  is the identity matrix,  $\mathbf{J}_\kappa$  is the covariance matrix of coloured noise, and  $\kappa$  is the spectral index.

**Table 7.3.** Statistics of white and coloured noise amplitudes and power law spectral indices estimated by CATS.

Statistics	White noise sigma ( $a_w$ ) [mm]	Coloured noise sigma ( $b_\kappa$ ) [mm/yr $^{\kappa/4}$ ]	Spectral Index ( $\kappa$ )
Max	9.4	8.1	0.0
Min	3.8	0.1	-3.0
Mean	6.4	3.8	-0.8
STD	$\pm 0.8$	$\pm 1.4$	$\pm 0.3$

Figure 7.12 shows histograms of white and coloured noise amplitudes and Figure 7.13 compares pixel-wise magnitudes of the two noise types. From Table 7.3, Figure 7.12, and Figure 7.13, the noise can be seen to be dominated by white noise of which the amplitudes range between 3.8 mm and 9.4 mm with a mean value of 6.4 mm. The coloured noise amplitudes vary between 0.1 mm and 8.1 mm with a mean value of 3.8 mm.

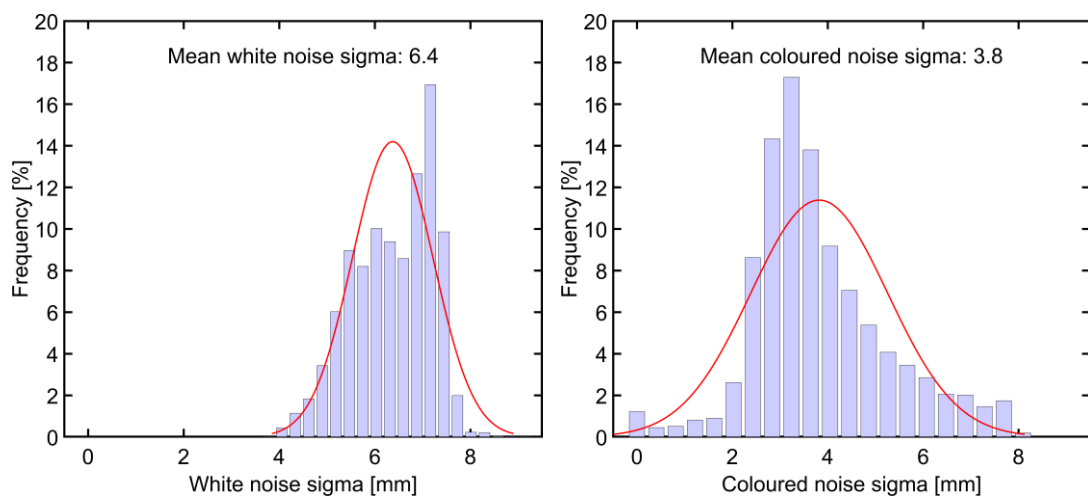


**Figure 7.12.** Histograms of white noise amplitudes (left) and coloured noise amplitudes (right).

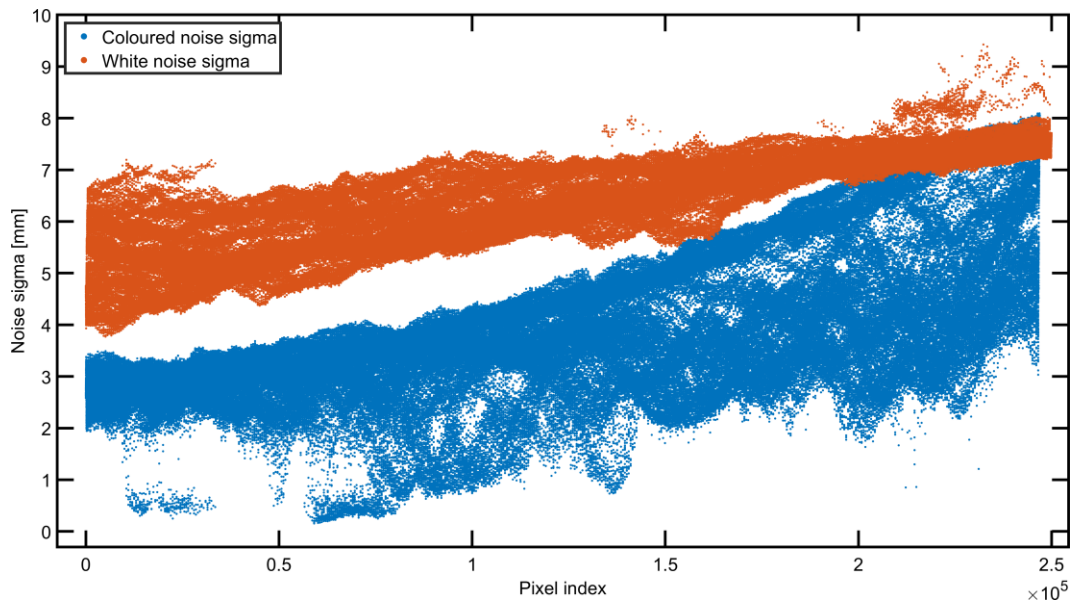


Figure 7.13. Comparison between white and coloured noise magnitudes over  $500 \times 500$  pixels. Pixel indices are set from top to bottom and left to right over the image.

Figure 7.14 shows spatial patterns (left panel) and the histograms of power law spectral indices estimated by running CATS over the entire image of  $500 \times 500$  pixels. The spectral indices vary between  $-3$  and  $0$  with a mean value of  $-0.8$  that is closer to flicker noise ( $\kappa = -1$ ) than random walk noise ( $\kappa = -2$ ).

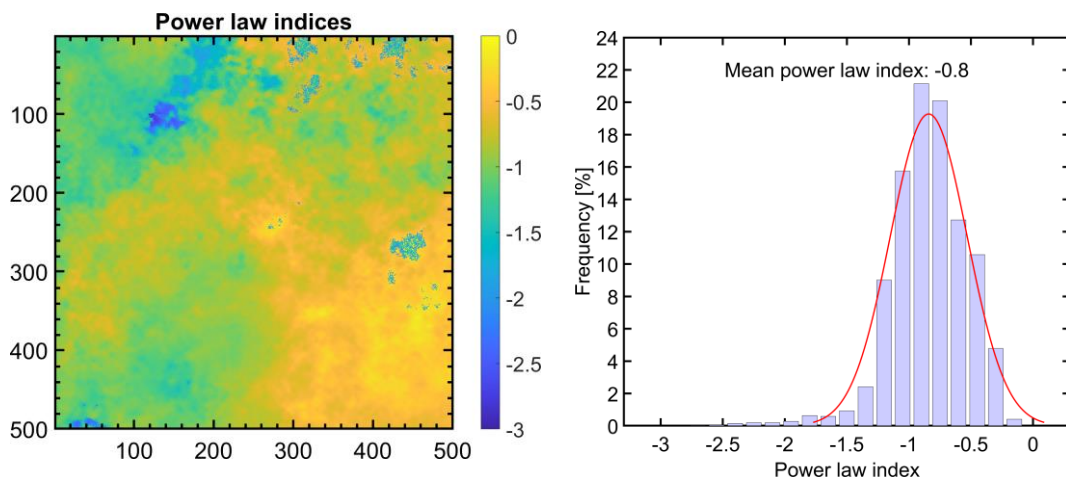
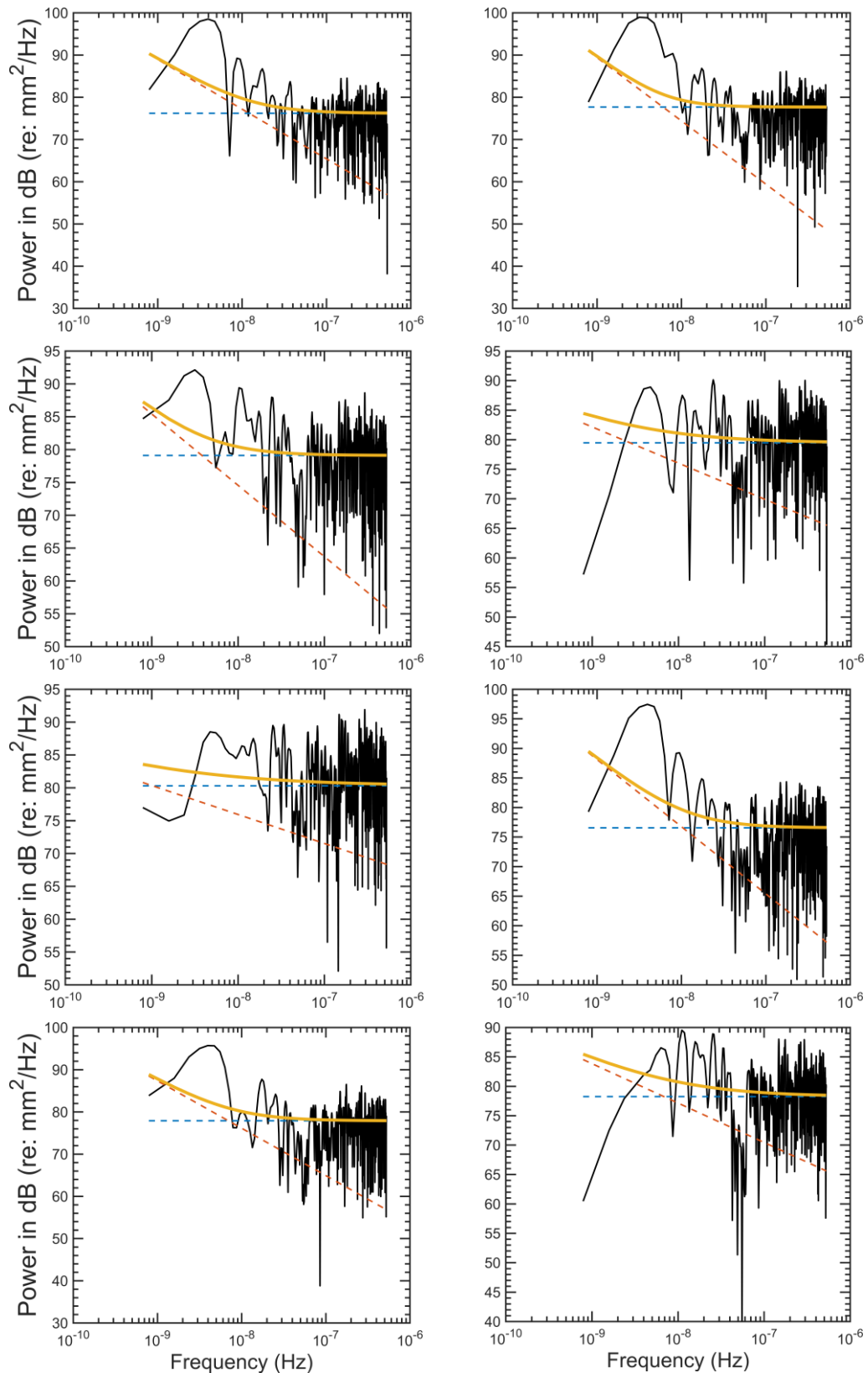


Figure 7.14. Spatial patterns (left) and histograms (right) of power law spectral indices tested over the entire image of  $500 \times 500$  pixels.

Experimental power spectral density (PSD) over the 25 regularly distributed pixels (see Figure 7.9) are shown in Figure 7.15 by black polylines, which is subsequently used for fitting the noise model by the MLE algorithm from which the

spectral indices are estimated. In [Figure 7.15](#), the theoretical PSD of white noise and coloured noise only are represented by blue and orange dashed lines, while solid yellow lines indicate the PSD of the combined model. Over the 25 pixels, the intersections between blue and orange dashed lines are referred to as crossover PSD between white and coloured noise, which is defined as the frequency where the power levels of these two types of noise are equal. In each pixel, the PSD is dominated by white noise at frequencies higher than this crossover frequency and the PSD of coloured noise is, in contrast, dominant in the other case. Combined with the spectral indices shown in [Table 7.3](#), the power spectra can be best described as the combination of white noise plus flicker noise.



**Figure 7.15.** Power spectral density in the deformation residuals of the 25 studied locations shown in [Figure 7.9](#). Blue and orange dashed lines represent the power of white noise and coloured noise with their combination indicated by yellow solid lines. The subfigures are arranged from top to bottom and left to right corresponding to pixels order from location-01 to location-25 in [Figure 7.9](#).

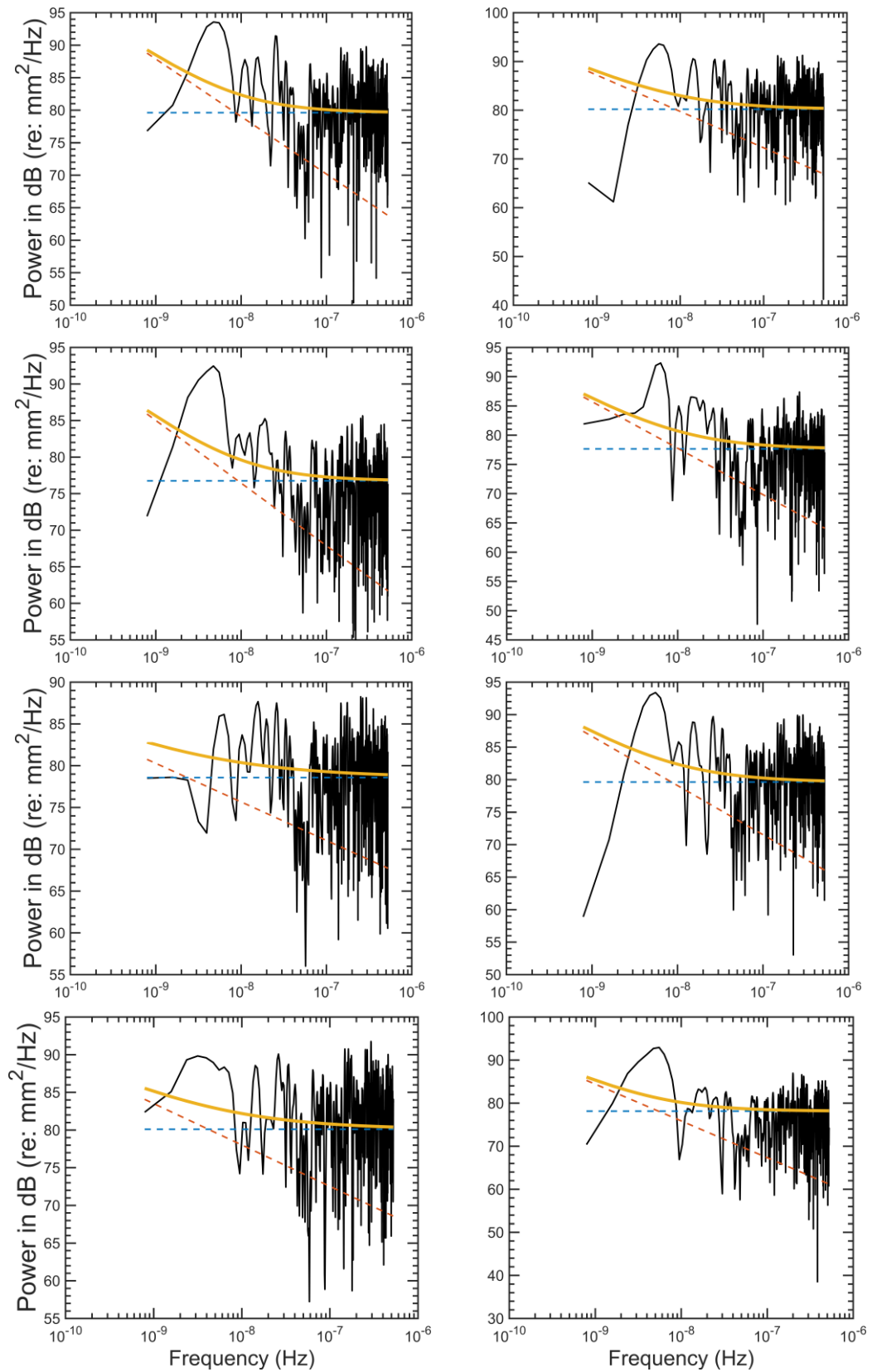


Figure 7.15. (Continued).

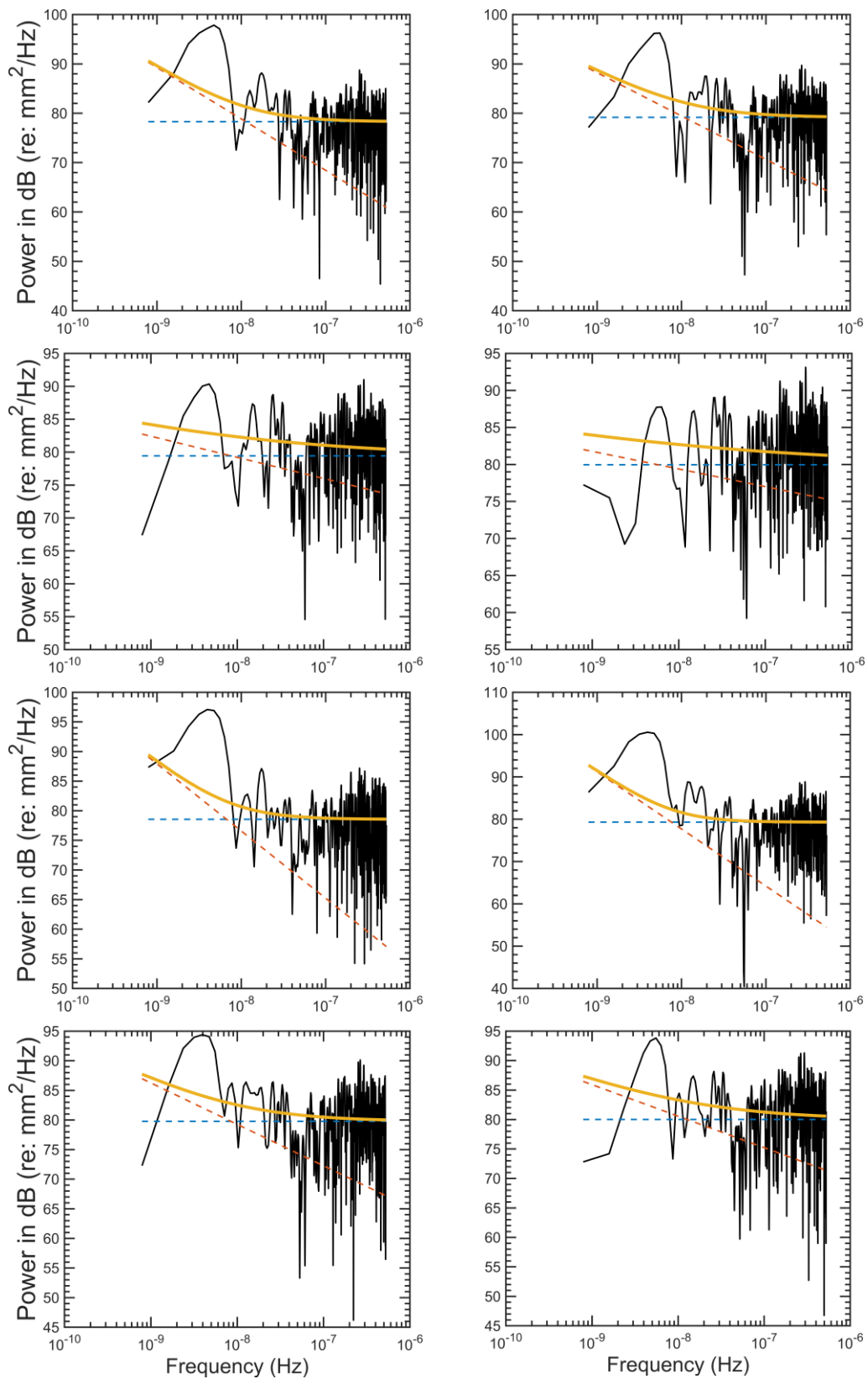


Figure 7.15. (Continued).

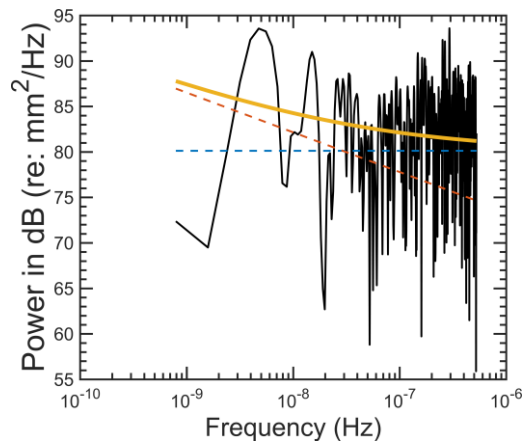


Figure 7.15. (Continued).

## 7.5 Chapter Summary

In this Chapter, the type of noise has been analysed based on simulated InSAR data including a signal following linear plus annual sinusoidal model and different error and noise sources. Those sources incorporated in the simulated model include interferogram error due to DSM uncertainties, atmospheric artefacts, orbital error and temporal decorrelation. Simulated deformation rates are assumed to be bounded by  $-40$  mm/yr and  $+40$  mm/yr, while the amplitudes of the annual signal are limited to be from 10 mm to 20 mm. 332 images of  $500 \times 500$  pixel size covering a 10-year period with a 12-day interval were simulated so as to be larger than the limit of 256 set by [Williams et al. \(2004\)](#).

After removing both linear and annual signals from the data, there are two noise types included in residuals that are both time-correlated and time-uncorrelated. The amplitude is dominated by white noise. Specifically, the amplitudes of white noise over the entire image of  $500 \times 500$  range between 3.8 mm and 8.4 mm, while those of coloured noise range from 0.1 mm to 8.1 mm. Spectral indices of coloured noise vary between  $-3.0$  and  $0$  with a mean value of  $-0.8$ .

It is demonstrated through this simulation study that the noise model should be best described by white plus coloured noise. Because of the existence of coloured noise in residuals time series, this source needs to be considered in the InSAR deformation time series modelling and interpretation and error estimation.

## 8. SUMMARY, CONCLUSIONS AND RECOMMENDATIONS

This dissertation has dealt with simulations of InSAR SBAS data to: 1) study the influence of residual interferometric error and noise and data gaps on SBAS-derived deformation rates and time series in Chapter 5; 2) the use of redundancy numbers to design an InSAR SBAS network in Chapter 6; and 3) carried out noise analysis of InSAR SBAS-derived deformation time series in Chapter 7. This final Chapter summarises the conclusions gained from the investigations conducted in this dissertation in Section 8.1 and recommends some further studies in Section 8.2.

### 8.1 Conclusions

#### 8.1.1 Influence of Simulated Residual Interferometric Errors and Noise on SBAS InSAR

The investigation on the influence of residual interferometric errors and noise on SBAS-derived deformation rates and time series was motivated by interferometric error and noise sources, which can be reduced by numerous methods but cannot be corrected completely, resulting in residuals. These residuals have an influence on SBAS results, particularly in the case of signals of a small deformation rate. As summarised in Chapter 3, InSAR interferograms are formed by combining two images and, in SBAS, even though they are of small temporal and/or perpendicular baselines, errors and noise still exist. In general, these error and noise sources include DSM uncertainties, atmospheric artefacts, orbital error, temporal and spatial decorrelation, and other noise.

In Chapters 3 and 4, the methods applied to reduce these errors and noise in SBAS were summarised and, as mentioned above, they cannot be employed perfectly. Therefore, in Chapter 5, simulated residual interferometric errors and noise assumed bounded within  $[-2; +2]$  mm,  $[-5; +5]$  mm and  $[-10; +10]$  mm were tested for their influence on SBAS-derived deformation rate and time series. This was examined with an InSAR signal simulated relying on a linear trend and a superposed annual sinusoidal oscillation of  $-2$  mm/yr plus 2 mm,  $-20$  mm/yr plus 5 mm, and  $-100$  mm/yr plus 10 mm. The experimental results from GIANt showed that the SBAS linear-fit deformation trends are sensitive to both the magnitude of residual interferometric noise and the deformation signal size. In particular, the trend may be contradictory when a

network with fewer interferograms is applied to low SNR, which results in a less robust SBAS network.

In the case of linear plus annual periodic signal contaminated by residual interferometric noise, linear-only-fit rates were biased compared to the simulated rates. In contrast, when a more appropriate functional model was adopted (i.e., linear plus annual) rather than just linear regression, the estimated rates were not biased indicating the potential for errors to be introduced by using a simple linear regression in the presence of a non-linear deformation signal.

The investigation on the influence of data gaps on SBAS InSAR was motivated by the likelihood of irregular temporal sampling of SAR data due to scheduling or other technical issues, such as temporal decorrelation during winter snow cover, and whether or not this influence is significant. Chapter 5, therefore, assessed this influence by simulating data gaps in the series of SAR images. Two cases were 1) random because of satellite mission scheduling issues and 2) blocks of missing images over a northern winter period. The simulation results showed that “winter gaps” cause a larger rate error and RMSs of the difference between simulated and SBAS-derived deformation time series compared to randomly missing acquisitions.

When the same number of interferograms were employed, which are chosen relying on temporal baseline thresholds and due to random data gaps, the results showed that the random data gaps resulted in lesser influence, indicating that the SBAS network configuration is more important. This is because the trade-off may be a geometrically weak SBAS network that is vulnerable to incorrect rate estimation in the presence of noisy data and non-linear deformation.

In comparison between SBAS networks selected based on temporal and perpendicular baseline thresholds and other types of interferogram networks, linear-fit rates from SBAS networks and hierarchical thresholds networks were identical. In contrast, the results from Delaunay triangulations and a minimum spanning tree were better. This is because it is assumed in this dissertation that interferograms with smaller baseline lengths are of smaller noise, and thus the Delaunay triangulation and minimum spanning tree networks incorporate interferograms with the smallest simulated noise. However, these two types of networks have their limitations. The minimum spanning tree network involves independent interferograms only, and thus it is impossible to detect unwrapping errors via computing the sum of the interferogram

loop. The Delaunay triangulation networks will be disconnected if small baseline thresholds are employed.

Like the SBAS networks, the networks of Delaunay triangulation, hierarchical thresholds and a minimum spanning tree were all affected by the nonlinearity of deformation signal that biases in rate errors are existent if the linear-fit rates are estimated. However, these biases will be removed if LS is applied with the appropriate functional model.

### 8.1.2 Design of InSAR SBAS Interferogram Networks

The design of InSAR SBAS interferogram networks examined in Chapter 6 was motivated by interferogram networks used in the literature, which were based on baseline thresholds that are often applied arbitrarily, or in an apparently subjective way. The summary of previous SBAS applications shown in Table 4.1 indicates that the temporal baseline threshold has been chosen varying from months to years, while the perpendicular baseline threshold has been chosen ranging between hundreds of metres and over one kilometre. This is reinforced by the investigation of the influence of residual interferometric errors and noise on SBAS InSAR in Chapter 5 that a contradictory trend may be derived if a network of fewer interferograms is applied with low SNR signal, in which more interferograms are needed.

The question then arose as to whether there are some more objective means by which to select these thresholds, which was considered in Chapter 6. This is also based on the finding in Chapter 5 that more interferograms used will result in smaller rate errors as well as RMSs of the difference between simulated and SBAS-derived deformation time series, but also increase the computational burden and require larger disk storage. As such, the redundancy number ( $r$ -number) used to design an “optimal” SBAS network to keep a minimal number of interferograms as possible in order to save processing time and disk storage was studied.

The background on the design of geodetic networks was reviewed in Section 6.1. This can be classified into the zero-order design targeting at an optimal reference system, the first-order design used to choose the best locations of network points, the second-order design to select optimal weights for observations, and the third-order design to improve, extend or densify an existing network in an optimal way by introducing new points and/or additional measurements. They can also be classified relying on the approach of using one or more objective functions, which are a single-

objective optimisation model, a bi-objective optimisation model or a multi-objective optimisation model.

The  $r$ -number was chosen as a diagnostic metric to determine the likely effectiveness of the SBAS network design in Chapter 6. The same simulations as those used in the previous investigations of the influence of residual errors and noise and data gaps on InSAR SBAS (i.e., in Chapter 5) were employed for this investigation. Interferogram networks determined by combinations of temporal baseline thresholds, from one month to four years long, with a one-month increment, and perpendicular baseline thresholds of 100 m, 200 m, and 300 m were tested. As a result, 144 networks were formed with the minimum and maximum number of interferograms being 251 and 8778, respectively.

The simulation results showed that  $r$ -values greater than  $\sim 0.8$  or  $\sim 0.9$  indicated a robust SBAS network design, and that including more interferograms beyond this provided little improvement in the precision of the rate estimation. Notably, an alarming artifact in a couple of different simulation scenarios was found, where uplift was indicated by the SBAS rather than true simulated subsidence. It, therefore, appears that the configuration (network design) is more important than simply the number of interferograms used, which is important given any limits on computing resources. For this reason, the use of  $r$ -numbers to help optimise SBAS network design is recommended.

In comparison with other types of interferogram networks of Delaunay triangulation, hierarchical thresholds and a minimum spanning tree, the results indicated that the  $r$ -number-based optimal network design approach did not work with these network types in terms of the precision represented by errors in rate determination. This is because low rate errors were found but low  $r$ -numbers were also estimated. However, this approach was useful from the other geodetic point of view of gross error detection that even good results of linear-fit and LS rates were achieved, most of these networks were of zero  $r$ -numbers due to some or all independent interferograms being included. The networks with independent interferograms should not be employed because if gross errors occur in those independent interferograms, they cannot be detected. Also, the method of detecting unwrapping errors based on the interferogram close loop (Subsection 4.3.3) is inapplicable.

### 8.1.3 Noise Analysis of Simulated InSAR Deformation Time Series

The third investigation on the noise analysis of InSAR deformation time series was motivated by correlated/coloured noise, which has been proven to exist in other geodetic data, e.g., GNSS, trilateration, or electronic distance measurements. It was also demonstrated that the uncertainties of functional model parameters, e.g., deformation rate or periodic coefficients, may be underestimated if a white-noise-only model is applied to the correlated data. In contrast, in InSAR SBAS data processing, deformation rates are often derived by fitting a linear regression to the deformation time series, i.e., an uncorrelated noise model is assumed. This assumption will be incorrect if the noise is of a type other than just white noise, e.g., coloured noise or a combination of coloured and white noise.

The motivation of this part of the simulation investigation was also that in InSAR SBAS data processing, noise models have been developed for InSAR interferograms, which can be applied to SBAS inversion to estimate the deformation phase of acquisitions and DSM error. However, a stochastic noise model used in the further step of deformation parameter estimation has not been investigated to date, apart from [Filmer et al. \(2020\)](#). The noise analysis was conducted in Chapter 7, relying on another data simulation, which was different to that employed in the previous investigations in Chapters 5 and 6. This was with the aim of quantifying the influence of residual interferometric noise at different signal-to-noise ratios (SNRs) on InSAR SBAS results, the interferometric noise used in Chapters 5 and 6 was simulated bounded within different assumed ranges of  $[-2, +2]$  mm,  $[-5, +5]$  mm and  $[-10, +10]$  mm.

In contrast, with the aim of analysing the type and quantifying the magnitude of noise in InSAR SBAS deformation time series, the interferometric noise used in Chapter 7 was simulated to be as realistic as possible, which consists of various error and noise sources of DSM uncertainties, orbital error, atmospheric artefacts, and temporal decorrelation. Specifically, the deformation signal from a linear trend plus annual sinusoid was applied with linear rates ranging between  $-40$  mm/yr and  $+40$  mm/yr and annual amplitudes bounded within the range  $[10, 20]$  mm. Interferograms estimated from this deformation signal were then assumed contaminated by simulated interferometric error and noise sources.

The experimental results showed that, after removing linear and annual signals, two noise types of time-correlated and time-uncorrelated were found with the

amplitudes of white noise over the entire image of  $500 \times 500$  pixels ranging between 3.8 mm and 8.4 mm and that of coloured noise being between 0.1 mm and 8.1 mm. The spectral indices analysed range between  $-3.0$  and  $0$  with a mean value of  $-0.8$ , which is close to flicker noise. Therefore, the noise model in SBAS InSAR may be best described by white plus flicker noise, albeit from simulations.

## 8.2 Recommendations

### 8.2.1 Further Investigations Relying on Actual InSAR Data

Due to the limited time span of SAR data that can be used to assess the influence of residual interferometric errors and noise and data gaps in InSAR SBAS in Chapter 5 and in the investigation of applying  $r$ -number in the design of an SBAS network in Chapter 6, simulated data were utilised throughout. Additionally, alternatively simulated data were adopted in Chapter 7 in the noise analysis of SBAS-derived deformation time series because of the requirement of long-term SAR data, which is not available to date. The use of simulated data may be a weakness of the investigations conducted in this dissertation, and thus other investigations based on actual data are necessary.

These further studies should be applied to actual data with various applications, particularly at different rate magnitudes, e.g., small at mm/yr, medium at cm/yr, and larger, as well as with the data of combined linear and non-linear signals. These could be tested with the application of interferometric error and noise reduction first, i.e., the reduction of interferometric contributions due to DSM uncertainties, atmospheric artefacts and orbital error. They should then be tested with similar investigations conducted in this dissertation, including the influence of residual errors and noise and data gaps on InSAR SBAS, the design of SBAS networks to see how effectively the approaches proposed in this dissertation may improve the results, as well as the noise analysis of InSAR-derived deformation time series.

These proposed studies can be employed with validated data from other observations with high precision such as GNSS and levelling and radar corner reflectors, which provide high coherence of the reflected signal.

### 8.2.2 Further Investigations with Other Noise Models and Methods

The design of an InSAR SBAS network studied in Chapter 6 was based on the  $r$ -number from geodetic network optimisation, indicating the effectiveness of this approach. Other methods have also been proven to be effective in designing a geodetic network such as one that relies on reliability measured by the minimal detectable bias, which can be applied to design an SBAS network in further studies. This further investigation could be to test whether it is consistent with the proposed method of  $r$ -numbers in this dissertation in the case of InSAR SBAS networks.

The noise analysis of the InSAR SBAS deformation time series was carried out in Chapter 7 with the white plus coloured noise model because it has been applied widely in previous geodetic time series research. Further studies are proposed to be conducted with other noise models, e.g., power-law, first-order Gauss Markov, generalised Gauss Markov and band-pass, to see how the noise behaviour in different models will be and how they may affect the estimated deformation parameters and their uncertainties.

Further studies of the estimation of functional parameters, e.g., deformation rate and other periodic coefficients and their uncertainties, are proposed to be investigated with the use of other approaches such as the minimal detectable bias, the minimal identifiable bias or the variance component estimation methods. These approaches include the least squares variance component estimation, the minimum norm quadratic unbiased estimator or the best invariant quadratic unbiased estimator.

## APPENDIX A RSE PAPER

Remote Sensing of Environment 247 (2020) 111941



Contents lists available at ScienceDirect

Remote Sensing of Environment

journal homepage: [www.elsevier.com/locate/rse](http://www.elsevier.com/locate/rse)

## Disruptive influences of residual noise, network configuration and data gaps on InSAR-derived land motion rates using the SBAS technique



Luyen K. Bui\*, W.E. Featherstone, M.S. Filmer

School of Earth and Planetary Sciences, Curtin University of Technology, GPO Box U1987, Perth, WA 6845, Australia

## ARTICLE INFO

## Keywords:

Small baseline radar interferometry (SBAS)  
 InSAR network configuration  
 Data gaps  
 Optimal network design  
 Redundancy number

## ABSTRACT

The interferometric synthetic aperture radar (InSAR) small baseline subset (SBAS) technique can be applied to land with varying deformation magnitudes ranging from mm/yr to tens of cm/yr. SBAS defines a network of interferograms that is limited by temporal and spatial baseline thresholds that are often applied arbitrarily, or in apparently subjective ways in the literature. We use simulated SAR data to assess (1) the influence of residual noise and SBAS network configuration on InSAR-derived deformation rates, and (2) how the number of interferograms and data gaps in the time series may further impact the estimated rates. This leads us to an approach for defining a SBAS network based on geodetic reliability theory represented by the redundancy number ( $r$ -number). Simulated InSAR datasets are generated with three subsidence signals of linear rates plus sinusoidal annual amplitudes of  $-2$  mm/yr plus 2 mm,  $-20$  mm/yr plus 5 mm and  $-100$  mm/yr plus 10 mm, contaminated by Gaussian residual noise bounded within  $[-2; +2]$  mm,  $[-5; +5]$  mm and  $[-10; +10]$  mm, corresponding to standard deviations of approximately 0.5 mm, 1.5 mm and 3.0 mm, respectively. The influence of data gaps is investigated through simulations with percentages of missing data ranging from 5% to 50% that are selected (1) randomly across the 4-year time series, and (2) for three-month windows to represent the northern winter season where snow cover may cause decorrelation. These simulations show that small deformation rates are most adversely affected by residual noise. In some extreme cases, the recovered trends can be contrary to the signal (i.e., indicating uplift when there is simulated subsidence). We demonstrate through simulations that the  $r$ -number can be used to pre-determine the reliability of SBAS network design, indicating the  $r$ -values between  $\sim 0.8$  and  $\sim 0.9$  are optimal.  $r$ -numbers less than  $\sim 0.3$  can deliver erroneous rates in the presence of noise commensurate with the magnitude of deformation. Finally, the influence of data gaps is not as significant compared to other factors such as a change in the number of interferograms used, although the blocks of "winter" gaps in the SBAS network show a larger effect on the rates than gaps at random intervals across the simulated time series.

### 1. Introduction and motivation

Interferometric synthetic aperture radar (InSAR) has been demonstrated to be a powerful tool for measuring the Earth's land-surface deformation owing to its high spatial and temporal resolution, wide spatial coverage, and ability to acquire data remotely (e.g., Hooper, 2008). However, InSAR measurements are contaminated by various error and noise sources, such as those caused by digital elevation models (DEMs), atmospheric signal path delay, orbital errors (ramps), temporal decorrelation, and other noise sources (e.g., Lee et al., 2012; Murray et al., 2019). Multi-temporal InSAR (MT-InSAR) methods were proposed to reduce these error and noise sources (e.g., Hooper, 2008). These methods work by analyzing a network of multiple acquisitions to

derive the deformation time series and thus deformation rate (e.g., Shanker et al., 2011).

MT-InSAR methods can be classified into two principal categories, comprising the persistent scatterer (PS) method (e.g., Ferretti et al., 2001; Hooper et al., 2007; Hooper et al., 2004) and the small baseline subset (SBAS) method (e.g., Berardino et al., 2002; Cavalié et al., 2007; Hetland et al., 2012; López-Quiroz et al., 2009; Lundgren et al., 2001; Schmidt and Bürgmann, 2003; Usai, 2003). SBAS is among the most commonly used methods that makes use of a network of interferograms from which temporal and perpendicular baselines are limited in time and length to reduce the effects of geometric decorrelation (e.g., Crosetto et al., 2016; Shanker et al., 2011; Zebker and Villasenor, 1992). This also incorporates an approach to connect multiple SBAS

\* Corresponding author.

E-mail address: [buihacluyen@hmg.edu.vn](mailto:buihacluyen@hmg.edu.vn) (L.K. Bui).<https://doi.org/10.1016/j.rse.2020.111941>Received 8 January 2020; Received in revised form 30 May 2020; Accepted 4 June 2020  
0034-4257/ Crown Copyright © 2020 Published by Elsevier Inc. All rights reserved.

that results in an increase in temporal and spatial sampling (Berardino et al., 2002). The SBAS method has been used to measure land deformation of various magnitudes, ranging from mm/yr (e.g., Elliott et al., 2010; Furuya et al., 2007; Jiang et al., 2011; Schmidt and Bürgmann, 2003) to cm/yr (e.g., Amelung et al., 1999; Cavalíe et al., 2013; Chaussard et al., 2014; Lee et al., 2012) or even tens of cm/yr (e.g., Chaussard et al., 2014; López-Quiroz et al., 2009; Motagh et al., 2007; Short et al., 2011).

InSAR data are degraded by various error and noise sources. The error caused by DEM uncertainty can be reduced by a number of methods correcting for interferograms (e.g., Berardino et al., 2002; Bombrun et al., 2009) or deformation time series (e.g., Fattahi and Amelung, 2013; Pepe et al., 2011). In order to reduce the effect of satellite orbital errors (ramps), polynomial models based on network-sense (Biggs et al., 2007; Cavalíe et al., 2008; Jolivet et al., 2012; Lin et al., 2010) or GPS data (e.g., Neely et al., 2020; Tong et al., 2013) can be used. A number of methods can be applied to correct atmosphere phase errors utilizing the stacking method (e.g., Biggs et al., 2007; Tymofeyeva and Fialko, 2015), using local data assimilation, e.g., local atmospheric data (e.g., Delacourt et al., 1998) or zenith total delay (ZTD) computed from GPS data (e.g., Williams et al., 1998; Yu et al., 2018a; Yu et al., 2017), utilizing global or regional atmospheric models (e.g., Doin et al., 2009; Jolivet et al., 2011), or integrating a global atmospheric model and GPS data to an atmospheric correction model (e.g., Yu et al., 2018b). Although these methods can be used to cope with different errors and noise in InSAR measurements, they cannot be conducted perfectly, which leads to remaining or residual errors and noise. Additionally, because of scheduling or other technical issues, SAR images are not always regularly captured, or in other cases, blocks of images acquired during extended periods (e.g., winter snowfall) may be omitted from processing due to very low coherence, both of which may have a detrimental influence on the estimated time series (e.g., Kim et al., 2015; Kohlase et al., 2003).

In InSAR SBAS data processing, pairs of scenes are chosen to form interferograms from which an interferogram network is built in such a way to reduce decorrelation noise through minimizing their time spans, and differences in look angle and squint angle (Hooper et al., 2012). Coherent pixels to which a specific SBAS approach are applied can subsequently be selected based on specific criteria, e.g., amplitude dispersion, spatial coherence, spectral coherence or their combination (Crossetto et al., 2016). Different proposed SBAS approaches are therefore based on thresholds that are, to a lesser or greater extent, different depending on various factors, e.g., applications, data availability or the critical baseline, which in turn depends on the wavelength of the radar sensor, spatial resolution and incidence angle (Gatelli et al., 1994; Zebker and Villasenor, 1992).

The temporal baseline threshold has been chosen varying from months to years (e.g., Lanari et al., 2007; López-Quiroz et al., 2009), while the perpendicular baseline threshold has been chosen ranging between hundreds of meters and over one thousand meters (e.g., Berardino et al., 2002; Chaussard et al., 2014). The SBAS network thresholds are used with the aim of maximizing the number of InSAR interferograms while minimizing their temporal and spatial decorrelation, as well as reducing the computation time and data burden. Baseline thresholds and pixel selection criteria used in several main SBAS approaches are listed in Table 1. The question then arises as to whether there is some more objective means by which to select these thresholds, which we consider herein. In this study, we deal with thresholds used to select InSAR image pairs with an assumption that all pixels are of relatively high coherence so as to be considered for SBAS processing.

We also consider the configuration of the SBAS network during our simulations. The so-called network “optimization” problem has been applied to geodetic (surveying) networks, which is traditionally divided among zero-, first-, second- and third-order problems (e.g., Grafarend and Sansò, 1985). The zero-order design (ZOD) is adopted for designing

a reference system, thus is also called “datum problem” (Teunissen, 1985). In the first-order design (FOD), a network configuration is adopted by choosing the “optimal” locations of points in a geodetic network that result in small changes in the positions of the preliminary chosen network points (Berné and Baselga, 2004; Koch, 1985). The objective of second-order design (SOD) is to select “optimal” weights for the sometimes-different observations in which three approaches can be utilized, including (i) direct approximation of the criterion matrix, (ii) iterative approximation of the criterion matrix, and (iii) direct approximation of the inverse criterion matrix (Schmitt, 1985a). By applying SOD, one seeks a network with high precision (Amiri-Simkooei, 2004). In the third-order design, an existing network is improved, extended or densified by introducing new points and/or additional measurements (Schmitt, 1985b). This is also called the densification problem and can be understood to be a mixture of FOD and SOD. A combined design, introduced by Vaníček and Krakiwsky (1986), refers to the case where FOD and SOD problems are solved simultaneously.

In the experiments presented here, we use a time series of simulated InSAR data for which we have control on the amount of error and residual noise introduced. We then investigate the following parameters to determine what effect they have on InSAR-derived rates of [simulated] land deformation. Our overarching aim is to find an “optimal” network of interferograms that results in reduced data processing time. We assess 1) the influence of residual errors and noise on SBAS-derived rates and the root mean square (RMS) of the difference between simulated and SBAS-derived deformation time series for different scenarios of the signal to noise ratio (SNR), 2) the effect of data gaps (i.e., missing scene acquisitions) for both random and the three-month “winter” cases, and 3) the use of redundancy numbers from geodetic network theory to design an “optimal” SBAS network.

## 2. InSAR SBAS algorithm used for this experiment

In summary, SBAS starts by forming an interferogram network using temporal and perpendicular baseline thresholds, followed by selecting coherent pixels in which noise is assumed to be negligible. Phase unwrapping is another step implemented in SBAS that can be carried out either before or after pixel selection, depending on the implementation strategy (Gong et al., 2016). The inversion step is subsequently implemented to convert small baseline interferograms phase differences to a time series of displacements at the acquisition times. With  $m$  interferograms generated from  $(n + 1)$  InSAR images, the inversion equation can be written as (Berardino et al., 2002):

$$A\phi = \delta\phi \quad (1)$$

where  $A$  is the design matrix of size  $m \times n$ ,  $\phi$  is the vector of  $n$  (unknown) time series phase displacements of InSAR images at a pixel,  $\delta\phi$  is the vector of  $m$  (known) phase differences between each small baseline interferogram. In the SBAS approach applied in these simulations, the interferogram phase measurements can be expressed as (Agram et al., 2012; Gong et al., 2016):

$$\delta\phi_{ij} = \phi_j - \phi_i = \sum_{n=i}^{j-1} \delta\varphi_n \quad (2)$$

where  $\delta\phi_{ij}$  is the interferogram phase connecting  $i^{\text{th}}$  and  $j^{\text{th}}$  images,  $\phi_i$  and  $\phi_j$  are the phase values at  $i^{\text{th}}$  and  $j^{\text{th}}$  acquisitions, respectively,  $\delta\varphi_n$  is the pixel phase increment between  $n^{\text{th}}$  and  $(n + 1)^{\text{th}}$  images. Eq. (2) is utilized with an assumption of linear deformation between acquisitions that are adjacent in time (Berardino et al., 2002).

In SBAS data processing, a network is formed by choosing interferometric pairs with short temporal and perpendicular baselines limited by user-prescribed thresholds, and this controls the structure of the design matrix  $A$  in Eq. (1). With the above assumption of  $(n + 1)$  InSAR images, the possible number of interferometric pairs ( $m$ ) satisfies (Berardino et al., 2002):

**Table 1**  
Summary of the main SBAS approaches.

Reference	Interferogram selection thresholds	Pixel selection mmriterion
Berardino et al. (2002)	Perpendicular baseline (130 m)	Coherence
Mora et al. (2003)	Perpendicular baseline (24 m)	Coherence
Schmidt and Bürgmann (2003)	Perpendicular baseline (200 m)	Coherence
Lanari et al. (2004)	Perpendicular baseline (130 m)	Coherence
Hooper (2008)	Perpendicular baseline Temporal baseline Doppler baseline	Amplitude and phase stability
López-Quiroz et al. (2009)	Perpendicular baseline (500 m) Temporal baseline (9 months)	Coherence
Goel and Adam (2014)	Perpendicular baseline (150 m) Temporal baseline (150 days)	Statistical homogeneity test

$$\frac{n+1}{2} \leq m \leq \frac{n(n+1)}{2} \quad (3)$$

For each pixel selected, Eq. (1) is applied to convert the phase difference from interferograms in the chosen network to the phase time series of displacements according to InSAR acquired times by applying least-squares (LS) (Schmidt and Bürgmann, 2003), singular value decomposition (SVD) (Berardino et al., 2002), or minimization of the L1-norm (Lauknes et al., 2011). In most SBAS approaches, the design matrix  $\mathbf{A}$  is fixed to be used in the inversion step for all selected pixels. This is an advantage in terms of convenience and reduced processing time, but may suffer from decorrelation, particularly in vegetated or snow-covered areas where many pixels may decorrelate, so that there are large gaps in the spatial distribution of its products, e.g., a velocity map (Sowter et al., 2013). Methods using a flexible design matrix  $\mathbf{A}$ , e.g., the intermittent SBAS method (Sowter et al., 2013), have been proposed as a solution. In this simulation, however, we use a fixed-size  $\mathbf{A}$  matrix.

### 3. Network design used in geodesy

Geodetic surveying network “optimization” aims at finding a geometric configuration and a set of observations of sufficient precision to satisfy the desired positional quality criteria with lower financial and logistical costs (e.g., Kuang, 1993). The quality of a geodetic network is defined by the criteria of precision, reliability and economy (i.e., cost) of the network (Schmitt, 1985a). In geodetic network design, one seeks to minimize the objective function of economy and/or maximize that of precision or reliability of the network (e.g., Amiri-Simkooei, 2004).

The observational precision and network geometry are two crucial factors that influence the precision of a geodetic network. The variance-covariance (VCV) matrix is normally adopted to represent the network's precision. With the assumption of a minimum constraint, the VCV matrix is expressed as (e.g., Kuang, 1996).

$$\mathbf{C}_x = \sigma_0^2 \left[ (\mathbf{A}^T \mathbf{P} \mathbf{A} + \mathbf{D} \mathbf{D}^T)^{-1} - \mathbf{H} (\mathbf{H}^T \mathbf{D} \mathbf{D}^T \mathbf{H})^{-1} \mathbf{H}^T \right] \quad (4)$$

where  $\sigma_0^2$  is the a priori variance factor,  $\mathbf{A}$  and  $\mathbf{P}$  are the design and weight matrices of observations,  $\mathbf{D}$  and  $\mathbf{H}$  are the minimum and inner constraint datum information matrices, respectively.

The reliability of geodetic networks, as defined classically by Baarda (1968), is the ability of a network to detect and resist against gross errors in observations. It is further divided into internal and external reliability as follows.

- 1) The internal reliability is defined as the ability of a network to detect gross errors, referring to the lower bounds of detectable gross errors (aka. The minimum detectable bias, MDB) that is expressed as (e.g., Baarda, 1968):

$$\nabla_0 l_i = \frac{\delta_0 \sigma_l}{\sqrt{r_i}} \quad (5)$$

where  $\delta_0$  is the lower bound for the non-centrality parameter,  $\sigma_l$  and  $r_i$  are the standard deviation and the redundancy or  $r$ -number of the  $i^{\text{th}}$  observation, respectively. The  $r$ -numbers of the observations are the diagonal elements of the matrix  $\mathbf{R}$  that are expressed as (e.g., Amiri-Simkooei et al., 2012):

$$\mathbf{R} = \mathbf{I} - \mathbf{A} (\mathbf{A}^T \mathbf{P} \mathbf{A})^{-1} \mathbf{A}^T \mathbf{P} \quad (6)$$

where  $\mathbf{I}$  is the identity matrix.

- 2) The external reliability refers to the maximum effect of an undetectable gross error ( $\nabla_0 l_i$ ) on the estimates of unknown parameters as:

$$\nabla_{0,i} \hat{x} = (\mathbf{A}^T \mathbf{P} \mathbf{A})^{-1} \mathbf{A}^T \mathbf{P} \nabla_{0,i} l \quad (7)$$

The internal reliability criterion is generally used as the measure for an “optimal” design of geodetic networks aiming at high reliability (Amiri-Simkooei, 2001), as shown in Eq. (6). In this paper, we examine the redundancy number ( $r$ -number) as a diagnostic metric to determine the likely effectiveness of the SBAS network design and verify this with simulation experiments. Specifically, for a given SBAS network with a corresponding design matrix  $\mathbf{A}$  as shown in Eq. (1), the  $r$ -number is computed using Eq. (6) with the weights  $\mathbf{P}$  of interferograms computed as the inverse of normalized (perpendicular and temporal) baseline lengths, which will be described in Section 4.

### 4. Generation of simulated data

A time series of independent pixels that are reasonably representative of the range of Earth deformations detected by InSAR are simulated, these being: mm/yr (e.g., Elliott et al., 2010; Furuya et al., 2007; Jiang et al., 2011; Schmidt and Bürgmann, 2003), cm/yr (e.g., Amelung et al., 1999; Cavalié et al., 2013; Chaussard et al., 2014; Lee et al., 2012), and tens of cm/yr (e.g., Chaussard et al., 2014; López-Quiroz et al., 2009; Motagh et al., 2007; Short et al., 2011). Our simulated data cover a four-year time span with 11-day sampling interval that corresponds to 133 equally time-spaced InSAR images. The baseline history of these 133 images, which is defined as the perpendicular baselines between images and the reference one (i.e., the first scene), is assumed to be within  $[-200, +200]$  m, which is approximately the order of modern SAR missions such as C-band Sentinel-1 (Yague-Martinez et al., 2016) or TerraSAR-X (TSX) (e.g., Chen et al., 2016; Lubitz et al., 2013). The simulated baseline history of 133 images is generated randomly with ranges between  $-200$  m and  $+200$  m with that of the first scene being fixed to be zero (so leaving 132), and are shown as a scatter plot in Fig. 1.

We take an interest in a land subsidence signal with both a linear trend and a superposed annual sinusoidal oscillation; all pixels are simulated to experience surface deformation in the SAR line of sight (LOS) with linear plus annual periodic terms, which are expressed as:

$$d_{i,j} = v_i t_j + a_i \sin(2\pi t_j) \quad (8)$$

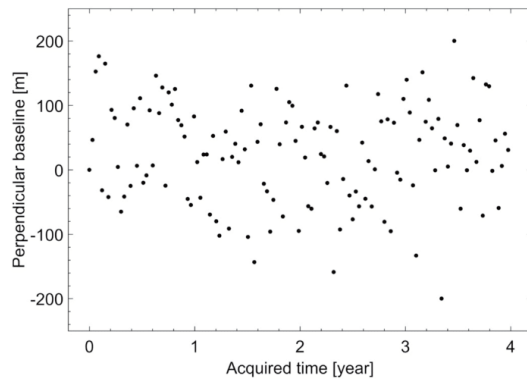


Fig. 1. Scatter plot of simulated perpendicular baseline history. Each black dot represents a SAR scene acquisition.

where  $d_{i,j}$  is the deformation of the  $i^{\text{th}}$  pixel at the  $j^{\text{th}}$  image with corresponding acquired time  $t_j$ ,  $v_i$  and  $a_i$  are the linear rate (velocity) and annual amplitude of the same pixel, respectively. We select this model form because time series analysis of other environmental phenomena do likewise (e.g., Davis et al., 2012; Didova et al., 2016).

The linear rates are chosen as  $-2$  mm/year,  $-20$  mm/year and  $-100$  mm/year over the four-year period, which are representative of Earth deformation rates measured by InSAR (e.g., Cavalié et al., 2013; Chaussard et al., 2014; Elliott et al., 2010). The sinusoidal annual amplitude of Earth surface deformation has been drawn from the literature, which can range from the order of millimeters to centimeters (e.g., Baldi et al., 2009; Bock et al., 2012; Davis et al., 2012; Dzurisin et al., 2009; Murray and Lohman, 2018; Osmanoglu et al., 2011). For example, Osmanoglu et al. (2011) report annual amplitudes of GNSS stations ranging from several millimeters up to  $\sim 2.6$  cm. Murray and Lohman (2018) found seasonal amplitudes up to  $\sim 5$  cm in California detected by InSAR and peak-to-peak amplitudes of  $\sim 6$  cm from GNSS in the Amazon Basin (cf. <http://geodesy.unr.edu/NGLStationPages/stations/NAUS.sta>).

While there can be large annual signals in various parts of the world, we simulate more conservative cases of simulated deformation signal with pairs of signal parameters of linear rate plus annual amplitudes that are shown in Table 2. We then apply a Monte Carlo simulation (e.g., Kroese et al., 2014) with 1000 pixels for each scenario. The number of tested pixels is chosen to avoid prohibitive computation times for the simulation experiments. The deformation time series of the 1000 pixels are then computed for the 133 equally spaced 11-day acquisition times using Eq. (8), and are termed herein the “simulated deformation time series”. These are considered to be the “true” or noise-free signal, and will be used to validate the SBAS InSAR data processing results later in this paper.

With 133 InSAR images, the maximum possible number of interferograms is 8778 (Eq. (3)). These 8778 noise-free interferograms are then computed based on this simulated deformation SAR time series: the phase difference of an interferogram connecting  $i^{\text{th}}$  and  $j^{\text{th}}$  images is computed by subtracting the simulated time series value at  $i^{\text{th}}$  time from

Table 2  
The three cases of simulated signals showing linear rates and annual amplitudes used for experiments in Sections 5–7.

Signal case	Linear rate [mm/yr]	Annual amplitude [mm]
1	$-2$	2
2	$-20$	5
3	$-100$	10

Table 3  
Simulated noise with various ranges and standard deviations.

Noise case	Range [mm]	Standard deviation [mm]
A	$[-2; +2]$	$\pm 0.5$
B	$[-5; +5]$	$\pm 1.5$
C	$[-10; +10]$	$\pm 3.0$

that at  $j^{\text{th}}$  time.

The simulated residual errors and noise, herein called the “residual interferogram noise”, are then added to the noise-free interferograms. Three sets of assumed 8778 Gaussian noise values with zero mean are generated for each of the 1000 pixels and bounded within  $[-2; +2]$  mm,  $[-5; +5]$  and  $[-10; +10]$  mm, which correspond to standard deviations of approximately  $\pm 0.5$  mm,  $\pm 1.5$  mm and  $\pm 3.0$  mm, respectively (Table 3). Specifically, for each pixel, we first generate 8778 random samples of a Gaussian distribution with a zero mean and a standard deviation of one. These are subsequently rescaled so that their ranges lie exactly within the bounds set in Table 3. We acknowledge that the residual errors and noise in real SAR data may not be Gaussian with zero mean because they originate from a variety of sources (e.g., DEM error, orbital ramp, atmospheric delay, etc). However, we would only ever be able to postulate the actual statistical distribution of real InSAR data errors, so instead make the simple assumption of Gaussian zero mean for our simulations.

The simulated residual interferogram noise is generated in such a way that longer baseline lengths are assigned with noise of higher magnitude. Additionally, they have different ranges with the temporal baselines being from  $\sim 0.03$  year to  $\sim 3.97$  years, whilst the perpendicular baselines being between  $\sim 376$  meters and 400 meters. Therefore, they are first “normalized” by dividing all elements by the maximum value:

$$\begin{aligned} \text{norm\_btemp}_i &= \frac{\text{btemp}_i}{\max(\text{btemp})} \\ \text{norm\_bperp}_i &= \frac{\text{abs}(\text{bperp}_i)}{\max[\text{abs}(\text{bperp})]} \end{aligned} \quad (9)$$

where  $\text{norm\_btemp}_i$  and  $\text{norm\_bperp}_i$  are the “normalized” temporal and perpendicular baselines of the  $i^{\text{th}}$  interferogram, respectively which correspond to their values before “normalization”  $\text{btemp}$  and  $\text{bperp}$ ,  $\text{abs}(\cdot)$  and  $\max(\cdot)$  indicate the absolute and maximum values, respectively.

By this “normalization”, the normalized temporal and perpendicular baselines will have ranges between  $\sim 0$  and 1. The normalized baseline lengths of all interferograms are then computed with the  $i^{\text{th}}$  interferogram being:

$$\text{norm\_bsln}_i = \sqrt{\text{norm\_btemp}_i^2 + \text{norm\_bperp}_i^2} \quad (10)$$

The normalized baseline lengths computed from Eq. (10) are then used to assign the residual interferogram noise. Specifically, for each pixel with corresponding noise set of 8778 samples, the noise is assigned to interferograms by a way that an interferogram with a longer normalized baseline length will be assigned with noise of larger magnitude. We acknowledge that the influences of temporal and perpendicular baselines on interferometric noise are different. While the influence of perpendicular baselines can be quantified via their relationship with DEM error (e.g., Lee et al., 2012), the influence of temporal baselines is more sophisticated, which is dependent on the change of atmosphere and target environment over time (Zebker et al., 1997; Zebker and Villasenor, 1992). Here, for the sake of simplicity, we assume the two types of baseline are equal in terms of their weights in calculating normalized baselines using Eq. (10).

**Table 4**

List of networks tested in this study based on various temporal baseline thresholds. The perpendicular baseline threshold is set fixed at 200 m (Fig. 1).

Temporal baseline threshold [days]	Number of interferograms
22	263
33	376
44	498
55	621
66	745
77	863
88	986

### 5. Disruptive influences of residual noise and network configuration

In order to assess the influence of residual noise and small baseline network configuration on SBAS-derived land deformation rates, various interferogram networks were formed through the use of different thresholds for the temporal baselines. Here, for the sake of simplicity initially, we restrict the perpendicular baseline length to 200 m and only vary the temporal baseline. Table 4 shows the temporal baseline thresholds that are applied with the resulting number of interferograms.

We apply the SBAS approach to subsets of our simulated noisy interferograms (Table 4) using the GIANt software package (Agram et al., 2013; Agram et al., 2012). GIANt incorporates most of the SBAS-based data processing approaches mentioned in the Introduction, including the “traditional” SBAS (e.g., Berardino et al., 2002; Cavalie et al., 2007; Schmidt and Bürgmann, 2003; Usai, 2003), the new SBAS (NSBAS) (Doin et al., 2011; López-Quiroz et al., 2009), and the Multiscale InSAR Time-Series (MINTS) (Hetland et al., 2012); cf. Table 1. Time series of deformation relative to the first-acquired SAR image time for each of the 1000 test pixels are generated assuming that there is no deformation in the first acquisition. Both unweighted linear regression and unweighted LS are then applied to those SBAS time series in order to compute SBAS-derived linear rates and annual sinusoids, which are then compared with our simulated parameters listed in Table 2. The RMS of the difference between simulated deformation time series (the “true” signal) and SBAS-derived deformation time series is also computed in order to test dependence on the number of interferograms chosen.

#### 5.1. Influences on simulated linear signals

We first examine a signal where Eq. (8) is adopted solely with the linear rate components of  $-2$  mm/yr,  $-20$  mm/yr and  $-100$  mm/yr (Table 2). Fig. 2 shows results from different combinations of simulated deformation rates and residual interferogram error and noise. Here, the assumed simulated linear rates are considered as the “true” rates to which the SBAS-derived rates are compared and the differences between them are herein termed the “errors in rate determination”. The SBAS rates are derived by fitting a linear regression to the corresponding deformation time series, then the errors in rate determination are calculated. The errors are shown in Fig. 2, and are the same in both magnitude and sign among all three simulated linear rate cases from Table 2. Generally, the larger simulated residual interferogram noise (i.e.,  $[-10; +10]$  mm vs.  $[-5; +5]$  mm vs.  $[-2; +2]$  mm) leads to larger errors in the rate determination (cf. blue, green and black plottines in Fig. 2), whereas an increase in the number of chosen interferograms (by choosing a larger temporal baseline threshold) can reduce this error.

Additionally, while their trends are in an agreement for the cases of larger signal rates (i.e.,  $-20$  mm/yr and  $-100$  mm/yr, Fig. 2, middle and right), contradictory trends exist in the cases of small deformation (i.e.,  $-2$  mm/year, Fig. 2, left), particularly when networks of fewer interferograms are used together with higher residual noise of  $[-5;$

$+5]$  mm and  $[-10; +10]$  mm. Importantly, the SBAS-derived deformation trends are affected by not only the magnitude of noise, but also its relation to the signal size (see Fig. 2, left), thus low SNR is more likely to result in incorrect or even contradictory trend estimates. In essence, small deformation rates in the presence of proportionally large noise may lead to spurious results, which become exacerbated in the presence of significant data gaps.

The “errors in rate determination” are next compared for the networks listed in Table 4 and shown in Fig. 3 for four example pixels. Within a specific network and pixel, the retrieved rate errors are identical when the same residual noise is applied regardless of the signal rates. In other words, if a specific network chosen from Table 4 with corresponding interferogram noise set is applied, then its error in rate determination will not depend on the magnitude of simulated rate (cf. blue, orange and yellow bars in Fig. 3). This is attributable to SBAS using the LS principle (Schmidt and Bürgmann, 2003) or the SVD method (Berardino et al., 2002). The results computed from applying the LS principle depend on redundant interferograms, together with residual interferogram error and noise that in turn depends on the configuration of the network (Berardino et al., 2002). The SBAS network configuration is specified by the design matrix  $A$  as per Eq. (1). Both the LS principle and SVD method result in the same InSAR-derived rates, except that the latter can cope with disconnected subsets of interferogram networks, whereas the former cannot (Berardino et al., 2002; Gong et al., 2016). Consequently, the same error in rate determination will result if the same residual noise is applied to a network regardless of the deformation rate.

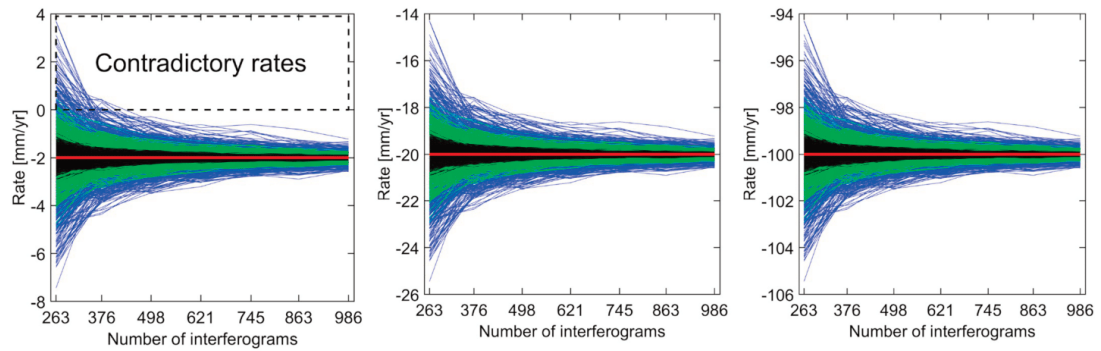
#### 5.2. Influences on non-linear signals

We next examine the signal combining both a linear trend and sinusoidal annual terms. As mentioned in Section 4, we apply pairs of signal parameters of linear rate plus annual amplitude, which are  $-2$  mm/yr plus 2 mm,  $-20$  mm/yr plus 5 mm, and  $-100$  mm/yr plus 10 mm (Eq. (8)) as listed in Table 2. Via this simulation, we will test the influence of non-linearity of signal on unweighted linear fit rates, which are derived by fitting a linear regression to the SBAS-derived deformation time series.

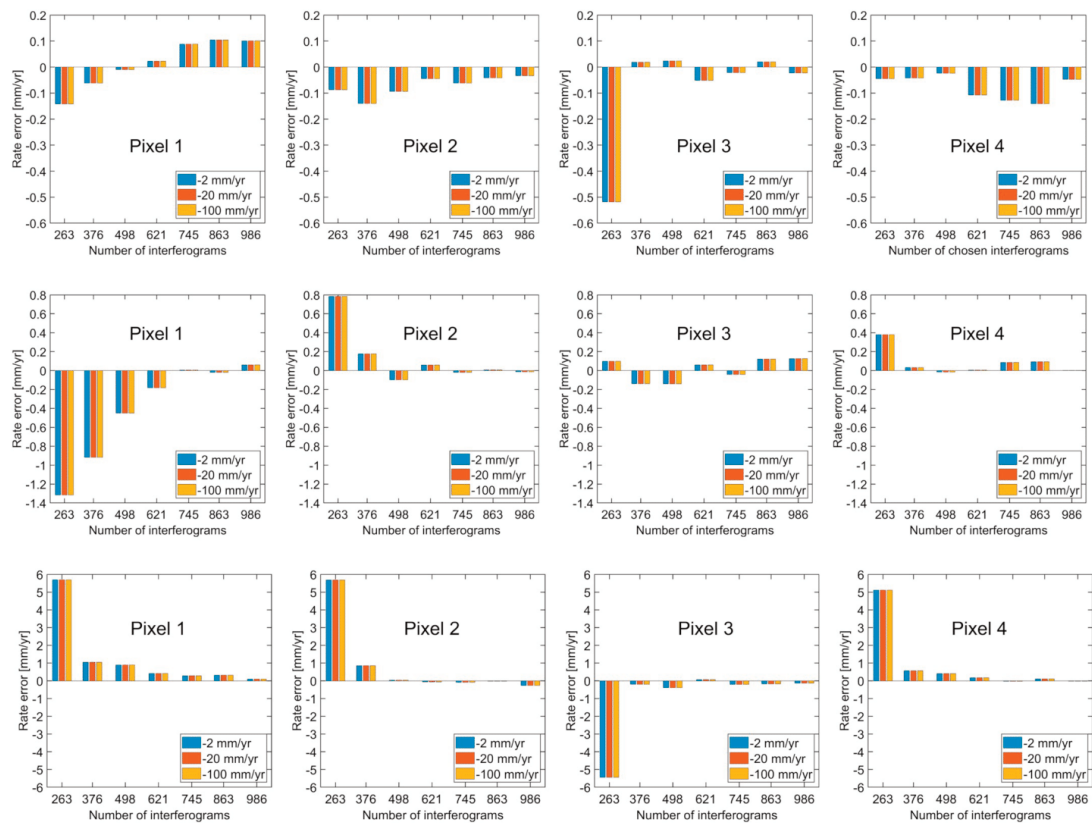
Like the previous test of a linear signal only, the simulated deformation time series is generated by first applying Eq. (8) for all 1000 pixels prior to forming 8778 noise-free interferograms and applying simulated residual interferogram noise. The networks shown in Table 4 are then applied in sequence to select corresponding stacks of interferograms, which are then utilized with the SBAS method. Both the unweighted linear fit and unweighted LS methods are subsequently adopted to derive linear rates and annual amplitudes. Additionally, the RMSs between simulated and SBAS-derived time series are calculated.

Fig. 4 shows unweighted linear-fit rates computed using the linear rates from Table 2 and the simulated noise in Table 3. These results in Fig. 4 reflect the influence of signal non-linearity on linear-fit rates through biases in rate errors, particularly the case of large annual amplitudes, i.e., strongly non-linear, (cf. Fig. 4 between red lines and coloured polylines). This is due to the inappropriate functional model used here to derive the linear rates, i.e., linear regression, which is applied to linear plus annual simulated signal.

The simulated signal function is known (Eq. (8)), so we adopt this for estimating both rates and annual amplitudes utilizing unweighted LS (Fig. 5). The results indicate similar behavior as that in the case of solely linear signals (cf. Fig. 5 (top) with Fig. 2) and those with biases removed (cf. Fig. 5 (top) and Fig. 4). Again, this is attributable to the SBAS method in which the results computed depend on the configuration of the network and residual interferogram noise but not the deformation rate. Also, it is due to the more appropriate functional model used to obtain the linear rates where the influence of the signal non-linearity cancel out. It is therefore an important warning that a suitable function should be utilized to calculate linear rates in case the



**Fig. 2.** Comparison of rates computed by unweighted linear fit from combinations of different deformation signals. From left to right are simulated linear rate cases 1 to 3 (Table 2) contaminated by simulated residual interferogram noise. Black, green and blue polylines are SBAS derived rates computed from simulated data with simulated noise cases A to C, respectively (Table 3). Red horizontal lines represent the simulated rates. The black dashed box in the left panel is used to contrast between positive and negative rates that indicates contradictory trends. (For interpretation of the references to colour in this figure legend, the reader is referred to the web version of this article.)



**Fig. 3.** Comparison of rate errors computed from different networks for four example pixels. The top, center and bottom rows correspond to simulated noise cases A, B and C (Table 3). Note the different scale on the y-axis for each noise case. (For interpretation of the references to colour in this figure legend, the reader is referred to the web version of this article.)

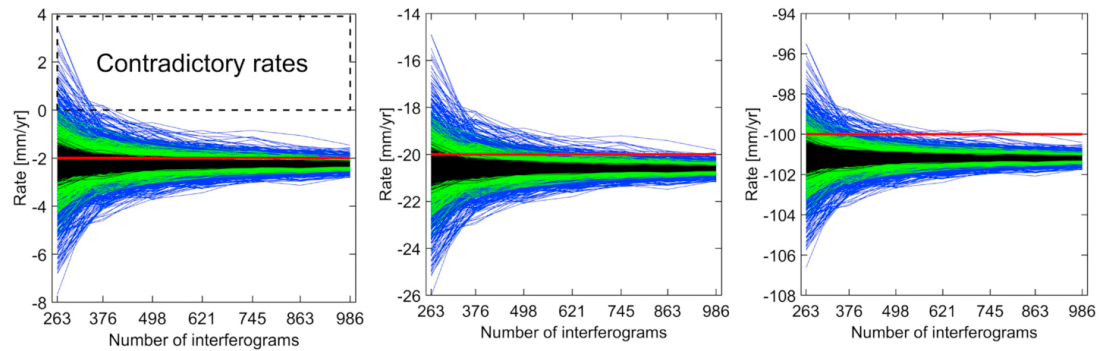


Fig. 4. Comparison of unweighted linear-fit rates from linear plus annual signals. From left to right are simulated signal cases 1 to 3 (Table 2) contaminated by various simulated residual interferogram noise. Black, green and blue polylines indicate the results computed from simulated data with noise cases A, B and C (Table 3). Red horizontal lines represent the simulated rates. The black dashed box in the left panel used to contrast between positive and negative rates that indicates contradictory trends in some cases. (For interpretation of the references to colour in this figure legend, the reader is referred to the web version of this article.)

Earth's surface experiences non-linear deformation, particularly in strongly non-linear cases.

In the case of applying LS estimation with an appropriate function, not only the linear rate, but also its accompanying parameters, e.g., the annual amplitude in this study, will be obtained. This is shown in Fig. 5

(bottom), where the computed annual amplitudes indicate that more interferograms in the SBAS network result in more accurate LS estimation of the annual amplitude. In addition, the errors in those computed parameters are dependent on the SBAS network configuration and residual interferogram noise, but not the signal magnitude.

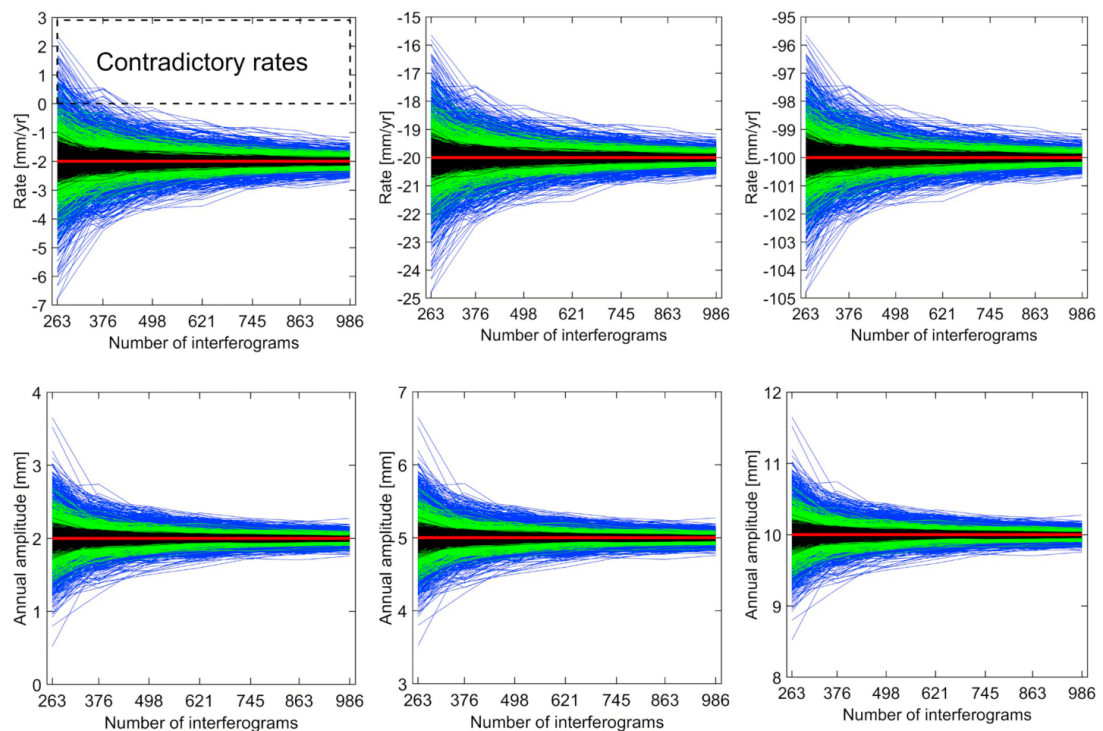
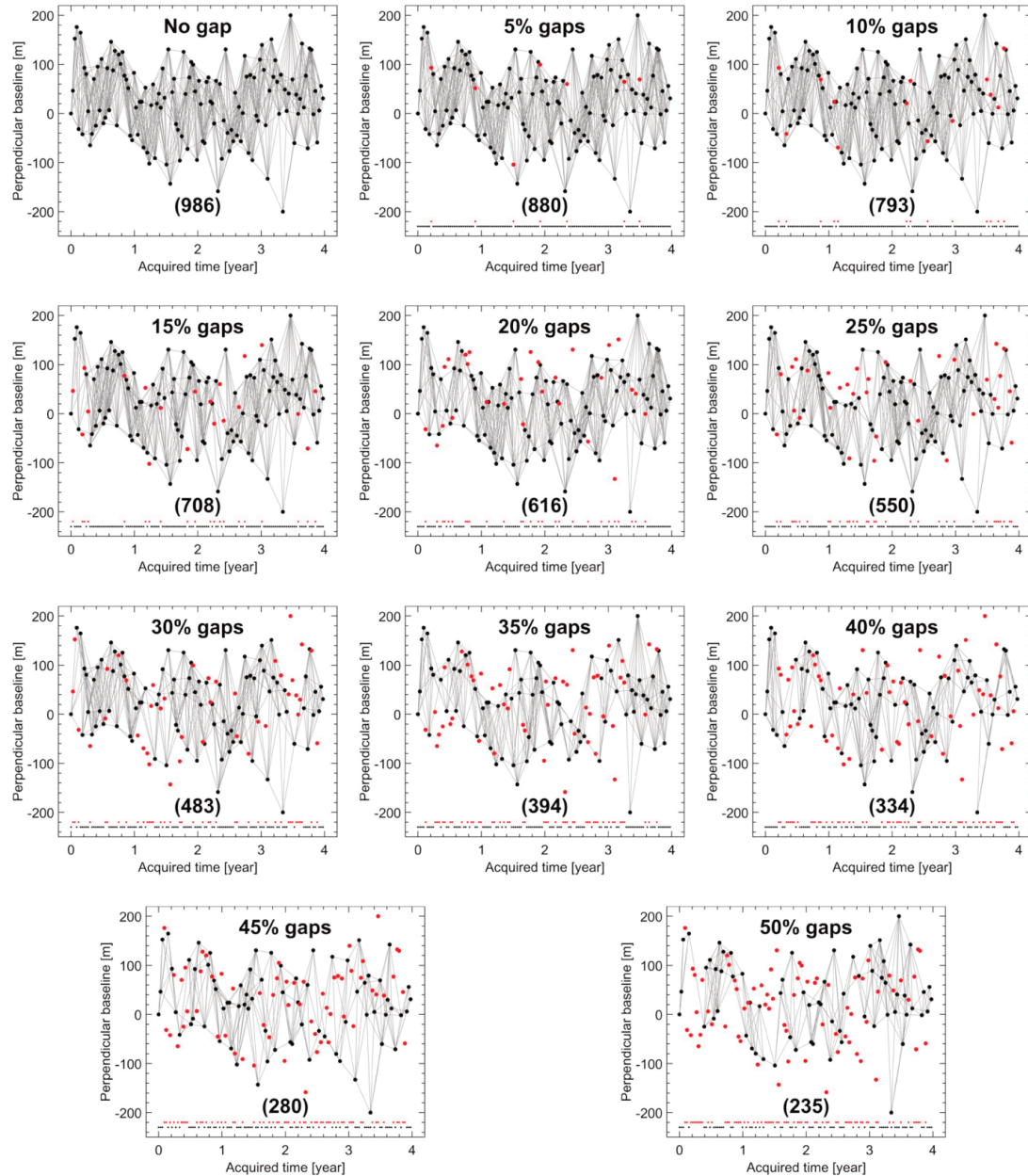


Fig. 5. Comparison of unweighted LS rates (top panel) and annual amplitudes (bottom panel) computed from linear plus annual signals. From left to right correspond to simulated signal cases 1 to 3 (Table 2) contaminated by various simulated residual interferogram noise. Black, green and blue polylines indicate the results computed from simulated data with noise cases A, B and C (Table 3). Red horizontal lines represent the simulated rates or annual amplitudes. The black dashed box in the top-left panel used to contrast between positive and negative rates that indicates contradictory trends in some cases. (For interpretation of the references to colour in this figure legend, the reader is referred to the web version of this article.)



**Fig. 6.** Comparison of the interferogram network gaps in percentage. Gray lines indicate InSAR interferograms connecting images denoted by black dots. Red dots indicate missing images (i.e., gaps). The number under each network refers to the number of interferograms. (For interpretation of the references to colour in this figure legend, the reader is referred to the web version of this article.)

## 6. Influence of data gaps on SBAS-derived rates

In this Section, we study the influence of SAR data gaps on SBAS-retrieved rates. This is motivated by the likelihood of irregular temporal

sampling of SAR data due to scheduling or other technical issues, such as decorrelation during winter snow cover. We now conduct simulations with a network of 986 interferograms formed by applying a temporal baseline threshold of 88 days ( $\sim 3$  months, Table 4), with two

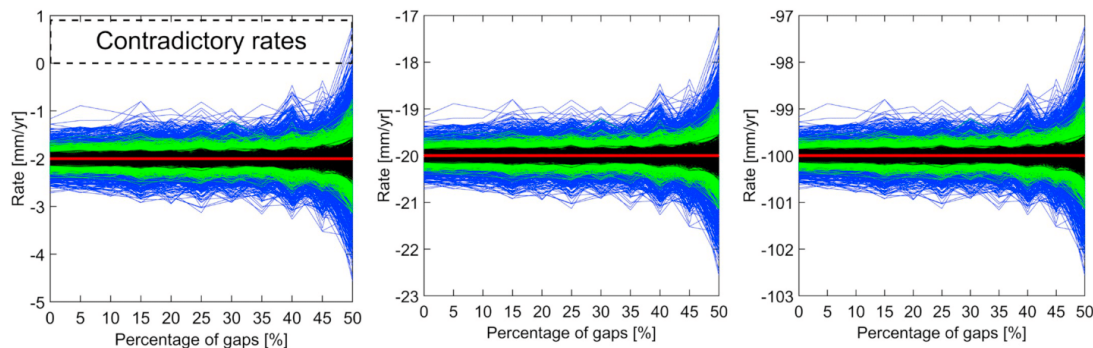


Fig. 7. Comparison of unweighted LS rates computed from linear plus annual signals between the interferogram network of no gaps and those with randomly chosen gaps of various percentages. From left to right correspond to simulated signal cases 1 to 3 (Table 2) contaminated by various simulated residual interferogram noise. Black, green and blue polylines indicate the results computed from simulated data with noise cases A, B and C (Table 3). Red horizontal lines represent the simulated rates. The black dashed box in the left panel used to contrast between positive and negative rates that indicates contradictory trends in some cases. (For interpretation of the references to colour in this figure legend, the reader is referred to the web version of this article.)

scenarios of data gaps. In the first scenario, missing images are due to technical and/or scheduling issues, which are considered random, and, in the second scenario, missing images are chosen in the northern winter season which are assumed to have low coherence due to extreme weather.

#### 6.1. Random data gaps

In this Sub-section, we assume there are, in turn, 5%, 10%, ..., 50% of acquisitions missing from our simulated time series. First, missing images are randomly chosen. Interferograms having connections with those missing images are subsequently identified and eliminated from the original list of 986 interferograms. Fig. 6 compares the network without gaps and those corresponding to various amount of gaps in percentage from 5% to 50% with an increment of 5%.

Here, we use the same linear plus annual signals as those used in Section 5.2 according to simulated signal cases shown in Table 2. For each network shown in Fig. 6, the SBAS approach in GIANt is applied to all 1000 pixels in which the deformation time series at each pixel is derived. The unweighted LS is then applied to calculate the deformation rates and the RMSs of the difference between simulated and SBAS-derived time series are then calculated.

Fig. 7 compares SBAS-derived unweighted LS rates between the SBAS network with no gaps and those of different percentages of data gaps. Fig. 8 shows the corresponding RMSs of the difference between simulated and SBAS-derived deformation time series. These RMSs are the same for all three cases of linear plus annual signal (Table 2). Fig. 7 and Fig. 8 confirm that data gaps have an effect on the retrieved rates and RMSs with a noticeably larger influence in cases of higher gap percentages, particularly the 50% case. Contradictory trends are obtained for some pixels the case of large residual interferogram noise and low magnitude rates (Fig. 7, left). This is likely caused by a weak SBAS network configuration (see Fig. 6 with the 50% gaps case).

The influence of random data gaps on the errors in rate determination and the RMSs of the difference between simulated and SBAS-derived deformation time series is caused by a reduction in the number of interferograms when the percentage of gaps increases. However, a reduction in interferograms in the SBAS network can be caused by random data gaps (Figs. 7 and 8) or by changing the temporal baseline thresholds (as shown in Section 5). We compare errors resulting from fewer interferograms in a SBAS network due to (1) random gaps and (2) temporal baseline thresholds in Fig. 9 (cf. blue and green polylines). This demonstrates the role of the network configuration, where a network may have the same number of interferograms, but will have

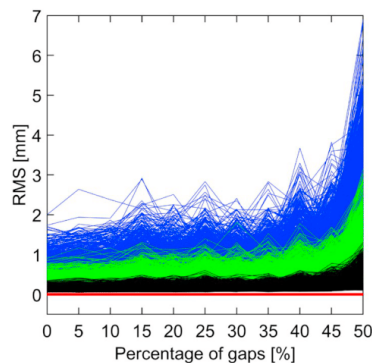


Fig. 8. Comparison of the RMSs of the difference between simulated and SBAS-derived deformation time series of all pixels between the SBAS interferogram network of no gap and those with random gaps. Black, green and blue polylines indicate the results computed from simulated data with noise cases A, B and C (Table 3). (For interpretation of the references to colour in this figure legend, the reader is referred to the web version of this article.)

higher errors depending on which interferograms are selected.

The random gap scenario results in more redundant interferograms, making the network more robust, especially in the case of noisier time series (Fig. 9, right plots). Therefore, in this case of randomly selected data gaps, mixed interferograms covering both short and long time spans makes the network more robust in recovering the deformation signal compared to the case of no gaps in which only short-time interferograms are chosen, which are limited by the threshold.

#### 6.2. "Winter" data gaps

The previous test on data gaps in Section 6.1 is based on the fact that SAR data is missing sometime due to technical and/or scheduling issues, which we consider random. There is an alternative situation where there may be "user-defined" data gaps in which data missing is due to, e.g., very low coherence caused, for instance, by snow cover. We term this situation "winter data gaps" where all images acquired in the winter season (we use December to February for the Northern Hemisphere) are removed (Fig. 10).

The results of this simulation experiment are shown in Fig. 11. We

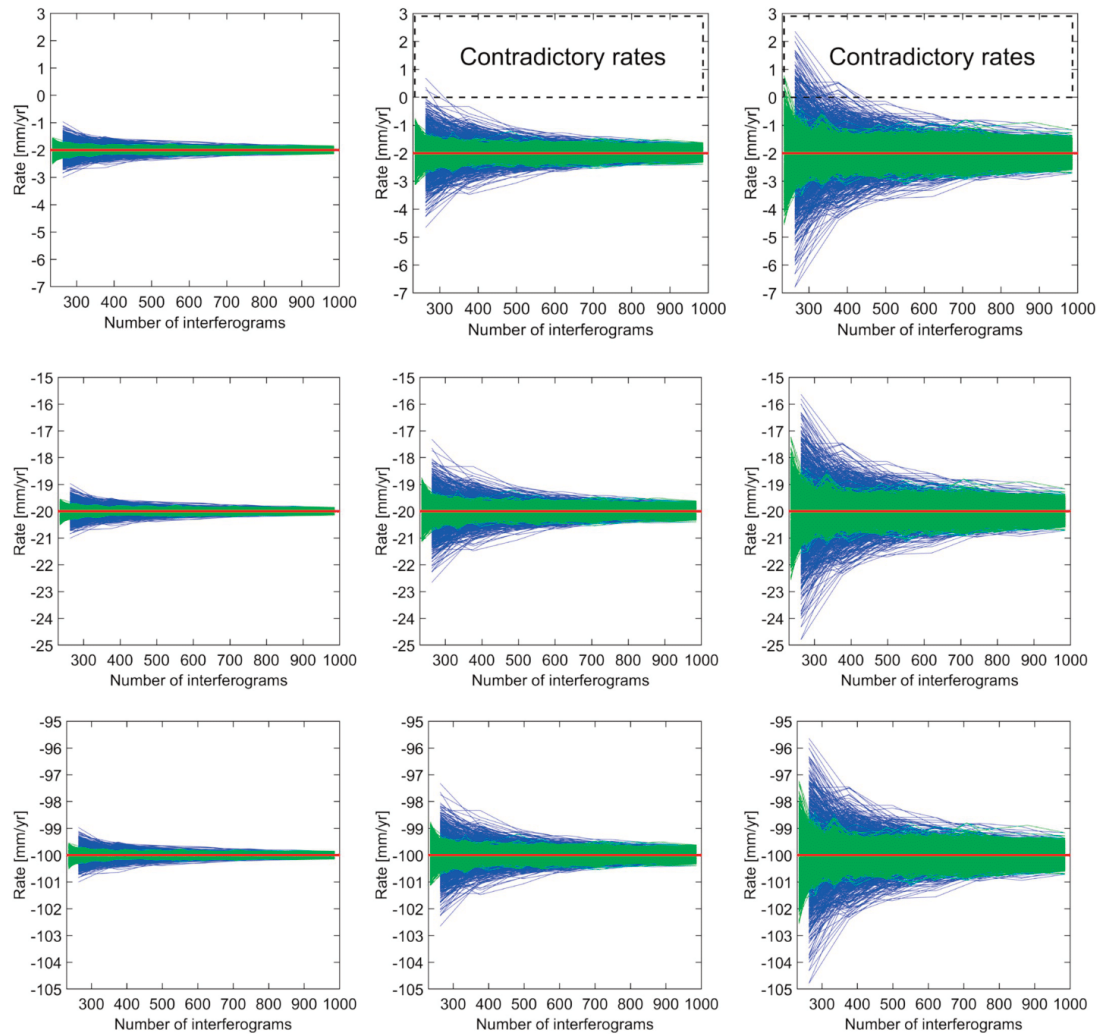


**Fig. 9.** The influence of the change in number of interferograms chosen by various temporal baseline thresholds (blue) and due to random data gaps (green) on SBAS-derived unweighted LS rates. From top to bottom: simulated signal cases 1, 2 and 3 (Table 2). From left to right: residual interferogram noise cases A to C (Table 3). Black dashed boxes in the top panel used to contrast between positive and negative rates that indicates contradictory trends in some cases. (For interpretation of the references to colour in this figure legend, the reader is referred to the web version of this article.)

compute unweighted LS rates and RMSs of the difference between simulated and SBAS-derived deformation time series for networks with no gaps, random data gaps and “winter data gaps”, with the latter two having the same number of images. To avoid a disconnection in the SBAS network, we apply a network of 1340 interferograms formed by applying a temporal baseline threshold of 121 days (~4 months), instead of ~3 months as in Section 6.1, and a perpendicular baseline threshold of 200 m.

Fig. 11 compares unweighted LS rates for each network with RMSs between simulated and SBAS-derived deformation time series shown in Fig. 12. Fig. 10 shows the number of missing images is the same between the two cases of data gaps, which is 34 out of 133, and, though the missing images are selected differently, the number of

interferograms linking the remaining images are nearly the same; 750 for random gaps and 744 winter gaps. However, the influence of these two different data gap cases are distinct with the “winter” gaps having a larger influence, as confirmed by both retrieved rates in Fig. 11 and RMSs in Fig. 12.

This is caused by the strength of the network configuration, which is more robust with interferograms at regular intervals in the random gaps network but with “blocks” of gaps in the “winter” case, leading to a less robust network (cf. Fig. 10 (middle) and (right)). This alerts users that, in addition to the effect of fewer interferograms and gap percentages, the strength of network configuration is another factor influencing the SBAS results, in which one should try to design a SBAS network that does not contain long gaps in the time series.

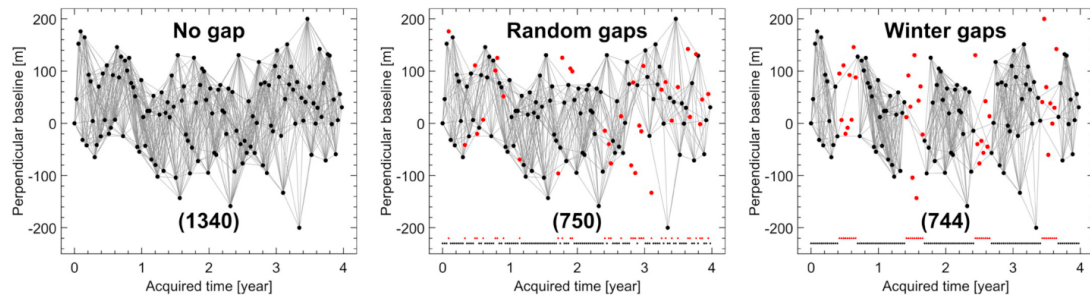


**Fig. 10.** Interferogram networks without (left) and with (middle, right) missing images. The number of missing images is 34 out of 133 corresponding to about 25%, which are selected randomly (middle) and in the northern winter season (right). The networks are formed using a temporal baseline threshold of  $\sim 4$  months and a perpendicular baseline threshold of 200 m. Gray lines indicate interferograms, with images denoted by black dots. Red dots indicate missing images (i.e., gaps). The number under each network refers to the number of interferograms. (For interpretation of the references to colour in this figure legend, the reader is referred to the web version of this article.)

### 7. Optimal design of InSAR SBAS networks using redundancy numbers

As has been demonstrated in Section 5, a spurious deformation trend (uplift instead of simulated subsidence) can be retrieved by applying SBAS, particularly in the case of small deformation in relation to large residual error and noise (i.e., a low SNR). By using more interferograms, the rate error can be decreased as the redundancy in the network is increased. However, an increased number of interferograms will also result in a higher computational burden. In this Section, “optimal” network design from geodesy is adopted for InSAR based on redundancy or  $r$ -numbers (Section 3). The motivation here is to investigate the relation between RMSs of the difference between simulated and SBAS-derived deformation time series, number of selected interferograms and the redundancy number.

Here, we test interferogram networks determined by combinations of temporal baseline thresholds, from one month to four years long, with a one-month increment, and perpendicular baseline thresholds of 100 m, 200 m and 300 m. As a result, 144 networks are formed with the minimum and maximum number of interferograms being 251 and 8778, respectively. Eq. (6) is then applied to each of these networks to compute the  $r$ -numbers.

The reliability matrix  $\mathbf{R}$  computed from Eq. (6) contains the  $r$ -numbers located on its diagonal ( $r_i$ ). The objective of this optimization

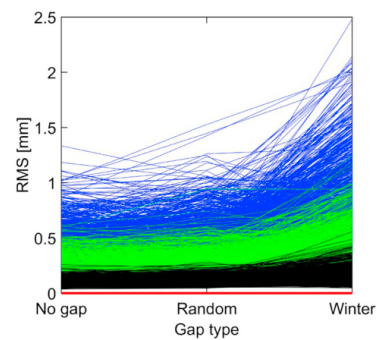


**Fig. 12.** Comparison of the RMSs of the difference between simulated and SBAS-derived deformation time series for all pixels between the interferogram networks of no gaps and those with randomly chosen gaps and “winter” gaps corresponding to  $\sim 25\%$  missing images. Black, green and blue polylines indicate the results computed from simulated data with noise cases A, B and C (Table 3). (For interpretation of the references to colour in this figure legend, the reader is referred to the web version of this article.)

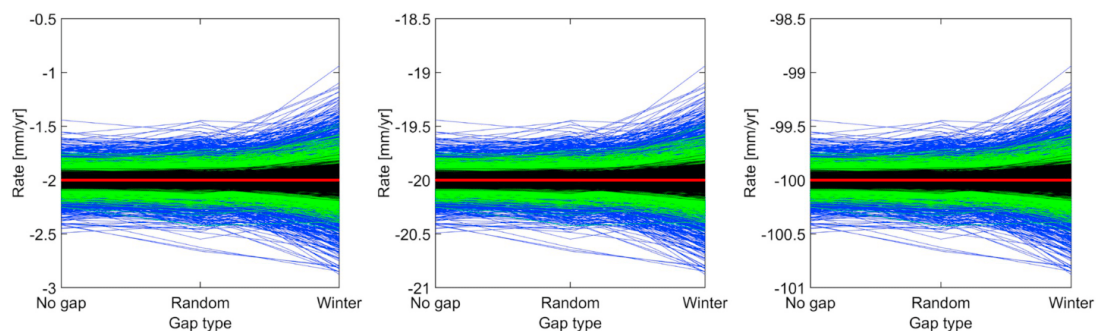


**Fig. 11.** Comparison of unweighted LS rates computed from linear plus annual signals according to interferogram networks with no gaps, random gaps and “winter” gaps. The networks adopt a temporal baseline threshold of  $\sim 4$  months and a perpendicular baseline threshold of 200 m. From left to right are simulated signal cases 1 to 3 (Table 2). Black, green and blue polylines indicate the results computed from simulated data with noise cases A, B, and C (Table 3). Red horizontal lines represent the simulated rate. (For interpretation of the references to colour in this figure legend, the reader is referred to the web version of this article.)

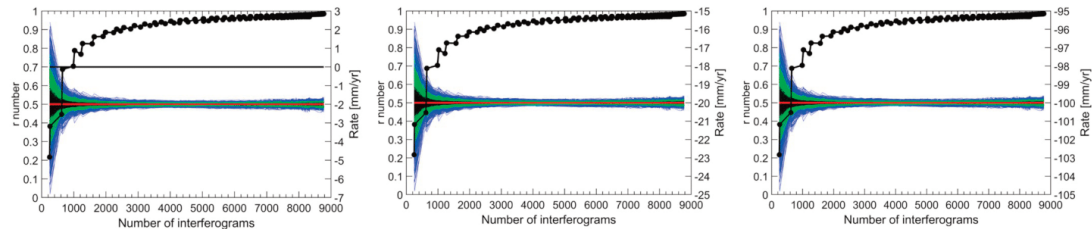


**Fig. 13.** The dependence of the  $r$ -numbers and SBAS-derived unweighted LS rates for 1000 pixels on the number of chosen interferograms with various linear plus annual signals. From left to right are simulated signal cases 1 to 3 (Table 2). Black, green and blue polylines show the results for noise cases A, B and C (Table 3). Red horizontal lines represent the simulated rates. (For interpretation of the references to colour in this figure legend, the reader is referred to the web version of this article.)

is to maximize these  $r$ -numbers by using their minimum value to represent the reliability of a network so that the  $r$ -numbers of all measurements in that network are larger or equal to this minimum value. The  $r$ -number of a network is thus defined as:

$$r = \min(r_i) \quad (11)$$

The SBAS method was then applied to derive deformation time series for all 1000 pixels, again using GIAN-T. We examine the same linear plus annual signals as those tested in Sections 5.1 and 6 (Table 2). The unweighted LS method is then utilized to derive SBAS-retrieved rates and the RMSs of the difference between simulated and SBAS-derived deformation time series are calculated.

The dependence of computed  $r$ -numbers and SBAS-retrieved annual rates on the number of selected interferograms are shown in Fig. 13, where the change in SBAS-derived unweighted LS rates presents the same patterns among the three cases (Table 2) of simulated signals. Furthermore, the higher the  $r$ -number, the closer the agreement between simulated and SBAS-retrieved rates. The two rates are, in particular, nearly identical when the  $r$ -numbers are greater than  $\sim 0.9$ .

The dependence of the RMSs of the difference between simulated and SBAS-retrieved deformation time series on the number of chosen interferograms are shown in Fig. 14 (left) for all three cases of simulated noise (Table 3). The  $r$ -number increases as the number of interferograms increases, constrained by temporal baseline thresholds, and a reduction in the RMSs. The RMSs decrease from a small  $r$ -number until  $\sim 0.8$ , after which the change becomes negligible.

We then apply 1/10 RMS as a trade-off value to identify the “optimal”  $r$ -number in which a network with a minimal number of interferograms selected and with all RMSs smaller than 1/10 noise range, which are 0.2 mm, 0.5 mm and 1.0 mm for the simulated residual interferogram noise ranges shown in Table 3. Recall that the RMSs are

dependent on the SBAS network and residual interferogram noise but not signal magnitude (Fig. 3). Thus, Fig. 14 indicates an “optimal”  $r$ -number being  $\sim 0.86$  for a SBAS network of 1911 interferograms, suggesting  $r$ -numbers between  $\sim 0.8$  and  $\sim 0.9$  to be a suitable range for the “optimal” design of SBAS networks.

The efficiency of the obtained “optimal”  $r$ -numbers are confirmed by not only the RMS trade-off, but also the computation time as shown in Fig. 14 (right), where the network of 1911 interferograms (for the “optimal”  $r$ -number) runs for less than four minutes compared to nearly 20 min for the largest network of 8778 interferograms. This shows efficiency in processing time for the SBAS inversion step only. In reality, SBAS data processing with a full workflow, which comprises additional steps of interferogram formation and error correction (e.g., DEM, orbital and atmospheric errors) the time difference between processing all 8778 interferograms and the optimal 1911 interferograms can be substantial. Additionally, this “optimal” design of SBAS networks keeps the number of interferograms to a minimum, which limits the disk storage space required.

Fig. 15 shows an example of the SBAS-derived deformation time series of a pixel compared with a simulated linear plus annual signal of  $-2$  mm/yr plus 2 mm (i.e., the simulated signal case 1 in Table 2) according to selected cases of computed  $r$ -number of  $\sim 0.2$ ,  $\sim 0.8$  and  $\sim 0.9$ . The results of applying residual noise cases A, B, and C (Table 3) are shown in Fig. 15. In all cases, the results corresponding to the computed  $r$ -numbers of  $\sim 0.8$  and  $\sim 0.9$  show close agreement with the simulated signal. In contrast, however, large differences between simulated and SBAS-derived deformation time series are shown in the case when the  $r$ -number is  $\sim 0.2$  (251 interferograms), particularly in the case of large residual interferogram noise (i.e., bounded within  $[-10; +10]$  mm) where the difference in both its trend (i.e., deformation or uplift) and magnitude is shown (cf. Fig. 15 (right) between

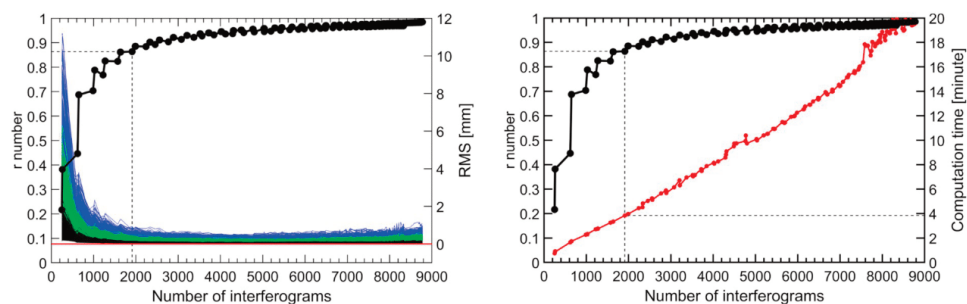


**Fig. 14.** (left): Comparison of the change in the  $r$ -numbers and the RMSs of the difference between simulated and SBAS-derived deformation time series. Black, green and blue polylines indicate the results computed from simulated data with noise cases A, B and C (Table 3). Dashed lines indicate the “optimal”  $r$ -numbers corresponding to the networks with smallest amount of interferograms chosen with all RMSs being smaller than the chosen trade-off values of 1/10 of the residual interferogram noise (Table 3). (right): Comparison of the change in the  $r$ -numbers according to SBAS network interferogram numbers and computation time.

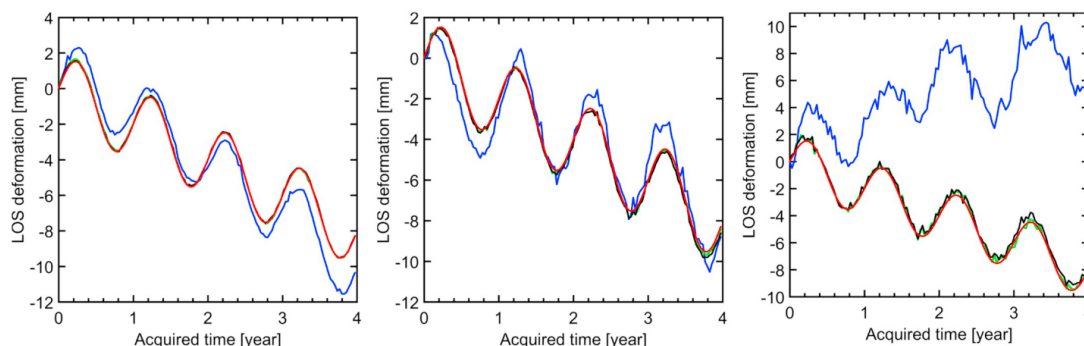


**Fig. 15.** An example of simulated and SBAS-derived deformation time series of simulated signal of linear rate plus annual amplitude of  $-2$  mm/yr plus  $2$  mm (simulated signal case 1 in Table 2) contaminated by residual interferogram noise cases A (left), B (middle) and C (right) as listed in Table 3. The results are computed from applying various SBAS interferogram networks corresponding to computed  $r$ -numbers of  $\sim 0.2$  (251 interferograms, blue polylines),  $\sim 0.8$  (1571 interferograms, green polylines), and  $\sim 0.9$  (2330 interferograms, black polylines), respectively. Red polylines indicate the simulated deformation time series. The blue line in the right panel shows the extreme case where spurious uplift is indicated, whereas subsidence is simulated. (For interpretation of the references to colour in this figure legend, the reader is referred to the web version of this article.)

the blue and red polylines).

Fig. 15 shows that if the  $r$ -number is too small ( $< 0.2$ ), spurious or even contradictory rates can result, as was shown similarly in Section 5. Therefore, caution must be exercised when using InSAR to detect small rates of deformation in the presence of large noise (low SNR). This is where the redundancy number may be of assistance in gauging the reliability of the estimated rates. This also shows that, though the reliability of a network is relevant to its ability to detect and resist against gross errors, in this specific case of InSAR SBAS networks, a good agreement between the  $r$ -numbers and errors in rate determination is present that is useful for “optimal” design of InSAR SBAS networks.

## 8. Conclusions

This study has used simulated Gaussian noise with zero mean applied to interferograms computed from simulated linear and annual sinusoidal trends to demonstrate the effects of interferometric noise on InSAR SBAS derived deformation. This extends to how different SBAS network configurations may influence the estimated deformation rates. Different simulated rates are tested (Table 2), including the addition of annual periodic amplitudes so as to represent a range of real SAR data. A Monte Carlo simulation with 1000 pixels for each scenario was adopted. Firstly, we investigated the linear deformation signal, finding that the SBAS linear-fit deformation trends were sensitive to both the magnitude of interferometric noise and signal size. The unweighted linear-fit rate error was the same in both magnitude and size for all rates if the same residual noise is applied to a given network. The trend may become contradictory for small magnitude deformation where, for example a  $-2$  mm/yr rate could be estimated from the SBAS least squares or SVD method as a spurious uplift. This contradictory result was shown when small temporal thresholds of 33 days or less were used, which resulted in a less robust SBAS network configuration with fewer interferograms.

When we tested the linear plus annual periodic signal with interferometric noise, the linear-fit rates were biased in the linear rate (from the 1000 pixels) compared to the simulated rate. Alternatively, when we estimated the rates using a more suitable periodic functional model, rather than just linear regression in the presence of non-linear terms, the estimated rates were not biased. This demonstrates the potential for errors to be introduced by using simple linear regression when non-linear deformation may also be occurring.

Because one of the strengths of the SBAS method is to provide redundant small interferogram baselines (in space and time), we

simulated the effect of missing SAR acquisitions in the time series. We presumed that these gaps in the time series would be (1) random that may be due to satellite mission scheduling issues, or (2) blocks of missing interferograms over, for example, a northern winter with snow covered ground that causes decorrelation. Our simulation results indicate that “winter” gaps causes a larger error in the estimated rates and in the RMSs of the differences between simulated and SBAS-derived deformation time series than for random gaps resulting from missed acquisitions. However, the RMS for both random gaps and no gaps were mostly 1 mm, while the winter gaps RMS was generally  $< 2$  mm, suggesting that random gaps have little influence. This is highlighted when random gaps are compared to temporal threshold limits, showing that for the same number of interferograms, limiting temporal thresholds can cause errors of up to 6 mm/yr with noisy simulated data, compared to  $\sim 3$  mm/yr for random gaps when using similar interferogram numbers. This suggests that it is the configuration of the SBAS network that is more important, to the point that caution should be exercised when reducing the temporal baseline to increase the coherence of the interferograms, because the trade-off may be a geometrically weak SBAS network that is vulnerable to incorrect rate estimation in the presence of noisy data and non-linear deformation.

We ran an additional simulation investigating whether redundancy numbers from geodetic theory could be adapted to design an optimal SBAS network. The simulation results suggest that  $r$ -values between  $\sim 0.8$  and  $\sim 0.9$  indicated a robust SBAS network design, and that including more interferograms beyond this provided little improvement in the accuracy of the rate estimation.

We conclude finally that SBAS network design can be critical to correctly estimate deformation rates, particularly in the case of low signal to noise ratios, and where the deformation may be non-linear. Notably, we found an alarming artifact in a couple of different simulation scenarios, where uplift was indicated by the SBAS rather than true simulated subsidence. It therefore appears that the configuration (network design) is more important than simply the number of interferograms used, which is important given any limits on computing resources. For this reason, we recommend the use of redundancy numbers to help optimize SBAS network design.

## Declaration of Competing Interest

The authors declare that they have no known competing financial interests or personal relationships that could have appeared to influence the work reported in this paper.

### Credit author statement

All authors participated in devising the simulations, writing, editing and revising the manuscript. Some additional aspects were based on the anonymous reviewers' comments, which we have placed in the Acknowledgements. Luyen K. Bui processed and analyzed the data simulations.

### Acknowledgements

Luyen Bui is supported by the Australia Awards Scholarships (AAS) provided for postgraduate study. Will Featherstone's InSAR projects are supported financially by Australian Research Council linkage project LP140100155, Landgate (the Western Australian geodetic agency), the Western Australian Department of Water, and Curtin University. We would like to thank California Institute of Technology (Caltech) for providing the source code of the Generic InSAR Analysis Toolbox (GIANT). Finally, we thank the editor and two anonymous reviewers for their thorough and constructive handling of our manuscript, particularly the advice to consider non-linear signals and "winter" gaps.

### References

- Amelung, F., Galloway, D.L., Bell, J.W., Zebker, H.A., Lacznak, R.J., 1999. Sensing the ups and downs of Las Vegas: InSAR reveals structural control of land subsidence and aquifer-system deformation. *Geology* 27 (6), 483–486. [https://doi.org/10.1130/0091-7613\(1999\)027<0483:STUADO>2.3.CO;2](https://doi.org/10.1130/0091-7613(1999)027<0483:STUADO>2.3.CO;2).
- Agram, P.S., Jolivet, R., Simons, M., 2012. GIANT - the Generic InSAR Analysis Toolbox - User Manual. Retrieved 09 June 2018, from [http://earthdef.caltech.edu/attachments/download/15/GIANT\\_doc.pdf](http://earthdef.caltech.edu/attachments/download/15/GIANT_doc.pdf).
- Agram, P.S., Jolivet, R., Riel, B., Lin, Y.N., Simons, M., Hetland, E., Doin, M.P., Lasserre, C., 2013. New radar interferometric time series analysis toolbox released. *Eos, Transactions, American Geophysical Union* 94 (7), 69–70. <https://doi.org/10.1002/2013EO070001>.
- Amiri-Simkooei, A.R., 2001. Comparison of reliability and geometrical strength criteria in geodetic networks. *J. Geod.* 75 (4), 231–233. <https://doi.org/10.1007/s001900100170>.
- Amiri-Simkooei, A.R., 2004. A new method for second order design of geodetic networks: aiming at high reliability. *Surv. Rev.* 37 (293), 552–560. <https://doi.org/10.1179/sre.2004.37.293.552>.
- Amiri-Simkooei, A.R., Asgari, J., Zangeneh-Nejad, F., Zaminpardaz, S., 2012. Basic concepts of optimization and design of geodetic networks. *J. Surv. Eng.* 138 (4), 172–183. [https://doi.org/10.1061/\(ASCE\)SU.1943-5428.0000081](https://doi.org/10.1061/(ASCE)SU.1943-5428.0000081).
- Baarda, W., 1968. A testing procedure for use in geodetic networks. In: *Publication on Geodesy, New Series, 2 Netherlands Geodetic Commission, Delft Number 5*.
- Baldi, P., Casula, G., Cenni, N., Loddo, F., Pesci, A., 2009. GPS-based monitoring of land subsidence in the Po plain (northern Italy). *Earth Planet. Sci. Lett.* 288 (1–2), 204–212. <https://doi.org/10.1016/j.epsl.2009.09.023>.
- Berardino, P., Fornaro, G., Lanari, R., Sansosti, E., 2002. A new algorithm for surface deformation monitoring based on small baseline differential SAR interferograms. *IEEE Trans. Geosci. Remote Sens.* 40 (11), 2375–2383. <https://doi.org/10.1109/TGRS.2002.803792>.
- Berné, J.L., Baselga, S., 2004. First-order design of geodetic networks using the simulated annealing method. *J. Geod.* 78 (1–2), 47–54. <https://doi.org/10.1007/s00190-003-0365-y>.
- Biggs, J., Wright, T., Lu, Z., Parsons, B., 2007. Multi-interferogram method for measuring interseismic deformation: Denali fault, Alaska. *Geophys. J. Int.* 170 (3), 1165–1179. <https://doi.org/10.1111/j.1365-246X.2007.03415.x>.
- Bock, Y., Wdowinski, S., Ferretti, A., Novali, F., Fumagalli, A., 2012. Recent subsidence of the Venice Lagoon from continuous GPS and interferometric synthetic aperture radar. *Geochem. Geophys. Geosyst.* 13 (3), Q03023. <https://doi.org/10.1029/2011GC003976>.
- Bombrun, L., Gay, M., Trouvé, E., Vasile, G., Mars, J., 2009. DEM error retrieval by analyzing time series of differential interferograms. *IEEE Geosci. Remote Sens. Lett.* 6 (4), 830–834. <https://doi.org/10.1109/LGRS.2009.2026434>.
- Cavalié, O., Doin, M.P., Lasserre, C., Briole, P., 2007. Ground motion measurement in the Lake Mead area, Nevada, by differential synthetic aperture radar interferometry time series analysis: probing the lithosphere rheological structure. *Journal of Geophysical Research: Solid Earth* 112 (3), 1–18. Article B03403. <https://doi.org/10.1029/2006JB004344>.
- Cavalié, O., Lasserre, C., Doin, M.-P., Peltzer, G., Sun, J., Xu, X., Shen, Z.-K., 2008. Measurement of interseismic strain across the Haiyuan fault (Gansu, China), by InSAR. *Earth Planet. Sci. Lett.* 275 (3–4), 246–257. <https://doi.org/10.1016/j.epsl.2008.07.057>.
- Cavalié, O., Pathier, E., Radiguet, M., Vergnolle, M., Cotte, N., Walpersdorf, A., Kostoglodov, V., Cotton, F., 2013. Slow slip event in the Mexican subduction zone: evidence of shallower slip in the Guerrero seismic gap for the 2006 event revealed by the joint inversion of InSAR and GPS data. *Earth Planet. Sci. Lett.* 367, 52–60. <https://doi.org/10.1016/j.epsl.2013.02.020>.
- Chaussard, E., Wdowinski, S., Cabral-Cano, E., Amelung, F., 2014. Land subsidence in Central Mexico detected by ALOS InSAR time-series. *Remote Sens. Environ.* 140, 94–106. <https://doi.org/10.1016/j.rse.2013.08.038>.
- Chen, M., Tomás, R., Li, Z., Motagh, M., Li, T., Hu, L., Gong, H., Li, X., Yu, J., Gong, X., 2016. Imaging land subsidence induced by groundwater extraction in Beijing (China) using satellite radar interferometry. *Remote Sens.* 8 (6). <https://doi.org/10.3390/rs8060468>. Article 468.
- Crosetto, M., Monserrat, O., Cuevas-González, M., Devanthéry, N., Crippa, B., 2016. Persistent Scatterer interferometry: a review. *ISPRS J. Photogramm. Remote Sens.* 115, 78–89. <https://doi.org/10.1016/j.isprsjprs.2015.10.011>.
- Davis, J.L., Wernicke, B.P., Tamisiea, M.E., 2012. On seasonal signals in geodetic time series. *Journal of Geophysical Research: Solid Earth* 117 (B1), B01403. <https://doi.org/10.1029/2011JB008690>.
- Delacourt, C., Briole, P., Achache, J., 1998. Tropospheric corrections of SAR interferograms with strong topography. Application to Etna. *Geophys. Res. Lett.* 25 (15), 2849–2852. <https://doi.org/10.1029/98GL02112>.
- Didova, O., Gunter, B., Riva, R., Klees, R., Roese-Koerner, L., 2016. An approach for estimating time-variable rates from geodetic time series. *J. Geod.* 90 (11), 1207–1221. <https://doi.org/10.1007/s00190-016-0918-5>.
- Doin, M.P., Lasserre, C., Peltzer, G., Cavalié, O., Doubre, C., 2009. Corrections of stratified tropospheric delays in SAR interferometry: validation with global atmospheric models. *J. Appl. Geophys.* 69 (1), 35–50. <https://doi.org/10.1016/j.jappgeo.2009.03.010>.
- Doin, M.P., Lodge, F., Guillaso, S., Jolivet, R., Lasserre, C., Ducret, G., Grandin, R., Pathier, E., Pinel, V., 2011. Presentation of the small baseline NSBAS processing chain on a case example: the Etna deformation monitoring from 2003 to 2010 using Envisat data. In: *ESA Fringe Symposium*, Frascati, Italy: ESA SP-697, pp. 3434–3437. [https://earth.esa.int/documents/10174/1573056/Presentation\\_small\\_baseline\\_NSBAS\\_Etna\\_deformation\\_Envisat.pdf](https://earth.esa.int/documents/10174/1573056/Presentation_small_baseline_NSBAS_Etna_deformation_Envisat.pdf).
- Dzurisin, D., Lisowski, M., Wicks, C.W., 2009. Continuing inflation at three sisters volcanic center, Central Oregon Cascade Range, USA, from GPS, leveling, and InSAR observations. *Bull. Volcanol.* 71 (10), 1091–1110. <https://doi.org/10.1007/s00445-009-0296-4>.
- Elliott, J.R., Walters, R.J., England, P.C., Jackson, J.A., Li, Z., Parsons, B., 2010. Extension on the Tibetan plateau: recent normal faulting measured by InSAR and body wave seismology. *Geophys. J. Int.* 183 (2), 503–535. <https://doi.org/10.1111/j.1365-246X.2010.04754.x>.
- Fattahi, H., Amelung, F., 2013. DEM error correction in InSAR time series. *IEEE Trans. Geosci. Remote Sens.* 51 (7), 4249–4259. <https://doi.org/10.1109/TGRS.2012.2227761>.
- Ferretti, A., Prati, C., Rocca, F., 2001. Permanent scatterers in SAR interferometry. *IEEE Trans. Geosci. Remote Sens.* 39 (1), 8–20. <https://doi.org/10.1109/36.898661>.
- Furuya, M., Mueller, K., Wahr, J., 2007. Active salt tectonics in the Needles District, Canyonlands (Utah) as detected by interferometric synthetic aperture radar and point target analysis: 1992–2002. *Journal of Geophysical Research: Solid Earth* 112 (6). <https://doi.org/10.1029/2006JB004302>. B06418, Article B06418.
- Gatelli, F., Guarnieri, A.M., Parizzi, F., Pasquali, P., Prati, C., Rocca, F., 1994. The wavenumber shift in SAR interferometry. *IEEE Trans. Geosci. Remote Sens.* 32 (4), 855–865. <https://doi.org/10.1109/36.298013>.
- Goel, K., Adam, N., 2014. A distributed scatterer interferometry approach for precision monitoring of known surface deformation phenomena. *IEEE Trans. Geosci. Remote Sens.* 52 (9), 5454–5468. Article 6679273. <https://doi.org/10.1109/TGRS.2013.2289370>.
- Gong, W., Thiele, A., Hinz, S., Meyer, F.J., Hooper, A., Agram, P.S., 2016. Comparison of small baseline interferometric SAR processors for estimating ground deformation. *Remote Sens.* 8 (4), 1–26. Article 330. <https://doi.org/10.3390/rs8040330>.
- Grafarend, E.W., Sansó, F., 1985. Optimization and Design of Geodetic Networks. Springer-Verlag, Berlin Heidelberg New York Tokyo. <https://doi.org/10.1007/978-3-642-70659-2>.
- Hetland, E.A., Musé, P., Simons, M., Lin, Y.N., Agram, P.S., DiCaprio, C.J., 2012. Multiscale InSAR time series (MINTs) analysis of surface deformation. *Journal of Geophysical Research: Solid Earth* 117 (B2), B02404. <https://doi.org/10.1029/2011JB008731>.
- Hooper, A., 2008. A multi-temporal InSAR method incorporating both persistent scatterer and small baseline approaches. *Geophys. Res. Lett.* 35 (16), L16302. Article L16302. <https://doi.org/10.1029/2008GL034654>.
- Hooper, A., Zebker, H.A., Segall, P., Kampes, B., 2004. A new method for measuring deformation on volcanoes and other natural terrains using InSAR persistent scatterers. *Geophys. Res. Lett.* 31 (23), L23611. <https://doi.org/10.1029/2004GL021737>.
- Hooper, A., Segall, P., Zebker, H.A., 2007. Persistent scatterer interferometric synthetic aperture radar for crustal deformation analysis, with application to Volcán Alcedo, Galápagos. *Journal of Geophysical Research: Solid Earth* 112, B7. <https://doi.org/10.1029/2006JB004763>.
- Hooper, A., Bekaert, D.P.S., Spaans, K., Arkan, M., 2012. Recent advances in SAR interferometry time series analysis for measuring crustal deformation. *Tectonophysics* 514–517, 1–13. <https://doi.org/10.1016/j.tecto.2011.10.013>.
- Jiang, L., Lin, H., Ma, J., Kong, B., Wang, Y., 2011. Potential of small-baseline SAR interferometry for monitoring land subsidence related to underground coal fires: Wuda (northern China) case study. *Remote Sens. Environ.* 115 (2), 257–268. <https://doi.org/10.1016/j.rse.2010.08.008>.
- Jolivet, R., Grandin, R., Lasserre, C., Doin, M.P., Peltzer, G., 2011. Systematic InSAR tropospheric phase delay corrections from global meteorological reanalysis data. *Geophys. Res. Lett.* 38 (17), L17311. Article L17311. <https://doi.org/10.1029/2011GL048757>.
- Jolivet, R., Lasserre, C., Doin, M.P., Guillaso, S., Peltzer, G., Dailu, R., Sun, J., Shen, Z.K.,

- Xu, X., 2012. Shallow creep on the Haiyuan fault (Gansu, China) revealed by SAR interferometry. *Journal of Geophysical Research: Solid Earth* 117 (B6), B06401. <https://doi.org/10.1029/2011JB008732>.
- Kim, J.W., Lu, Z., Jia, Y., Shum, C.K., 2015. Ground subsidence in Tucson, Arizona, monitored by time-series analysis using multi-sensor InSAR datasets from 1993 to 2011. *ISPRS J. Photogramm. Remote Sens.* 107, 126–141. <https://doi.org/10.1016/j.isprsjprs.2015.03.013>.
- Koch, K.R., 1985. First order design: Optimization of the configuration of a network by introducing small position changes. In: Grafarend, E.W., Sansò, F. (Eds.), *Optimization and Design of Geodetic Networks*. Springer-Verlag, Berlin Heidelberg New York Tokyo, pp. 56–73. <https://doi.org/10.1007/978-3-642-70659-2>.
- Kohlhase, A.O., Feigl, K.L., Massonnet, D., 2003. Applying differential InSAR to orbital dynamics: a new approach for estimating ERS trajectories. *J. Geod.* 77 (9), 493–502. <https://doi.org/10.1007/s00190-003-0336-3>.
- Kroese, D.P., Brereton, T., Taimre, T., Botev, Z.I., 2014. Why the Monte Carlo method is so important today. *Wiley Interdisciplinary Reviews: Computational Statistics* 6 (6), 386–392. <https://doi.org/10.1002/wics.1314>.
- Kuang, S., 1993. On optimal design of levelling networks. *Australian Surveyor* 38 (4), 257–273. <https://doi.org/10.1080/00050326.1993.10438874>.
- Kuang, S., 1996. *Geodetic network analysis and optimal design: concepts and applications*. Ann Arbor Press, Chelsea, Michigan, pp. 368.
- Lanari, R., Mora, O., Manunta, M., Mallorquí, J.J., Berardino, P., Sansosti, E., 2004. A small-baseline approach for investigating deformations on full-resolution differential SAR interferograms. *IEEE Trans. Geosci. Remote Sens.* 42 (7), 1377–1386. <https://doi.org/10.1109/TGRS.2004.828196>.
- Lanari, R., Casu, F., Manzo, M., Zeni, G., Berardino, P., Manunta, M., Pepe, A., 2007. An overview of the small Baseline subset algorithm: a DInSAR technique for surface deformation analysis. *Pure Appl. Geophys.* 164 (4), 637–661. <https://doi.org/10.1007/s00024-007-0192-9>.
- Lauknes, T.R., Zebker, H.A., Larsen, Y., 2011. InSAR deformation time series using an L1-norm small-baseline approach. *IEEE Trans. Geosci. Remote Sens.* 49 (1 PART 2), 536–546. Article 5512638. <https://doi.org/10.1109/TGRS.2010.2051951>.
- Lee, C.W., Lu, Z., Jung, H.S., 2012. Simulation of time-series surface deformation to validate a multi-interferogram InSAR processing technique. *Int. J. Remote Sens.* 33 (22), 7075–7087. <https://doi.org/10.1080/01431161.2012.700137>.
- Lin, Y.N.N., Simons, M., Hetland, E.A., Muse, P., Dicaprio, C., 2010. A multiscale approach to estimating topographically correlated propagation delays in radar interferograms. *Geochem. Geophys. Geosyst.* 11, 9), 1–17. Article Q09002. <https://doi.org/10.1029/2010GC003228>.
- López-Quiroz, P., Doin, M.-P., Tupin, F., Briole, P., Nicolas, J.-M., 2009. Time series analysis of Mexico City subsidence constrained by radar interferometry. *J. Appl. Geophys.* 69 (1), 1–15. <https://doi.org/10.1016/j.jappgeo.2009.02.006>.
- Lubitz, C., Motagh, M., Wetzel, H.U., Kaufmann, H., 2013. Remarkable urban uplift in Staufen im Breisgau, Germany: observations from terraSAR-X InSAR and leveling from 2008 to 2011. *Remote Sens.* 5 (6), 3082–3100. <https://doi.org/10.3390/rs5063082>.
- Lundgren, P., Usai, S., Sansosti, E., Lanari, R., Tesauro, M., Fornaro, G., Berardino, P., 2001. Modeling surface deformation observed with synthetic aperture radar interferometry at Campi Flegrei caldera. *Journal of Geophysical Research: Solid Earth* 106 (B9), 19355–19366. Article 2001jb000194.
- Mora, O., Mallorquí, J.J., Broquetas, A., 2003. Linear and nonlinear terrain deformation maps from a reduced set of interferometric SAR images. *IEEE Trans. Geosci. Remote Sens.* 41, 2243–2253. <https://doi.org/10.1109/TGRS.2003.814657>. 10 PART I.
- Motagh, M., Djamour, Y., Walter, T.R., Wetzel, H.U., Zschau, J., Arabi, S., 2007. Land subsidence in Mashhad Valley, Northeast Iran: results from InSAR, levelling and GPS. *Geophys. J. Int.* 168 (2), 518–526. <https://doi.org/10.1111/j.1365-246X.2006.03246.x>.
- Murray, K.D., Lohman, R.B., 2018. Short-lived pause in Central California subsidence after heavy winter precipitation of 2017. *Sci. Adv.* 4 (8). <https://doi.org/10.1126/sciadv.aar8144>. Article eaar8144.
- Murray, K.D., Bekaert, D.P.S., Lohman, R.B., 2019. Tropospheric corrections for InSAR: statistical assessments and applications to the Central United States and Mexico. *Remote Sens. Environ.* 232. <https://doi.org/10.1016/j.rse.2019.111326>. Article 111326.
- Neely, W.R., Borsa, A.A., Silverii, F., 2020. GInSAR: a cGPS correction for enhanced InSAR time series. *IEEE Trans. Geosci. Remote Sens.* 58 (1), 136–146. Article 8839742. <https://doi.org/10.1109/TGRS.2019.2934118>.
- Osmanoğlu, B., Dixon, T.H., Wdowinski, S., Cabral-Cano, E., Jiang, Y., 2011. Mexico City subsidence observed with persistent scatterer InSAR. *Int. J. Appl. Earth Obs. Geoinf.* 13 (1), 1–12. <https://doi.org/10.1016/j.jag.2010.05.009>.
- Pepe, A., Ortiz, A.B., Lundgren, P.R., Rosen, P.A., Lanari, R., 2011. The Stripmap-ScanSAR SBAS Approach to Fill Gaps in Stripmap Deformation Time Series With ScanSAR Data. In: *IEEE Transactions on Geoscience and Remote Sensing*, <https://doi.org/10.1109/TGRS.2011.2167979>. 49(12 PART 1), 4788–4804, Article 6045335.
- Schmidt, D.A., Bürgmann, R., 2003. Time-dependent land uplift and subsidence in the Santa Clara valley, California, from a large interferometric synthetic aperture radar data set. *Journal of Geophysical Research: Solid Earth* 108 (B9). <https://doi.org/10.1029/2002JB002267>.
- Schmitt, G., 1985a. Review of network designs: Criteria, risk functions, design ordering. In: Grafarend, E.W., Sansò, F. (Eds.), *Optimization and Design of Geodetic Networks*. Springer-Verlag, Berlin Heidelberg New York Tokyo, pp. 6–10. <https://doi.org/10.1007/978-3-642-70659-2>.
- Schmitt, G., 1985b. Third order design. In: Grafarend, E.W., Sansò, F. (Eds.), *Optimization and Design of Geodetic Networks*. Springer-Verlag, Berlin Heidelberg New York Tokyo, pp. 122–131. <https://doi.org/10.1007/978-3-642-70659-2>.
- Shanker, P., Casu, F., Zebker, H.A., Lanari, R., 2011. Comparison of persistent scatterers and small baseline time-series InSAR results: a case study of the San Francisco bay area. *IEEE Geosci. Remote Sens. Lett.* 8 (4), 592–596. Article 5692806. <https://doi.org/10.1109/LGRS.2010.2095829>.
- Short, N., Brisco, B., Couture, N., Pollard, W., Murnaghan, K., Budkewitsch, P., 2011. A comparison of TerraSAR-X, RADARSAT-2 and ALOS-PALSAR interferometry for monitoring permafrost environments, case study from Herschel Island, Canada. *Remote Sens. Environ.* 115 (12), 3491–3506. <https://doi.org/10.1016/j.rse.2011.08.012>.
- Sowter, A., Bateson, L., Strange, P., Ambrose, K., Fifiksafiudin, M., 2013. DInSAR estimation of land motion using intermittent coherence with application to the south derbyshire and leicestershire coalfields. *Remote Sensing Letters* 4 (10), 979–987. <https://doi.org/10.1080/2150704X.2013.823673>.
- Teunissen, P.J.G., 1985. Zero order design: Generalized inverses, adjustment, the datum problem and S-transformations. In: Grafarend, E.W., Sansò, F. (Eds.), *Optimization and Design of Geodetic Networks*. Springer-Verlag, Berlin Heidelberg New York Tokyo, pp. 11–55. <https://doi.org/10.1007/978-3-642-70659-2>.
- Tong, X., Sandwell, D.T., Smith-Konter, B., 2013. High-resolution interseismic velocity data along the San Andreas fault from GPS and InSAR. *Journal of Geophysical Research: Solid Earth* 118 (1), 369–389. <https://doi.org/10.1029/2012JB009442>.
- Tymofeyeva, E., Fialko, Y., 2015. Mitigation of atmospheric phase delays in InSAR data, with application to the eastern California shear zone. *Journal of Geophysical Research: Solid Earth* 120 (8), 5952–5963. <https://doi.org/10.1002/2015JB011886>.
- Usai, S., 2003. A least squares database approach for SAR Interferometric data. In: *IEEE Transactions on Geoscience and Remote Sensing*, 41(4 PART 1), pp. 753–760. <https://doi.org/10.1109/TGRS.2003.810675>.
- Vaniček, P., Krakiwsky, E.J., 1986. *Geodesy: The Concepts*, 2nd ed. Elsevier Science Publisher, Amsterdam, The Netherlands.
- Williams, S., Bock, Y., Fang, P., 1998. Integrated satellite interferometry: tropospheric noise, GPS estimates and implications for interferometric synthetic aperture radar products. *Journal of Geophysical Research: Solid Earth* 103 (B11), 27051–27067. Article 98jb02794. <https://doi.org/10.1029/98jb02794>.
- Yague-Martinez, N., Prats-Iraola, P., Gonzalez, F.R., Bricic, R., Shau, R., Geudtner, D., Eineder, M., Bamler, R., 2016. Interferometric processing of Sentinel-1 TOPS data. *IEEE Trans. Geosci. Remote Sens.* 54 (4), 2220–2234. Article 7390052. <https://doi.org/10.1109/TGRS.2015.2497902>.
- Yu, C., Penna, N.T., Li, Z., 2017. Generation of real-time mode high-resolution water vapor fields from GPS observations. *J. Geophys. Res.* 122 (3), 2008–2025. <https://doi.org/10.1002/2016JD025753>.
- Yu, C., Li, Z., Penna, N.T., 2018a. Interferometric synthetic aperture radar atmospheric correction using a GPS-based iterative tropospheric decomposition model. *Remote Sens. Environ.* 204, 109–121. <https://doi.org/10.1016/j.rse.2017.10.038>.
- Yu, C., Li, Z., Penna, N.T., Crippa, P., 2018b. Generic atmospheric correction model for Interferometric synthetic aperture radar observations. *Journal of Geophysical Research: Solid Earth* 123 (10), 9202–9222. <https://doi.org/10.1029/2017JB015305>.
- Zebker, H.A., Villasenor, J., 1992. Decorrelation in interferometric radar echoes. *IEEE Trans. Geosci. Remote Sens.* 30 (5), 950–959. <https://doi.org/10.1109/36.175330>.
- Zebker, H.A., Rosen, P.A., Hensley, S., 1997. Atmospheric effects in interferometric synthetic aperture radar surface deformation and topographic maps. *Journal of Geophysical Research: Solid Earth* 102 (B4), 7547–7563. Article 96JB03804.

## REFERENCES

- Agnew, D. C. (1992). The time-domain behavior of power-law noises. *Geophysical Research Letters*, 19(4), 333-336. <https://doi.org/10.1029/91GL02832>
- Agram, P. S., Jolivet, R., Riel, B., Lin, Y. N., Simons, M., Hetland, E., Doin, M. P., & Lasserre, C. (2013). New radar interferometric time series analysis toolbox released. *Eos, Transactions, American Geophysical Union*, 94(7), 69-70. <https://doi.org/10.1002/2013EO070001>
- Agram, P. S., Jolivet, R., & Simons, M. (2012). GIAN T - The Generic InSAR Analysis Toolbox - User Manual. Retrieved 09 June 2018, from [http://earthdef.caltech.edu/attachments/download/15/GIAN\\_T\\_doc.pdf](http://earthdef.caltech.edu/attachments/download/15/GIAN_T_doc.pdf)
- Agram, P. S., & Simons, M. (2015). A noise model for InSAR time series. *Journal of Geophysical Research: Solid Earth*, 120(4), 2752-2771. <https://doi.org/10.1002/2014JB011271>
- Ahmed, S., Warren, H. R., Symonds, M. D., & Cox, R. P. (1990). The Radarsat System. *IEEE Transactions on Geoscience and Remote Sensing*, 28(4), 598-602. <https://doi.org/10.1109/TGRS.1990.572961>
- Alizadeh-Khameneh, M. A., Eshagh, M., & Sjöberg, L. E. (2015). Optimisation of Lilla Edet landslide GPS monitoring network. *Journal of Geodetic Science*, 5(1), 57-66. <https://doi.org/10.1515/jogs-2015-0005>
- Alizadeh-Khameneh, M. A., Eshagh, M., & Sjöberg, L. E. (2016). The effect of instrumental precision on optimisation of displacement monitoring networks. *Acta Geodaetica et Geophysica*, 51(4), 761-772. <https://doi.org/10.1007/s40328-015-0150-4>
- Amelung, F., Galloway, D. L., Bell, J. W., Zebker, H. A., & Lacznik, R. J. (1999). Sensing the ups and downs of Las Vegas: InSAR reveals structural control of land subsidence and aquifer-system deformation. *Geology*, 27(6), 483-486. [https://doi.org/10.1130/0091-7613\(1999\)027<0483:STUADO>2.3.CO;2](https://doi.org/10.1130/0091-7613(1999)027<0483:STUADO>2.3.CO;2)
- Amiri-Simkooei, A. R. (2001a). Comparison of reliability and geometrical strength criteria in geodetic networks. *Journal of Geodesy*, 75(4), 231-233. <https://doi.org/10.1007/s001900100170>
- Amiri-Simkooei, A. R. (2001b). Strategy for designing geodetic network with high reliability and geometrical strength. *Journal of Surveying Engineering*, 127(3), 104-117. [https://doi.org/10.1061/\(ASCE\)0733-9453\(2001\)127:3\(104\)](https://doi.org/10.1061/(ASCE)0733-9453(2001)127:3(104))
- Amiri-Simkooei, A. R. (2004). A new method for second order design of geodetic networks: Aiming at high reliability. *Survey Review*, 37(293), 552-560. <https://doi.org/10.1179/sre.2004.37.293.552>

- Amiri-Simkooei, A. R., Asgari, J., Zangeneh-Nejad, F., & Zaminpardaz, S. (2012). Basic concepts of optimization and design of geodetic networks. *Journal of Surveying Engineering*, 138(4), 172-183. [https://doi.org/10.1061/\(ASCE\)SU.1943-5428.0000081](https://doi.org/10.1061/(ASCE)SU.1943-5428.0000081)
- Amiri-Simkooei, A. R., & Sharifi, M. A. (2004). Approach for equivalent accuracy design of different types of observations. *Journal of Surveying Engineering*, 130(1), 1-5. [https://doi.org/10.1061/\(ASCE\)0733-9453\(2004\)130:1\(1\)](https://doi.org/10.1061/(ASCE)0733-9453(2004)130:1(1))
- Andersen, M. L., Stenseng, L., Skourup, H., Colgan, W., Khan, S. A., Kristensen, S. S., Andersen, S. B., Box, J. E., Ahlstrøm, A. P., Fettweis, X., & Forsberg, R. (2015). Basin-scale partitioning of Greenland ice sheet mass balance components (2007-2011). *Earth and Planetary Science Letters*, 409, 89-95. <https://doi.org/10.1016/j.epsl.2014.10.015>
- Baarda, W. (1968). A testing procedure for use in geodetic networks. Publication on Geodesy, New Series, Volume 2, Number 5. In *Netherlands Geodetic Commission, Delft*.
- Bagherbandi, M., Eshagh, M., & Sjöberg, L. E. (2009). Multi-objective versus single-objective models in geodetic network optimization. *Nordic Journal of Surveying and Real Estate Research*, 6(1), 7-20.
- Baker, S., & Amelung, F. (2012). Top-down inflation and deflation at the summit of Kilauea Volcano, Hawaii observed with InSAR. *Journal of Geophysical Research B: Solid Earth*, 117(12), Article B12406. <https://doi.org/10.1029/2011JB009123>
- Baldi, P., Casula, G., Cenni, N., Loddo, F., & Pesci, A. (2009). GPS-based monitoring of land subsidence in the Po Plain (Northern Italy). *Earth and Planetary Science Letters*, 288(1-2), 204-212. <https://doi.org/10.1016/j.epsl.2009.09.023>
- Bamler, R., & Eineder, M. (1996). Scansar processing using standard high precision sar algorithms. *IEEE Transactions on Geoscience and Remote Sensing*, 34(1), 212-218. <https://doi.org/10.1109/36.481905>
- Bamler, R., & Eineder, M. (2005). Accuracy of differential shift estimation by correlation and split-bandwidth interferometry for wideband and Delta-k SAR systems. *IEEE Geoscience and Remote Sensing Letters*, 2(2), 151-155. <https://doi.org/10.1109/LGRS.2004.843203>
- Bamler, R., & Hartl, P. (1998). Synthetic aperture radar interferometry. *Inverse Problems*, 14(4), r1-r54. <https://doi.org/10.1088/0266-5611/14/4/001>
- Bamler, R., & Just, D. (1993, 18-21 August). Phase statistics and decorrelation in SAR interferograms. *IEEE International Geoscience and Remote Sensing Symposium (IGARSS '93)*, Tokyo, Japan. 980-984 <https://doi.org/10.1109/IGARSS.1993.322637>

- Baran, I., Stewart, M. P., Kampes, B. M., Perski, Z., & Lilly, P. (2003). A modification to the goldstein radar interferogram filter. *IEEE Transactions on Geoscience and Remote Sensing*, 41(9 PART II), 2114-2118. <https://doi.org/10.1109/TGRS.2003.817212>
- Beauducel, F., Briole, P., & Froger, J. L. (2000). Volcano-wide fringes in ERS synthetic aperture radar interferograms of Etna (1992-1998): Deformation or tropospheric effect? *Journal of Geophysical Research: Solid Earth*, 105(B7), 16391-16402, Article 2000jb900095. <https://doi.org/10.1029/2000jb900095>
- Bekaert, D. P. S., Hooper, A., & Wright, T. J. (2015). A spatially variable power law tropospheric correction technique for InSAR data. *Journal of Geophysical Research: Solid Earth*, 120(2), 1345-1356. <https://doi.org/10.1002/2014JB011558>
- Berardino, P., Fornaro, G., Lanari, R., & Sansosti, E. (2002). A new algorithm for surface deformation monitoring based on small baseline differential SAR interferograms. *IEEE Transactions on Geoscience and Remote Sensing*, 40(11), 2375-2383. <https://doi.org/10.1109/TGRS.2002.803792>
- Bernard, P., Briole, P., Meyer, B., Lyon-Caen, H., Gomez, J. M., Tiberi, C., Berge, C., Cattin, R., Hatzfeld, D., Lachet, C., Lebrun, B., Deschamps, A., Courboux, F., Larroque, C., Rigo, A., Massonnet, D., Papadimitriou, P., Kassaras, J., Diagourtas, D., Makropoulos, K., Veis, G., Papazisi, E., Mitsakaki, C., Karakostas, V., Papadimitriou, E., Papanastassiou, D., Chouliaras, M., & Stavrakakis, G. (1997). The Ms=6.2, June 15, 1995 Aigion earthquake (Greece): Evidence for low angle normal faulting in the Corinth rift. *Journal of Seismology*, 1(2), 131-150. <https://doi.org/10.1023/A:1009795618839>
- Berné, J. L., & Baselga, S. (2004). First-order design of geodetic networks using the simulated annealing method. *Journal of Geodesy*, 78(1-2), 47-54. <https://doi.org/10.1007/s00190-003-0365-y>
- Biggs, J., Wright, T., Lu, Z., & Parsons, B. (2007). Multi-interferogram method for measuring interseismic deformation: Denali Fault, Alaska. *Geophysical Journal International*, 170(3), 1165-1179. <https://doi.org/10.1111/j.1365-246X.2007.03415.x>
- Blewitt, G., Hammond, W. C., & Kreemer, C. (2018). Harnessing the GPS Data Explosion for Interdisciplinary Science. *Eos*, 99, 1-2. <https://doi.org/10.1029/2018eo104623>
- Bock, Y., Wdowinski, S., Ferretti, A., Novali, F., & Fumagalli, A. (2012). Recent subsidence of the Venice Lagoon from continuous GPS and interferometric synthetic aperture radar. *Geochemistry, Geophysics, Geosystems*, 13(3), Q03023. <https://doi.org/10.1029/2011GC003976>
- Bombrun, L., Gay, M., Trouvé, E., Vasile, G., & Mars, J. (2009). DEM error retrieval by analyzing time series of differential interferograms. *IEEE Geoscience and*

*Remote Sensing Letters*, 6(4), 830-834, Article 5226568.  
<https://doi.org/10.1109/LGRS.2009.2026434>

- Bruderer, B., Steuri, T., Aschwanden, J., & Liechti, F. (2012). From a military target tracking radar for bird radar. *Ornithologische Beobachter*, 109(3), 157-176.
- Buckley, S. M., Rosen, P. A., Hensley, S., & Tapley, B. D. (2003). Land subsidence in Houston, Texas, measured by radar interferometry and constrained by extensometers. *Journal of Geophysical Research: Solid Earth*, 108(11), ETG 8-1 - ETG 8-13. <https://doi.org/10.1029/2002jb001848>
- Buderi, R. (1996). *The invention that changed the world: How a small group of radar pioneers won the Second World War and launched a technological revolution* (p. 576). Simon and Schuster, New York.
- Bui, L. K., Featherstone, W. E., & Filmer, M. S. (2020). Disruptive influences of residual noise, network configuration and data gaps on InSAR-derived land motion rates using the SBAS technique. *Remote Sensing of Environment*, 247, 111941. <https://doi.org/10.1016/j.rse.2020.111941>
- Bui, L. K., Le, P. V. V., Dao, P. D., Nguyen, N. Q., Pham, H. V., Tran, H. H., & Xie, L. (2021). Recent land deformation detected by Sentinel-1A InSAR data (2016–2020) over Hanoi, Vietnam, and the relationship with groundwater level change. *GIScience and Remote Sensing*, 58(2), 191-179. <https://doi.org/10.1080/15481603.2020.1868198>
- Bürgmann, R., Rosen, P. A., & Fielding, E. J. (2000). Synthetic aperture radar interferometry to measure earth's surface topography and its deformation. *Annual Review of Earth and Planetary Sciences*, 28, 169-209. <https://doi.org/10.1146/annurev.earth.28.1.169>
- Byrd, R. H., Peihuang, L., Jorge, N., & Ciyou, Z. (1995). A limited memory algorithm for bound constrained optimization. *SIAM Journal on scientific computing*, 16(5), 1190-1208. <https://doi.org/10.2172/204262>
- Cai, B., Liang, D., & Dong, Z. (2008). A new adaptive multiresolution noise-filtering approach for SAR interferometric phase images. *IEEE Geoscience and Remote Sensing Letters*, 5(2), 266-270, Article 4464107. <https://doi.org/10.1109/LGRS.2008.915942>
- Calero, E. J. (2018). *Sentinels POD service file format specifications* [Technical Report]. European Space Agency, Frascati, Italy. [https://sentinel.esa.int/documents/247904/351187/GMES\\_Sentinels\\_POD\\_Service\\_File\\_Format\\_Specification](https://sentinel.esa.int/documents/247904/351187/GMES_Sentinels_POD_Service_File_Format_Specification)
- Cao, Y., Li, Z., Wei, J., Hu, J., Duan, M., & Feng, G. (2018). Stochastic modeling for time series InSAR: with emphasis on atmospheric effects. *Journal of Geodesy*, 92(2), 185-204. <https://doi.org/10.1007/s00190-017-1055-5>

- Castañeda, C., Gutiérrez, F., Manunta, M., & Galve, J. P. (2009). DInSAR measurements of ground deformation by sinkholes, mining subsidence, and landslides, Ebro River, Spain. *Earth Surface Processes and Landforms*, 34(11), 1562-1574. <https://doi.org/10.1002/esp.1848>
- Casu, F., Manzo, M., & Lanari, R. (2006). A quantitative assessment of the SBAS algorithm performance for surface deformation retrieval from DInSAR data. *Remote Sensing of Environment*, 102(3-4), 195-210. <https://doi.org/10.1016/j.rse.2006.01.023>
- Catalão, J., Nico, G., Hanssen, R., & Catita, C. (2009). Integration of InSAR and GPS for vertical deformation monitoring: a case study in Faial and Pico Islands. Proceedings of Fringe 2009 Workshop, Frascati, Italy, 30 November - 4 December 2009, ESA Publications SP-677, 1-6.
- Cavalié, O., Doin, M. P., Lasserre, C., & Briole, P. (2007). Ground motion measurement in the Lake Mead area, Nevada, by differential synthetic aperture radar interferometry time series analysis: Probing the lithosphere rheological structure. *Journal of Geophysical Research: Solid Earth*, 112(3), 1-18, Article B03403. <https://doi.org/10.1029/2006JB004344>
- Cavalié, O., Lasserre, C., Doin, M.-P., Peltzer, G., Sun, J., Xu, X., & Shen, Z.-K. (2008). Measurement of interseismic strain across the Haiyuan fault (Gansu, China), by InSAR. *Earth and Planetary Science Letters*, 275(3-4), 246-257. <https://doi.org/10.1016/j.epsl.2008.07.057>
- Cavalié, O., Pathier, E., Radiguet, M., Vergnolle, M., Cotte, N., Walpersdorf, A., Kostoglodov, V., & Cotton, F. (2013). Slow slip event in the Mexican subduction zone: Evidence of shallower slip in the Guerrero seismic gap for the 2006 event revealed by the joint inversion of InSAR and GPS data. *Earth and Planetary Science Letters*, 367, 52-60. <https://doi.org/10.1016/j.epsl.2013.02.020>
- Cenzo, A. D. (1988). Strip Mode Processing of Spotlight Synthetic Aperture Radar Data. *IEEE Transactions on Aerospace and Electronic Systems*, 24(3), 225-230. <https://doi.org/10.1109/7.192090>
- Chang, L., & Hanssen, R. F. (2016). Functional model selection for InSAR time series. Geoscience and Remote Sensing Symposium (IGARSS), 2016 IEEE International, 3390-3393.
- Chaussard, E., Amelung, F., Abidin, H., & Hong, S. H. (2013). Sinking cities in Indonesia: ALOS PALSAR detects rapid subsidence due to groundwater and gas extraction. *Remote Sensing of Environment*, 128, 150-161. <https://doi.org/10.1016/j.rse.2012.10.015>
- Chaussard, E., Wdowinski, S., Cabral-Cano, E., & Amelung, F. (2014). Land subsidence in central Mexico detected by ALOS InSAR time-series. *Remote Sensing of Environment*, 140, 94-106. <https://doi.org/10.1016/j.rse.2013.08.038>

- Chen, A. C., & Zebker, H. A. (2014). Reducing ionospheric effects in InSAR data using accurate coregistration. *IEEE Transactions on Geoscience and Remote Sensing*, 52(1), 60-70, Article 6428644. <https://doi.org/10.1109/TGRS.2012.2236098>
- Chen, C. W., & Zebker, H. A. (2000). Network approaches to two-dimensional phase unwrapping: Intractability and two new algorithms. *Journal of the Optical Society of America A: Optics and Image Science, and Vision*, 17(3), 401-414. <https://doi.org/10.1364/JOSAA.17.000401>
- Chen, C. W., & Zebker, H. A. (2001). Two-dimensional phase unwrapping with use of statistical models for cost functions in nonlinear optimization. *Journal of the Optical Society of America A: Optics and Image Science, and Vision*, 18(2), 338-351. <https://doi.org/10.1364/JOSAA.18.000338>
- Chen, C. W., & Zebker, H. A. (2002). Phase unwrapping for large SAR interferograms: Statistical segmentation and generalized network models. *IEEE Transactions on Geoscience and Remote Sensing*, 40(8), 1709-1719. <https://doi.org/10.1109/TGRS.2002.802453>
- Chen, G. Y., Bui, T. D., & Krzyzak, A. (2005). Image denoising with neighbour dependency and customized wavelet and threshold. *Pattern Recognition*, 38(1), 115-124. <https://doi.org/10.1016/j.patcog.2004.05.009>
- Chen, J., & Zebker, H. A. (2012). Ionospheric artifacts in simultaneous L-band InSAR and GPS observations. *IEEE Transactions on Geoscience and Remote Sensing*, 50(4), 1227-1239, Article 6035969. <https://doi.org/10.1109/TGRS.2011.2164805>
- Chen, M., Tomás, R., Li, Z., Motagh, M., Li, T., Hu, L., Gong, H., Li, X., Yu, J., & Gong, X. (2016). Imaging land subsidence induced by groundwater extraction in Beijing (China) using satellite radar interferometry. *Remote Sensing*, 8(6), Article 468. <https://doi.org/10.3390/rs8060468>
- Colesanti, C., Ferretti, A., Prati, C., & Rocca, F. (2003). Monitoring landslides and tectonic motions with the Permanent Scatterers Technique. *Engineering Geology*, 68(1-2), 3-14. [https://doi.org/10.1016/S0013-7952\(02\)00195-3](https://doi.org/10.1016/S0013-7952(02)00195-3)
- Colesanti, C., & Wasowski, J. (2006). Investigating landslides with space-borne Synthetic Aperture Radar (SAR) interferometry. *Engineering Geology*, 88(3-4), 173-199. <https://doi.org/10.1016/j.enggeo.2006.09.013>
- Crosetto, M., Monserrat, O., Cuevas-González, M., Devanthéry, N., & Crippa, B. (2016). Persistent Scatterer Interferometry: A review. *ISPRS Journal of Photogrammetry and Remote Sensing*, 115, 78-89. <https://doi.org/10.1016/j.isprsjprs.2015.10.011>
- Cross, P. A. (1985). Numerical methods in network design. In E. W. Grafarend & F. Sansò (Eds.), *Optimization and design of geodetic networks* (pp. 132-168).

Springer-Verlag, Berlin Heidelberg New York Tokyo.  
<https://doi.org/10.1007/978-3-642-70659-2>

- Cuenca, M. C., Hanssen, R., Hooper, A., & Arikan, M. (2011). Surface deformation of the whole Netherlands after PSI analysis. Proceedings of Fringe 2011 Workshop, Frascati, Italy, 19-23 September 2011, ESA Publications SP-697, 1-8.
- Curlander, J. C. (1982). Location of Spaceborne SAR Imagery. *IEEE Transactions on Geoscience and Remote Sensing*, *GE-20*(3), 359-364.  
<https://doi.org/10.1109/TGRS.1982.350455>
- Dabov, K., Foi, A., Katkovnik, V., & Egiazarian, K. (2007). Image denoising by sparse 3-D transform-domain collaborative filtering. *IEEE Transactions on Image Processing*, *16*(8), 2080-2095. <https://doi.org/10.1109/TIP.2007.901238>
- Davis, J. L., Wernicke, B. P., & Tamisiea, M. E. (2012). On seasonal signals in geodetic time series. *Journal of Geophysical Research: Solid Earth*, *117*(B1), B01403. <https://doi.org/10.1029/2011JB008690>
- Dawson, J., & Tregoning, P. (2007). Uncertainty analysis of earthquake source parameters determined from InSAR: A simulation study. *Journal of Geophysical Research: Solid Earth*, *112*(9), Article B09406.  
<https://doi.org/10.1029/2007JB005209>
- De Michele, M., Raucoules, D., Lasserre, C., Pathier, E., Klinger, Y., Van Woerd, J. D., De Sigoyer, J., & Xu, X. (2010). The Mw 7.9, 12 May 2008 Sichuan earthquake rupture measured by sub-pixel correlation of ALOS PALSAR amplitude images. *Earth, planets and space*, *62*(11), 875-879.  
<https://doi.org/10.5047/eps.2009.05.002>
- De Zan, F., & Guarnieri, A. M. (2006). TOPSAR: Terrain observation by progressive scans. *IEEE Transactions on Geoscience and Remote Sensing*, *44*(9), 2352-2360, Article 1677745. <https://doi.org/10.1109/TGRS.2006.873853>
- De Zan, F., Guarnieri, A. M., & Rocca, F. (2008). Advances in SAR interferometry for Sentinel-1 with TOPS. *Proceedings of the 2008 IEEE Radar Conference*. IEEE Radar Conference, Rome, Italy, 1-6.  
<https://doi.org/10.1109/radar.2008.4720871>
- Delacourt, C., Briole, P., & Achache, J. (1998). Tropospheric corrections of SAR interferograms with strong topography. Application to Etna. *Geophysical Research Letters*, *25*(15), 2849-2852. <https://doi.org/10.1029/98GL02112>
- Dereniowski, D., & Kubale, M. (2003). Cholesky factorization of matrices in parallel and ranking of graphs. International Conference on Parallel Processing and Applied Mathematics, Czestochowa, Poland, 985-992.  
[https://doi.org/10.1007/978-3-540-24669-5\\_127](https://doi.org/10.1007/978-3-540-24669-5_127)

- Didova, O., Gunter, B., Riva, R., Klees, R., & Roese-Koerner, L. (2016). An approach for estimating time-variable rates from geodetic time series. *Journal of Geodesy*, 90(11), 1207-1221. <https://doi.org/10.1007/s00190-016-0918-5>
- Doin, M. P., Lasserre, C., Peltzer, G., Cavalié, O., & Doubre, C. (2009). Corrections of stratified tropospheric delays in SAR interferometry: Validation with global atmospheric models. *Journal of Applied Geophysics*, 69(1), 35-50. <https://doi.org/10.1016/j.jappgeo.2009.03.010>
- Doin, M. P., Lodge, F., Guillaso, S., Jolivet, R., Lasserre, C., Ducret, G., Grandin, R., Pathier, E., & Pinel, V. (2011, 19-23 September). Presentation of the small baseline NSBAS processing chain on a case example: the Etna deformation monitoring from 2003 to 2010 using Envisat data. *ESA Fringe Symposium*, Frascati, Italy: ESA SP-697. 3434-3437 [https://earth.esa.int/documents/10174/1573056/Presentation\\_small\\_baseline\\_NSBAS\\_Etna\\_deformation\\_Envisat.pdf](https://earth.esa.int/documents/10174/1573056/Presentation_small_baseline_NSBAS_Etna_deformation_Envisat.pdf)
- Donelan, M. A., & Pierson Jr, W. J. (1987). Radar scattering and equilibrium ranges in wind-generated waves with application to scatterometry. *Journal of Geophysical Research*, 92(C5), 4971-5029. <https://doi.org/10.1029/JC092iC05p04971>
- Dong, S., Samsonov, S., Yin, H., Ye, S., & Cao, Y. (2014). Time-series analysis of subsidence associated with rapid urbanization in Shanghai, China measured with SBAS InSAR method. *Environmental Earth Sciences*, 72(3), 677-691. <https://doi.org/10.1007/s12665-013-2990-y>
- Ducret, G., Doin, M. P., Grandin, R., Lasserre, C., & Guillaso, S. (2011). DEM corrections before unwrapping in a Small Baseline strategy for InSAR time series analysis. *International Geoscience and Remote Sensing Symposium (IGARSS)*, 1353-1356. <https://doi.org/10.1109/IGARSS.2011.6049316>
- Ducret, G., Doin, M. P., Grandin, R., Lasserre, C., & Guillaso, S. (2014). DEM corrections before unwrapping in a small baseline strategy for InSAR time series analysis. *IEEE Geoscience and Remote Sensing Letters*, 11(3), 696-700, Article 6587729. <https://doi.org/10.1109/LGRS.2013.2276040>
- Dzurisin, D., Lisowski, M., & Wicks, C. W. (2009). Continuing inflation at Three Sisters volcanic center, central Oregon Cascade Range, USA, from GPS, leveling, and InSAR observations. *Bulletin of Volcanology*, 71(10), 1091-1110. <https://doi.org/10.1007/s00445-009-0296-4>
- Ebmeier, S. K., Biggs, J., Mather, T. A., & Amelung, F. (2013). Applicability of InSAR to tropical volcanoes: Insights from central america. *Geological Society Special Publication*, 380(1), 15-37. <https://doi.org/10.1144/SP380.2>
- Eineder, M., Hubig, M., & Milcke, B. (1998). Unwrapping large interferograms using the minimum cost flow algorithm. *Proceedings of the IGARSS '98 Sensing and Managing the Environment*. International Geoscience and Remote Sensing

Symposium (IGARSS), Seattle, WA, USA, 83-87.  
<https://doi.org/10.1109/igarss.1998.702806>

- Elliott, J. R., Biggs, J., Parsons, B., & Wright, T. J. (2008). InSAR slip rate determination on the Altyn Tagh Fault, northern Tibet, in the presence of topographically correlated atmospheric delays. *Geophysical Research Letters*, 35(12), Article L12309. <https://doi.org/10.1029/2008GL033659>
- Elliott, J. R., Walters, R. J., England, P. C., Jackson, J. A., Li, Z., & Parsons, B. (2010). Extension on the Tibetan plateau: Recent normal faulting measured by InSAR and body wave seismology. *Geophysical Journal International*, 183(2), 503-535. <https://doi.org/10.1111/j.1365-246X.2010.04754.x>
- Emardson, T. R., & Johansson, J. M. (1998). Spatial interpolation of the atmospheric water vapor content between sites in a ground-based GPS network. *Geophysical Research Letters*, 25(17), 3347-3350. <https://doi.org/10.1029/98GL02504>
- Emardson, T. R., Simons, M., & Webb, F. H. (2003). Neutral atmospheric delay in interferometric synthetic aperture radar applications: Statistical description and mitigation. *Journal of Geophysical Research: Solid Earth*, 108(5), ETG 4-1 - 4-8. <https://doi.org/10.1029/2002JB001781>
- Eshagh, M., & Alizadeh-Khameneh, M. A. (2015). The effect of constraints on bi-objective optimisation of geodetic networks. *Acta Geodaetica et Geophysica*, 50(4), 449-459. <https://doi.org/10.1007/s40328-014-0085-1>
- Eshagh, M., & Kiamehr, R. (2007). A strategy for optimum designing of the geodetic networks from the cost, reliability and precision views. *Acta Geodaetica et Geophysica Hungarica*, 42(3), 297-308. <https://doi.org/10.1556/AGeod.42.2007.3.4>
- Fang, D., Lv, X., Wang, Y., Lin, X., & Qian, J. (2016). A sparsity-based InSAR phase denoising algorithm using nonlocal wavelet shrinkage. *Remote Sensing*, 8(10), Article 830. <https://doi.org/10.3390/rs8100830>
- Farina, A., & Pardini, S. (1980). Survey of radar data-processing techniques in air-traffic-control and surveillance systems. *IEE Proceedings F: Communications Radar and Signal Processing*, 127(3), 190-204. <https://doi.org/10.1049/ip-f-1.1980.0030>
- Farr, T. G., & Kobrick, M. (2000). Shuttle radar topography mission produces a wealth of data. *Eos*, 81(48), 583-585. <https://doi.org/10.1029/EO081i048p00583>
- Farr, T. G., Rosen, P. A., Caro, E., Crippen, R., Duren, R., Hensley, S., Kobrick, M., Paller, M., Rodriguez, E., Roth, L., Seal, D., Shaffer, S., Shimada, J., Umland, J., Werner, M., Oskin, M., Burbank, D., & Alsdorf, D. E. (2007). The shuttle radar topography mission. *Reviews of Geophysics*, 45(RG2004), 1-33, Article 2005RG000183. <https://doi.org/10.1029/2005RG000183>

- Fattahi, H., Agram, P., & Simons, M. (2017). A Network-Based Enhanced Spectral Diversity Approach for TOPS Time-Series Analysis. *IEEE Transactions on Geoscience and Remote Sensing*, 55(2), 777-786, Article 7637021. <https://doi.org/10.1109/TGRS.2016.2614925>
- Fattahi, H., & Amelung, F. (2013). DEM error correction in InSAR time series. *IEEE Transactions on Geoscience and Remote Sensing*, 51(7), 4249-4259, Article 6423275. <https://doi.org/10.1109/TGRS.2012.2227761>
- Fattahi, H., & Amelung, F. (2015). InSAR bias and uncertainty due to the systematic and stochastic tropospheric delay. *Journal of Geophysical Research: Solid Earth*, 120(12), 8758-8773. <https://doi.org/10.1002/2015JB012419>
- Featherstone, W., Penna, N., Filmer, M., & Williams, S. (2015). Nonlinear subsidence at Fremantle, a long-recording tide gauge in the Southern Hemisphere. *Journal of Geophysical Research: Oceans*, 120(10), 7004-7014. <https://doi.org/10.1002/2015jc011295>
- Ferretti, A. (2014). *Satellite InSAR data: reservoir monitoring from space* (p. 160). EAGE Publications. <https://doi.org/10.3997/9789462820036>
- Ferretti, A., Fumagalli, A., Novali, F., Prati, C., Rocca, F., & Rucci, A. (2011). A new algorithm for processing interferometric data-stacks: SqueeSAR. *IEEE Transactions on Geoscience and Remote Sensing*, 49(9), 3460-3470, Article 5765671. <https://doi.org/10.1109/TGRS.2011.2124465>
- Ferretti, A., Prati, C., & Rocca, F. (2001). Permanent scatterers in SAR interferometry. *IEEE Transactions on Geoscience and Remote Sensing*, 39(1), 8-20. <https://doi.org/10.1109/36.898661>
- Fialko, Y., Sandwell, D., Simons, M., & Rosen, P. (2005). Three-dimensional deformation caused by the Bam, Iran, earthquake and the origin of shallow slip deficit. *Nature*, 435(7040), 295-299. <https://doi.org/10.1038/nature03425>
- Fialko, Y., Simons, M., & Agnew, D. (2001). The complete (3-D) surface displacement field in the epicentral area of the 1999 Mw 7.1 Hector Mine earthquake, California, from space geodetic observations. *Geophysical Research Letters*, 28(16), 3063-3066. <https://doi.org/10.1029/2001GL013174>
- Filmer, M. S., Williams, S. D. P., Hughes, C. W., Wöppelmann, G., Featherstone, W. E., Woodworth, P. L., & Parker, A. L. (2020). An experiment to test satellite radar interferometry-observed geodetic ties to remotely monitor vertical land motion at tide gauges. *Global and Planetary Change*, 185, Article 103084. <https://doi.org/10.1016/j.gloplacha.2019.103084>
- Foster, J., Brooks, B., Cherubini, T., Shacat, C., Businger, S., & Werner, C. L. (2006). Mitigating atmospheric noise for InSAR using a high resolution weather model. *Geophysical Research Letters*, 33(16), Article L16304. <https://doi.org/10.1029/2006GL026781>

- Foster, J., Kealy, J., Cherubini, T., Businger, S., Lu, Z., & Murphy, M. (2013). The utility of atmospheric analyses for the mitigation of artifacts in InSAR. *Journal of Geophysical Research: Solid Earth*, 118(2), 748-758. <https://doi.org/10.1002/jgrb.50093>
- Fournier, T., Pritchard, M. E., & Finnegan, N. (2011). Accounting for atmospheric delays in InSAR data in a search for long-wavelength deformation in South America. *IEEE Transactions on Geoscience and Remote Sensing*, 49(10 PART 2), 3856-3867, Article 5771553. <https://doi.org/10.1109/TGRS.2011.2139217>
- Fuhrmann, T., & Garthwaite, M. C. (2019). Resolving three-dimensional surface motion with InSAR: Constraints from multi-geometry data fusion. *Remote Sensing*, 11(3), Article 241. <https://doi.org/10.3390/rs11030241>
- Furuya, M., Mueller, K., & Wahr, J. (2007). Active salt tectonics in the Needles District, Canyonlands (Utah) as detected by interferometric synthetic aperture radar and point target analysis: 1992-2002. *Journal of Geophysical Research: Solid Earth*, 112(6), B06418, Article B06418. <https://doi.org/10.1029/2006JB004302>
- Galloway, D. L., Hudnut, K. W., Ingebritsen, S. E., Phillips, S. P., Peltzer, G., Rogez, F., & Rosen, P. A. (1998). Detection of aquifer system compaction and land subsidence using interferometric synthetic aperture radar, Antelope Valley, Mojave Desert, California. *Water Resources Research*, 34(10), 2573-2585. <https://doi.org/10.1029/98wr01285>
- Gatelli, F., Guarnieri, A. M., Parizzi, F., Pasquali, P., Prati, C., & Rocca, F. (1994). The Wavenumber Shift in SAR Interferometry. *IEEE Transactions on Geoscience and Remote Sensing*, 32(4), 855-865. <https://doi.org/10.1109/36.298013>
- Gerum, W., Lippert, G., Malzahn, P., & Schneider, K. (2001). 94-GHz TWT for military radar applications. *IEEE Transactions on Electron Devices*, 48(1), 72-73. <https://doi.org/10.1109/16.892170>
- Gesch, D. B., Muller, J. P., & Farr, T. G. (2006). The shuttle radar topography mission - Data validation and applications. *Photogrammetric Engineering and Remote Sensing*, 72(3), 233-235.
- Goel, K., & Adam, N. (2014). A distributed scatterer interferometry approach for precision monitoring of known surface deformation phenomena. *IEEE Transactions on Geoscience and Remote Sensing*, 52(9), 5454-5468, Article 6679273. <https://doi.org/10.1109/TGRS.2013.2289370>
- Goldstein, R. M. (1995). Atmospheric limitations to repeat-track radar interferometry. *Geophysical Research Letters*, 22(18), 2517-2520. <https://doi.org/10.1029/95GL02475>
- Goldstein, R. M., Engelhardt, H., Kamb, B., & Frolich, R. M. (1993). Satellite radar interferometry for monitoring ice sheet motion: Application to an Antarctic ice

- stream. *Science*, 262(5139), 1525-1530.  
<https://doi.org/10.1126/science.262.5139.1525>
- Goldstein, R. M., & Werner, C. L. (1998). Radar interferogram filtering for geophysical applications. *Geophysical Research Letters*, 25(21), 4035-4038.  
<https://doi.org/10.1029/1998gl900033>
- Golub, G. H., & Van Loan, C. F. (1996). *Matrix Computation*. (3rd ed.). The Johns Hopkins University Press.
- Gong, W., Meyer, F. J., Liu, S., & Hanssen, R. F. (2015). Temporal Filtering of InSAR Data Using Statistical Parameters from NWP Models. *IEEE Transactions on Geoscience and Remote Sensing*, 53(7), 4033-4044, Article 7036125.  
<https://doi.org/10.1109/TGRS.2015.2389143>
- Gong, W., Thiele, A., Hinz, S., Meyer, F. J., Hooper, A., & Agram, P. S. (2016). Comparison of small baseline interferometric SAR processors for estimating ground deformation. *Remote Sensing*, 8(4), 1-26, Article 330.  
<https://doi.org/10.3390/rs8040330>
- González, P. J., & Fernández, J. (2011). Error estimation in multitemporal InSAR deformation time series, with application to Lanzarote, Canary Islands. *Journal of Geophysical Research: Solid Earth*, 116(10), B10404, Article B10404.  
<https://doi.org/10.1029/2011JB008412>
- Gough, P. T., & Hawkins, D. W. (1997). Unified framework for modern synthetic aperture imaging algorithms. *International Journal of Imaging Systems and Technology*, 8(4), 343-358. [https://doi.org/10.1002/\(sici\)1098-1098\(1997\)8:4%3C343::aid-ima2%3E3.0.co;2-a](https://doi.org/10.1002/(sici)1098-1098(1997)8:4%3C343::aid-ima2%3E3.0.co;2-a)
- Gourmelen, N., Amelung, F., Casu, F., Manzo, M., & Lanari, R. (2007). Mining-related ground deformation in Crescent Valley, Nevada: Implications for sparse GPS networks. *Geophysical Research Letters*, 34(9), Article L09309.  
<https://doi.org/10.1029/2007GL029427>
- Gourmelen, N., Amelung, F., & Lanari, R. (2010). Interferometric synthetic aperture radar-GPS integration: Interseismic strain accumulation across the Hunter Mountain fault in the eastern California shear zone. *Journal of Geophysical Research: Solid Earth*, 115(9), 1-16, Article B09408.  
<https://doi.org/10.1029/2009JB007064>
- Grafarend, E. W., & Sansò, F. (1985). *Optimization and design of geodetic networks*. Springer-Verlag, Berlin Heidelberg New York Tokyo.  
<https://doi.org/10.1007/978-3-642-70659-2>
- Gray, A. L., Mattar, K. E., & Sofko, G. (2000). Influence of Ionospheric Electron Density Fluctuations on Satellite Radar Interferometry. *Geophysical Research Letters*, 27(10), 1451-1454. <https://doi.org/10.1029/2000GL000016>

- Griffiths, H., Knott, P., & Koch, W. (2019). Christian Hülsmeyer: Invention and Demonstration of Radar, 1904. *IEEE Aerospace and Electronic Systems Magazine*, 34(9), 56-60. <https://doi.org/10.1109/maes.2019.2934814>
- Guarnieri, A. M., & Tebaldini, S. (2007). Hybrid Cramér-Rao bounds for crustal displacement field estimators in SAR interferometry. *IEEE Signal Processing Letters*, 14(12), 1012-1015. <https://doi.org/10.1109/LSP.2007.904705>
- Guo, J., Zhou, L., Yao, C., & Hu, J. (2016). Surface subsidence analysis by multi-temporal InSAR and GRACE: A case study in Beijing. *Sensors (Switzerland)*, 16(9), 1-18, Article 1495. <https://doi.org/10.3390/s16091495>
- Hanssen, R. (2001). Radar Interferometry: Data Interpretation and Error Analysis. In *Remote Sensing and Digital Image Processing* (Vol. 2, pp. XVIII, 308). Springer Netherlands. <https://doi.org/10.1007/0-306-47633-9>
- Haykin, S., Stehwien, W., Deng, C., Weber, P., & Mann, R. (1991). Classification of radar clutter in an air traffic control environment. *Proceedings of the IEEE*, 79(6), 742-772. <https://doi.org/10.1109/5.90155>
- Hetland, E. A., Musé, P., Simons, M., Lin, Y. N., Agram, P. S., & DiCaprio, C. J. (2012). Multiscale InSAR Time Series (MInTS) analysis of surface deformation. *Journal of Geophysical Research: Solid Earth*, 117(B2), B02404. <https://doi.org/10.1029/2011JB008731>
- Hirt, C., Filmer, M. S., & Featherstone, W. E. (2010). Comparison and validation of the recent freely available ASTER-GDEM ver1, SRTM ver4.1 and GEODATA DEM-9s ver3 digital elevation models over Australia. *Australian Journal of Earth Sciences*, 57(3), 337-347. <https://doi.org/10.1080/08120091003677553>
- Hooper, A. (2008). A multi-temporal InSAR method incorporating both persistent scatterer and small baseline approaches. *Geophysical Research Letters*, 35(16), L16302, Article L16302. <https://doi.org/10.1029/2008GL034654>
- Hooper, A., Bekaert, D. P. S., Spaans, K., & Arıkan, M. (2012). Recent advances in SAR interferometry time series analysis for measuring crustal deformation. *Tectonophysics*, 514-517, 1-13. <https://doi.org/10.1016/j.tecto.2011.10.013>
- Hooper, A., Segall, P., & Zebker, H. A. (2007). Persistent scatterer interferometric synthetic aperture radar for crustal deformation analysis, with application to Volcán Alcedo, Galápagos. *Journal of Geophysical Research: Solid Earth*, 112(B7). <https://doi.org/10.1029/2006JB004763>
- Hooper, A., & Zebker, H. A. (2007). Phase unwrapping in three dimensions with application to INSAR time series. *Journal of the Optical Society of America A: Optics and Image Science, and Vision*, 24(9), 2737-2747. <https://doi.org/10.1364/JOSAA.24.002737>

- Hooper, A., Zebker, H. A., Segall, P., & Kampes, B. (2004). A new method for measuring deformation on volcanoes and other natural terrains using InSAR persistent scatterers. *Geophysical Research Letters*, 31(23), L23611. <https://doi.org/10.1029/2004GL021737>
- Hou, H. S., & Andrews, H. C. (1978). Cubic splines for image interpolation and digital filtering. *IEEE Transactions on Acoustics, Speech, and Signal Processing*, 26(6), 508-517. <https://doi.org/10.1109/TASSP.1978.1163154>
- Hu, J., Zhu, J. J., Li, Z. W., Ding, X. L., Wang, C. C., & Sun, Q. (2011). Robust estimating three-dimensional ground motions from fusion of InSAR and GPS measurements. 2011 International Symposium on Image and Data Fusion (ISIDF), 1-4. <https://doi.org/10.1109/isidf.2011.6024238>
- Huang, J., & Turcotte, D. L. (1989). Fractal mapping of digitized images: application to the topography of Arizona and comparisons with synthetic images. *Journal of Geophysical Research: Solid Earth*, 94(B6), 7491-7495. <https://doi.org/10.1029/JB094iB06p07491>
- Jackson, M., & Bilham, R. (1994). Constraints on Himalayan deformation inferred from vertical velocity fields in Nepal and Tibet. *Journal of Geophysical Research*, 99(B7), 13,897-813,912. <https://doi.org/10.1029/94jb00714>
- Janssen, V., Ge, L., & Rizos, C. (2004). Tropospheric corrections to SAR interferometry from GPS observations. *GPS solutions*, 8(3), 140-151. <https://doi.org/10.1007/s10291-004-0099-1>
- Jarlemark, P. O. J., & Emardson, T. R. (1998). Strategies for spatial and temporal extrapolation and interpolation of wet delay. *Journal of Geodesy*, 72(6), 350-355. <https://doi.org/10.1007/s001900050174>
- Jiang, L., Lin, H., Ma, J., Kong, B., & Wang, Y. (2011). Potential of small-baseline SAR interferometry for monitoring land subsidence related to underground coal fires: Wuda (Northern China) case study. *Remote Sensing of Environment*, 115(2), 257-268. <https://doi.org/10.1016/j.rse.2010.08.008>
- Johnson, H. O., & Agnew, D. C. (1995). Monument motion and measurements of crustal velocities. *Geophysical Research Letters*, 22(21), 2905-2908. <https://doi.org/10.1029/95GL02661>
- Jolivet, R., Agram, P. S., Lin, N. Y., Simons, M., Doin, M. P., Peltzer, G., & Li, Z. (2014). Improving InSAR geodesy using Global Atmospheric Models. *Journal of Geophysical Research: Solid Earth*, 119(3), 2324-2341. <https://doi.org/10.1002/2013JB010588>
- Jolivet, R., Grandin, R., Lasserre, C., Doin, M. P., & Peltzer, G. (2011). Systematic InSAR tropospheric phase delay corrections from global meteorological reanalysis data. *Geophysical Research Letters*, 38(17), L17311, Article L17311. <https://doi.org/10.1029/2011GL048757>

- Jolivet, R., Lasserre, C., Doin, M. P., Guillaso, S., Peltzer, G., Dailu, R., Sun, J., Shen, Z. K., & Xu, X. (2012). Shallow creep on the Haiyuan fault (Gansu, China) revealed by SAR interferometry. *Journal of Geophysical Research: Solid Earth*, 117(B6), B06401. <https://doi.org/10.1029/2011JB008732>
- Jónsson, S., Zebker, H., Segall, P., & Amelung, F. (2002). Fault slip distribution of the 1999 Mw 7.1 Hector Mine, California, earthquake, estimated from satellite radar and GPS measurements. *Bulletin of the Seismological Society of America*, 92(4), 1377-1389. <https://doi.org/10.1785/0120000922>
- Kampmann, G., & Krause, B. (1996). Balanced observations with a straight line fit. *Bollettino di Geodesia e Scienze Affini*, 55(2), 133-141.
- Khaki, M., Filmer, M. S., Featherstone, W. E., Kuhn, M., Bui, L. K., & Parker, A. L. (2019). A Sequential Monte Carlo Framework for Noise Filtering in InSAR Time Series. *IEEE Transactions on Geoscience and Remote Sensing*, 1-9. <https://doi.org/10.1109/TGRS.2019.2950353>
- Kim, E., & Sivits, K. (2015). Blended secondary surveillance radar solutions to improve air traffic surveillance. *Aerospace Science and Technology*, 45, 203-208. <https://doi.org/10.1016/j.ast.2015.05.018>
- Koch, K. R. (1985). First order design: Optimization of the configuration of a network by introducing small position changes. In E. W. Grafarend & F. Sansò (Eds.), *Optimization and design of geodetic networks* (pp. 56-73). Springer-Verlag, Berlin Heidelberg New York Tokyo. <https://doi.org/10.1007/978-3-642-70659-2>
- Kostenko, A. A., Nosich, A. I., & Tishchenko, I. A. (2001). Radar prehistory, Soviet side: Three-coordinate L-band pulse radar developed in Ukraine in the late 30's. *IEEE Antennas and Propagation Society, AP-S International Symposium (Digest)*, 4, 44-47. <https://doi.org/10.1109/APS.2001.959396>
- Krieger, G., Moreira, A., Fiedler, H., Hajnsek, I., Werner, M., Younis, M., & Zink, M. (2007). TanDEM-X: A satellite formation for high-resolution SAR interferometry. *IEEE Transactions on Geoscience and Remote Sensing*, 45(11), 3317-3340. <https://doi.org/10.1109/TGRS.2007.900693>
- Kroese, D. P., Brereton, T., Taimre, T., & Botev, Z. I. (2014). Why the Monte Carlo method is so important today. *Wiley Interdisciplinary Reviews: Computational Statistics*, 6(6), 386-392. <https://doi.org/10.1002/wics.1314>
- Kruskal, J. B., Jr. (1956). On the shortest spanning subtree of a graph and the traveling salesman problem. *Proceedings of the American Mathematical Society*, 7(1), 48-50. <https://doi.org/10.1090/S0002-9939-1956-0078686-7>
- Kuang, S. (1993). On optimal design of levelling networks. *Australian Surveyor*, 38(4), 257-273. <https://doi.org/10.1080/00050326.1993.10438874>

- Kuang, S. (1996). *Geodetic network analysis and optimal design: concepts and applications* (p. 368). [Book]. Ann Arbor Press, Chelsea, Michigan.
- Kummerow, C., Barnes, W., Kozu, T., Shiue, J., & Simpson, J. (1998). The Tropical Rainfall Measuring Mission (TRMM) sensor package. *Journal of Atmospheric and Oceanic Technology*, 15(3), 809-817. [https://doi.org/10.1175/1520-0426\(1998\)015<0809:TTRMMT>2.0.CO;2](https://doi.org/10.1175/1520-0426(1998)015<0809:TTRMMT>2.0.CO;2)
- Lam, N. S. (1983). Spatial interpolation methods: A review. *American Cartographer*, 10(2), 129-150. <https://doi.org/10.1559/152304083783914958>
- Lanari, R., Casu, F., Manzo, M., Zeni, G., Berardino, P., Manunta, M., & Pepe, A. (2007). An overview of the Small Baseline Subset algorithm: A DInSAR technique for surface deformation analysis. *Pure and Applied Geophysics*, 164(4), 637-661. <https://doi.org/10.1007/s00024-007-0192-9>
- Lanari, R., Lundgren, P., Manzo, M., & Casu, F. (2004). Satellite radar interferometry time series analysis of surface deformation for Los Angeles, California. *Geophysical Research Letters*, 31(23), 1-5. <https://doi.org/10.1029/2004GL021294>
- Lanari, R., Mora, O., Manunta, M., Mallorquí, J. J., Berardino, P., & Sansosti, E. (2004). A small-baseline approach for investigating deformations on full-resolution differential SAR interferograms. *IEEE Transactions on Geoscience and Remote Sensing*, 42(7), 1377-1386. <https://doi.org/10.1109/TGRS.2004.828196>
- Langbein, J. (2004). Noise in two-color electronic distance meter measurements revisited. *Journal of Geophysical Research: Solid Earth*, 109(B4), B04406. <https://doi.org/10.1029/2003JB002819>
- Langbein, J. (2008). Noise in GPS displacement measurements from Southern California and Southern Nevada. *Journal of Geophysical Research: Solid Earth*, 113(5), B05405, Article B05405. <https://doi.org/10.1029/2007JB005247>
- Langbein, J., & Johnson, H. (1997). Correlated errors in geodetic time series: Implications for time-dependent deformation. *Journal of Geophysical Research: Solid Earth*, 102(B1), 591-603. <https://doi.org/10.1029/96JB02945>
- Lauknes, T. R., Piyush Shanker, A., Dehls, J. F., Zebker, H. A., Henderson, I. H. C., & Larsen, Y. (2010). Detailed rockslide mapping in northern Norway with small baseline and persistent scatterer interferometric SAR time series methods. *Remote Sensing of Environment*, 114(9), 2097-2109. <https://doi.org/10.1016/j.rse.2010.04.015>
- Lauknes, T. R., Zebker, H. A., & Larsen, Y. (2011). InSAR deformation time series using an L1-norm small-baseline approach. *IEEE Transactions on Geoscience and Remote Sensing*, 49(1 PART 2), 536-546, Article 5512638. <https://doi.org/10.1109/TGRS.2010.2051951>

- Lee, C. W., Lu, Z., & Jung, H. S. (2012). Simulation of time-series surface deformation to validate a multi-interferogram InSAR processing technique. *International Journal of Remote Sensing*, 33(22), 7075-7087. <https://doi.org/10.1080/01431161.2012.700137>
- Lee, D. T., & Schachter, B. J. (1980). Two algorithms for constructing a Delaunay triangulation. *International Journal of Computer & Information Sciences*, 9(3), 219-242. <https://doi.org/10.1007/BF00977785>
- Levanon, N. (1988). *Radar principles* (p. 320). New York: Wiley.
- Li, Z., Fielding, E. J., Cross, P., & Muller, J. P. (2006). Interferometric synthetic aperture radar atmospheric correction: GPS topography-dependent turbulence model. *Journal of Geophysical Research: Solid Earth*, 111(2), Article B02404. <https://doi.org/10.1029/2005JB003711>
- Li, Z., Fielding, E. J., Cross, P., & Preusker, R. (2009). Advanced InSAR atmospheric correction: MERIS/MODIS combination and stacked water vapour models. *International Journal of Remote Sensing*, 30(13), 3343-3363. <https://doi.org/10.1080/01431160802562172>
- Li, Z., Muller, J. P., Cross, P., Albert, P., Fischer, J., & Bennartz, R. (2006). Assessment of the potential of MERIS near-infrared water vapour products to correct ASAR interferometric measurements. *International Journal of Remote Sensing*, 27(2), 349-365. <https://doi.org/10.1080/01431160500307342>
- Li, Z., Muller, J. P., Cross, P., & Fielding, E. J. (2005). Interferometric synthetic aperture radar (InSAR) atmospheric correction: GPS, Moderate Resolution Imaging Spectroradiometer (MODIS), and InSAR integration. *Journal of Geophysical Research: Solid Earth*, 110(3), 1-10, Article B03410. <https://doi.org/10.1029/2004JB003446>
- Lin, C., Vasić, S., Kilambi, A., Turner, B., & Zawadzki, I. (2005). Precipitation forecast skill of numerical weather prediction models and radar nowcasts. *Geophysical Research Letters*, 32(14), 1-4. <https://doi.org/10.1029/2005GL023451>
- Lin, Y. N. N., Simons, M., Hetland, E. A., Muse, P., & Dicaprio, C. (2010). A multiscale approach to estimating topographically correlated propagation delays in radar interferograms. *Geochemistry, Geophysics, Geosystems*, 11(9), 1-17, Article Q09002. <https://doi.org/10.1029/2010GC003228>
- Lohman, R. B., & Simons, M. (2005). Some thoughts on the use of InSAR data to constrain models of surface deformation: Noise structure and data downsampling. *Geochemistry, Geophysics, Geosystems*, 6(1), Q01007, Article Q01007. <https://doi.org/10.1029/2004GC000841>
- López-Martínez, C., & Fàbregas, X. (2002). Modeling and reduction of SAR interferometric phase noise in the wavelet domain. *IEEE Transactions on*

*Geoscience and Remote Sensing*, 40(12), 2553-2566.  
<https://doi.org/10.1109/TGRS.2002.806997>

- López-Quiroz, P., Doin, M.-P., Tupin, F., Briole, P., & Nicolas, J.-M. (2009). Time series analysis of Mexico City subsidence constrained by radar interferometry. *Journal of Applied Geophysics*, 69(1), 1-15.  
<https://doi.org/10.1016/j.jappgeo.2009.02.006>
- Lu, Z., & Dzurisin, D. (2014). InSAR Imaging of Aleutian Volcanoes. In *InSAR Imaging of Aleutian Volcanoes* (pp. 87-345). Springer-Verlag Berlin Heidelberg. <https://doi.org/10.1007/978-3-642-00348-6>
- Lu, Z., Kwoun, O., & Rykhus, R. (2007). Interferometric synthetic aperture radar (InSAR): Its past, present and future. *Photogrammetric Engineering and Remote Sensing*, 73(3), 217-221.
- Lu, Z., Masterlark, T., & Dzurisin, D. (2005). Interferometric synthetic aperture radar study of Okmok volcano, Alaska, 1992-2003: Magma supply dynamics and postemplacement lava flow deformation. *Journal of Geophysical Research: Solid Earth*, 110(2), 1-18, Article B02403.  
<https://doi.org/10.1029/2004JB003148>
- Lubitz, C., Motagh, M., Wetzel, H. U., & Kaufmann, H. (2013). Remarkable urban uplift in Staufen im Breisgau, Germany: Observations from terraSAR-X InSAR and leveling from 2008 to 2011. *Remote Sensing*, 5(6), 3082-3100.  
<https://doi.org/10.3390/rs5063082>
- Lundgren, P., Usai, S., Sansosti, E., Lanari, R., Tesauro, M., Fornaro, G., & Berardino, P. (2001). Modeling surface deformation observed with synthetic aperture radar interferometry at Campi Flegrei caldera. *Journal of Geophysical Research: Solid Earth*, 106(B9), 19355-19366, Article 2001jb000194.  
<https://doi.org/10.1029/2001JB000194>
- Lyon, T. J., Filmer, M. S., & Featherstone, W. E. (2018). On the Use of Repeat Leveling for the Determination of Vertical Land Motion: Artifacts, Aliasing, and Extrapolation Errors. *Journal of Geophysical Research: Solid Earth*, 123(8), 7021-7039. <https://doi.org/10.1029/2018JB015705>
- Lyons, S., & Sandwell, D. (2003). Fault creep along the southern San Andreas from interferometric synthetic aperture radar, permanent scatterers, and stacking. *Journal of Geophysical Research: Solid Earth*, 108(B1), ETG 11-11 - 11-24.  
<https://doi.org/10.1029/2002JB001831>
- Mahapatra, P. S., Samiei-Esfahany, S., & Hanssen, R. F. (2015). Geodetic Network Design for InSAR. *IEEE Transactions on Geoscience and Remote Sensing*, 53(7), 3669-3680, Article 7006811.  
<https://doi.org/10.1109/TGRS.2014.2381598>
- Mandelbrot, B. B. (1982). *The fractal geometry of nature*. (Vol. 2). WH Freeman, New York.

- Mandelbrot, B. B., & Van Ness, J. W. (1968). Fractional Brownian motions, fractional noises and applications. *SIAM review*, 10(4), 422-437. <https://doi.org/10.1137/1010093>
- Mao, A., Harrison, C. G., & Dixon, T. H. (1999). Noise in GPS coordinate time series. *Journal of Geophysical Research: Solid Earth*, 104(B2), 2797-2816. <https://doi.org/10.1029/1998JB900033>
- Mario Costantini, T. (1998). A novel phase unwrapping method based on network programming. *IEEE Transactions on Geoscience and Remote Sensing*, 36(3), 813-821. <https://doi.org/10.1109/36.673674>
- Martínez, C. L., Cànovas, X. F., & Chandra, M. (2001). SAR interferometric phase noise reduction using wavelet transform. *Electronics Letters*, 37(10), 649-651. <https://doi.org/10.1049/el:20010438>
- Massonnet, D., & Feigl, K. L. (1995). Discrimination of geophysical phenomena in satellite radar interferograms. *Geophysical Research Letters*, 22(12), 1537-1540. <https://doi.org/10.1029/95GL00711>
- Massonnet, D., & Feigl, K. L. (1998). Radar interferometry and its application to changes in the earth's surface. *Reviews of Geophysics*, 36(4), 441-500. <https://doi.org/10.1029/97RG03139>
- Massonnet, D., Feigl, K. L., Vadon, H., & Rossi, M. (1996). Coseismic deformation field of the M=6.7 Northridge, California Earthquake of January 17, 1994 recorded by two radar satellites using interferometry. *Geophysical Research Letters*, 23(9), 969-972. <https://doi.org/10.1029/96GL00729>
- Massopust, P. R. (1990). Fractal surfaces. *Journal of Mathematical Analysis and Applications*, 151(1), 275-290. [https://doi.org/10.1016/0022-247X\(90\)90257-G](https://doi.org/10.1016/0022-247X(90)90257-G)
- Mattar, K. E., & Gray, A. L. (2002). Reducing ionospheric electron density errors in satellite radar interferometry applications. *Canadian Journal of Remote Sensing*, 28(4), 593-600. <https://doi.org/10.5589/m02-051>
- Maxwell, J. C. (1865). *A dynamical theory of the electromagnetic field* (p. 54). Philosophical Transactions of the Royal Society of London. <https://doi.org/10.5479/sil.423156.39088007130693>
- Mesinger, F., DiMego, G., Kalnay, E., Mitchell, K., Shafran, P. C., Ebisuzaki, W., Jović, D., Woollen, J., Rogers, E., Berbery, E. H., Ek, M. B., Fan, Y., Grumbine, R., Higgins, W., Li, H., Lin, Y., Manikin, G., Parrish, D., & Shi, W. (2006). North American regional reanalysis. *Bulletin of the American Meteorological Society*, 87(3), 343-360. <https://doi.org/10.1175/BAMS-87-3-343>

- Meta, A., Mittermayer, J., Prats, P., Scheiber, R., & Steinbrecher, U. (2010). TOPS imaging with TerraSAR-X: Mode design and performance analysis. *IEEE Transactions on Geoscience and Remote Sensing*, 48(2), 759-769, Article 5280302. <https://doi.org/10.1109/TGRS.2009.2026743>
- Meyer, F., Bamler, R., Jakowski, N., & Fritz, T. (2006a). Methods for small scale ionospheric TEC mapping from broadband L-band SAR data. Proc. of International Geoscience and Remote Sensing Symposium (IGARSS), 3718-3721. <https://doi.org/10.1109/igarss.2006.957>
- Meyer, F., Bamler, R., Jakowski, N., & Fritz, T. (2006b). The potential of low-frequency SAR systems for mapping ionospheric TEC distributions. *IEEE Geoscience and Remote Sensing Letters*, 3(4), 560-564, Article 1715317. <https://doi.org/10.1109/LGRS.2006.882148>
- Moore, R. K., Claassen, J. P., & Lin, Y. H. (1981). Scanning Spaceborne Synthetic Aperture Radar with Integrated Radiometer. *IEEE Transactions on Aerospace and Electronic Systems*, AES-17(3), 410-421. <https://doi.org/10.1109/TAES.1981.309069>
- Mora, O., Mallorqui, J. J., & Broquetas, A. (2003). Linear and nonlinear terrain deformation maps from a reduced set of interferometric SAR images. *IEEE Transactions on Geoscience and Remote Sensing*, 41(10 PART I), 2243-2253. <https://doi.org/10.1109/TGRS.2003.814657>
- Moreira, A., Mittermayer, J., & Scheiber, R. (1996). Extended chirp scaling algorithm for air- and spaceborne SAR data processing in stripmap and ScanSAR imaging modes. *IEEE Transactions on Geoscience and Remote Sensing*, 34(5), 1123-1136. <https://doi.org/10.1109/36.536528>
- Mortazavi, S. M. J., Taeb, S., & Dehghan, N. (2013). Alterations of visual reaction time and short term memory in military radar personnel. *Iranian Journal of Public Health*, 42(4), 428-435.
- Motagh, M., Djamour, Y., Walter, T. R., Wetzell, H. U., Zschau, J., & Arabi, S. (2007). Land subsidence in Mashhad Valley, northeast Iran: Results from InSAR, levelling and GPS. *Geophysical Journal International*, 168(2), 518-526. <https://doi.org/10.1111/j.1365-246X.2006.03246.x>
- Munson, D. C., O'Brien, J. D., & Kenneth Jenkins, W. (1983). A Tomographic Formulation of Spotlight-Mode Synthetic Aperture Radar. *Proceedings of the IEEE*, 71(8), 917-925. <https://doi.org/10.1109/PROC.1983.12698>
- Murray, K. D., & Lohman, R. B. (2018). Short-lived pause in Central California subsidence after heavy winter precipitation of 2017. *Science Advances*, 4(8), Article eaar8144. <https://doi.org/10.1126/sciadv.aar8144>
- Nahin, P. J. (1992). Maxwell's grand unification. *IEEE Spectrum*, 29(3), 45. <https://doi.org/10.1109/6.123329>

- Ng, A. H. M., Ge, L., Yan, Y., Li, X., Chang, H. C., Zhang, K., & Rizos, C. (2010). Mapping accumulated mine subsidence using small stack of SAR differential interferograms in the Southern coalfield of New South Wales, Australia. *Engineering Geology*, 115(1-2), 1-15. <https://doi.org/10.1016/j.enggeo.2010.07.004>
- Nico, G. (2002). Exact closed-form geolocation for SAR interferometry. *IEEE Transactions on Geoscience and Remote Sensing*, 40(1), 220-222. <https://doi.org/10.1109/36.981366>
- Nico, G., Tomé, R., Catalao, J., & Miranda, P. M. A. (2011). On the use of the WRF model to mitigate tropospheric phase delay effects in SAR interferograms. *IEEE Transactions on Geoscience and Remote Sensing*, 49(12 PART 2), 4970-4976, Article 5951757. <https://doi.org/10.1109/TGRS.2011.2157511>
- Nitti, D. O., Bovenga, F., Nutricato, R., Intini, F., & Chiaradia, M. T. (2013). On the use of COSMO/SkyMed data and weather models for interferometric DEM generation. *European Journal of Remote Sensing*, 46(1), 250-271. <https://doi.org/10.5721/EuJRS20134614>
- Novellino, A., Cigna, F., Brahmi, M., Sowter, A., Bateson, L., & Marsh, S. (2017). Assessing the Feasibility of a National InSAR Ground Deformation Map of Great Britain with Sentinel-1. *Geosciences (Switzerland)*, 7(2), 1-14, Article 19. <https://doi.org/10.3390/geosciences7020019>
- Onn, F., & Zebker, H. A. (2006). Correction for interferometric synthetic aperture radar atmospheric phase artifacts using time series of zenith wet delay observations from a GPS network. *Journal of Geophysical Research: Solid Earth*, 111(9), Article B09102. <https://doi.org/10.1029/2005JB004012>
- Osmanoğlu, B., Dixon, T. H., Wdowinski, S., Cabral-Cano, E., & Jiang, Y. (2011). Mexico City subsidence observed with persistent scatterer InSAR. *International journal of applied earth observation and geoinformation*, 13(1), 1-12. <https://doi.org/10.1016/j.jag.2010.05.009>
- Papoutsis, I., Papanikolaou, X., Floyd, M., Ji, K. H., Kontoes, C., Paradissis, D., & Zacharis, V. (2013). Mapping inflation at Santorini volcano, Greece, using GPS and InSAR. *Geophysical Research Letters*, 40(2), 267-272. <https://doi.org/10.1029/2012GL054137>
- Parker, A. L., Biggs, J., & Lu, Z. (2014). Investigating long-term subsidence at Medicine Lake Volcano, CA, using multitemporal InSAR. *Geophysical Journal International*, 199(2), 844-859. <https://doi.org/10.1093/gji/ggu304>
- Parker, A. L., Biggs, J., & Lu, Z. (2016). Time-scale and mechanism of subsidence at Lassen Volcanic Center, CA, from InSAR. *Journal of Volcanology and Geothermal Research*, 320, 117-127. <https://doi.org/10.1016/j.jvolgeores.2016.04.013>

- Parker, A. L., Biggs, J., Walters, R. J., Ebmeier, S. K., Wright, T. J., Teanby, N. A., & Lu, Z. (2015). Systematic assessment of atmospheric uncertainties for InSAR data at volcanic arcs using large-scale atmospheric models: Application to the Cascade volcanoes, United States. *Remote Sensing of Environment*, 170, 102-114. <https://doi.org/10.1016/j.rse.2015.09.003>
- Parker, A. L., Filmer, M. S., & Featherstone, W. E. (2017). First results from sentinel-1A InSAR over Australia: Application to the Perth Basin. *Remote Sensing*, 9(3), Article 299. <https://doi.org/10.3390/rs9030299>
- Pepe, A., & Lanari, R. (2006). On the extension of the minimum cost flow algorithm for phase unwrapping of multitemporal differential SAR interferograms. *IEEE Transactions on Geoscience and Remote Sensing*, 44(9), 2374-2383, Article 1677747. <https://doi.org/10.1109/TGRS.2006.873207>
- Pepe, A., & Lanari, R. (2017). DEM correction and mean surface displacement rate retrieval from a stack of wrapped multi-temporal DInSAR interferograms. International Geoscience and Remote Sensing Symposium (IGARSS), 3798-3801. <https://doi.org/10.1109/IGARSS.2017.8127827>
- Pepe, A., Ortiz, A. B., Lundgren, P. R., Rosen, P. A., & Lanari, R. (2011). The Stripmap-ScanSAR SBAS Approach to Fill Gaps in Stripmap Deformation Time Series With ScanSAR Data. *IEEE Transactions on Geoscience and Remote Sensing*, 49(12 PART 1), 4788-4804, Article 6045335. <https://doi.org/10.1109/TGRS.2011.2167979>
- Pepe, A., Sansosti, E., Berardino, P., & Lanari, R. (2005). On the generation of ERS/ENVISAT DInSAR time-series via the SBAS technique. *IEEE Geoscience and Remote Sensing Letters*, 2(3), 265-269. <https://doi.org/10.1109/LGRS.2005.848497>
- Pettitt, A. N. (1976). A two-sample Anderson-Darling rank statistic. *Biometrika*, 63(1), 161-168. <https://doi.org/10.1093/biomet/63.1.161>
- Pilgram, B., & Kaplan, D. T. (1998). A comparison of estimators for 1/f noise. *Physica D: Nonlinear Phenomena*, 114(1-2), 108-122. [https://doi.org/10.1016/S0167-2789\(97\)00188-7](https://doi.org/10.1016/S0167-2789(97)00188-7)
- Pollitz, F. F., Peltzer, G., & Bürgmann, R. (2000). Mobility of continental mantle: Evidence from postseismic geodetic observations following the 1992 Landers earthquake. *Journal of Geophysical Research: Solid Earth*, 105(B4), 8035-8054, Article 1999jb900380. <https://doi.org/10.1029/1999JB900380>
- Prati, C., & Guarnieri, A. M. (1996). Scansar focusing and interferometry. *IEEE Transactions on Geoscience and Remote Sensing*, 34(4), 1029-1038. <https://doi.org/10.1109/36.508420>

- Press, W. H., Flannery, B. P., Teukolsky, S. A., & Vetterling, W. T. (1986). *Numerical recipes: The art of scientific computing* (p. 818). Cambridge University Press, New York.
- Pritchard, M. E., & Simons, M. (2002). A satellite geodetic survey of large-scale deformation of volcanic centres in the central Andes. *Nature*, *418*(6894), 167-171. <https://doi.org/10.1038/nature00872>
- Pritchard, M. E., Simons, M., Rosen, P. A., Hensley, S., & Webb, F. H. (2002). Co-seismic slip from the 1995 July 30 Mw = 8.1 Antofagasta, Chile, earthquake as constrained by InSAR and GPS observations. *Geophysical Journal International*, *150*(2), 362-376. <https://doi.org/10.1046/j.1365-246X.2002.01661.x>
- Raney, R. K. (1971). Synthetic Aperture Imaging Radar and Moving Targets. *IEEE Transactions on Aerospace and Electronic Systems*, *AES-7*(3), 499-505. <https://doi.org/10.1109/TAES.1971.310292>
- Raucoules, D., & De Michele, M. (2010). Assessing ionospheric influence on L-Band SAR data: Implications on coseismic displacement measurements of the 2008 Sichuan Earthquake. *IEEE Geoscience and Remote Sensing Letters*, *7*(2), 286-290, Article 5313903. <https://doi.org/10.1109/LGRS.2009.2033317>
- Raucoules, D., Maisons, C., Carnec, C., Le Mouelic, S., King, C., & Hosford, S. (2003). Monitoring of slow ground deformation by ERS radar interferometry on the Vauvert salt mine (France): Comparison with ground-based measurement. *Remote Sensing of Environment*, *88*(4), 468-478. <https://doi.org/10.1016/j.rse.2003.09.005>
- Refice, A., Bovenga, F., & Nutricato, R. (2006). MST-based stepwise connection strategies for multipass radar data, with application to coregistration and equalization. *IEEE Transactions on Geoscience and Remote Sensing*, *44*(8), 2029-2040, Article 1661792. <https://doi.org/10.1109/TGRS.2006.872907>
- Remy, D., Bonvalot, S., Briole, P., & Murakami, M. (2003). Accurate measurements of tropospheric effects in volcanic areas from SAR interferometry data: Application to Sakurajima volcano (Japan). *Earth and Planetary Science Letters*, *213*(3-4), 299-310. [https://doi.org/10.1016/s0012-821x\(03\)00331-5](https://doi.org/10.1016/s0012-821x(03)00331-5)
- Rexer, M., & Hirt, C. (2014). Comparison of free high resolution digital elevation data sets (ASTER GDEM2, SRTM v2.1/v4.1) and validation against accurate heights from the Australian National Gravity Database. *Australian Journal of Earth Sciences*, *61*(2), 213-226. <https://doi.org/10.1080/08120099.2014.884983>
- Rienecker, M. M., Suarez, M. J., Gelaro, R., Todling, R., Bacmeister, J., Liu, E., Bosilovich, M. G., Schubert, S. D., Takacs, L., Kim, G. K., Bloom, S., Chen, J., Collins, D., Conaty, A., Da Silva, A., Gu, W., Joiner, J., Koster, R. D., Lucchesi, R., Molod, A., Owens, T., Pawson, S., Pegion, P., Redder, C. R., Reichle, R., Robertson, F. R., Ruddick, A. G., Sienkiewicz, M., & Woollen, J.

- (2011). MERRA: NASA's modern-era retrospective analysis for research and applications. *Journal of Climate*, 24(14), 3624-3648. <https://doi.org/10.1175/JCLI-D-11-00015.1>
- Rignot, E., Bamber, J. L., Van Den Broeke, M. R., Davis, C., Li, Y., Van De Berg, W. J., & Van Meijgaard, E. (2008). Recent Antarctic ice mass loss from radar interferometry and regional climate modelling. *Nature Geoscience*, 1(2), 106-110. <https://doi.org/10.1038/ngeo102>
- Rocca, F. (2007). Modeling interferogram stacks. *IEEE Transactions on Geoscience and Remote Sensing*, 45(10), 3289-3299, Article 4305374. <https://doi.org/10.1109/TGRS.2007.902286>
- Rodríguez, E., & Martin, J. M. (1992). Theory and design of interferometric synthetic aperture radars. *IEE Proceedings, Part F: Radar and Signal Processing*, 139(2), 147-159. <https://doi.org/10.1049/ip-f-2.1992.0018>
- Rodríguez, E., Morris, C., Belz, J., Chapin, E., Martin, J., Daffer, W., & Hensley, S. (2005). *An assessment of the SRTM topographic products. Technical Report JPL D-31639*. [https://www2.jpl.nasa.gov/srtm/SRTM\\_D31639.pdf](https://www2.jpl.nasa.gov/srtm/SRTM_D31639.pdf)
- Rodríguez, E., Morris, C. S., & Belz, J. E. (2006). A global assessment of the SRTM performance. *Photogrammetric Engineering and Remote Sensing*, 72(3), 249-260. <https://doi.org/10.14358/PERS.72.3.249>
- Rofatto, V. F., Matsuoka, M. T., & Klein, I. (2018). Design of geodetic networks based on outlier identification criteria: An example applied to the leveling network. *Boletim de Ciencias Geodesicas*, 24(2), 152-170. <https://doi.org/10.1590/S1982-21702018000200011>
- Rosen, P. A., Gurrola, E. M., Agram, P., Cohen, J., Lavallo, M., Riel, B. V., Fattahi, H., Aivazis, M. A. G., Simons, M., & Buckley, S. M. (2018). The InSAR scientific computing environment 3.0: A flexible framework for NISAR operational and user-led science processing. *International Geoscience and Remote Sensing Symposium (IGARSS)*, 4897-4900. <https://doi.org/10.1109/IGARSS.2018.8517504>
- Rosen, P. A., Hensley, S., & Chen, C. (2010). Measurement and mitigation of the ionosphere in L-band Interferometric SAR data. *IEEE National Radar Conference - Proceedings*, 1459-1463. <https://doi.org/10.1109/RADAR.2010.5494385>
- Rosen, P. A., Hensley, S., Joughin, I. R., Li, F., Madsen, S. N., Rodriguez, E., & Goldstein, R. M. (2000, March). Synthetic Aperture Radar Interferometry. *Proceedings of the IEEE*, 333-382 <https://doi.org/10.1109/5.838084>
- Rosen, P. A., Hensley, S., Zebker, H. A., Webb, F. H., & Fielding, E. J. (1996). Surface deformation and coherence measurements of Kilauea Volcano, Hawaii, from SIR-C radar interferometry. *Journal of Geophysical Research E: Planets*, 101(E10), 23109-23125. <https://doi.org/10.1029/96JE01459>

- Saastamoinen, J. (2013). Atmospheric Correction for the Troposphere and Stratosphere in Radio Ranging Satellites. In *The use of artificial satellites for geodesy* (pp. 247--251). American Geophysical Union. <https://doi.org/10.1029/gm015p0247>
- Samsonov, S. (2010). Topographic correction for ALOS PALSAR interferometry. *IEEE Transactions on Geoscience and Remote Sensing*, 48(7), 3020-3027, Article 5444896. <https://doi.org/10.1109/TGRS.2010.2043739>
- Samsonov, S., d'Oreye, N., & Smets, B. (2013). Ground deformation associated with post-mining activity at the French-German border revealed by novel InSAR time series method. *International journal of applied earth observation and geoinformation*, 23(1), 142-154. <https://doi.org/10.1016/j.jag.2012.12.008>
- Sansosti, E. (2004). A simple and exact solution for the interferometric and stereo SAR geolocation problem. *IEEE Transactions on Geoscience and Remote Sensing*, 42(8), 1625-1634. <https://doi.org/10.1109/TGRS.2004.831442>
- Sansosti, E., Berardino, P., Manunta, M., Serafino, F., & Fornaro, G. (2006). Geometrical SAR image registration. *IEEE Transactions on Geoscience and Remote Sensing*, 44(10), 2861-2870, Article 1704979. <https://doi.org/10.1109/TGRS.2006.875787>
- Santoro, M., Wegmüller, U., & Askne, J. I. H. (2010). Signatures of ERS-Envisat interferometric SAR coherence and phase of short vegetation: An analysis in the case of maize fields. *IEEE Transactions on Geoscience and Remote Sensing*, 48(4 PART 1), 1702-1713, Article 5357427. <https://doi.org/10.1109/TGRS.2009.2034257>
- Scargle, J. D. (1982). Studies in astronomical time series analysis. II-Statistical aspects of spectral analysis of unevenly spaced data. *The Astrophysical Journal*, 263, 835-853. <https://doi.org/10.1086/160554>
- Scharroo, R., & Visser, P. (1998). Precise orbit determination and gravity field improvement for the ERS satellites. *Journal of Geophysical Research: Oceans*, 103(C4), 8113-8127. <https://doi.org/10.1029/97JC03179>
- Scheiber, R., & Moreira, A. (2000). Coregistration of interferometric SAR images using spectral diversity. *IEEE Transactions on Geoscience and Remote Sensing*, 38(5 I), 2179-2191. <https://doi.org/10.1109/36.868876>
- Schmidt, D. A., & Bürgmann, R. (2003). Time-dependent land uplift and subsidence in the Santa Clara valley, California, from a large interferometric synthetic aperture radar data set. *Journal of Geophysical Research: Solid Earth*, 108(B9). <https://doi.org/10.1029/2002JB002267>
- Schmitt, G. (1985a). Review of network designs: criteria, risk functions, design ordering. In E. W. Grafarend & F. Sansò (Eds.), *Optimization and design of*

- geodetic networks* (pp. 6-10). Springer-Verlag, Berlin Heidelberg New York Tokyo. <https://doi.org/10.1007/978-3-642-70659-2>
- Schmitt, G. (1985b). Third order design. In E. W. Grafarend & F. Sansò (Eds.), *Optimization and design of geodetic networks* (pp. 122-131). Springer-Verlag, Berlin Heidelberg New York Tokyo. <https://doi.org/10.1007/978-3-642-70659-2>
- Schroeder, M. R. (2015). Radar. In N. Xiang & G. M. Sessler (Eds.), *Acoustics, Information, and Communication* (pp. 329-336). Springer Nature Switzerland. [https://doi.org/10.1007/978-3-319-05660-9\\_17](https://doi.org/10.1007/978-3-319-05660-9_17)
- Sevgi, L. (2006). Radar. In R. Bansal (Ed.), *Engineering Electromagnetics* (pp. 1-35). Taylor & Francis Group. <https://doi.org/10.1201/9781420007251>
- Shanker, P., Casu, F., Zebker, H. A., & Lanari, R. (2011). Comparison of persistent scatterers and small baseline time-series InSAR results: A case study of the San Francisco bay area. *IEEE Geoscience and Remote Sensing Letters*, 8(4), 592-596, Article 5692806. <https://doi.org/10.1109/LGRS.2010.2095829>
- Shirzaei, M., & Bürgmann, R. (2012). Topography correlated atmospheric delay correction in radar interferometry using wavelet transforms. *Geophysical Research Letters*, 39(1), Article L01305. <https://doi.org/10.1029/2011GL049971>
- Shirzaei, M., & Bürgmann, R. (2013). Time-dependent model of creep on the Hayward fault from joint inversion of 18 years of InSAR and surface creep data. *Journal of Geophysical Research: Solid Earth*, 118(4), 1733-1746. <https://doi.org/10.1002/jgrb.50149>
- Shirzaei, M., & Walter, T. R. (2011). Estimating the effect of satellite orbital error using wavelet-based robust regression applied to InSAR deformation data. *IEEE Transactions on Geoscience and Remote Sensing*, 49(11 PART 2), 4600-4605, Article 5779729. <https://doi.org/10.1109/TGRS.2011.2143419>
- Short, N., Brisco, B., Couture, N., Pollard, W., Murnaghan, K., & Budkewitsch, P. (2011). A comparison of TerraSAR-X, RADARSAT-2 and ALOS-PALSAR interferometry for monitoring permafrost environments, case study from Herschel Island, Canada. *Remote Sensing of Environment*, 115(12), 3491-3506. <https://doi.org/10.1016/j.rse.2011.08.012>
- Simons, M., Fialko, Y., & Rivera, L. (2002). Coseismic deformation from the 1999 Mw 7.1 Hector Mine, California, earthquake as inferred from InSAR and GPS observations. *Bulletin of the Seismological Society of America*, 92(4), 1390-1402. <https://doi.org/10.1785/0120000933>
- Simons, M., & Rosen, P. A. (2015). Interferometric Synthetic Aperture Radar Geodesy. In G. Schubert (Ed.), *Treatise on Geophysics: Second Edition* (2nd ed., Vol. 3, pp. 339-385). Elsevier. <https://doi.org/10.1016/B978-0-444-53802-4.00061-0>

- Skamarock, W. C., Klemp, J. B., Dudhia, J., Gill, D. O., Barker, D. M., Wang, W., & Powers, J. G. (2008). A description of the Advanced Research WRF version 3. NCAR Technical note-475+ STR.
- Skolnik, M. I. (1970). *Radar Handbook*. McGraw-Hill Book Company.
- Skolnik, M. I. (2002). *Introduction to Radar Systems* (p. 784). (3rd ed.). McGraw-Hill Education, New York.
- Smith, B., & Sandwell, D. (2003). Accuracy and resolution of shuttle radar topography mission data. *Geophysical Research Letters*, 30(9), 20-21 - 20-24. <https://doi.org/10.1029/2002GL016643>
- Sowter, A., Bateson, L., Strange, P., Ambrose, K., & Fifiksiyafudin, M. (2013). DInSAR estimation of land motion using intermittent coherence with application to the south derbyshire and leicestershire coalfields. *Remote Sensing Letters*, 4(10), 979-987. <https://doi.org/10.1080/2150704X.2013.823673>
- Sun, L., Muller, J. P., & Chen, J. (2017). Time Series Analysis of Very Slow Landslides in the Three Gorges Region through Small Baseline SAR Offset Tracking. *Remote Sensing*, 9(12), 1-21, Article 1314. <https://doi.org/10.3390/rs9121314>
- Tatarskii, V. I. (1971). The effects of the turbulent atmosphere on wave propagation. *Jerusalem: Israel Program for Scientific Translations, 1971*, 472 pp.
- Teatini, P., Tosi, L., Strozzi, T., Carbognin, L., Cecconi, G., Rosselli, R., & Libardo, S. (2012). Resolving land subsidence within the Venice Lagoon by persistent scatterer SAR interferometry. *Physics and Chemistry of the Earth*, 40-41, 72-79. <https://doi.org/10.1016/j.pce.2010.01.002>
- Teunissen, P. J. G. (1985a). Quality control in geodetic networks. In E. W. Grafarend & F. Sansò (Eds.), *Optimization and design of geodetic networks* (pp. 526-547). Springer-Verlag, Berlin Heidelberg New York Tokyo. <https://doi.org/10.1007/978-3-642-70659-2>
- Teunissen, P. J. G. (1985b). Zero Order Design: Generalized Inverses, Adjustment, the Datum Problem and S-Transformations. In E. W. Grafarend & F. Sansò (Eds.), *Optimization and design of geodetic networks* (pp. 11-55). Springer-Verlag, Berlin Heidelberg New York Tokyo. <https://doi.org/10.1007/978-3-642-70659-2>
- Tian, X., Malhotra, R., Xu, B., Qi, H., & Ma, Y. (2018). Modeling orbital error in InSAR interferogram using frequency and spatial domain based methods. *Remote Sensing*, 10(4), Article 508. <https://doi.org/10.3390/rs10040508>
- Tizzani, P., Bernardino, P., Casu, F., Euillades, P., Manzo, M., Ricciardi, G. P., Zeni, G., & Lanari, R. (2007). Surface deformation of Long Valley caldera and Mono

- Basin, California, investigated with the SBAS-InSAR approach. *Remote Sensing of Environment*, 108(3), 277-289. <https://doi.org/10.1016/j.rse.2006.11.015>
- Tomiyasu, K. (1981). Conceptual Performance of a Satellite Borne, Wide Swath Synthetic Aperture Radar. *IEEE Transactions on Geoscience and Remote Sensing*, GE-19(2), 108-116. <https://doi.org/10.1109/TGRS.1981.350361>
- Torres, R., Snoeij, P., Geudtner, D., Bibby, D., Davidson, M., Attema, E., Potin, P., Rommen, B., Floury, N., Brown, M., Traver, I. N., Deghaye, P., Duesmann, B., Rosich, B., Miranda, N., Bruno, C., L'Abbate, M., Croci, R., Pietropaolo, A., Huchler, M., & Rostan, F. (2012). GMES Sentinel-1 mission. *Remote Sensing of Environment*, 120, 9-24. <https://doi.org/10.1016/j.rse.2011.05.028>
- Treuhaft, R. N., & Lanyi, G. E. (1987). The effect of the dynamic wet troposphere on radio interferometric measurements. *Radio science*, 22(2), 251-265. <https://doi.org/10.1029/RS022i002p00251>
- Tymofyeyeva, E., & Fialko, Y. (2015). Mitigation of atmospheric phase delays in InSAR data, with application to the eastern California shear zone. *Journal of Geophysical Research: Solid Earth*, 120(8), 5952-5963. <https://doi.org/10.1002/2015JB011886>
- Usai, S. (2003). A Least Squares Database Approach for SAR Interferometric Data. *IEEE Transactions on Geoscience and Remote Sensing*, 41(4 PART I), 753-760. <https://doi.org/10.1109/TGRS.2003.810675>
- Uys, D. (2016). InSAR: an introduction. *Preview*, 2016(182), 43-48. <https://doi.org/10.1071/pvv2016n182p43>
- Vaniček, P., Craymer, M. R., & Krakiwsky, E. J. (2001). Robustness analysis of geodetic horizontal networks. *Journal of Geodesy*, 75(4), 199-209. <https://doi.org/10.1007/s001900100162>
- Vaniček, P., & Krakiwsky, E. J. (1986). *Geodesy: the concepts*. (2nd ed.). Elsevier Science Publisher, Amsterdam, The Netherlands.
- Vaniček, P., Krakiwsky, E. J., Craymer, M. R., G., Y., & Ong, P. S. (1991). *Robustness analysis*. Department of Surveying Engineering, University of New Brunswick.
- Voronovich, A. G., & Zavorotny, V. U. (2001). Theoretical model for scattering of radar signals in Ku- and C-bands from a rough sea surface with breaking waves. *Waves Random Media*, 11(3), 247-269. <https://doi.org/10.1080/13616670109409784>
- Walters, R. J., Elliott, J. R., Li, Z., & Parsons, B. (2013). Rapid strain accumulation on the Ashkabad fault (Turkmenistan) from atmosphere-corrected InSAR. *Journal of Geophysical Research: Solid Earth*, 118(7), 3674-3690. <https://doi.org/10.1002/jgrb.50236>

- Webley, P. W., Bingley, R. M., Dodson, A. H., Wadge, G., Waugh, S. J., & James, I. N. (2002). Atmospheric water vapour correction to InSAR surface motion measurements on mountains: Results from a dense GPS network on Mount Etna. *Physics and Chemistry of the Earth*, 27(4-5), 363-370. [https://doi.org/10.1016/S1474-7065\(02\)00013-X](https://doi.org/10.1016/S1474-7065(02)00013-X)
- Wermuth, M., Hauschild, A., Montenbruck, O., & Kahle, R. (2012). TerraSAR-X precise orbit determination with real-time GPS ephemerides. *Advances in Space Research*, 50(5), 549-559. <https://doi.org/10.1016/j.asr.2012.03.014>
- Werninghaus, R., & Buckreuss, S. (2010). The TerraSAR-X mission and system design. *IEEE Transactions on Geoscience and Remote Sensing*, 48(2), 606-614, Article 5339240. <https://doi.org/10.1109/TGRS.2009.2031062>
- Wicks, C. W., Dzurisin, D., Ingebritsen, S., Thatcher, W., Lu, Z., & Iverson, J. (2002). Magmatic activity beneath the quiescent Three Sisters volcanic center, central Oregon Cascade Range, USA. *Geophysical Research Letters*, 29(7), 26-21 - 26-24. <https://doi.org/10.1029/2001GL014205>
- Williams, S., Bock, Y., & Fang, P. (1998). Integrated satellite interferometry: Tropospheric noise, GPS estimates and implications for interferometric synthetic aperture radar products. *Journal of Geophysical Research: Solid Earth*, 103(B11), 27051-27067, Article 98jb02794. <https://doi.org/10.1029/98jb02794>
- Williams, S. D. (2003). The effect of coloured noise on the uncertainties of rates estimated from geodetic time series. *Journal of Geodesy*, 76(9-10), 483-494. <https://doi.org/10.1007/s00190-002-0283-4>
- Williams, S. D. (2008). CATS: GPS coordinate time series analysis software. *GPS solutions*, 12(2), 147-153. <https://doi.org/10.1007/s10291-007-0086-4>
- Williams, S. D., Bock, Y., Fang, P., Jamason, P., Nikolaidis, R. M., Prawirodirdjo, L., Miller, M., & Johnson, D. J. (2004). Error analysis of continuous GPS position time series. *Journal of Geophysical Research: Solid Earth*, 109(B3). <https://doi.org/10.1029/2003JB002741>
- Xu, P. (1989). Multi-objective optimal second order design of networks. *Bulletin Géodésique*, 63(3), 297-308. <https://doi.org/10.1007/BF02520478>
- Xu, P. (1990). The second order design of geodetic networks using multiobjective optimization theory. *Bollettino di Geodesia e Scienze Affini*, 49(3), 185-194. <https://www.scopus.com/inward/record.uri?eid=2-s2.0-0025659044&partnerID=40&md5=9833d04348aca1b0ce4840775a3e7329>
- Xu, P. (1993). Multiobjective second order optimization and criterion matrix design. *Bollettino di Geodesia e Scienze Affini*, 52(4), 305-323. <https://www.scopus.com/inward/record.uri?eid=2-s2.0-0027869566&partnerID=40&md5=7ddebdfcb186bb9faedf80f09742aa7c>

- Xu, P., & Grafarend, E. W. (1995). A multi-objective second-order optimal design for deforming networks. *Geophysical Journal International*, 120(3), 577-589. <https://doi.org/10.1111/j.1365-246X.1995.tb01840.x>
- Xu, W. B., Li, Z. W., Ding, X. L., & Zhu, J. J. (2011). Interpolating atmospheric water vapor delay by incorporating terrain elevation information. *Journal of Geodesy*, 85(9), 555-564. <https://doi.org/10.1007/s00190-011-0456-0>
- Xu, X., Sandwell, D. T., Tymofyeyeva, E., Gonzalez-Ortega, A., & Tong, X. (2017). Tectonic and Anthropogenic Deformation at the Cerro Prieto Geothermal Step-Over Revealed by Sentinel-1A InSAR. *IEEE Transactions on Geoscience and Remote Sensing*, 55(9), 5284-5292, Article 7938636. <https://doi.org/10.1109/TGRS.2017.2704593>
- Yague-Martinez, N., Prats-Iraola, P., Gonzalez, F. R., Brcic, R., Shau, R., Geudtner, D., Eineder, M., & Bamler, R. (2016). Interferometric Processing of Sentinel-1 TOPS Data. *IEEE Transactions on Geoscience and Remote Sensing*, 54(4), 2220-2234, Article 7390052. <https://doi.org/10.1109/TGRS.2015.2497902>
- Yoon, Y. T., Eineder, M., Yague-Martinez, N., & Montenbruck, O. (2009). TerraSAR-X precise trajectory estimation and quality assessment. *IEEE Transactions on Geoscience and Remote Sensing*, 47(6), 1859-1868, Article 4760272. <https://doi.org/10.1109/TGRS.2008.2006983>
- Yu, C., Li, Z., & Penna, N. T. (2018). Interferometric synthetic aperture radar atmospheric correction using a GPS-based iterative tropospheric decomposition model. *Remote Sensing of Environment*, 204, 109-121. <https://doi.org/10.1016/j.rse.2017.10.038>
- Yu, C., Li, Z., Penna, N. T., & Crippa, P. (2018). Generic Atmospheric Correction Model for Interferometric Synthetic Aperture Radar Observations. *Journal of Geophysical Research: Solid Earth*, 123(10), 9202-9222. <https://doi.org/10.1029/2017JB015305>
- Yu, C., Penna, N. T., & Li, Z. (2017). Generation of real-time mode high-resolution water vapor fields from GPS observations. *Journal of Geophysical Research*, 122(3), 2008-2025. <https://doi.org/10.1002/2016JD025753>
- Yu, L., Yang, T., Zhao, Q., Liu, M., & Pepe, A. (2017). The 2015-2016 ground displacements of the Shanghai coastal area inferred from a combined COSMO-SkyMed/Sentinel-1 DInSAR analysis. *Remote Sensing*, 9(11), 1-19, Article 1194. <https://doi.org/10.3390/rs9111194>
- Yu, Q., Yang, X., Fu, S., Liu, X., & Sun, X. (2007). An adaptive contoured window filter for interferometric synthetic aperture radar. *IEEE Geoscience and Remote Sensing Letters*, 4(1), 23-26. <https://doi.org/10.1109/LGRS.2006.883527>

- Zebker, H. A., Rosen, P. A., Goldstein, R. M., Gabriel, A., & Werner, C. L. (1994). On the derivation of coseismic displacement fields using differential radar interferometry: the Landers earthquake. *Journal of Geophysical Research: Solid Earth*, 99(B10), 19,617-619,634. <https://doi.org/10.1029/94jb01179>
- Zebker, H. A., Rosen, P. A., & Hensley, S. (1997). Atmospheric effects in interferometric synthetic aperture radar surface deformation and topographic maps. *Journal of Geophysical Research B: Solid Earth*, 102(B4), 7547-7563, Article 96JB03804. <https://doi.org/0148-0227/97/96JB-03804509.00>
- Zebker, H. A., & Villasenor, J. (1992). Decorrelation in interferometric radar echoes. *IEEE Transactions on Geoscience and Remote Sensing*, 30(5), 950-959. <https://doi.org/10.1109/36.175330>
- Zha, X., Fu, R., Dai, Z., & Liu, B. (2008). Noise reduction in interferograms using the wavelet packet transform and wiener filtering. *IEEE Geoscience and Remote Sensing Letters*, 5(3), 404-408, Article 4505316. <https://doi.org/10.1109/LGRS.2008.916066>
- Zhang, J., Bock, Y., Johnson, H., Fang, P., Williams, S., Genrich, J., Wdowinski, S., & Behr, J. (1997). Southern California Permanent GPS Geodetic Array: Error analysis of daily position estimates and site velocities. *Journal of Geophysical Research: Solid Earth*, 102(B8), 18035-18055. <https://doi.org/10.1029/97JB01380>
- Zhao, W. (2017). *Small deformation detected from InSAR time-series and their applications in geophysics* [Doctoral dissertation, University of Miami]. [https://scholarship.miami.edu/discovery/fulldisplay/alma991031447547902976/01UOML\\_INST:ResearchRepository](https://scholarship.miami.edu/discovery/fulldisplay/alma991031447547902976/01UOML_INST:ResearchRepository)
- Zhou, L., Guo, J., Hu, J., Li, J., Xu, Y., Pan, Y., & Shi, M. (2017). Wuhan surface subsidence analysis in 2015-2016 based on sentinel-1A data by SBAS-InSAR. *Remote Sensing*, 9(10), 1-21, Article 982. <https://doi.org/10.3390/rs9100982>
- Zink, M., Bachmann, M., Bräutigam, B., Fritz, T., Hajnsek, I., Krieger, G., Moreira, A., & Wessel, B. (2014). TanDEM-X: The new global DEM takes shape. *IEEE Geoscience and Remote Sensing Magazine*, 2(2), 8-23, Article 6841793. <https://doi.org/10.1109/MGRS.2014.2318895>

**BIBLIOGRAPHY STATEMENT**

Every reasonable effort has been made to acknowledge the owners of copyright material. I would be pleased to hear from any copyright owner who has been omitted or incorrectly acknowledged.